

# IVW - Schriftenreihe Band 159

Leibniz-Institut für Verbundwerkstoffe GmbH  
Kaiserslautern

---

**Johannes Alexander Lutz**

**Contribution to the improvement of the  
characterisation of the friction and  
wear behaviour of coated ski bases on ice**

Bibliografische Information Der Deutschen Bibliothek

Die Deutsche Bibliothek verzeichnet diese Publikation in der Deutschen Nationalbibliografie; detaillierte bibliografische Daten sind im Internet über <<http://dnb.dnb.de>> abrufbar.

Bibliographic information published by Die Deutsche Bibliothek

Die Deutsche Bibliothek lists this publication in the Deutsche Nationalbibliografie; detailed bibliographic data is available in the Internet at <<http://dnb.dnb.de>>.

Herausgeber: Leibniz-Institut für Verbundwerkstoffe GmbH  
Prof. Dr.-Ing. Ulf Breuer  
Erwin-Schrödinger-Straße 58  
67663 Kaiserslautern  
<http://www.ivw.uni-kl.de>

Verlag: Leibniz-Institut für Verbundwerkstoffe GmbH

Druck: pri-me Printservice & Medienservice  
Barbarossastraße 1  
67655 Kaiserslautern  
D-386

© Leibniz-Institut für Verbundwerkstoffe GmbH, Kaiserslautern 2024

Alle Rechte vorbehalten, auch das des auszugsweisen Nachdrucks, der auszugsweisen oder vollständigen Wiedergabe (Photographie, Mikroskopie), der Speicherung in Datenverarbeitungsanlagen und das der Übersetzung.

Als Manuskript gedruckt. Printed in Germany.  
ISSN 1615-021X  
ISBN: 978-3-944440-56-9

# **Contribution to the improvement of the characterisation of the friction and wear behaviour of coated ski bases on ice**

Vom Fachbereich Maschinenbau und Verfahrenstechnik  
der Rheinland-Pfälzischen Technischen Universität Kaiserslautern-Landau  
zur Erlangung des akademischen Grades

**Doktor-Ingenieur (Dr.-Ing.)**

genehmigte

**Dissertation**

von

Herrn

Johannes Alexander Lutz, M. Eng  
aus Rodalben - Neuhof

Tag der mündlichen Prüfung: 11.12.2023

Dekan

Prof. Dr. rer. nat. Roland Ulber

Prüfungsvorsitzender

Prof. Dr.-Ing. Joachim Hausmann

1. Berichterstatter

Prof. Dr.-Ing. Ulf Breuer

2. Berichterstatter

Jun. Prof. Dr.-Ing. Manuel Oehler

3. Berichterstatter

Prof. Dr.-Ing. Jens Schuster

D386



## **Acknowledgements**

First, I would like to thank Prof. Ulf Breuer for supervising this thesis, Jun. Prof. Manuel Oehler for reviewing it and Prof. Joachim Hausmann for chairing the examination committee. Additional thanks go to Prof. Jens Schuster for his profound support throughout the years and to all colleagues at the University of Applied Sciences in Pirmasens for their friendly cooperation. Special thanks go to Dr.-Ing. Andreas Gebhard for his exceptional academic support, Jürgen Dully for his constant personal and technical support over all these years, David Müller for the great conversations and encouragement in all areas, and to Konstantin Luttenberger for his interdisciplinary support and excellent technical debates. Furthermore, I would also like to thank Amanda Wyatt for her fantastic linguistic support, Stefan Brunner for his help with the technical realisation of many key design concepts, and Jacqueline König-Lutz as well as Julia Luttenberger for reviewing my work along with their moral support. Last but not least, I would like to thank my family, especially Dieter and Harald Spieß, Maya Luttenberger as well as Emira vom Leykopf.

I dedicate this work to my parents Franz Ferdinand and Monika Lutz. Without their support, nothing would work anyway.

Rodalben-Neuhof, December 2023



## Contents

Contents .....	I
Abstract .....	V
Kurzfassung.....	VII
Glossary .....	XI
1 State of the art.....	1
1.1 Competition setup .....	1
1.1.1 Jumping hill.....	1
1.1.2 The judging of the ski jump.....	3
1.1.3 In-run velocity .....	4
1.1.4 Ice ramp.....	5
1.2 Ski characteristics .....	6
1.2.1 Length.....	6
1.2.2 Profile width .....	7
1.2.3 Contour, length and height of the shovel .....	7
1.2.4 Contour of the tail .....	8
1.2.5 Running surface.....	8
1.3 Contact pressure .....	10
1.4 Summary and comparison of publications in the field of friction on ice and snow.....	11
1.5 Conclusion and summary of the literature review.....	27
1.6 Comparison of contemporary ice-tribometers .....	31
2 Methodological design of an ice tribometer .....	35
2.1 Methodological design structure according to VDI 2221 .....	36
2.2 Planning phase .....	37
2.2.1 Target group report.....	39
2.2.2 Methods of product idea generation .....	40
2.2.3 General list of requirements.....	41
2.2.4 Conceptual phase.....	45

---

2.2.5	Black-Box .....	45
2.2.6	Functional structure .....	46
2.2.7	Subfunctions .....	48
2.2.7.1	Subfunction I: Type of movement .....	48
2.2.7.2	Subfunction II: Mounting of the ski base sample .....	49
2.2.7.3	Subfunction III: Mounting of the ice sample .....	49
2.2.7.4	Subfunction IV: Load application .....	50
2.2.7.5	Subfunction V: Friction measurement.....	50
2.2.7.6	Subfunction VI: Cooling .....	50
2.2.8	List of requirements allocated to subfunctions .....	50
2.3	Solution concept for subfunction I: Type of movement.....	54
2.4	Solution concept for subfunction II: Mounting of the ski base sample .....	57
2.5	Solution concept for subfunction III: Mounting of the ice sample.....	58
2.6	Solution concept for subfunction IV: Load application .....	59
2.7	Solution concept for subfunction V: Friction measurement .....	60
2.8	Solution concept for subfunction VI: Cooling .....	61
2.9	Weighting factors determination .....	61
2.10	Assessment for subfunction VI .....	63
2.11	Morphological box – the determination of the overall function.....	63
2.12	Quality function deployment (QFD) .....	67
3	Ice tribometer architecture .....	73
3.1	Proof of concept .....	73
3.1.1	Compulsory calculations .....	74
3.1.1.1	Operating pattern.....	74
3.1.1.2	Dimensioning of the motor.....	74
3.1.1.3	Preload force .....	76
3.1.1.4	Torsion analysis of the driving shaft .....	77
3.1.1.5	Bending analysis of the driving shaft .....	77
3.1.1.6	Bending analysis of the plate's guidance.....	77



---

3.1.1.7	Bending analysis of the parallel springs .....	77
3.1.2	Frame and base .....	79
3.1.3	Main rollers and bearings .....	80
3.1.4	Weight force and force measurement.....	82
3.2	Ice tribometer .....	84
3.2.1	Frame design .....	85
3.2.2	Bearings .....	86
3.2.3	Guidance rollers .....	87
3.2.4	Carriage and force measurement.....	88
3.2.5	Weight force .....	90
3.2.6	Ice sample .....	94
3.2.7	Ski base sample .....	96
3.2.8	Motor .....	97
3.2.9	Concept visualisation.....	97
3.2.10	Parameter settings of the tribometer .....	99
4	Ice tribometer verification .....	101
4.1	Sample preparation .....	101
4.2	Surface characterisation.....	101
4.3	Tribometer experiments .....	105
4.4	Precision analysis.....	110
4.5	Results and discussion.....	114
4.5.1	Fluorine content experiments .....	114
4.5.2	Surface roughness .....	117
4.5.3	Surface structure .....	121
4.5.4	Wear-related surface alteration .....	122
4.5.5	Contact angle measurements.....	123
4.5.6	Sliding speed and temperature.....	125
4.5.7	Acceleration and deceleration .....	126
4.5.8	Contact pressure .....	130
5	Limitations .....	133

---

6	Summary .....	135
	References .....	139
	Figures.....	150
	Tables.....	153
	Formulas.....	155
	Appendix.....	156
	Publications contributions .....	194
	Conference contributions.....	194
	Patents .....	194
	Curriculum Vitae .....	195

## Abstract

In contrast to motorbike tyres, whose friction during cornering has to be as high as possible, the desired effect in skiing is the opposite, that of low friction. The reduced friction between skis and ice or snow is made possible by a film of meltwater that forms as a function of friction power. To support this friction mechanism, skis are waxed with different waxes in both hobby and professional sports, depending on a variety of conditions. Waxes with fluorine additives show best performance in most conditions, corresponding to the lowest friction coefficients. However, for health and environmental reasons, the International Ski Federation (FIS) and the Biathlon Union (IBU) have imposed a complete ban on fluorine additives at all FIS races and IBU events with effect from the 2023/2024 season. As a result, wax manufacturers are required to develop and extensively test fluorine-free waxes in order to remain competitive.

Traditional tests take place either indoors or outdoors in the field. Athletes, who complete a particular distance and whose time is measured, also note the impressions that the prepared skis provide to the skiers. The time and cost involved in numerous individual tests is a drawback, and the presence of only a single type of snow in the hall or field, air resistance, changing environmental conditions and variations in the athlete's movement, limit the depth of information. For the need of reducing the time-consuming procedure of indoor and outdoor tests, a tribometer offers a solution where friction measurements can be performed on a laboratory scale. Due to the consistent adjustable conditions such as temperature, speed and load applied to the friction partners, scientific studies can be carried out with reduced disturbance variables. At present, the tribometric results of laboratory instruments for predicting friction values do not translate into application in practice. The reasons for this are the compromises that have to be made in the design of the tribometers.

This work reviews the existing tribometers for their operating conditions and confirms the need for a scientific method of characterising different waxes. In order to fill the gap between friction results obtained in laboratory tests which cannot yet be used in the selection of waxes, and traditional field tests, this thesis is dedicated to the methodical design and manufacture of a linear tribometer capable of measuring friction between a ski base made of UHMWPE (ultra high molecular weight polyethylene) and an ice

sample. The tribometer provides for the first time results that allow differentiating between different modified waxes with regard to their running performance. Friction-influencing factors such as speed, temperature and the surface pressure below the ski base can be adjusted within the range relevant for ski sports. Furthermore, the laboratory-scale test stand, which is located in a cold chamber, is capable of accommodating not only typical ski jumping base lengths and widths, but also cross-country and alpine ski bases. To verify the tribometer, a ski base is treated with three waxes of different fluorine content and measured comparatively. With a minimum of 95% confidence, the friction differences between the tested waxes depending on their fluorine content is validated and proven at the end of this work.

## Kurzfassung

Im Gegensatz zu Motorradreifen, deren Reibung bei Kurvenfahrten möglichst hoch sein sollte, ist beim Skifahren das Gegenteil erwünscht, nämlich eine möglichst geringe Reibung. Die reduzierte Reibung zwischen Ski und Eis beziehungsweise Schnee, wird durch einen Schmelzwasserfilm ermöglicht, welcher sich in Abhängigkeit der Reibungskraft bildet. Um diesen Reibungsmechanismus zu unterstützen, werden die Ski-beläge aus ultrahochmolekularem Polyethylen sowohl im Hobby- als auch im Profisport, in Abhängigkeit der vorherrschenden Bedingungen, mit unterschiedlichen Schlif-fen versehen, als auch mit Wachsen behandelt. Wachse mit fluorierten Additiven zeigen bei den häufigsten Bedingungen die beste Performance, also den niedrigsten Reibungskoeffizienten. Jedoch aus Gründen des Gesundheits- und Umweltschutzes, haben der internationale Skiverband (FIS) und der Biathlonverband (IBU) für die Saison 2023/2024 ein komplettes Verbot von Fluoradditiven bei allen FIS-Rennen und IBU-Veranstaltungen verhängt. Dies hat zur Folge, dass die Wachshersteller gezwungen sind, um weiter wettbewerbsfähig zu sein, fluorfreie Zusatzstoffe zu entwickeln und diese auch ausgiebig testen müssen. Traditionelle Gleittests zur Auswahl von Ski, Belägen, Schliffen und Wachsen finden entweder in der Skihalle oder im Freien statt. Bewertungskriterien sind zum einen die gemessene Zeit von Skifahrern, die eine definierte Strecke zurücklegen und zudem die Fahreindrücke, welche den Fahrern während der Fahrt vermittelt werden. Die Vorteile liegen im Fall der Skihalle bei der Konstanz der äußeren Bedingungen im Vergleich zu den Feldtests, welche zeitlich und geografisch nah an den Wettkämpfen stattfinden können. Eine ausreichende Vorbereitung und Erfahrung bezüglich der lokalen Gegebenheiten ist hierfür jedoch Voraussetzung. Der Zeit- und Kostenaufwand für die zahlreichen Einzeltests stellt bei beiden Varianten einen entscheidenden Nachteil dar und das Vorhandensein von nur einer Schneesorte in der Halle, eine begrenzte Testkapazität pro Testtag, der sich ändernde Luftwiderstand je nach Fahrerposition, die wechselnden Umgebungsbedingungen und die Schwankungen in der Bewegung des Sportlers schränken die Informationstiefe ebenfalls ein.

Um die zeitaufwändige Prozedur von Indoor- und Outdoor-Tests zu reduzieren, bietet ein Tribometer, mit dessen Hilfe Reibungsmessungen im Labormaßstab bei gleichzei-

tiger Steuerung der äußeren Bedingungen durchgeführt werden können, eine mögliche Lösung. Mittels konstant einstellbarer Parameter wie Temperatur, Geschwindigkeit und Belastung der Probe können wissenschaftliche Untersuchungen mit reduziertem Störgrößenumfang durchgeführt werden. Von Laborgeräten zur Vorhersage von Wachseignungen ermittelte tribometrische Ergebnisse nehmen derzeit in der Praxis nur eine untergeordnete Rolle ein. Die Gründe dafür liegen in den Kompromissen, wie z.B. Probengröße, Geschwindigkeit und Last, welche bei der Konstruktion der Tribometer eingegangen werden müssen.

In dieser Arbeit werden die vorhandenen Tribometer in Bezug auf ihre Einsatzfähigkeit überprüft und die Notwendigkeit einer wissenschaftlichen Methode zur Charakterisierung unterschiedlicher Wachse bestätigt. Um die Lücke zwischen Feldtests und verwendbaren Reibungsergebnissen aus Labortests zu schließen, widmet sich diese Arbeit der methodischen Konstruktion und Fertigung eines Linear-Tribometers, mit dessen Hilfe wachsende Reibkraftunterschiede zwischen einem Skibelag aus ultrahochmolekularem Polyethylen (UHMWPE) und einer Eisplatte gemessen werden können. Die notwendigen Anforderungen an die Unterfunktionen der Baugruppenkonstruktion wurden mittels Lastenheft definiert und Teillösungen mit Hilfe von Gewichtsfaktoren bewertet. Eine zuvor durchgeführte Machbarkeitsstudie half Schwachpunkte für die finale Lösungsvariante zu ermitteln und basierend auf diesen Ergebnissen wurde das Konzept mit der höchsten Bewertung gefertigt und in Betrieb genommen. Der in einer Kältekammer untergebrachte Platte-Platte-Prüfstand im Labormaßstab ist in der Lage, neben skisprungtypischen Belagslängen und -breiten auch Langlauf- und Alpinbeläge aufzunehmen. Der in Meterware erhältliche Skisprungbelag wird an den Enden geschäftet, verklebt und so zu einem endlosen Band verbunden. Ähnlich einem Förderband bringen zwei Walzen den Belag, unter Spannung stehend, in Rotation. Eine Vorrichtung mit montierten gummierten Rollen leitet die Normalkraft auf den Skibelag und auf die sich darunter befindliche Eisprobe. Abhängig von den aufgelegten Gewichtsscheiben, kann die Kraft in Stufen eingestellt werden und führt so zu unterschiedlichen Flächenpressungen unter dem Skibelag.

Das Auslenken der Eisprobe infolge der entstehenden Reibung führt zu einer Betätigung eines Kraftaufnehmers, welcher mit der Eisprobe auf einem Gleittisch federvor-

gespannt montiert ist. Mit Hilfe des Tribometers können Messparameter wie Geschwindigkeit, Beschleunigung, Temperatur und Flächenpressung im skisportrelevanten Bereich frei eingestellt werden, so dass der Prüfstand hierdurch skidisziplinübergreifend einsetzbar ist.

Die Verifizierung des Tribometers erfolgt durch stationäre Versuchsreihen unter Verwendung eines Belages ohne Strukturierung und drei applizierten Flüssigleitwachsen gleicher Basis, jedoch mit unterschiedlichem Fluorgehalt. Nach einer gewährten Trocknungszeit wird das aufgetragene Wachs mit einer Nylonbürste ausgebürstet und für jede intermittierende Messreihe wird eine neue Eisprobe eingelegt. Zur Bestimmung der mittleren Reibungskraft eines Wachses werden jeweils 100 konsekutive Messungen bei 3 m/s und 140 N Normalkraft durchgeführt und der Mittelwert im Bereich der konstanten Geschwindigkeit erfasst. Zur Wiederverfestigung eines möglicherweise entstehenden Wasserfilms wird zudem eine Pausenzeit zwischen den Messungen eingehalten. Für jede Wachsmodifikation wird die Prozedur insgesamt sechsmal wiederholt. Im Bereich der stationären Ausprägung der Messwerte wird schließlich der jeweilige Gesamtmittelwert für ein Wachs bestimmt.

Mit einer Konfidenz von mindestens 95% konnten die Unterschiede hinsichtlich der mittleren Reibkraft zwischen den getesteten Wachsen in Abhängigkeit von ihrem Fluorgehalt validiert und nachgewiesen werden. Es konnte gezeigt werden, dass während den gemessenen Bedingungen ein steigender Fluoradditivanteil eine signifikant geringere Reibung erzeugt und dies der Eignungsreihenfolge des Deutschen Skiverbandes und des Wachsherstellers entspricht. Weiterhin konnte das Vorhandensein eines Mischreibungsregimes mit ausgeprägtem Festkörperkontakt bei den Versuchen mittels Profilometrie nachgewiesen werden.

Das Tribometer liefert erstmals Ergebnisse, die es erlauben, zwischen unterschiedlich fluorierten Wachsen hinsichtlich ihres Laufverhaltens zu differenzieren. Die im Labor gemessenen tribometrischen Werte machen zwar Hallen- und Feldversuche nicht gänzlich obsolet, jedoch stellen sie eine Möglichkeit zur Vorselektierung von Wachsupadditiven dar. Die sinnvolle Kombination der verschiedenen Skitests erlaubt schließlich eine schnellere und kostengünstigere Beurteilung des Laufverhaltens der optimierungsfähigen Parameter: Ski(-belag), Schliff und Wachs.





## Glossary

### Abbreviations and Acronyms

---

AFM	Atomic force microscope
Avg	Average
BMI	Body mass index
BPMN	Business process model and notation
COF	Coefficient of friction
CSD	Constant speed duration
DIN	German institute for standardization
DSV	German Ski Association
FIS	International Ski and Snowboard Federation
$H_0$	Null hypothesis
$H_1$	Alternative hypothesis
HoQ	House of quality
HS	Hill size
ICR	International ski competition rules
ISL	Inter-segment latency
L-Point	End of the landing area
PA	Polyamide
PE	Polyethylene
PTFE	Polytetrafluoroethylene
QFD	Quality function deployment
T-Point	Edge of the ramp
UHMWPE	Ultra high molecular weight polyethylene
VDI	The association of German engineers
Wf	Water film
$X_{1-2}$	Mean values

### Latin symbols

---

A	$\text{mm}^2$	Cross section
d	mm	Diameter of the driven roller
E	MPa	Young's modulus
F	N	Force
$F_C$	N	Circumferential force
$F_{\text{ice}}$	N	Friction force ice sample
$F_N$	N	Normal force

$F_P$	N	Preload force
$F_{PTFE}$	N	Friction force PTFE plate
$h$	$\mu\text{m}$	Water film thickness
$I$	$\text{mm}^4$	Area moment of inertia
$L$	mm	Length
$M_a$	Nm	Acceleration torque
$M_l$	Nm	Load torque
$m_L$	kg/m	Length weight of the belt
$M_t$	Nm	Starting torque
$n$		Sample rate
$n_{in}$	$\text{min}^{-1}$	Difference in rotational speed
$R_a$	$\mu\text{m}$	Arithmetical mean deviation of the assessed profile, a roughness parameter
$R_{p0.2}$	N	Yield strength
$R_t$	$\mu\text{m}$	Total height of profile is the vertical distance between the maximum profile peak height and the maximum profile valley depth along the evaluation length
$R_z$	$\mu\text{m}$	Average of the maximum peak to valley heights of the various sampling lengths of a surface profile
$s$	m	Sliding distance
$t$	s	Time
$t_a$	s	Acceleration time
$T_{air}$	$^{\circ}\text{C}$	Ambient temperature
$v_{max}$	m/s	Maximum speed
wt.-%	%	Weight percentage

### Greek symbols

---

$\sigma_i^2$		Variance
$\mu$		Coefficient of friction
$\Delta$	mm	Displacement
$\Theta$	$\text{kgm}^2$	Mass moment of inertia
$\tau_t$	Nm	Maximum torque
$\varphi$	rad	Belt's contact angle
$\lambda$		Dimensionless film parameter, the lambda ratio
$\sigma$	$\mu\text{m}$	Combined root mean square roughness

# 1 State of the art

Ski jumping as well as cross-country, nordic and alpine skiing are organised by the International Ski and Snowboard Federation (FIS) with competitions held at international level.

## 1.1 Competition setup

### 1.1.1 Jumping hill

In professional ski jumping the approach is performed on an artificial tower, the jumping hill. Jumping hills that are homologated by the FIS, are in compliance with the International Ski Competition Rules (ICR) [2] and with the implementing provisions of the “Construction Norm” [3]. Determined by the FIS in its competition rules, the jumping hills are classified in Hill Sizes (HS), more precisely in the distance of the T-Point, the edge of the ramp, to the L-Point, the end of the landing area (see Figure 1.1). The classification of the jumping hills is shown in Table 1.1 below with the declaration for the jumping hill’s width and respective width shown in Figure 1.1.

Table 1.1: Classification of jumping hills [2]

Description	Width “HS”	Respective width “w”
Small hills	To 49 m	To 44 m
Medium hills	50 m to 84 m	45 m to 74 m
Normal hills	85 m to 109 m	75 m to 99 m
Large hills	110 m and larger	100 m and larger
Flying hills	185 m and larger	170 m and larger

The HS is directly proportional to the length of the in-run section and thus to the jumping distance the jumper can possibly achieve. More in-run length therefore equals more jumping distance.

Table 1.2: Nomenclature for Figure 1.1

<b>Indices In-run characteristics</b>	
A	highest start place
B	lowest start place
E <sub>1</sub>	the beginning of the radius curve
E <sub>2</sub>	the end of the curve, the beginning of the take-off
T	the edge of the take-off
e <sub>1</sub>	the length of the in-run from the highest start place to the edge of the take-off table
e <sub>2</sub>	the length of the in-run from the lowest start place to the edge of the take-off table
e <sub>s</sub>	the length of the starting place area
t	the length of the take-off
Y	the gradient of the straight section of the in-run
$\alpha$	the gradient of the take-off
r <sub>1</sub>	the radius of the curve of the in-run at point E <sub>2</sub>

<b>Indices Profile of the landing area</b>	
T	the edge of the take-off of the hill (= coordinate origin)
s	the height of the take-off
P	the beginning of the landing area
K	construction point
L	the end of the landing area
U	the start of the outrun area, lowest point of the profile
HS	the measured distance (Hill Size) from the edge to the take-off to the end of the landing area L
W	distance between the edge of the take-off and the construction point K
H	the height difference from the edge of the take-off to the K point
N	the horizontal distance from the edge of the take-off to the K point
z <sub>U</sub>	the height difference from the edge of the take-off to the lowest point U
l <sub>1</sub>	the length of the curve P-K
l <sub>2</sub>	the length of the curve K-L
L	the length of the curve of the landing area P-L
A	the length of the outrun
B <sub>o</sub>	the tangent angle of the landing hill knoll at the base of the take-off
$\beta_P$	the tangent angle at P point
B	the tangent angle at K point
$\beta_L$	the tangent angle at L
r <sub>L</sub>	the landing hill radius P-L
r <sub>2L</sub>	the radius curve at L
r <sub>2</sub>	the radius curve at U
b <sub>1</sub>	the clear width of the in-run
b <sub>2</sub>	width at the base of the take-off
b <sub>k</sub>	the prepared width at the K point
b <sub>u</sub>	the prepared width at the end of the r <sub>2</sub> radius and the start of the outrun

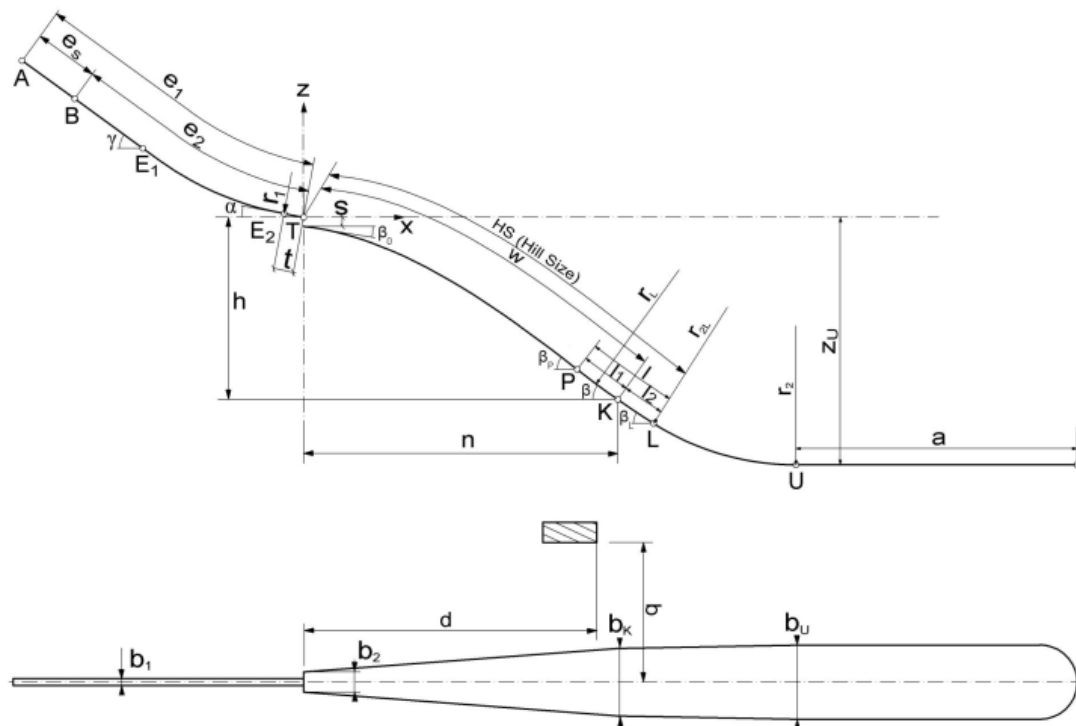


Figure 1.1: Geometrical elements for the jumping hill, based on [2]

### 1.1.2 The judging of the ski jump

As in the ICR specified, the overall result in ski jumping consists the jumping distance covered by the ski jumper and the style points achieved during the jump. Paragraph 431.1 lays down the principles for the evaluation of the jump's performance. The outer appearance of the jumper's movements, beginning from end of the take off and ending with the passing of the "fall line" in the outrun is judged with the main focus in aspect of timing, carrying out the movements, stability and general impression [2]. The key points for an evaluation of the performance and therefore the calculated points given for it, are shown as followed

- "utilization of the aerodynamic efficiency of body and ski"
- "posture of arms and legs, as well as ski position during flight"
- "succession of movements during landing"
- "conduct during outrun." [2]

Hence, as displayed in Figure 1.2, jumps can be divided into four technical parts: in-run, take-off, flight and landing. In this elaboration, the main focus is set on the section “in-run” and its frictional properties of the jump. The in-run phase starts at the “starting bar” and ends with the take-off phase. At the beginning of the first section, the jumper sits on the starting bar, whose position on the ramp is determined anew before each competition round. This procedure prevents the best jumpers from jumping too far and increasing the risk of accidents. As the “red phase” begins, the jumper has to leave the starting bar within 10 seconds and has to adopt an aerodynamic body posture to reach velocities of about 25 m/s during the in-run section. [2,4]

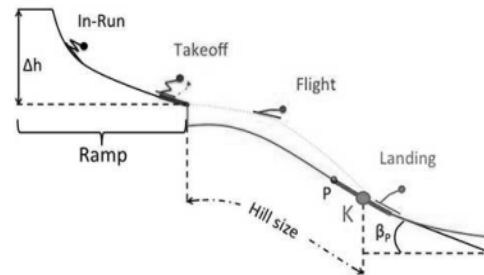


Figure 1.2: The four technical parts of a ski jump [1]

However, the in-run, which consists of a curved path in between two straights, is also considered to be important because the athlete’s performance during the in-run determines the initial conditions for take-off. During all jumps, the horizontal take-off force was predominantly a backwards braking force, and so the athlete’s horizontal velocity was substantially reduced during the take-off. The distance achieved in a long jump is strongly determined by the athlete’s horizontal velocity at the end of the in-run phase [5].

### 1.1.3 In-run velocity

Virmavirta et al. [4] investigated during the Torino Olympics 2006 the interrelationship between the length of a jump with parameters as in-run velocity, angular velocity of the hip joint during take-off, body weight influence and take-off techniques of the jumpers. As a result, a significant correlation of the length of a jump with the in-run velocity has been observed and furthermore the influence of the upper body movement during the take-off phase, which corresponds to a length of approximately 6 meters, was identified. Despite the appearance of higher air resistance due to the variation of the upper body, only a little effect on the jumping distance could be determined as the possible negative-aerodynamic body position is maintained only for a short period of time.

### 1.1.4 Ice ramp

To this day, two types of in-run tracks are used in ski jumping. The traditional version is the in-run track milled into ice. Here, a 15 – 20 mm thick layer of ice is built up via a combined irrigation and cooling system and then the track is milled into it. The system also suitable for summer training is a run-up track with ceramic tiles [6]. Figure 1.3 shows the end of the approximately 100 m long in-run section of the ski jump in Klingenthal, Germany. The two tracks milled in the ice, each 135 mm wide, are framed by plastic surrounds and cooled during the competition event.

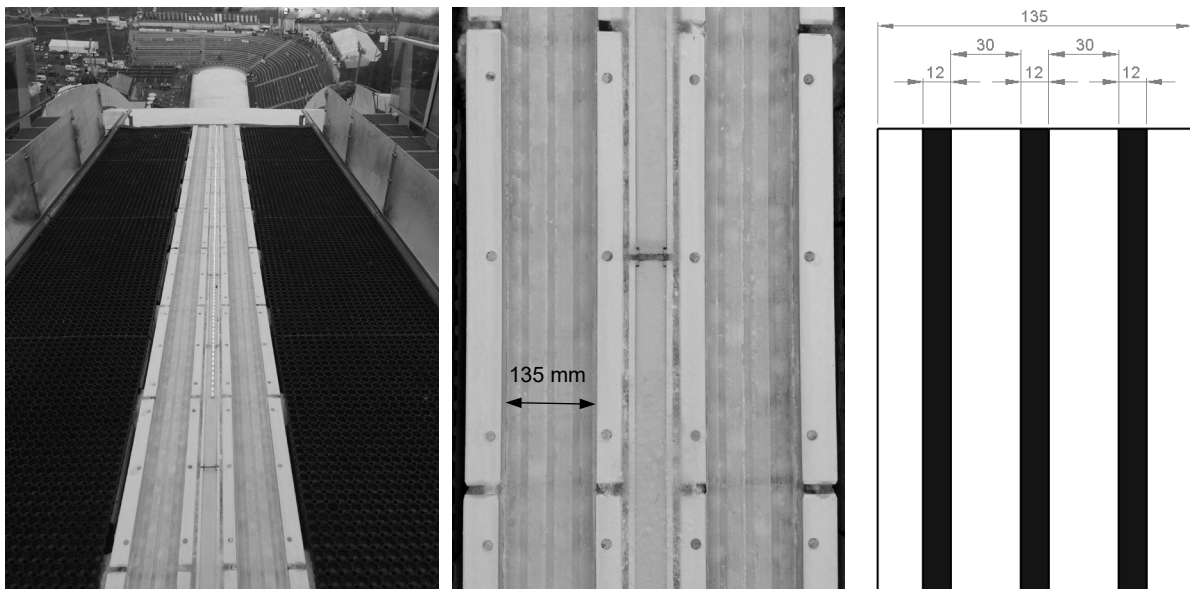


Figure 1.3: In-run track in Klingenthal, Germany (left), track milled into ice surface (middle) and milled grooves in ice track (shown as black areas)

The ice surface of each track is separated by three grooves with a width of 12 mm and a depth of 5 mm. This results in a reduction of the contact surface to approximately 73 % of the nominal surface. The following pictures were taken after the ski jumping event in Klingenthal, Germany. The milled-in profile of the running surface has been broken up to some extent due to the load caused by the jumpers and the changing ambient conditions during the day with partial use of leaf blowers to remove freshly

fallen snow. Furthermore, accumulations of ice have clearly formed on the running surface.

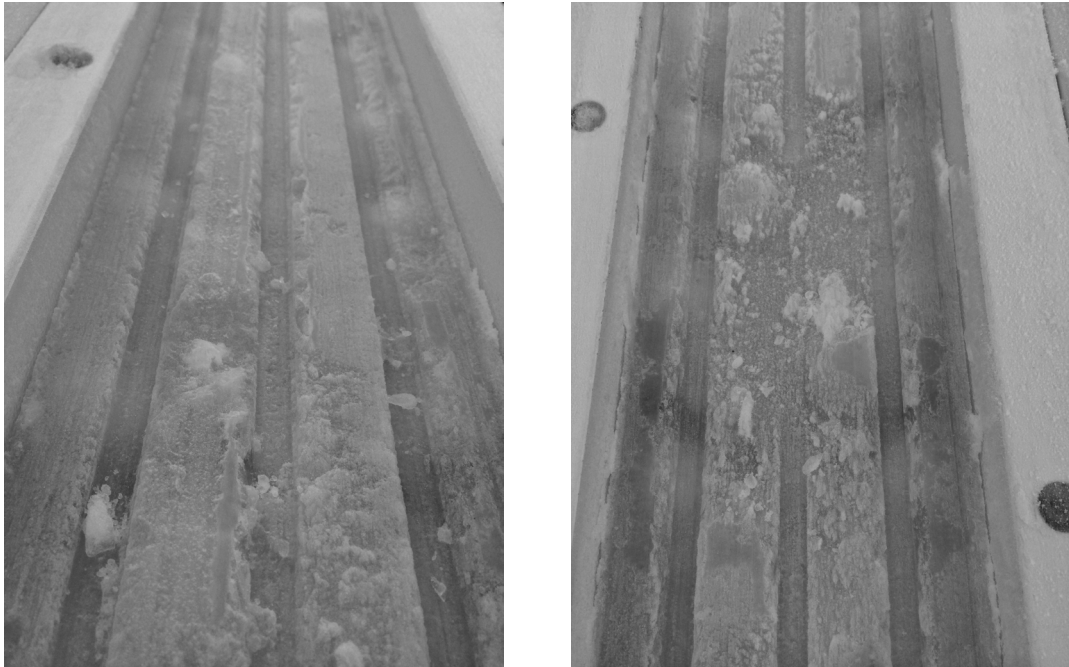


Figure 1.4: Ice track after competition with accumulations of ice (left) and damage to the ice profile due to occurring load (right) in Klingenthal, Germany

## 1.2 Ski characteristics

### 1.2.1 Length

The current state of regulations related to geometric features of a jumping ski are defined in the “Specification For Competition Equipment” [7], issued by the FIS. The ski jumper’s individual ski length is calculated with the help of the body mass index (BMI). The BMI relationship, developed by A. Quetelet in 1832 [8], is defined as a body mass to the body height squared ratio, as shown in Eqn. 1.1.

$$\text{BMI} = \frac{\text{Body Weight [kg]}}{\text{Body Height}^2 [\text{m}^2]} \quad \text{Eqn. 1.1}$$



According to the regulations, the “maximum ski length is 145 % of the total body height of the competitor based on a minimum BMI of 21” [7], for both men or women. “For athletes with less than the BMI minimum, a grading table of  $0.125 \times \text{BMI}$  will be applied” [7] and according to this, the ski length needs to be shortened to meet the regulation. A shorter ski length (this accordingly leads to a smaller surface area) results in a shorter “wing” and thus tends to reduce the jumping distance due to a negative effect in terms of aerodynamic forces. [9,10]

### 1.2.2 Profile width

The profile width of the ski is regulated in article 1.2.1.2 of the FIS specifications [7] and is displayed in Table 1.3 and Figure 1.5. The rectangular shape of the ski (at points A and C) tapers symmetrically from a defined length to point B - this is called a side cut in the regulations. At point b the width is to be designed in a range of 95 to 105 mm. The edges must be at a  $90^\circ$  angle to the running surface as well as to the ski top surface. The maximum difference between the width in the front and tail section must not exceed 5 mm. [7]

Table 1.3: Nomenclature for Figure 1.6 [7]

L	Ski Length	
a	Max. width at front portion	115 mm
b	Max. width at 57 % of front portion (f)	105 mm
c	Max. width at tail portion	115 mm
d	Max. length between tip and begin of side cut	300 mm
e	Max. length between tail and begin of side cut	150 mm
f	Control point of b	

### 1.2.3 Contour, length and height of the shovel

As stated in article 1.2.1.3 of the FIS regulations, “the ski tip may be individually modified as long as it remains symmetric and centred to the middle part and that the minimum distance to the ground of 30 mm is observed” [7].

### 1.2.4 Contour of the tail

Article 1.2.1.4 specifies the contour of the tail to a maximum height of 10 mm from the tail to the ground. [7]

### 1.2.5 Running surface

The requirements for the running surface are defined as: the running surface must be flat and may have a fine base structure in a longitudinal direction and one or more grooves on the bottom side of the surface, as seen in Figure 1.6. Any additional shapes, except of the base structure and the grooves, are prohibited. Even though the number of grooves is not defined, “the total amount of the measured surface area of all the grooves may not exceed 50 % of the minimal width of the ski. The width of a single groove may not exceed 10 mm. The base must be of a polyethylene material”. [7]

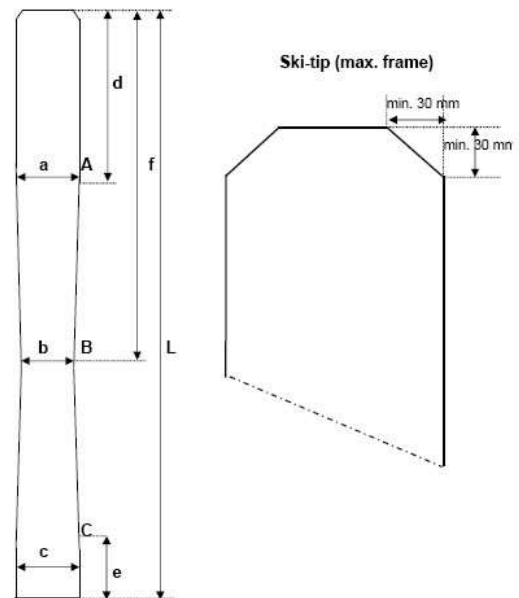


Figure 1.5: Profile width according to the FIS specifications [7]

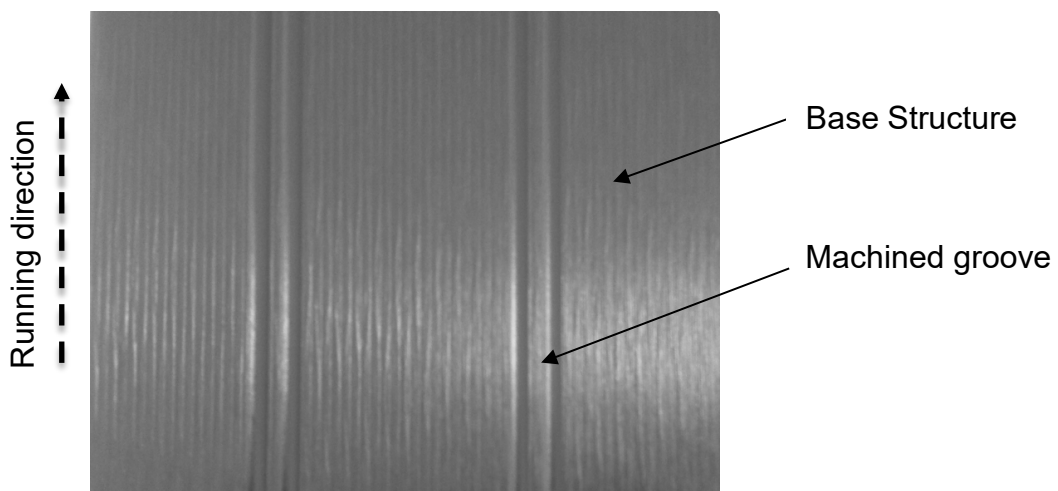


Figure 1.6: Running surface with longitudinal structure and grooves

Furthermore, the FIS is regulating the ski's shape and flexibility and its mass. Aerodynamic coverings and stabilizers are prohibited and a ski design, which allows an aerodynamic flex during flight, is forbidden through the regulations. In addition, the minimum weight of a single non-mounted ski is determined by: the ski length in meter results in a ski weight in kilogram (e.g., 2.5 m = 2.5 kg). Nevertheless, for balancing the centre of gravity, additional weights are permitted. [7]

The ski base is generally prepared for a competition as follows and thus defines the potential ski sample configurations with regard to their surface characteristics: The raw ski base, which is either produced from a sintered cylindrical polyethylene block using a peeling process or is manufactured in an extrusion process, is given its final structure through a stone grinding or structuring device [11]. The structured ski base is then waxed and brushed or rather corked in various stages. Four constellations of ski base samples are derived from this: raw, raw and waxed, structured, structured and waxed. Figure 1.7 shows an overview of the different ski surface finishes.

The images of the surfaces were taken with a digital microscope (VHX-7000, Keyence GmbH, Germany). The raw base features production-related, unevenly distributed, grooves in running direction (a) and the structured base (b) has a macroscopic diamond-shaped pattern that is usually customised in shape and incision depth depending on the competition conditions [11]. At 5x magnification, the base showed distinct grooves approximately 0.2 mm wide, which are clearly visible in the surface image below. These grooves were no longer as prominent in the waxed modification as a result of the waxing process (c).

A more detailed analysis of the sliding distance dependent roughness of the ski base and the ice sample will be carried out in chapter 4.5.2.

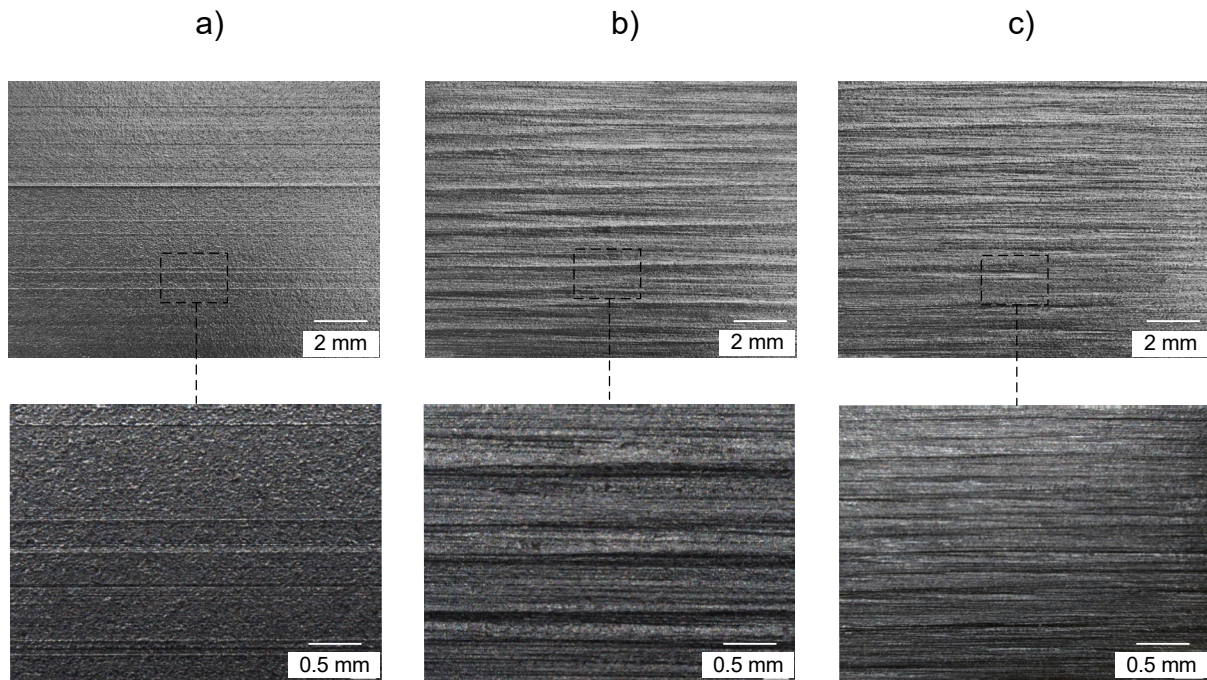


Figure 1.7: Surface images of the a) raw, b) structured, and c) structured and waxed ski base

### 1.3 Contact pressure

At present, there is no definitive statement on the real contact area between ski and ice or snow. No established measurement method have yet been developed and no validated experimental tests have been carried out to determine the real contact area during sliding. Furthermore, the determination of the contact area is made difficult since only small sections of the ski contact area can be investigated with standard methods for contact area determination such as SEM, AFM and profilometry [12–15]. The spatial distribution of the contact areas and thus the resulting contact pressure between ski and ice or snow is highly inhomogeneous and during the sliding process the contact points are constantly changing [16–18]. In addition, calculations can only be estimations of the location-dependent highly dynamic process [19,20]. Estimates of the contact pressure can be found in the literature, which range from  $< 10$  kPa [21] to  $> 1$  Mpa [11].

Due to this uncertainty, the nominal contact pressure is used for further consideration, which is estimated as follows: the front and rear parts of the ski lift off the ice surface

to a greater or lesser extent during the ski jump downhill, thus significantly reducing the contact area. Neglecting this effect and based on the specified maximum geometric dimensions of Table 1.3 in conjunction with Figure 1.5, an assumed ski length of 2,400 mm with an average width of 108.3 mm, results in a nominal surface area of 520,000 mm<sup>2</sup> for both skis. Due to the curved shape of the tip and the rear of the ski in relation to the design of the ski architecture like camber and rocker, only between 1/3 (173,000 mm<sup>2</sup>) [22] and 1/2 (260,000 mm<sup>2</sup>) [22,23] of the apparent surface is truly in contact with the ice during the in-run. On the surface of a milled ice track, representing only 73 % of the nominal surface area (cf. chapter 1.1.4), the nominal ski contact on ice is accordingly reduced to a range of about 126,500 mm<sup>2</sup> to 190,000 mm<sup>2</sup>. With an assumed jumper weight of 50 kg, the nominal contact pressure below the skis therefore ranges between 2.58 kPa and 3.88 kPa.

#### **1.4 Summary and comparison of publications in the field of friction on ice and snow**

For a long time, there has been increasing interest in snow and specifically ice friction, as a result of numerous ski sport activities. The prevailing goal in the field of skiing materials is to achieve the lowest possible friction, and thus generate the highest possible sliding speed and this has been the impetus of several scientific studies on ice friction. At this point, an overview describing the pioneering stages in the scientific processing of ice friction, in particular the friction between a ski base and ice surface, is provided. As early as 1859, seminal ice adhesion experiments by Faraday lead to suggestions of the existence of a melted layer present on ice caused by pre-melting of its surface [24]. Since the properties of this layer are not the same as those of a usual liquid, the layer was designated as “quasi-liquid” or as “liquid-like”.

Bowden and Hughes carried out various experimental studies of the friction on ice and snow surfaces on the glaciological expedition to the “Jungfrauoch” in 1938 [25]. They observed low friction on ice surfaces at temperatures near the melting point of ice and drew conclusions that these low frictional forces occur as a result of a thin water film on the surface. This film was shown to be caused by frictional heat which lubricates the contact points between the sliding surfaces, rather than by pressure melting as

Osborne Reynolds 1901 and others had supported at this time [26]. Within their experiments, Bowden and Hughes discovered the independency of the coefficient of kinetic friction from load, apparent contact area, and sliding speed and recognized a significant increase of friction at decreasing ice temperatures as the formation of the water film was impeded. As different slider materials were used in each these studies, the importance and influence of the thermal conductivity of these materials on the ice friction could be appreciated (differing rates of water melting due to differences in frictional heating). As a key outcome of their work, they provided proof that pressure melting alone is not responsible for creating the water film found on ice surfaces.

In 1953, Bowden continued his experimental studies of friction on snow and ice and could demonstrate that friction is indeed independent of the apparent surface area by showing in sliding experiments that the measured friction values with a full-sized ski are the same as those of a very small sledge [27]. Furthermore, he could show that Amontons' law - friction is directly proportional to the (normal) applied load and the friction coefficient is constant and independent of the contact area, surface roughness, and sliding speed - is applicable in the field of ice friction.

It was shown that the minimum contact area is mainly determined by the load and loading time and therefore by the plastic deformation of the surface with the lowest hardness. Since the hardness of ice is temperature dependent, which surface provides the real contact area is therefore also dependent on temperature. The difference between the apparent and the minimum real contact area was estimated to be about 1/30000 of the apparent surface area (depending on ice temperature). Temperature effects on static and kinetic friction were observed, as well as an increase in friction with decreasing sliding speed. Within this paper, Bowden could demonstrate measurably higher friction values when using an adequately thermally conductive slider, alongside an enhanced difficulty to create a friction-decreasing water film. Additionally, Bowden reported overall lower friction values (load and speed independent) when using Polytetrafluoroethylene (PTFE) as a sliding material on the ice surface.

Functional studies by Cohen and Tabor in 1966 investigated polymers with both polar (polyamide 6.6) and nonpolar (polyethylene) characteristics in combination with either lubricated or unlubricated glass and metal surfaces [28]. Water and alcohol-water solutions were chosen as lubricants to analyse the differences in sliding properties of the

friction partners. Water was shown to be an effective lubricant for polyamide sliding against a glass surface, due to its hydrophilic properties. When, however, hydrophobic polyethylene or polytetrafluoroethylene polymers were used instead, measurement results demonstrated water to be an entirely ineffective lubricant. A series of experiments were then made with polyethylene sliding against itself and utilizing either water or dilute alcohol solutions. Starting with water, insufficient lubrication was observed until the alcohol content was increased to point at which the polyethylene's surface tension was reduced, making it possible to sufficiently wet the surface and subsequently reducing the coefficient of friction (COF). Furthermore, they examined the frictional properties of polyamide following a prolonged exposure time with water and could show a subsequent increase in friction values. It was assumed that this increase in friction is due to plasticization of the surface following moisture absorption and a consequent reduction in bulk strength of the surface's irregularities, leading to an increase of the contact area.

In 1976 Evans et al. further developed the frictional heating theory of Bowden and Hughes (1938) [29]. Instead of estimating the energy used in sliding over the interface, they calculated the energy loss in the form of heat in the contact area. It has been shown that frictional heat is conducted into the slider samples as well as into the ice surface thereby raising the surface temperature until the ice's melting point has been reached. Accordingly, if the thermal energy required for melting the ice is low, most of the energy is conducted into the sample and ice surface.

Numerous experiments by D. Kuroiwa in 1977 investigated the kinetic friction between a metallic or plastic-resin slider and snow or ice in relation to skiing and skating [30]. In line with Bowden's conclusions in 1953, Kuroiwa and his team could also show that friction induced by low-speed sliding induced plastic deformation within the snow, while sliding with increased speed lead to a stick-slip friction which was accompanied by fractures and abrasions of snow grains. The real contact area between a transparent flat glass-sample and snow was measured and calculated. As a result, microscopic examination of the friction surfaces revealed an ice grain content of 37% in the snow, resulting in a total cumulative ice area of 220 mm<sup>2</sup>. They demonstrated that the real contact area created by a 5 min friction test is only 3.8 % of the nominal contact area of the ice grains. This translates to an average real contact area of approximately

0.04 mm<sup>2</sup> and, if a circular shape of the contact areas is assumed, an average contact diameter of around 200 µm. By comparing the energy required to melt snow and the total energy required to slide the snow sample on the glass (frictional resistance was measured), this study estimated that only 1 % of frictional energy was used to melt snow while the majority is transferred to the snow and to the glass sample in the form of heat.

Four years later in 1981, Ambach and Mayr examined the thickness of a water film during frictional measurements on snow by measuring the dielectric constant in the contact zone with a comb-shaped capacitor which was installed directly into the ski [31]. They found that high values of the dielectric constant correspond to high values of water film thicknesses, since the dielectric constant for water is much higher than for snow. In order to prevent freezing of water films, the tests were carried out during the actual sliding process, using real skis under natural sliding conditions. To achieve different thicknesses of water films, the tests were performed with different types of waxes and under different temperature conditions. As a result, Ambach and Mayr showed the presence of a water film which was several micrometres thick during sliding (5 µm at -4°C snow temperature).

In 1982, the frictional heating theory of Evans et al. was further developed by Oksanen and Keinonen with a mathematical model to calculate the COF [32]. The authors proposed that the frictional force is caused by viscous shearing of the water film layer between a slider composed of different materials and the ice surface. They assumed a real (true) contact area by calculation from the quotient of the normal force and indentation hardness of the ice. Furthermore, they calculated the friction partner's COF and its dependence on temperature, speed and normal force. Their theory was confirmed by pin-on-disc tribometer tests at a maximum speed of 3 m/s and at temperatures as low as -15 °C with loads up to 45 N.

Glenne, 1987, considered the influence of dry and wet snow on kinetic friction and further developed the previously mentioned mathematical models [33]. It was assumed, that the total sliding resistance is the sum of dry friction, wet friction, compaction, and impact resistances caused by the displacement and compression of the snow.



Between 1988 and 1994, S. C. Colbeck developed the mathematical description of friction on snow in a quantitative way and highlighted the importance of researching the formation of friction caused by the water film [34–36]. Friction experiments with a slider on a snow surface were undertaken, demonstrating three friction mechanisms which are each prevalent to varying degrees across different film thicknesses: dry ploughing, lubrication and capillary suction, which result in dry friction, boundary lubrication as a result of melt water, and capillary drag effects due to water bridge formation respectively. These mechanisms occur simultaneously and are influenced by the emerging amount of melt water, at least as far as friction on snow is concerned. With only a small amount of water, the surfaces are just partially separated and the lubricating water film arises insufficiently. Experiments have shown that if the amount of melt water exceeds a certain point, the contact area increases along with potential capillary effects and, as a result, the COF raises. Through experimental observations and the development of analytical solutions, the dependence of the snow temperature and grain size, and the applied slider's roughness, hardness, speed, load, and length have been analysed. It has also been shown that heat generated by friction is stored in the snow grains and generates water, which acts to lubricate contact points between ski and snow. Additionally, similarities to ice friction could be demonstrated by a drastic increase of the contact area as a result of the slider passing over the snow surface, showing that the snow surface becomes similar to that of an ice surface. Water film thicknesses of approximately 0.2 to 1.2  $\mu\text{m}$  have been determined by snow friction experiments and calculations.

Studies of mirror-like single crystal ice surfaces by Dosch et al. in 1995 using glancing-angle X-ray scattering investigated the surface melting of the high symmetry ice surfaces and its quasi-liquid layers [37]. Previous X-ray experiments carried out in 1994 had provided strong evidence that water layers, produced by surface melting or more specifically by “pre-melting” of the surface, build up at well below 0 °C [38]. The results gained by Dosch et al. in 1995 confirmed these previous findings and could further refine the conclusion by showing that ice begins to build up a quasi-liquid layer at approximately -13 °C and this water layer develops to several nanometres in thickness by -5°C. They did not, however, confirm the predicted end of growth of the quasi-liquid layer at 3 nm of thickness (“blocked surface melting”) presented by Elbaum et al. [39].

The experimental results of Dosch et al. have indicated that van-der-Waals interactions start to dominate the surface melting of the quasi-liquid layer over a layer thickness of 15 nm.

Fluorescence spectroscopy experiments utilizing sliding plastic materials on ice with a view to identify interfacial water layers caused by frictional heat were conducted in 1998 by Strausky et al. with the aid of a pin-on-disc apparatus [16]. As plastic samples they utilized polymethyl methacrylate (PMMA) with a polished sliding surface of optical quality and a second not specifically identified ski running base material from Fischer GmbH, Austria, characterized by optically transparent properties and a common ski base grooved surface structure with groove depths of approximately 30  $\mu\text{m}$ . The investigation took place under limited speed conditions of 0.005 to 0.1 m/s and at a temperature environment of  $-2^\circ\text{C}$  (surrounding gas, ice and sample) with a chosen contact pressure which is assumed to develop during skiing conditions. The detection limit of their experiment setup was 50 nm for PMMA and 250 nm for the running base material. Strausky et al. stated as a result that under these conditions, no water film above the level of detection could be identified and they concluded that the water layer present for PMMA must be smaller than 50 nm (250 nm respectively for the ski base material). Furthermore, a COF of 0.03 at  $-2^\circ\text{C}$  was measured during the executed experiments.

In 2000, Bo Persson published a handbook with general principles of heat flow during sliding with support of the Research Centre of Jülich, Germany [40]. The publication dealt with fundamental aspects of sliding friction with a strong accent on experimental and theoretical results that were new at that time. This handbook described key points regarding general physical effects as well as a broad overview of sliding friction with a detailed discussion of interfacial lubrication. Further topics such as hydrodynamic boundary conditions in the region of a solid-fluid interface were also addressed and an emphasis was placed on interfacial lubrication and dry friction dynamics. The concepts presented in this resource later formed the theoretical basis for the explanation of snow and ice friction as well as the development of a numerical simulation by L. Bäurle et al. in 2006 [19].

In the year 2000, A. Döppenschmidt and H.-J. Butt used atomic force microscopy (AFM) to study the surface melting of ice, formed from distilled water in a temperature

range down to  $-35^{\circ}\text{C}$  [12]. The authors measured a liquid-like film thickness of approximately 11 nm at  $-10^{\circ}\text{C}$  and 32 nm at a temperature of  $-1^{\circ}\text{C}$ , which corresponds to values similar to those of Dosch et al. Beyond that, the influence of impurities on the surface melting process, previously investigated by Wettlaufer et al. was further studied [41]. Salt was used as an impurity material to investigate the increasing effect on surface melting.

In 2001, Buhl et al. investigated the sliding behaviour of polyethylene on snow with variable snow temperature and normal force in both laboratory and field tests [42]. A pin-on-disc tribometer in a cooling chamber was used to determine the coefficient of friction on a laboratory scale. This approach allowed series of tests to be carried out between  $-25^{\circ}\text{C}$  and  $0^{\circ}\text{C}$ , for both air and snow temperature. The surface pressure varied between 0.05 and 0.3 MPa (corresponding to a normal force between 5 N and 30 N in the test), with a limited test speed of 5 m/s. Based on these test series, a large dependence of the COF on the snow temperature could be identified, demonstrating a minimum COF of 0.02 at about  $-3^{\circ}\text{C}$  snow temperature. Due to the design of the tribometer, repeated travel of the ski base sample over the ice or snow surface per test run resulted in a temperature increase of the surface. Field test studies were conducted measuring snow temperature and controlling for test person weight over 2500 runs. Using different ski materials, the tests were always conducted on the same track, and the time required for a run for each material was measured. These field friction tests showed a similar dependence of the COF on temperature as was revealed in the laboratory tests. The fastest conditions were measured between  $-3^{\circ}\text{C}$  and  $-4^{\circ}\text{C}$ . At higher snow temperatures from  $-3^{\circ}\text{C}$  to  $0^{\circ}\text{C}$  and at low temperatures below  $-10^{\circ}\text{C}$ , the measured downhill times were higher, and a difference in surface pressure (weight) could only be detected below  $-6^{\circ}\text{C}$ .

Bluhm et al. in 2002 addressed the existence of a liquid-like layer at the ice surface near its melting point using electron spectroscopy [43]. A novel, high-pressure electron spectrometer was developed to overcome the limitation of operating in high vacuum, usual in this method, which is incompatible with the high vapour pressure of ice when it is near its melting point. The authors could show that a liquid-like water film exists, even at temperatures down to  $-20^{\circ}\text{C}$ , is approximately 2 nanometres in thickness at  $0^{\circ}\text{C}$ . In contrast to Döppenschmidt and Butt, who investigated the effect of surface

contamination with salt, Bluhm et al. conducted experiments with hydrocarbon as the contamination material and showed that the pre-melting of ice could be highly increased in the presence of hydrocarbon particles.

In 2004, Albracht et al. developed a pin-on-disc design tribometer in continuous rotating motion with the company TETRA, Society for Sensor, Robotics and Automation mbH and the Ilmenau University of Technology, in order to test different materials with regard to their friction behaviour against an ice surface [44]. The special feature of the tribometer was the spiral inward movement of the measuring arm during a measurement to prevent smoothing and polishing of the ice surface. The utilization of two measuring arms, the sample holder and measuring sensor mounted on one arm and a grinding tool on the other arm, enabled subsequent reconditioning of the ice surface. Both arms rotated around the central axis of the 1.2 m stationary disc at a maximum speed of 9.4 m/s with normal forces of up to 10 N. The specimen materials that were tested were Cr-Ni steel, an aluminium alloy, polytetrafluoroethylene and polyamide on a specimen holder with a hemispherical surface (radius 8 mm). The air temperature as well as the ice temperature could be adjusted separately by two cryostats over the range from -30 °C to +30 °C.

In 2006 during his dissertation at the ETH Zurich, Baurle et al. developed a pin-on-disc tribometer which enabled investigation of the formation of the water film caused by friction on ice or snow [19,45]. This work was also undertaken in cooperation with the Swiss Federal Institute for Snow and Avalanche Research Davos (SLF), together with the ski manufacturer Stöckli Swiss Sports AG and the wax company Toko AG. In addition to the development and construction of the tribometer and the friction measurements, a primary focus of the work was the characterization of the contact surface between ski base and ice using scanning electron microscopy, X-ray computed tomography and optical profilometry. Using numerical modelling of snow and ice friction, they sought to explain energy dissipation mechanisms including dry friction and melt-water film generation. Dynamic friction, expressed by the COF between the polyethylene ski base and ice, was measured as a function of temperature, sliding speed, load, contact area, and surface topography. The test rig with a disc size of 1.8 m was equipped with two measuring arms, following a similar principle to that employed by Albracht et al. in

2004. The rig was placed in a cold chamber that allowed changes in temperature between  $-15\text{ }^{\circ}\text{C}$  and  $+1\text{ }^{\circ}\text{C}$ . Sliding experiments were carried out over the range from  $0.55\text{ m/s}$  to  $10\text{ m/s}$ , without the ability to adjust the acceleration. UHMW-PE samples were subjected to forces perpendicular to the sliding surface between  $25\text{ N}$  and  $84\text{ N}$ , corresponding to surface pressures between  $0.025\text{ MPa}$  to  $0.084\text{ MPa}$  at a sample macroscopic contact area of between  $2 - 10\text{ cm}^2$ . The two main factors influencing the friction between a ski base and an ice or snow surface were observed to be water film thickness and the relative contact area of the two friction partners. The unevenly distributed water film was shown to be especially responsible for low friction values. Due to the difficulty to directly measure a water film forming, a mathematical model was developed to describe this water film. The authors calculated a film thickness between  $30$  and  $250\text{ nm}$  at a temperature of  $-5\text{ }^{\circ}\text{C}$ . The average total static contact area between the ski base and a finely textured snow surface was found to be  $5\%$  of the total surface area, with a diameter of the contact points approximating  $100\text{ }\mu\text{m}$  (at  $-10\text{ }^{\circ}\text{C}$ ). As previously highlighted by Baurle et al., these values depend on temperature level, snow type and the friction process [19]. Even without capillary action as assumed by Glenne and Colbeck, the friction process can be explained solely by the meltwater film, the surface topology and the most critical parameter, the real contact area [33–36]. Depending on sliding speed and sample size, COFs of about  $0.06$  were measured at  $-10\text{ }^{\circ}\text{C}$ . A strong dependence of the coefficient on the normal force was observed, especially at higher temperatures; when the normal force was increased, the COF decreased. In addition, the measurement results showed a temperature dependence of the COF with respect to the varying degree of generation of the water film both above and below  $-2^{\circ}\text{C}$ .

In 2007, Winkler et al. at the Ilmenau University of Technology investigated the frictional behaviour of various ski surfaces against an ice surface using a pin-on-disc tribometer [46]. In 2004 using an earlier version of that tribometer, Albracht, Winkler and others investigated factors influencing the tribological behaviour of various materials such as Cr-Ni steel, PTFE, PA, and aluminium alloys against ice [44]. In the 2007 publication, UHMW-PE was used as a ski surface in comparison to a stainless-steel sheet as reference, which exhibited the lowest friction to ice. The sample size measured  $100\text{ mm}$  in width and was mounted on a curved fixture with a radius of  $25\text{ mm}$ .

This created a very narrow contact area between the specimen and the ice, referred to by the authors as an approximate line load. The objective was to research possible improvements to jump pads in combination with an icy run-up track. Both the ambient and ice temperature could be precisely adjusted down to  $-30\text{ }^{\circ}\text{C}$  using a cryostat. The maximum friction speed was specified at  $9\text{ m/s}$ , but reproducible measurements were only possible up to a maximum of  $2\text{ m/s}$ . The surface pressures were identical to those commonly used in ski jumping and were achieved by a curved sample holder and a resulting line load on the ice sample. To ensure reproducible measurements of the ice surface, it was planed off in a defined manner with machining tools and subsequently thermomechanically polished. The tests showed a decrease in the COF relative to an increase in the normal force, independent of the sliding speed and temperature. In addition, the COF decreased with increasing friction speed with a measured COF of the racing ski base of  $0.013$  at  $-5\text{ }^{\circ}\text{C}$  and  $3\text{ N}$ . The authors of the study concluded that by structuring the ski base, the surface pressure can be increased (increased water film formation is stimulated) and thus lower friction force values are achieved. This also improved tracking and allowed the athlete to train on run-up tracks with a snow surface.

Between 2009 and 2010, Kietzig et al. performed friction experiments using a modified parallel-plate rheometer, placed in an environmental chamber and capable of realizing temperatures as low as  $-150\text{ }^{\circ}\text{C}$  [13,47,48]. By means of the rheometer, the influence of surface roughness, structure and hydrophobicity on ice friction was studied over a range of temperatures ( $-10\text{ }^{\circ}\text{C}$  to  $-1.5\text{ }^{\circ}\text{C}$ ) and sliding velocities ( $0.0036\text{ m/s}$  to  $1.45\text{ m/s}$ ) on a number of metallic samples. These samples were thermally insulated by utilization of fiberglass discs and the surface roughness modified at the nanoscale level using a femtosecond laser to achieve hydrophobic surface behaviour. As a result of the studies, the authors classified ice friction in dry, boundary, mixed and hydrodynamic friction. However, one of the key findings of these experiments was that under atmospheric conditions no real dry friction can develop, since even at low temperatures a very thin liquid-like film is formed. Furthermore, the authors indicated that the temperature in the contact zone is below the melting temperature and that mixed friction occurs when the surface temperature within this zone exceeds the melting temperature of ice. These statements are still in controversy with later publications. By comparing several samples with different insulation properties, the influence of thermal conduc-

tivity was investigated. It was found within the study that the influence of thermal conductivity on ice friction decreases with increasing sliding speed, while surface wettability becomes more important. It was stated that the lower the thermal conductivity and therefore the higher the insulation performance of the sample, the lower the measured COF values are, both in the interfacial friction range and partly in the mixed friction range. Further, it was observed across all measured temperatures that the COF decreased sharply in relation to increasing sliding speed and that the COF approaches a minimum at about  $-4\text{ }^{\circ}\text{C}$ . At sliding velocities above  $1\text{ m/s}$ , the COF increased slightly again after passing through a minimum (similar observations of this kind have been reported by Colbeck, Winkler and Bäumle [19,34–36,46]). This effect was assigned to the capillary attraction force already mentioned by Colbeck in 1988 [34]. For temperature ranges below this minimum ( $< -4\text{ }^{\circ}\text{C}$ ) and with increasing temperature, a shift of the COF toward lower values was observed as a result of improved lubrication and reduced solid-solid contact. An opposite effect was found at temperatures above  $-4\text{ }^{\circ}\text{C}$ ; sliding friction increased with increasing temperature.

Different steel surface structures were obtained by polishing the sample surfaces and structuring them by laser. Laser structuring produced a hydrophobic lotus-like surface (contact angle to water of  $128^{\circ}$ ) with approximately twice the roughness compared to the hydrophilic polished steel surface (contact angle to water of  $84^{\circ}$ ). The investigation of the influence of surface texturing at  $-15\text{ }^{\circ}\text{C}$  and  $-7\text{ }^{\circ}\text{C}$  showed a decreasing COF with increasing friction speed but this was independent of the surface quality. However, at very low velocities of less than  $0.01\text{ m/s}$ , the laser-textured samples gave higher friction values than the polished samples due to interlocking of roughness peaks, but the COF values of the two samples converged again over the speed range between  $0.1$  and  $0.5\text{ m/s}$ . At  $-1.5\text{ }^{\circ}\text{C}$  test temperature, the polished sample again showed a clear increase in friction force values at velocities greater than  $0.5\text{ m/s}$ . Only at very low velocities were the COF values of the polished samples higher than those of the laser-structured samples.

In 2012, a linear tribometer with continuous motion was developed by Hasler et al. during the project "Alpine Sport Technology: Gliding on Snow and Ice", funded by the K-Regio programme of the Federal Province of Tirol [49]. This project was undertaken in cooperation with the Technology Centre Ski and Alpine Sports (TSA), the Institute

for Sports Science (ISW) and the Institute of Physical Chemistry of the University of Innsbruck as well as Austrian sports associations and several companies. According to a press report, the costs of the tribometer were about 1.15 million EUR [50]. The linear-type tribometer used a complete ski structure which is mounted in a guiding rail and accelerated by means of a carriage system. The total length of the glide path was 24 m and divided into three sections; acceleration, sliding and deceleration. During the sliding phase, the friction force under the ski was recorded. The ski could be accelerated to 27.8 m/s (100 km/h) in approx. 0.4 seconds over a speed-dependent acceleration distance of 1 – 7 m [51]. The subsequent measurement section was maximally 18 m. Loads could be simulated via two spring-loaded parallel bars over a range of 50 to 700 N. The measurement data was recorded at 8.3 kHz in a cooling chamber which allowed temperatures as low as - 20 °C and transmitted wirelessly to a control room. The system resolution, which was reported to be 3 mm with an accuracy of 3 µm, was published by Hasler et al. in 2016 [49]. COFs in the range of 0.04 with a friction speed of 6 m/s at a snow temperature of -5 °C have been measured. During the determination of the tribometer's precision, repeated passes over the snow surface revealed that a plateau occurs after approximately 10 passes and that the COF changes only linearly after this point. This is particularly significant for tribometer designs, which, due to their nature, pass over the ice or snow surface several times per measurement.

In 2014, Makkonen et al. developed a thermodynamic model of kinetic ice friction based in part on the wet friction model of Oksanen and Keinonen and incorporating Makkonen's theory of dry friction (friction on ice without a water film, i.e. dry, due to very low temperature or sliding speed) [20,32,52,53]. Newer approaches such as the squeeze-out of water and the effect of the contact pressure on the equilibrium temperature were included in the model. Yet, the validity of the model was limited by the absence of mechanical deformation mechanisms and the necessary estimation of the size of the contact area and its fixed rectangular shape. Furthermore, a constantly behaving contact surface was assumed within the calculation. The model has however been successfully tested in combination with experimental tribometer series, such as those conducted by Scherge et al. [54]. However, the new interpretation of ice friction led to the development of the following central statement: the energy of the surface is reduced due to heat dissipation into the environment. The thermodynamic system is not able to perform mechanical work parallel to the sliding movement at the formed



contact points. Furthermore, they highlighted the dependence of the ice temperature on the sliding speed due to the frictional heat and proposed that the regions of friction mechanisms of ice differ from those discussed in the literature [47,48]. Thus, Makkonen disagrees with Kietzig et al. in that the authors do not see any relevance of the region of boundary friction for ice friction. Additionally, they show that the temperature in the mixed friction region cannot be above the melting temperature of ice. Similar to experimentally measured values, the authors calculated a COF of 0.05 and a water film thickness of 0.05  $\mu\text{m}$  at  $-10\text{ }^\circ\text{C}$  [19,46].

Between 2015 and 2017, Böttcher et al. focused on determining the COF of structured ski bases by means of tribometric measurement series through utilization of a developed plate-on-plate linear tribometer [55,56]. This tribometer, with a total length of 1.6 m and a measuring length of 1 m was developed at the MicroTribology Centrum Karlsruhe together with the Fraunhofer Institute for Mechanics of Materials. UHMW-PE ski bases with a sample size of 65 x 40 mm were tested and moved in an oscillatory motion in relation to the ice surface. Direct forces of up to 100 N and tangential forces of up to 20 N were measured. The tribometer is enclosed in a housing with a cooling system and can be cooled down to  $-20\text{ }^\circ\text{C}$ . For this work, friction tests were only performed at low speeds of 1 m/s and generated a measured COF of approximately 0.05 at  $-10\text{ }^\circ\text{C}$  [56]. By combining the friction model of Makkonen et al. and the elastic contact model of Hertz, it was possible to link the measured friction values with the characteristics of the ski structuring [20,57]. The authors followed the interpretation of the sliding process as an energetic dissipative process, whereby the generated frictional heat leads to the melting of a thin surface layer. The resulting viscous water film has a lubricating effect on the contact and thus reduces the COF. The temperature of the sliding partners was identified as a decisive factor and this temperature subsequently modulates the hardness of the sliding bodies. Both factors are significantly responsible for the temperature-dependent behaviour of the COF.

In 2017, Scherge presented his view of ski grinds on snow [58]. In his opinion, analysis of friction processes from an overly mechanistic view is prone to generate contradictory data. A more target-oriented view would be an energetic one, which investigates how much frictional power is generated during sliding contact. Accordingly, capillary forces account for a large proportion of the resistance when a ski glides over snow. During

friction, most of the power is converted into heat and the water film thickness increases with increasing sliding speed or a heavier weight force on the skis (increase of friction power density when the contact area between ski and snow becomes smaller). Therefore, an increase in speed and/or decrease in pressure on the ski, results in a decrease in friction. Opposing effects occur when the quantity of water increases with increasing friction power density, but the water film is squeezed out of the friction contact more quickly with increasing pressure. In his opinion, a skier does not come within the range of hydrodynamics because the skis offer too little surface area.

In 2019, Canale et al. explored the microscopic mechanisms of ice lubrication using a stroke-probe atomic force microscope (AFM) in combination with a glass bead moving on an ice surface [59]. By measuring the shear friction, film thickness and quantifying the mechanical properties of the interfacial film of ice at different temperatures and velocities, viscoelastic properties of meltwater were observed. As an example, the measured viscosity was up to 2 orders of magnitude higher than that of pure, Newtonian, water. The high viscosity combined with an elastic response makes meltwater an excellent lubricant, which explains the low friction. The authors used an infrared camera that recorded the temperature during the friction process. They could not measure any significant temperature increase, which is in line with the friction results of Lever et al. on snow which attributed the formation of the water film to abrasion and not to melting due to temperature increase [60].

Velkavrh et al. conducted ice friction experiments with steel samples of different roughness on both an inclined ice track tribometer and an oscillating plate-on-plate tribometer [61]. It has been observed that on the ice track tribometer, samples with higher roughness produced higher friction (lower velocity), and on the oscillating tribometer exactly the contrary was measured; samples with higher roughness produced higher velocities, thus lower friction. With the identical experimental set-up, later experiments by Velkavrh included friction tests at different temperatures, which also yielded an inverse roughness-friction correlation [62]. The authors emphasized the need for a carefully designed measurement setup in order to enable comparison of laboratory and real scale measurements due to the development of possible opposing friction regimes during the measurement.

In 2021, Liefferink et al. studied the correlation of temperature, contact pressure, and speed by rheometer experiments with spheres of different materials [63]. They addressed the hardness of the ice surface as one of the dominant variables, which is itself temperature and pressure dependent. At contact pressures well below the hardness of ice and at temperatures in the range of the melting temperature of ice, low friction was identified, as expected, which is dependent on the mobility of water molecules. However, if the contact pressure was increased to within the range of ice hardness, ploughing of the friction partner through the ice surface becomes dominant and a completely new dynamic is created by the particles that are formed and reshaped in the process and this effect is highly correlated with speed. Furthermore, a low material dependence could be observed, which was explained by the hydrophilic character of all samples. No friction-related dependence was found at very low velocities (approximately 1 m/s) for samples with different thermal conductivity.

Lemmettylä et al. introduced in 2021 a linear tribometer for testing real skis on snow [64]. Located in two construction containers and covering a length of approx. 14 m, the sliding characteristics can be carried out in classic sliding as well as under skating and simulated kicking situations. A huge influence of the ski and snow on the measurement results and a large variation as a result of the ski preparation was found. Therefore, the authors were unable to obtain comparable results.

Similar to [49], Auganæs et al. developed in their study a ski-snow tribometer that can accommodate full-size cross-country skis [65]. The linear tribometer can be operated up to a speed of 8 m/s over a length of 6.5 m on a total of four different snow tracks. Between 50 and 800 N of normal force can be transmitted to the skis. The measurements with differently prepared skis took place at  $-3^\circ$  degrees at different speeds. A strong focus was given to the investigation of the precision under different test situations such as snow type, speed, ski tracks and snow surface preparation. Within the study, a decrease in precision by half was found when switching between different tracks compared to measurements on the same track. Overall, results were similar to those measured by Hasler et al., but without examining waxes in particular.

For a better overview, the key results of the various authors are listed in a short summary in Table AP 1 in the appendix. Table 1.4 summarises the key statements regarding the topics "water film", "COF" and "contact area".

Table 1.4: Conclusions of the literature review

Topic	Author	References	Year	Statement
Water film (Wf)	Faraday	[24]	1859	Pre-melted quasi-liquid layer of water on ice
	Bowden	[25]	1939	Lubricating water layer formed by frictional heat
	Ambach	[31]	1981	Assumed several micrometres thick (5 $\mu\text{m}$ / -4 $^{\circ}\text{C}$ )
	Colbeck	[34]	1988	Measured and calculated thicknesses of 0.2 to 1.2 $\mu\text{m}$
	Dosch	[37]	1995	Layer builds up below 0 $^{\circ}\text{C}$ . Layer thickness several nanometres at -5 $^{\circ}\text{C}$
	Döppenschmidt	[12]	2000	Measured 11 nm at -10 $^{\circ}\text{C}$ and 32 nm at -1 $^{\circ}\text{C}$
	Bluhm	[43]	2002	Layer thickness of 2 nm at 0 $^{\circ}\text{C}$
	Bäurle	[19]	2006	Wf thickness and relative contact area are main influencing factors. Calculated water layer between 30 and 250 nm at -5 $^{\circ}\text{C}$
	Makkonen	[20]	2014	Squeeze-out of water. Calculated a layer thickness of 0.05 $\mu\text{m}$ at -10 $^{\circ}\text{C}$
	Scherge	[58]	2017	Contrary effects: Wf increases with friction power / Wf squeeze out increases with surface pressure
	Canale	[59]	2019	Wf is created due to abrasion and not melting and Wf viscosity is up to 2 times higher than of pure water
	Liefferink	[63]	2021	Wf due to weakly bonded water molecules on surface
COF	Bowden	[25]	1939	COF is independent of velocity, normal force, and contact area. Decreases with decreasing temperature
	Strausky	[16]	1998	COF of 0.03 at -2 $^{\circ}\text{C}$ (measurements)
	Buhl	[42]	2001	Minimum COF of 0.02 between -3 $^{\circ}\text{C}$ and 0 $^{\circ}\text{C}$ (measurements)
	Bäurle	[19]	2006	COF of 0.06 at -10 $^{\circ}\text{C}$ (measurements)
	Winkler	[46]	2007	Decrease of COF due to increase in normal force. COF decreased with increasing friction speed. COF of 0.013 at -5 $^{\circ}\text{C}$ (measurements)
	Kietzig	[48]	2010	The higher the sample insulation, the lower the COF. Existence of a temperature-dependent minimum of COF
	Hasler	[49]	2016	COF of 0.04 at -5 $^{\circ}\text{C}$ (measurements)
	Makkonen	[20]	2014	COF of 0.05 at -10 $^{\circ}\text{C}$ (calculation)
	Böttcher	[56]	2017	COF of 0.05 at -10 $^{\circ}\text{C}$ (measurements)
	Velkavrh	[62]	2021	COF between 0.02 and 0.08 at -5 $^{\circ}\text{C}$ (measurements)
Auganæs	[65]	2022	COF of 0.04 at -3 $^{\circ}\text{C}$ with racing wax (measurements)	
Contact area	Bowden	[27]	1953	Friction is independent of the apparent surface area
	Kuroiwa	[30]	1977	Real contact area is only a fraction of the nominal contact area
	Bäurle	[19]	2006	Average static contact area is 5 % of total surface area
	Scherge	[58]	2017	No hydrodynamic friction is generated by skis

## 1.5 Conclusion and summary of the literature review

Ski jumping, despite its athletic and aerodynamic components, is basically the conversion of potential energy into kinetic energy during the acceleration phase of the ski jump and its subsequent conversion into jumping distance [4]. One important factor that reduces the efficiency of this conversion is the friction between the base of the athlete's ski and the iced in-run section of the ski jump. The resistances applied to the ski base when sliding on snow and ice are: ploughing in front of the ski, snow and ice compaction below the ski, deformation and fracture of asperities, shearing of the meltwater film, drag by dirt particles, and possibly capillary attachments between snow and ice grains and ski base [34,66]. Figure 1.8 shows the tribological system ski base – ice for ski jumping. The wax-coated ski base slides under load of approximately 500 N, corresponding to a nominal contact pressure of 2-4 kPa, at a maximum speed of 28 m/s on a milled ice surface (see chapter 1.1.4). The surrounding medium is air mostly below 0 °C and, depending on weather conditions, mixed with more or less moisture. Furthermore, the friction partners are surrounded by contaminants resulting from dirt, wax and polyethylene residues, etc.

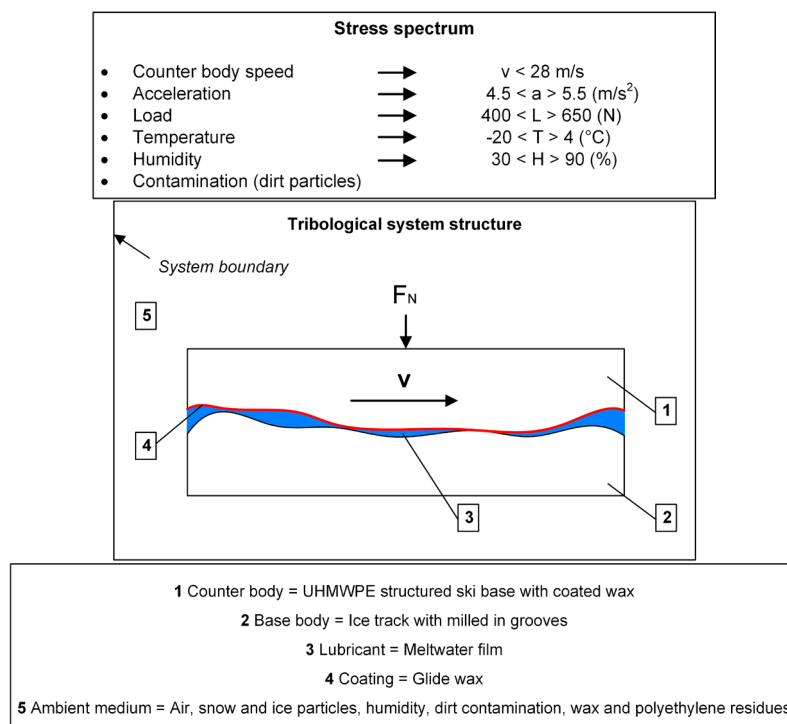


Figure 1.8: Tribological system ski base on ice for ski jumping

The Stribeck curve for ice friction is shown schematically in Figure 1.9. Low friction is considered to result from the formation of a thin lubricating film of water during the sliding of the ski [24,25]. The actual formation is assumed to happen due to frictional heating of the asperities which form the constantly evolving real contact area [19,27,30,45]. Depending on ice and ambient temperature, sliding speed, surface pressure, and meltwater layer, three different friction regimes are typically identified: dry, mixed and hydrodynamic friction [34–36]. Dry friction occurs in the sliding contact between two surfaces under the absence of a lubricating intermediate layer and manifests itself in a high coefficient of friction. However, even without any frictional heating, pre-melting causes a water film to be present on the ice surface even at temperatures below the bulk melting temperature of water [24,37,41]. The diffusion movement of weakly bonded surface water molecules was recently reported as a potential physical explanation [67]. It has been shown, that the pre-melted layer continues to grow due to compression and frictional heating and that equilibrium pre-melting, pressure melting and frictional heating occur simultaneously [68]. Its formation is the reason why there cannot be real dry sliding on snow or ice [48]. The liquid-like water film thickness has been estimated to be 1.5 - 2.0 nm at temperatures from -8 to -4 °C [43]. If an energy input due to e.g. friction causes the surface temperature to rise above the melting point of the ice at some points within the contact zone, meltwater is partially formed and mixed friction takes place. The COF subsequently decreases as the liquid-like layer increases [9,35,48]. If the thickness of the water film rises above the roughness peaks of the sliding surfaces due to an increase in temperature and the surfaces are separated entirely from each other, hydrodynamic friction occurs [34,49,69].

The COF between two interacting surfaces in relative motion varies with the dimensionless film parameter  $\lambda$ , the lambda ratio, defined as

$$\frac{h}{\sigma} \quad \text{Eqn. 1.2}$$

when the mean values of the centre lines of the rough surfaces are separated by a water film thickness  $h$  and when the combined root mean square (RMS) roughness of the surfaces is  $\sigma$  [70]. Using  $\lambda$ , the friction regime can generally be assessed, if  $\lambda < 1$ , the contact is in dry/boundary lubrication,  $1 < \lambda < 3$ , the contact is in a mixed lubrication

regime, and  $\lambda > 3$ , where hydrodynamic lubrication is present [71–73]. Cann et al. stated that the lambda ratio does not describe the collapse of the lubricating film and does not take into account the structure of the surface roughness, but only its numerical values. Further underestimated  $\lambda$  the enhanced wetting of smooth surfaces in contrast to rough surfaces. Depending on the temperature conditions and the resulting melt water film formation, the optimum of  $\lambda$  and the derived optimum surface roughness shifts [74]. Since reliable values for the lambda ratio under certain conditions are not yet available, it is of great interest to determine the proportion of mixed/boundary lubrication for modelling  $\lambda$  and to measure the change in the ratio experimentally [75,76].

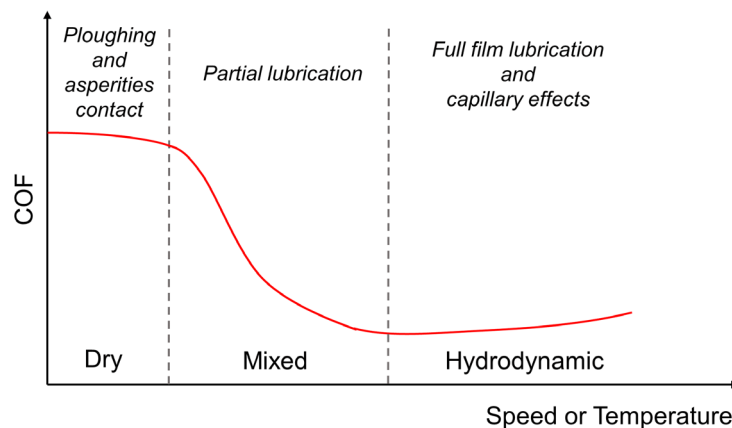


Figure 1.9: Stribeck curve illustration for ice friction based on [34,61]

Overall, with a friction coefficient of approximately 0.05 at  $-10\text{ }^{\circ}\text{C}$  between polyethylene and ice [19,42,45], the combined action of pre-melting and frictional heating is considered to result in water film heights in the range of several nanometres to several micrometres [12,19,20,31]. Due to the intermittent introduction of frictional heat into the top layer of a ski-jump's running track during a competition, the formed water films are not in thermodynamic equilibrium and therefore consist of a time-dependent mixture of water, pre-molten ice and ice. Such mixtures have been found to exhibit viscosities of up to two orders of magnitude higher than that of pure water [59]. The effect of surface roughness on friction between ice and snow conversely yielded varying results. In

dry/mixed conditions, friction increased with increasing roughness [30,48–51]. With hydrodynamic friction conditions, friction decreased with increasing roughness [30,47,50].

Traditionally, waxes are applied to ski bases in order to reduce friction [77–79]. Their friction-reducing effect results from their hydrophobicity which decreases the surface energy and increases the contact angle towards water [78,80–82], from reducing the viscosity of the mixed-phase of water film [11] and from influencing surface topography [83]. Waxes containing perfluorinated and polyfluorinated alkyl compounds have been found to be more effective in producing hydrophobicity than other waxes [78]. However, in 2019 the FIS decided to ban fluorine-containing waxes from all disciplines and all levels of competition [84]. It is going to come effective with the 2023/24 season and results in the need to develop new fluorine-free waxes. This has given the decades-old question of how to quantify the friction reducing effect of waxes new actuality. The sheer overwhelming number of parameters influencing sliding performance require constant adjustments of ski preparations to the given conditions for competition. The longstanding method of determining waxes and ski grinds still involves outdoor tests with full-size equipment and athletes or with laboratory tests, i.e. with tribometers that operate on reduced-size test specimens, regardless of the discipline of skiing, such as ski jumping, alpine or cross-country.

Using a light barrier, the time required for a predefined course is measured in order to obtain information about the sliding behaviour [85]. Furthermore, the runners' impressions of the sliding process are noted. Field tests offer the advantage of being operationally close to competitions but also exhibit a series of drawbacks - they are costly compared to laboratory tests, environmental conditions may change between test days, non-friction-related factors cannot be excluded (like air drag), reproducibility may be limited and the observed quantities, e.g. jumping distance or take-off velocity, may only indirectly represent friction between ski base and ski jump track or be subject to a series of other contributing factors [49,65,86,87].



## 1.6 Comparison of contemporary ice-tribometers

Laboratory tests are much more economically efficient, offer the advantage of controlled environments and the possibility to study the impact of individual factors in isolation and with high measuring resolution and accuracy [14,30,61,88–95]. Therefore, a wide range of tribometers have been developed, see Table 1.5.

Overall, the existing tribometers can be classified into rotational and linear movement based on their type of motion. In the first group, the pin-on-disc principle is mostly adopted in which a disc (ice/snow) is set in rotation and a pin (ski sample) is loaded onto the disc [45]. The second group moves the samples on the ice linearly [49]. One key difference between laboratory and field tests is the reduced test specimen size in laboratory tests. Therefore, concepts that have been developed for reducing the contact area between ski and snow, e.g. ski curvature to reduce the overall contact area and therefore to increase the average contact pressure, cannot be reproduced in laboratory testing. Three existing tribometers have tried to use a full ski as a test specimen [49,64,65]. However, this required the construction of snow tracks of up to 27 m in length and has caused costs of up to 1.15 million EUR [44]. Other tribometers use much smaller test specimens which are only sections of a ski base that is attached to a specimen substrate. This follows the philosophy of assessing the friction reducing properties of waxes in isolation and to compensate any missing geometric effects by choosing appropriate pressures. Other issues of reduced sample sizes are potential differences in the formation of lubricating water films, the availability of only a reduced section of the ski base's topography and the very low absolute normal and friction forces at realistic pressures, leading to issues with the signal-to-noise ratio. Tribometers which used realistic pressures (2 - 4 kPa) with reduced samples sizes suffered from very low normal forces which, in combination with COFs below 0.1, resulted in very low absolute friction force signals [88].

In order to compensate this, many studies used pressures that are significantly higher than the 2 - 4 kPa that are typically found in ski jumping. As a consequence, it is subject to scrutiny whether the conducted tests reproduced the micro-mechanical, thermal and frictional situation during ski jumping correctly. Also, another aspect of laboratory testing is that tests are usually done in multi-pass mode, i.e. every individual area of the

ice sample is slid-over multiple times during a test. This can lead to time-dependent effects like changes in surface roughness [19,88] and melting [66]. Typically, this is compensated by regular re-conditioning of the ice surface and by intermittent test operation to allow for the re-solidification of molten ice [42,46].

Additionally, for the rotational tribometer types, there is by design a potential misalignment between the main orientation of the surface topography of the ski base and the sliding direction. Furthermore, it has been hypothesized, that any formed water film might be forced radially outwards of the frictional contact and that its thickness might depend on the rotation speed of the disk [87]. Due to the sample length, linear tribometers are either very short and allow only low sliding speeds [56,61] or exceed a usual laboratory size and are therefore costly [49,64].

Table 1.5: Overview of existing tribometers for measuring friction between ski base and snow/ice. Reported parameter values or ranges represent either the maximum value range of the respective parameter or the actually realized experimental range, whichever is higher or available.

Author	Year of first publication	References	Method <sup>T</sup>	Type of motion <sup>M</sup>	Air temperature in °C	Does not centrifugate water film	Uses full-size ski base	Single-pass	Configurable acceleration	Nominal contact area in cm <sup>2</sup>	Normal force in N	Contact pressure in kPa	Maximum sliding speed in m/s	Reported COF range in 10 <sup>-2</sup>
<b>Full-ski samples</b>														
Hasler	2016	[49]	P	LC	Up to -20	●	●	●	○	845 <sup>E</sup>	50 - 700	5.9 - 82.9	30	3 - 7
Lemmettylä	2021	[64]	P	LC	-20 to +10	●	●	●	●	840 <sup>E</sup>	600 - 1200	71.4 - 142.8	6	1 - 3
Auganæs	2022	[65]	P	LC	-3	●	●	●	●	845 <sup>E</sup>	50 - 800	5.9 - 94.7	8	4 - 14
<b>Reduced-size / simplified samples</b>														
Buhl	2001	[42]	D	RC	-20 to 0	○	○	○	○	1	5 - 30	50 - 300	5	3 - 17
Winkler	2006	[46]	D	RC	-30 to 30	○	○	○	-	HC	3 - 9	HC	9	1 - 3
Bäurle	2006	[45]	D	RC	-20 to 1	○	○	○	○	2 - 10	20 - 100	20 - 500	20	3 - 11
Takeda	2010	[88]	D	RC	-15 to -1	○	○	○	-	55	2.5 - 10	0.5 - 1.8	1	3 - 13
Scherge	2013	[89]	P	LC	-5	●	○	○	-	HC	100 - 500	HC	28	1-10
Böttcher	2017	[56]	P	LO	Up to -20	●	○	○	-	26	40 - 80	15.4 - 30.8	1	2 - 7
Velkavrh	2019	[61]	P	LC	-20 to 0	●	○	●	○	6	52	82.5	3.5	3 - 24
Kim	2022	[96]	D	RC	-10 to -2	○	○	○	-	3	0.6	2	28	3 - 14
Lutz	2023	*	P	LC	-25 to -1	●	●	○	●	160/330	40 - 140	1.2 - 8.8	28	1 - 10

\* Presented in this work

- Data not available

HC: Hertzian contact

<sup>T</sup> P: Plate-on-Plate, D: Pin-on-Disk

<sup>M</sup> LC: Linear, continuous, RC: Rotatory, continuous, LO: Linear, oscillating

<sup>E</sup> Ski width estimated

The analysis shows that no laboratory tribometer so far can reproduce the suitability sequence observed in the competition or field test and thus no reliable tool is yet available for the preliminary assessment of newly developed waxes. A final evaluation of new developments still requires a costly trial programme indoor or outdoor that is vulnerable to interfering factors. The limitations of the previously presented tribometers led to a new development of the tribological method for friction measurement of skis on ice. In this work, a novel tribometer design that effectively uses a full-size ski base test sample that is slid linearly against an ice sheet sample is presented. The nominal contact area is 160 mm x 100 mm and 330 mm x 100 mm, which results in a normal force of 66 - 99 N for simulating 2 kPa - 3 kPa with the larger sample. Its intended use is the assessment of waxes by measuring their impact on friction force when applied to an actual ski base. The tribometer will contribute to developing future fluorine-free waxes with their various additives in reduced development time.



## 2 Methodological design of an ice tribometer

As shown in Figure 2.1, based on [97] and the handbook “Production und Management” [98], the types of design can be classified in new, adaptive, variant and fixed principle design, depending on the degree of innovation. The design types start in different phases depending on whether development results are already available or not. Starting with the planning phase, the basic phase for product ideas, the tasks to be completed are clarified and specified. Within the conceptual phase, the overall development is divided into subfunctions and solution principles are compiled. In the following design phase, drafts are worked out and in the last phase, the development phase, the final design is elaborated and developed.

The tribometer test rig to be created in the present work has to have more application- and reality-oriented measurement characteristics compared to existing tribometer systems to ensure better transferability into practice. Thus, a “new design” approach was carried out according to methodological guidelines and thought concepts such as those contained in the VDI (association of German engineers) guidelines.

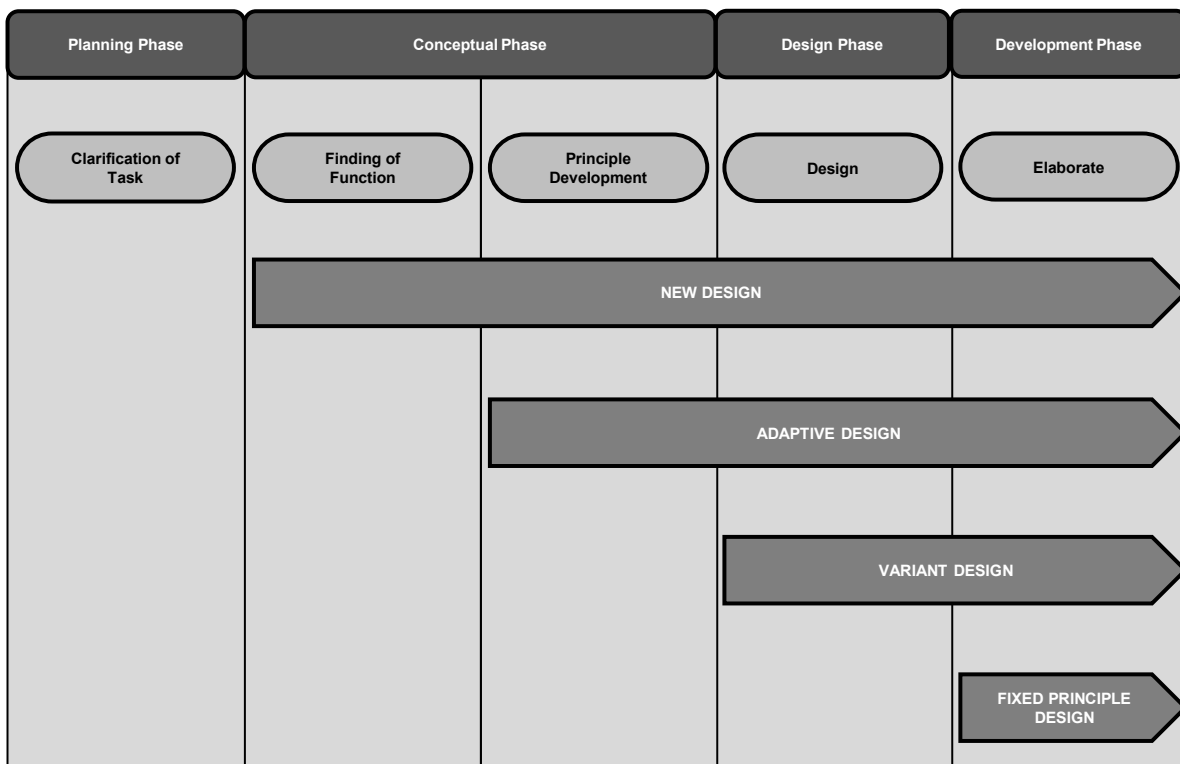


Figure 2.1: Types of design (based on [97–99])

## 2.1 Methodological design structure according to VDI 2221

The general procedure for a methodological design process is laid down according to the standard 2221 of the VDI [100]. The procedure is divided into eight work steps, shown in Figure 2.2. In order to make the methods of product development more process-oriented and thus more company-oriented, the 1993 VDI standard 2221 [97] has been fundamentally revised and restructured in 2019.

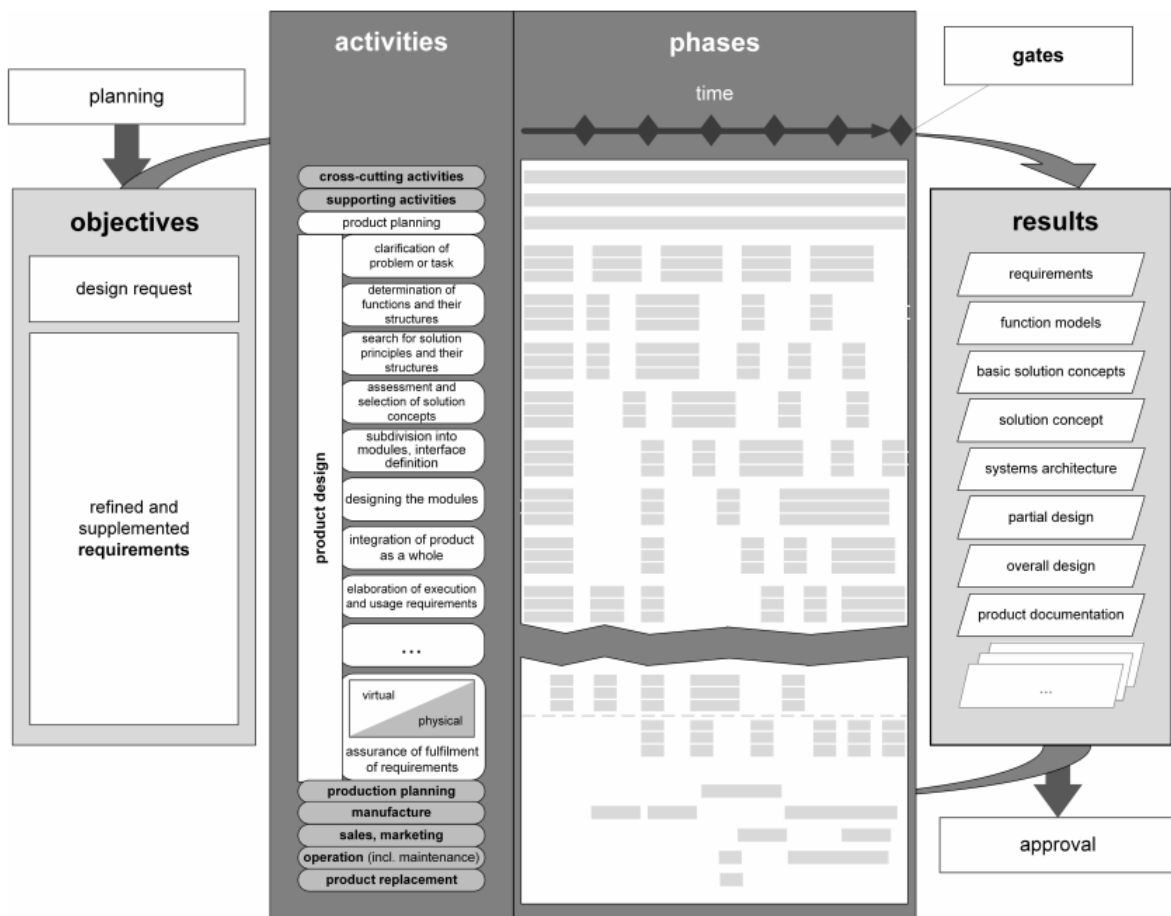


Figure 2.2: General procedure for developing and designing (specific model of a product design process) [101]

This procedure is a guideline, but not strictly sequential procedural steps to which detailed work processes are assigned. During the design process, it is often necessary to perform deliberate repeat cycles of previous work steps and revise them as changes

occur due to the design. The innovation process for the design of a tribometer, in form of a BPMN diagram, is shown in Figure 2.3 and discussed in the following paragraph.

## **2.2 Planning phase**

During the first phase, the planning phase of the tribometer design, the tasks and objectives to be performed by the developer need to be clarified and specified in concrete terms. These activities consist of gathering all available information regarding the product context, including the identification of information gaps, verification and completion of the requirements received, the addition of specific requirements and, the conscious formulation of the problem from the developer's point of view. This, includes the analysis of current processes and necessary restructuring and planning of the procedure in its entirety. A structured collection of requirements therefore forms a central aspect of the work [100,101].

These requirements will change depending on the development process and must therefore be constantly updated and adapted to the current development stage. Normative changes in the course of development or changes on the part of the project partners must also be included in the list of requirements. The changes or additions will be ongoing and consistently implemented and documented [100,101].

As described below the planning phase is subdivided into the four steps of: development of product ideas, list of requirements, house of quality and requirement and functional specification.

The product "Tribometer - wear test rig" has been a development project for which the objectives were clearly defined. The application area (field of ski jumping) and the prevailing system there, are largely known. By clarifying the task, information has been obtained that was incorporated into the requirements list. The clarification of the task and a consideration of the current market situation are carried out in the following chapters.

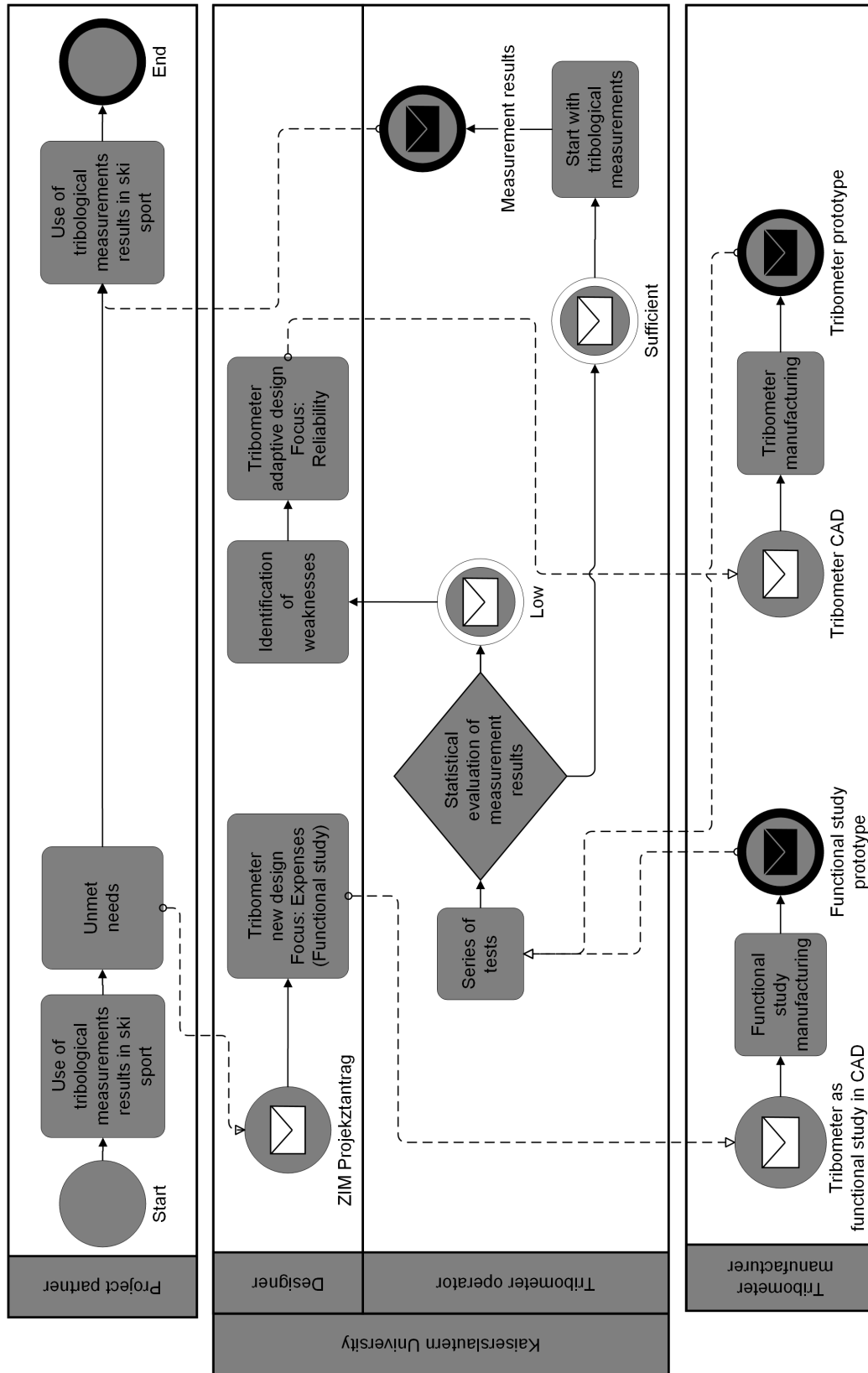


Figure 2.3: Tribometer design process as business process diagram



### 2.2.1 Target group report

State of the art techniques and their practical uses were presented in a discussion with the project partners. When a ski jumping competition takes place, there are, aside from the choice of wax and the coating itself, entirely different approaches which are followed in order to achieve the lowest possible friction of the ski base. These approaches are strongly dependent on the weather, temperature, humidity, the presence of snow or rain and of course how strong the wind is. During a competition weekend, the skis and their running characteristics are not tested but the preparation is based solely on the experience of the service staff. Some ski preparers cover the skis with snow overnight, while others take the skis to the hotel room so that the skis are stored overnight at a higher temperature. The effects of these radically different approaches cannot be categorized on the day of the races, and no correlation can be drawn with the results of the jumpers.

During the development of the different ski bases, the project partner already relied on measurements with tribometers. Due to differences between measurement conditions and the conditions prevailing on the race weekend, no correlation could be drawn between the measurement results obtained and the actual experienced running characteristics of the skis. According to the project partner, the evaluation of the running characteristics of the skis is still best accomplished with field tests.

Table 2.1: Project partners' list of requirements

Reliable results
Results obtained under the same conditions as in competition (speed, acceleration, temperature, load)
Possibility of a transportable system for friction measurement on site

## 2.2.2 Methods of product idea generation

“Idea generation is the identification of new product ideas within predefined search fields, taking into account the company's potential.” [99]

There are two methods of finding new product ideas: Collecting product ideas and searching for product ideas. The first approach consists of collecting and evaluation of internal and external information [102]. The second approach is characterized by the use of intuitive or systematic idea search methods. The generation of ideas as an on-going task of product development, requires the application of both approaches [99]. Since the "product idea" for the design of a tribometer has already been established, the product idea identification methods are used to identify vulnerabilities of the existing tribometers and their possible solutions. Possible internal and external sources available within the university environment are displayed in Table 2.2. In a subsequent process, the collected and documented ideas are evaluated with regard to their realization and economic efficiency.

Table 2.2: Internal and external sources related to university environment

Internal sources	External sources
Discussion with project partners and faculty members	Competitive research and literature review
Involving other departments and their professors and staff members	Exhibition visits
Contacting people with technical backgrounds in the university environment	Analysis of patents
Scouting of the involved staff	Trend analysis
	Lead-User-Analysis

In order to find approaches that address the vulnerabilities of the existing tribometers' measurement methods, creativity techniques can be applied to search for ideas, with the aim of obtaining promising and feasible solutions to the identified weaknesses.

Table 2.3 shows a brief selection of creative techniques that were chosen and applied based on selection criteria, such as available time, available money, qualification of employees and complexity of the task, for idea generation and the assessment of developed solutions.

During the process, “problem ideas” might emerge within the creativity process, for which solutions must first be found before definitive improvements of the tribometer’s method of operation can be proposed.

Table 2.3: Creativity techniques

---

Brainstorming recorded in a mind map
Morphological methods
Delphi-Method
Method 635 / Brainwriting

---

### 2.2.3 General list of requirements

In order to generate the list of requirements, current state of the art developments in the field of skiing were reviewed and methods for friction measurements of different materials, especially for the friction partner ice, were assessed.

Following the use of internal and external sources, and based on the target group report, a rough selection was made using creativity techniques. Various other requirements were derived from internal experience with past projects and were added to the rough selection.

With the completion of the rough selection, the selection was further refined with the help of a cost-effectiveness analysis to finalize the requirements list. Figure 2.4 illustrates the procedure for creating the requirements list shown in Table 2.4.

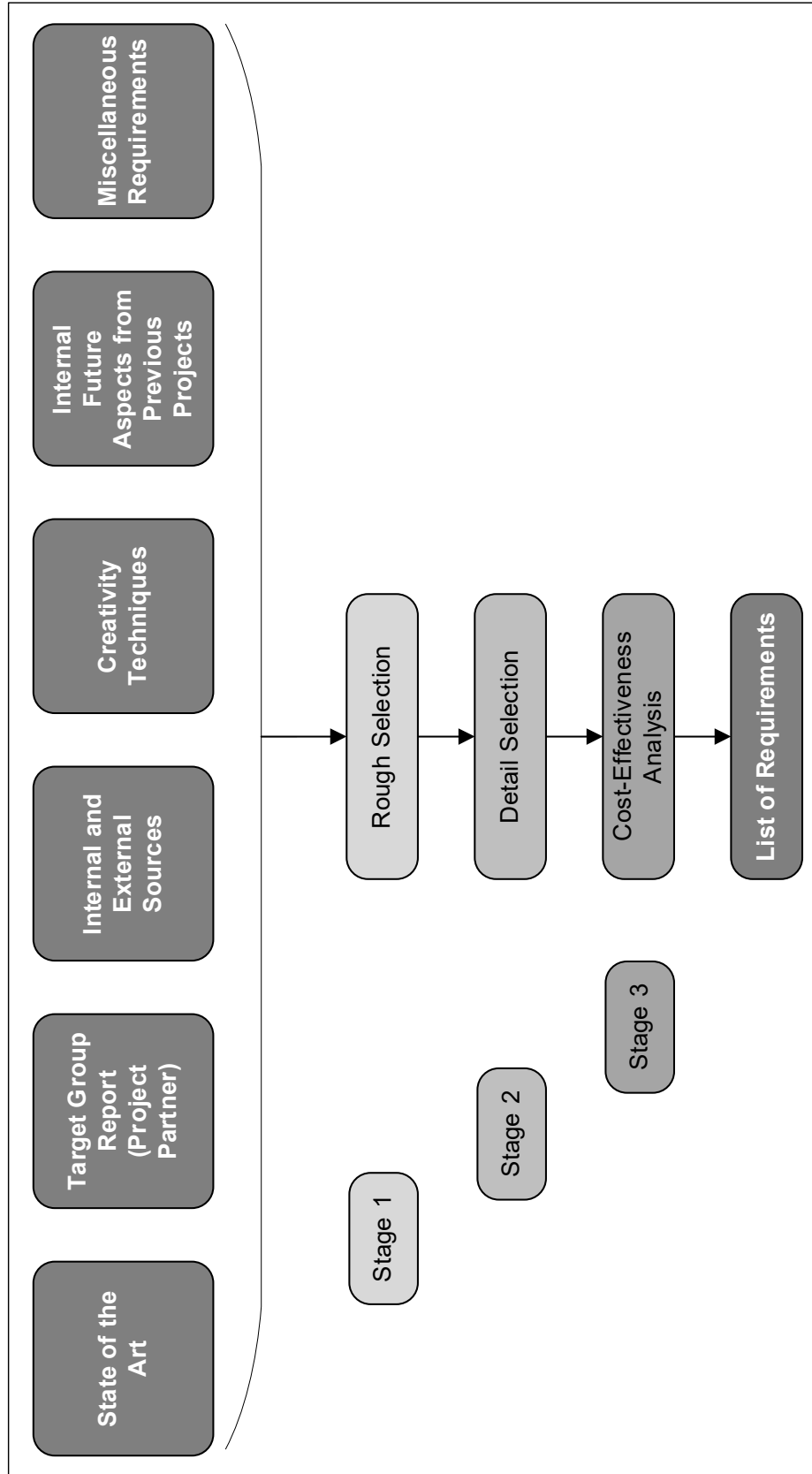


Figure 2.4: Process of creating the list of requirements

Table 2.4: General list of requirements

---

Cost-effective (manufacturing / operation)
Fast realization
Possibility of disassembly
Space saving (lab size)
Safety and security
Functions manageable in university environment (no trained mechanics, changing staff)
Operable by instructed personal
Low maintenance and easy to maintain (low wear)
Low incidence of vibrations
Tilt stable
Measurement with practice-oriented loads and conditions possible (surface pressure, temperature, speed, acceleration, time)
High reproducibility
Transportable system

---

In order to obtain a better overview of essential and desirable properties, the general requirements for the test rig was subdivided into “Demands” and “Requests” based on the hierarchical structure of [103] as displayed in Figure 2.5.

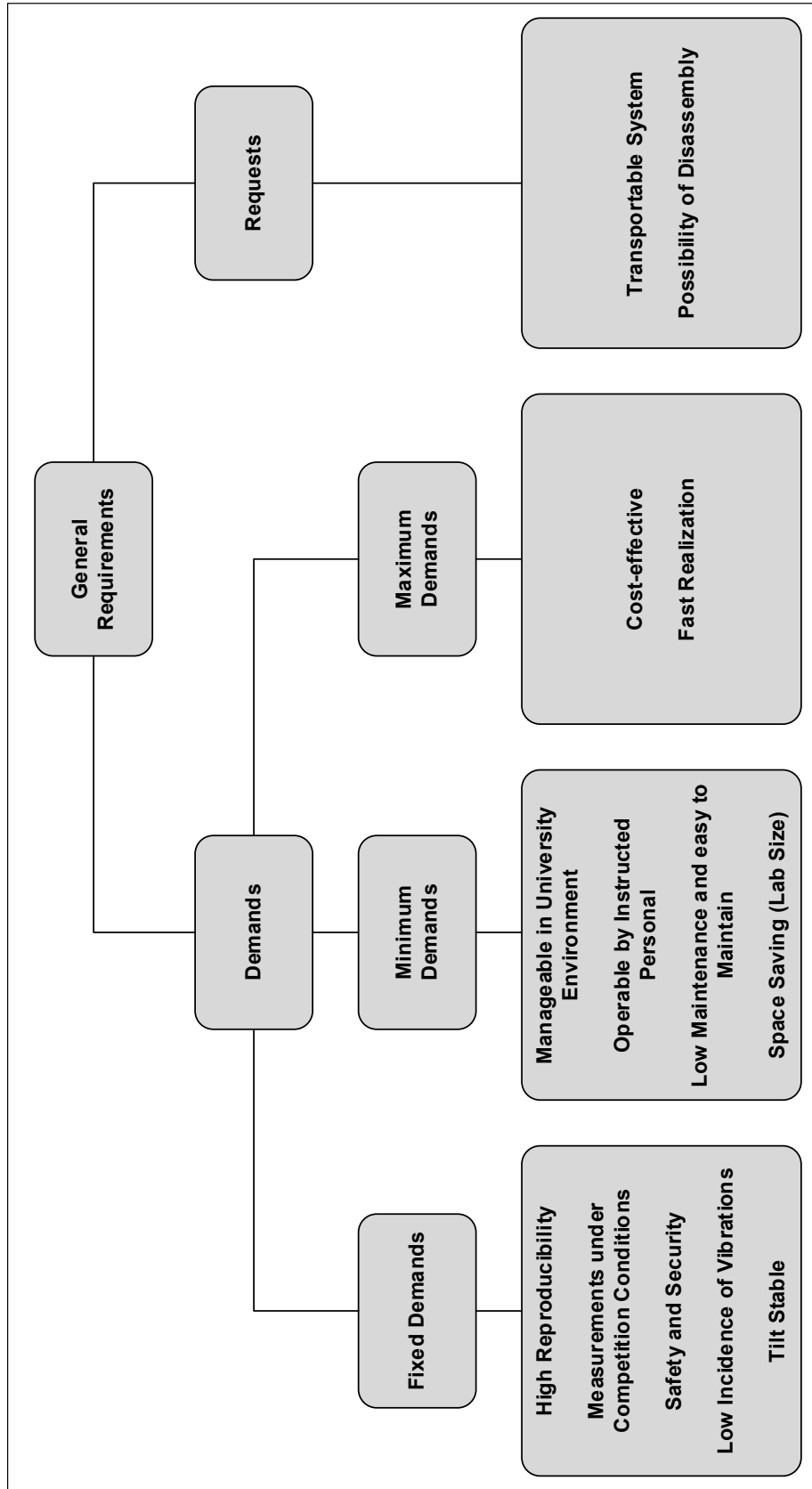


Figure 2.5: Hierarchical structure of general requirements on the test rig  
(based on [103])

## 2.2.4 Conceptual phase

During the conceptual phase, the general determination of technical solutions is made. This phase starts immediately after the requirements list has been defined. A functional structure is created and suitable operating principles are sought for the respective sub-functions, which are then defined as solution variants. This phase is initiated as soon as the task is clearly defined, no further information on the tasks is required and the list of requirements drawn up can be fulfilled or the goals formulated in the specifications can be achieved. In this phase, increased consideration must be given to the technological options in order to select a suitable solution principle. The solution principle must take into account the existing conditions and must be in accordance with the objectives from the requirements catalogue and the specifications. On the basis of this solution principle, solution variants are developed, which must be evaluated. Variants, that do not meet the goals of the particular requirement list, are eliminated following the evaluation. [104–107] The evaluation is carried out based on the aspects selected in Table 2.7.

## 2.2.5 Black-Box

In order to simplify the structure of complex systems, top-down methods in which the field of view for certain problems and their solutions is first broadened and then narrowed down step by step have proven themselves to be essential. One such top-down method is the "black box" method [107].

The black-box method is a representation of the input and output variables for the description of processes and functions without consideration of the

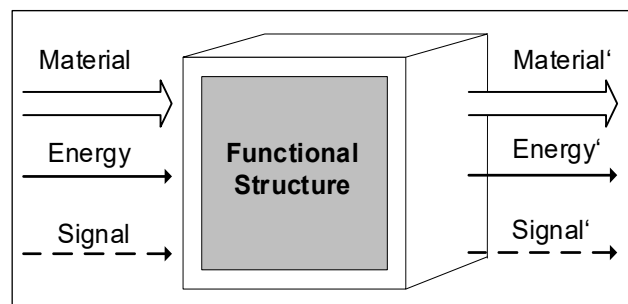


Figure 2.6: Black-Box (according to [88])

internal structure of the system for which the solution is not known (cf. Figure 2.6). The overall function is located inside that black-box, in which the input variables "material", "energy" and "signal" are converted to output variables. Furthermore, a splitting of the

overall function into subfunctions is created [100,106,107]. For the top level of a tribometer, the black box could appear as shown in Figure 2.7.

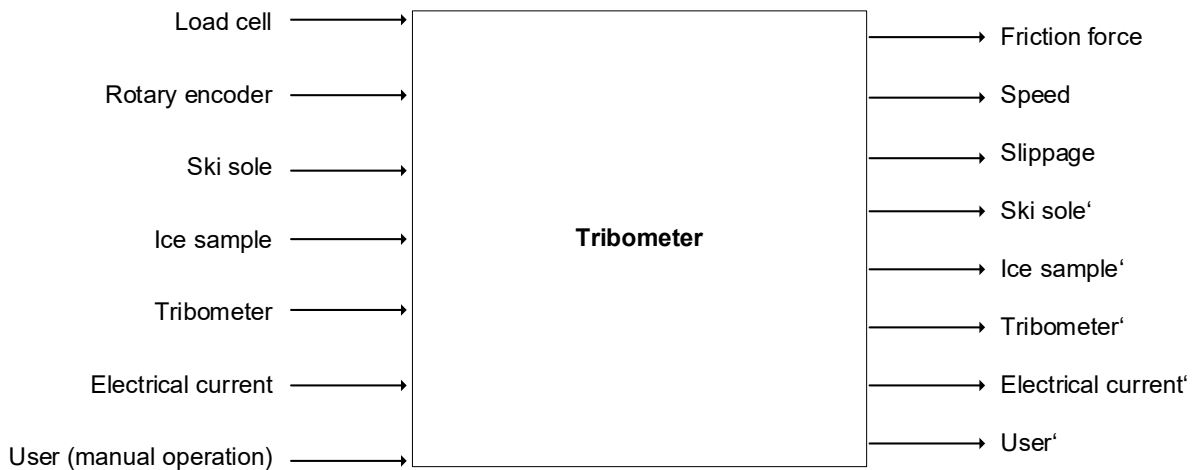


Figure 2.7: Black box of a tribometer (based on [107])

Since it is difficult to represent complex tasks with the black-box method, it has a limited range of application for systems with many subfunctions. By the black-box method, a principle solution is developed step by step from the physical effects and the geometrical arrangement of operations. [104,105]

### 2.2.6 Functional structure

Based on the black-box method and by linking subfunctions in a reasonable and compatible way to an overall function, systems with high complexity can be represented abstractly in a functional structure step by step [104]. A functional structure describes the essence of a technical task in a few words or with symbols. This functional structure is basically solution-independent and describes the realization of the subfunctions. It describes the links between subfunctions and the overall function. The description includes the relationships between input and output variables. With the aid of the description of these interrelationships, a solution is created with which the objective can be realized. These interrelationships have to be unambiguous. [104,105] A function is the formulation of the solution task on an abstract and solution-neutral level. An example of such a function could be the method of reaching the test temperature. In the



functional diagram, functions are generally represented with input and output as introduced with the black-box method in the previous chapter. Figure 2.8 shows the top-level functional structure of a tribometer. The functions are each assigned to an input variable. Within the total function a combination of the input variables follows, whereby the function structure is decisively determined by some influencing variables such as the counter body or the input of energy. [104,105] There are three types of input and output variables: energy flows, material flows and signal/information flows [105–107]. When creating a functional structure, the quantities and properties of the input and output variables are known. The overall function mentioned above describes the tasks and implementation of these flows and is broken down into subtasks, which are compiled step by step. [100,101] The different order and arrangement of the subfunctions results in a solution principle on which the solution variants are based [104,107].

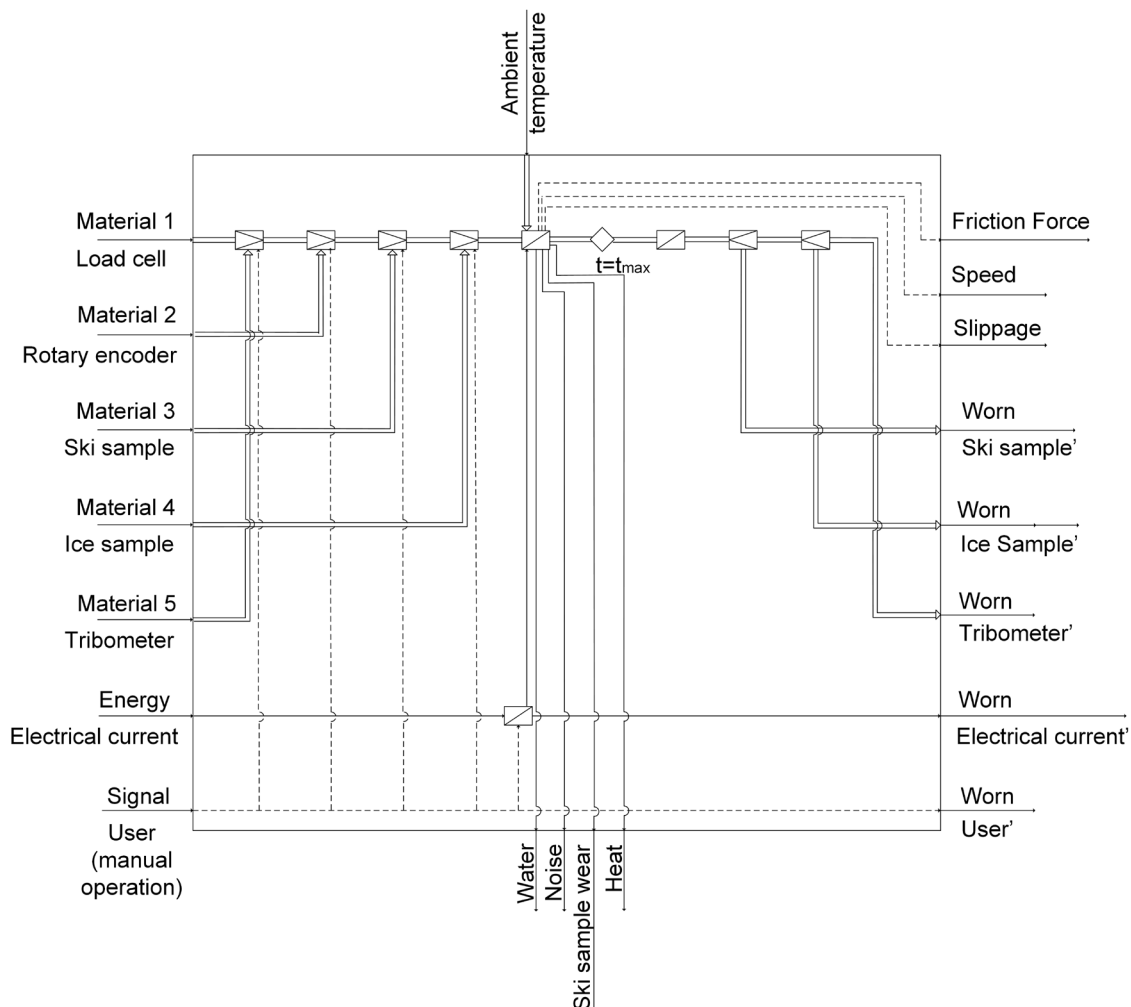


Figure 2.8: Top level functional structure of a tribometer

## 2.2.7 Subfunctions

The evaluation of the tribometers yields important criteria for the methodical selection of the design to be implemented. After the subfunctions have been defined and a list of requirements has been developed, the way in which the friction partners are moved is determined in the following chapters. Accordingly, the overall design has first been divided into six subfunctions as shown in Table 2.5.

Table 2.5: List of subfunctions

Indices	Subfunction
I	Type of movement
II	Mounting of ski base sample
III	Mounting of ice sample
IV	Application of load normal to the wear direction
V	Friction measurement
VI	Cooling

### 2.2.7.1 Subfunction I: Type of movement

The first subfunction involves moving the ski base or the ice surface. The drive and effect types known from conventional tribometers (e.g., pin-on-disc, pin-on-plate, plate-on-plate, etc.) may be used for the concept development. The drive needs to be reproducible and introduce as little vibrations as possible into the system. Simultaneously, the drive must meet the acceleration and terminal speed of the required demands. The requirements must also be met under load (simulation of the jumper weight). Since only a motor driven by electricity is realistic for the application to be described, this subfunction determines the way in which one of the samples is driven. Of course, no solution is excluded without evaluating it in more detail.

### **2.2.7.2 Subfunction II: Mounting of the ski base sample**

Subfunction two includes the assembly of the ski base sample and disassembly after a measurement. The size of the ski base sample will be defined taking into account the necessary surface pressure in relation to the ice sample. A central requirement for the shape of the sample is a planar contact with the ice surface. Thus, point and line loads are ruled out for the mounting selection. As wear occurs on both bodies, the ski base has to be replaced after an interval to be defined, irrespective of the test length, in order to ensure consistent test conditions. Due to the wax coating of the ski base and its influence on the friction properties, it is necessary to determine how quickly it wears off as a result of friction. In order to evaluate the influence of the wax and the structuring of the ski base surface on the friction properties, three different modifications are to be tested; the ski base without structuring and without wax, the ski base with structuring only and the finished racing ski base, structured and waxed.

### **2.2.7.3 Subfunction III: Mounting of the ice sample**

The third subfunction covers the mounting of the ice sample as well as the dismounting after a test. The size of the sample is defined in consideration of the necessary surface pressure in relation to the ski base sample. A central requirement for the shape of the sample is a planar contact with the ice surface. Thus, point and line loads are ruled out for the mounting selection. Due to the assumed rapid wear of the ice surface, it must be replaced or reconditioned after each measurement procedure. Also, with respect to subfunction two and three, a parallel alignment of the samples to each other must be ensured during the entire measurement. Any ice particles that may come loose from the ice surface as a result of friction must be able to be guided in a safe direction away from the operator.

#### **2.2.7.4 Subfunction IV: Load application**

To simulate the jumper weight, both samples must be subjected to an equivalent force and thus be compressed together. This force must be distributed homogeneously and vibration-independently to the samples during the entire test run and must not change. In this subfunction, the mechanism for applying the normal force as well as the initiation into the samples will be developed.

#### **2.2.7.5 Subfunction V: Friction measurement**

The fourth subfunction involves measuring the friction force to determine the coefficient of friction. The friction measurement should be carried out as directly as possible and should be designed with low friction in order to avoid distortions in the measured values.

#### **2.2.7.6 Subfunction VI: Cooling**

In subfunction five, the cooling of the samples or the entire system will be developed. Since the test temperature reaches the double-digit minus range, encapsulation from the environment is necessary. The test temperature must be adjustable over as wide a range as possible in order to be able to detect differences due to the temperature change.

### **2.2.8 List of requirements allocated to subfunctions**

The analysis of the tribological system in chapter 1.5 leads to the following general conditions describing the system:

Table 2.6: Analysis of the tribological system for ski jumping [22,108]

Normal load	400 – 650 N
Maximum ski width	115 mm
(Nominal) contact pressure	Between 2 – 4 kPa
Relative sliding speed	Up to 28 m/s
Acceleration	Up to 5.5 m/s <sup>2</sup>
Contact partner	Milled ice surface and UHMWPE ski base
Surface quality ice	Constantly changing surface – partly severely damaged
Surface quality ski	Condition-dependent structured and coated with wax (see chapter 4.5.2)
Ambient temperature	Between -20 and +4 °C (most competitions at approx. -6 °C)
Ice temperature	-7 °C (cooling system dependent – actively cooled)
Air humidity	30 – 90 %

The information gained from the analysis finally leads to the list of requirements. Table 2.4 has been expanded partially and subdivided into the following Table 2.7 for the respective subfunctions. This includes the general but also the special requirements for the realisation of the individual assemblies. Please note that the list of requirements does not represent a weighting.

Table 2.7: List of requirements

<b>Subfunction I</b>  <b>Type of movement</b>	Low induced vibration
	Acceleration of 5.5 m/s <sup>2</sup> can be achieved
	Speed of 28 m/s can be achieved
	At least several speed and acceleration gradations possible
	Friction direction of the ski base in the direction of structuring
	Sufficient sample size to achieve real surface pressure
	Planar contact of the samples to each other
	No transversal movement of samples to each other
	Low polishing effect
	Temperature measurement of ski and ice sample during friction measurement
Fast change of ski and ice sample	

<b>Subfunction II</b> <b>Mounting</b> <b>ski base sample</b>	Cost-effective Possibility for a pre-version with a lower cost input Manageable bearings installation Fast replacement of the ski base Low induced vibrations
<b>Subfunction III</b> <b>Mounting</b> <b>ice sample</b>	Planar contact with ski base sample Sufficient size to achieve real surface pressure Low inherent friction Fast change of ice sample Low-vibration mounting Exclusion of tilting of the ice sample Possibility of temperature measurement on surface and close to surface
<b>Subfunction IV</b> <b>Load</b> <b>application</b>	Load (surface pressure) equivalent to real jumper weight Homogeneous load distribution Vibration-independent Adjustable Load must be defined at all times
<b>Subfunction V</b> <b>Force</b> <b>measurement</b>	Force measurement with low inherent friction Direct force measurement (no influence by bending of attachments) Vibration resistant Minus temperature range
<b>Subfunction VI</b> <b>Cooling</b>	Adjustable Ski base and ice sample are cooled during measurement Ski base and ice are at the same temperature during measurement Consistent during measurement Possibility to examine ice and ski sample during measurement

For overview reasons provides Figure 2.9 the different subfunctions and the corresponding lists of requirements.

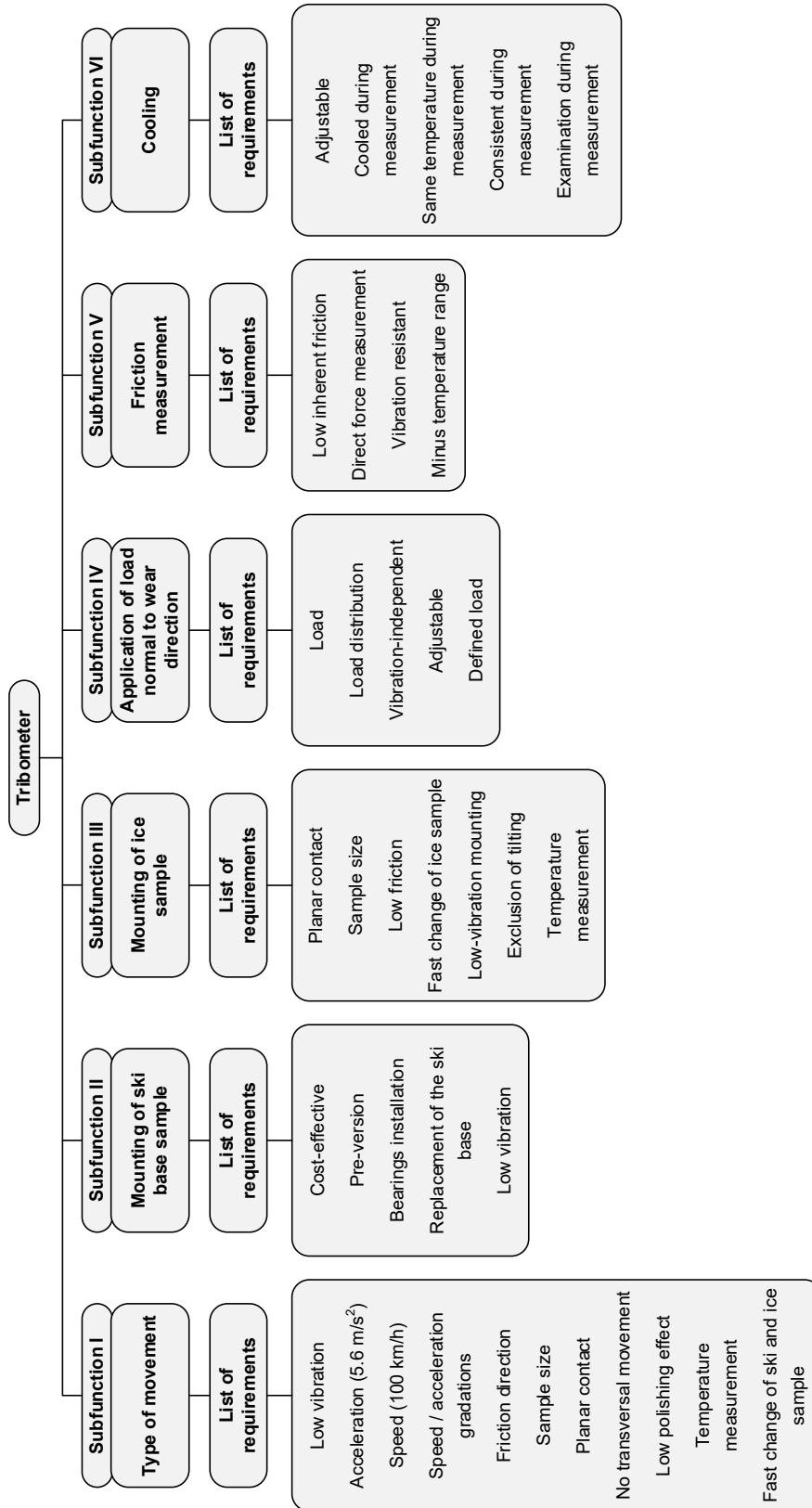


Figure 2.9: Tribometer's subfunctions and their lists of requirements

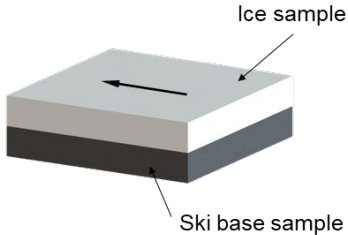
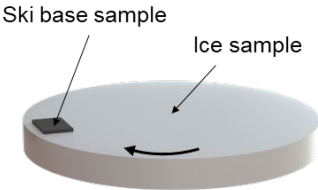
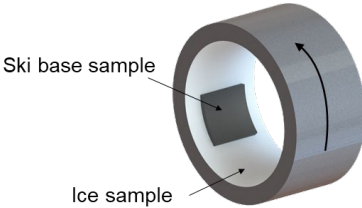
### 2.3 Solution concept for subfunction I: Type of movement

Using the functional structure defined in chapter 2.2.6, various solution concepts are drawn to describe subfunctions. Active principles must be found for these subfunctions, which are later combined to form an active structure, from which the possible solution (solution concept) emerges. The active principle contains the physical effect required for the fulfilment of a function as well as the geometric and material characteristics [97,103,104]. In general, all methods described previously can be used to search for active principles. However, in addition to literature research, methods for analysing natural and known systems, intuitively emphasized methods and, if initial solution ideas from previous developments (competitor products) are available, a systematic analysis of the physical occurrence and systematic search with the aid of order schemes and variant formation are of particular importance. A helpful option for finding solutions are design catalogues, for example by Koller, who proposed solutions for physical effects and principles of action [104,105,109], or Roth [110]. During the determination of possible solutions, the solution concepts described below were developed.

The subfunctions cannot be selected independently of each other because subfunction I influences to a large extent all other subfunctions and their implementation. For this reason, the remaining subfunctions are evaluated and selected only after the general concept of subfunction I has been evaluated and selected. As displayed in Table 2.8, three possible concepts have been selected based on existing tribometers. As a result of the rectangular shape of a ski there is, at least macroscopically, a flat contact surface directed towards the ice. A central requirement for the shape and the mounting of the ski sample is therefore a planar contact to the ice surface. This means that point and line loads, such as those that occur with ball-on-plate or block-on-ring tribometers, are excluded as possible of the types of movement for selection. Furthermore, an oscillating motion would be disadvantageous due to the resulting polishing effect of the ice surface which would create a consistent measurement of the friction properties as observed by [19]. To minimize surface polishing occurring simply as a result of the type of movement, the two bodies need to be moved continuously with respect to each other.



Table 2.8: Solution concept for subfunction I

Subfunction I: Type of movement		
Variant 1	Variant 2	Variant 3
		
Plate-On-Plate	Plate-On-Disc	Plate-On-Ring
Translational Continuous	Rotatory Continuous	Rotatory Continuous

Three variants were developed as potential modes of movement. In variant 1, one of the samples is fixed and the other sample is moved continuously in parallel with respect to the first. For this type of movement, the decision regarding which of the two samples (ice and ski) will constitute the fixed and moving samples can be made at a later time point based on the sample arrangement. Variant 2 features a rotating disk with a rigid sample or a rigid disk and rotating sample. By an involute inward trajectory, it could be avoided that the sample always runs over the same ice track. Due to the rectangular shape of the ski base (the shape is a result of the peeling process during the production of the UHMWPE base), it could already be assumed that the disc and plate represent the ice and ski samples respectively. In variant 3, one of the samples is formed as a ring and the other sample is pressed concentrically either inside or outside. With this arrangement, it is conceivable that both elements could represent either ice or ski surfaces. The ice surface could be located in or on a ring and the ski base is arranged tangentially or, as an alternative, a ring is formed with the ski base on a support structure and a curved ice sample is again arranged tangentially.

For all three identified movement options, the selection of which element will later comprise the ice sample and which will be the ski sample is made after the weighting is completed. After the requirements for subfunction I have been defined according to chapter 2.2.8 and the solution concept has been determined, the requirements are classified according to their importance. This weighting was carried out with the help

of weighting factors [109]. To determine these weighting factors, a 2x2 dominance matrix (pairwise comparison) was created based on [109], in which the requirements of the respective subfunctions are compared with each other. At this point, it is differentiated whether a requirement is more important, equally important or less important than another of the requirements specified in the previous chapters. Table AP 2 shows this pairwise comparison. The result of the weighting factors' determination reflects which aspects are most important to the measurement test rig. The ability to generate measurements with a surface pressure comparable to those found in competition, reach a speed of at least 28 m/s in order to represent the acceleration typical for a ski jump, and a frictional force direction in line with the structuring direction of the ski base were given the highest weighting. In contrast to the wishes of the future operator, the fast change of the friction partners was given a lower rating compared to the measurement-relevant features.

The solution variants for the various subfunctions presented in Table 2.8 are evaluated according to their ability to meet the requirements listed in Table 2.7. The scores obtained are multiplied by the weighting factors derived from Table AP 2 and the products are summarized [104,105]. The final result is the total score achieved by a solution variant for a subfunction, as can be seen in Table AP 3 to Table AP 5. Such a rating is performed with each subfunction. Solution variants with a particularly low total score in relation to the mean value of the total scores of all variants are eliminated and not considered further [104,105].

As previously described, the solution variants with rating results below the calculated average, are eliminated in the next step for each subfunction, cf. [104,105,111]. After evaluation, the mean value of all scores for the first subfunction is approximately 3.2. Solution variants 1 and 3 received similar total scores of 3.7 and 3.5 respectively. The score of 2.5 generated for variant 2, resulted in its elimination from the following process. Due to the higher assessment score of variant 1 compared to variant 3, the plate-on-plate version is thus the final variant of the tribometer to be designed. In the following chapters, the methodical approach to finding solutions for the remaining subfunctions will be shown and discussed. After the variant to be realised had been selected, a suitable experimental setup was sought. Due to the expected costs and the lack of

storage space at the university for a sufficiently long gliding track, a linear, non-oscillating tribometer system has been excluded for the further design process. Figure 2.10 displays the variant of the tribometer to be realised. In order to achieve a linear form of movement without the disadvantages of costs and space requirements mentioned above, the ski base in a belt from can be driven by a roller drive similar to a conveyor belt. In this way, a linear direction of friction is created between the ski base and the ice, and costs and space requirements are within the scope of the project.

#### 2.4 Solution concept for subfunction II: Mounting of the ski base sample

As presented in Figure 2.11, the ski base must be tensioned in a belt shape by a tensioning device to prevent it from slipping on the rollers during running. In order to increase the adhesion between the ski base and the rollers, a surface rubber coating of the rollers is envisaged. As is a common practice with conveyor belts, the driving roller is given a conical-cylindrical design of the rubber coating [112].

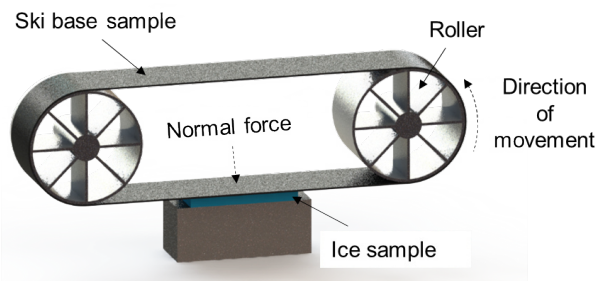


Figure 2.10: Plate-on-plate variant

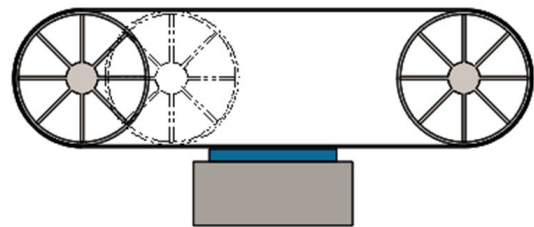
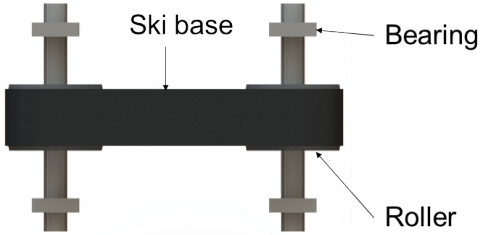
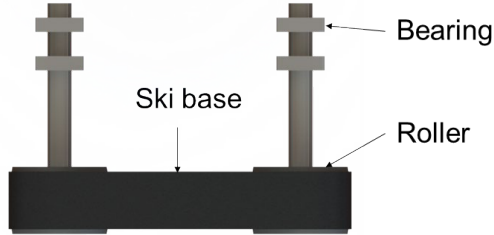


Figure 2.11: Ski base tensioning

Table 2.9 shows the two possible installation setups for the rollers that guide the ski base. In the two-sided bearing arrangement, the force is applied between the bearings. In the cantilever bearing arrangement, the force is applied outside the bearings. To evaluate the two solutions, a pairwise comparison of the evaluation criteria is first carried out with subsequent determination of the weighting factors. In a further step, the solution to be implemented is determined by assigning points and summing them to a total score.

Table 2.9: Solution concept for subfunction II

Subfunction II: Mounting of the ski base sample	
<b>Variant 1</b> 	<b>Variant 2</b> 
Two-sided bearing	Cantilevered bearing

Furthermore, the consistent plane-parallel alignment of the ski base to the ice surface must be ensured. For this purpose, two additional rollers are installed to guide the belt. This ensures parallel alignment as well as the evenness of the flexible belt. Figure 2.12 displays the principle of operation of the guidance rollers.

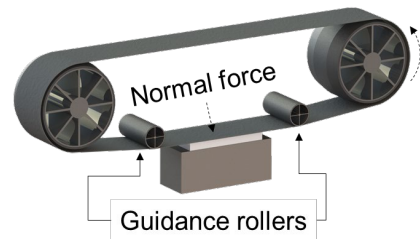


Figure 2.12: Guidance rollers installation

## 2.5 Solution concept for subfunction III: Mounting of the ice sample

When mounting the ice sample, the plane-parallel alignment to the ski base is decisive as well as the fact that the ice sample is slightly deflected due to friction. The deflection of the ice sample is used to measure the frictional force, and must therefore be linearly guided. Given the low friction to be expected between the ski base and the ice, the ice sample bearing must be implemented without significant inherent friction.

Bäurle et al. [19] used a simple and cost-effective test setup comprising two brass parallel springs supporting the ice plate without generating friction as friction theoretically only occurs in the material of the springs themselves. The second variant, which is more cost-intensive but less critical with regard to vibrations, consists of a sliding table for the ice sample mounted on precision rail guides. The precision rail guides feature a coefficient of friction of approximately 0.003 [113], which is less than one tenth of the coefficient of friction of polyethylene to ice [19]. Both variants are shown in Table 2.10.

Table 2.10: Solution concept for subfunction III

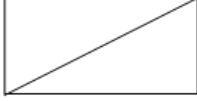

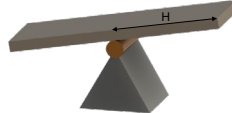
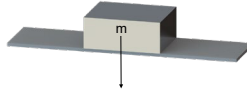
Subfunction III: Mounting of the ice sample	
<p><b>Variant 1</b></p>	<p><b>Variant 2</b></p>
Parallel springs	Rail guide

## 2.6 Solution concept for subfunction IV: Load application

The design catalogue according to Koller [114] was applied to determine the principle of the fourth subfunction. The possible variants of normal force application are discussed below and listed in Table 2.11. The first solution variant describes here the pressing of the sample by a mechanical spring. A mechanical load leads to elastic deformation of the spring. The work expended for this purpose is stored in the spring and released again when the load is removed. This release leads to the ice sample and ski base being pressed against each other. The dependence of the force is shown in spring characteristic curves. The steeper a spring characteristic curve, the greater the forces required for deformation [115]. As a second solution variant, pressing the sample via a lever arm has been selected. The lever arm is a mechanical force transducer consisting of a rigid body and a pivot point. If the lever arm is multiplied by the acting force, the result is the acting torque. In the equilibrium of forces, the lever arm is the shortest connecting line between the reference point and the acting force. With the help of the lever arm, a moment is transmitted to the counter body via a rocker-like construction. This is done by loading the sample-free side of the rigid body with a weight, while the side on which the sample is clamped is pressed against the mating body with the sample [116]. The third solution variant listed in Table 2.11 involves the application of force via a defined load. The sample is firmly clamped above or below the counter body and pressed onto the counter body by a weight. The weight is positioned in a guidance system and is pressed onto the sample by the acceleration due

to gravity. The sample then transmits the acting force to the counter body via the resulting moment and is thus pressed against it [116].

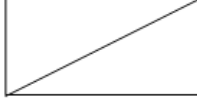
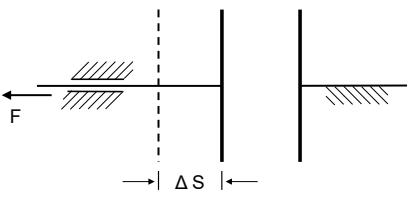
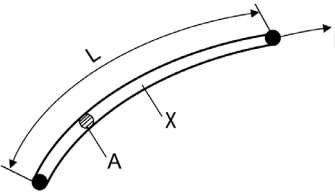
Table 2.11: Solution concept for subfunction IV

Subfunction IV: Load application (normal force)			
Basic Operation	Variant 1	Variant 2	Variant 3
			
<b>Transform</b>	Mechanical spring	Lever arm	Weight

## 2.7 Solution concept for subfunction V: Friction measurement

Subfunction V discusses ways to measure the frictional force. Principles such as the use of the change of a plate spacing due to the frictional force or the use of the change of a conductor length with accompanying change of the electrical resistance during a deflection as used in strain gauges or torque transducers were adopted from the catalogue according to Koller [114], and are shown in Table 2.12.

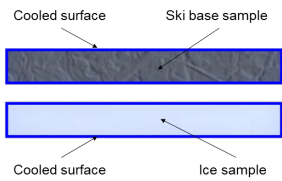
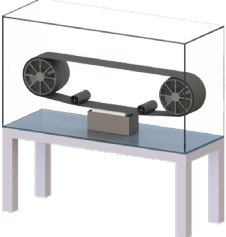

Table 2.12: Solution concept for subfunction V

Subfunction V: Friction measurement		
Basic Operation	Variant 1	Variant 2
		
<b>Transform</b>	Plate distance	Conductor

## 2.8 Solution concept for subfunction VI: Cooling

In Table 2.13, three different variants of cooling options for the measuring test rig are shown. Variant 1 involves the cooling of both specimens in an independent way. In variant 2, the tribometer is encapsulated in an insulated enclosure and, within this enclosure, the test rig is cooled down to the required measurement temperature. In contrast to the previous variants, the tribometer in variant 3 is placed in a cooling cell where the machine operator can be present while a measurement is being carried out.

Table 2.13: Solution concept for subfunction VI

Subfunction VI: Cooling		
Variant 1	Variant 2	Variant 3
		
Both samples cooled individually	Tribometer encapsulated	Cooling cell

As performed in the previous chapter, after the requirements for the subfunctions have been selected and the solution concepts are determined, the requirements of the subfunctions are classified according to their importance. As shown in Table AP 2, the weighting is carried out by generating weighting factors with the help of a 2x2 matrix.

## 2.9 Weighting factors determination

Table AP 6 shows the pairwise comparison including the determination of the weighting factors of the bearing installation variants required for evaluation. Due to the exceptional position of the financial capabilities within the project, the costs and the possibility of first carrying out preliminary tests with a pre-version were evaluated as the strongest and therefore most important position. The following tables reveal the points assigned for the selection of the bearing installation versions. Due to the higher

fulfilment of the cost parameter and the possibility of first gaining the necessary experience with a pre-version, variant 1, the two-sided bearing arrangement, achieves a higher result with a total score of 3.2 compared to variant 2 with an overall score of 2.5. From a design point of view, both bearing variants can be designed with sufficient rigidity for the planned project, although the cantilevered bearing arrangement requires a more rigid design due to the non-centric force application, which would result in a greater cost input. If the locating/non-locating bearing arrangement is preloaded with springs, sufficiently smooth running is also achieved with variant 1. The cost advantage exceeds the advantage of the simpler ski base change of the cantilever bearing. Table AP 9 displays the pairwise comparison of the evaluation criteria including the determination of the weighting factors. In order to obtain a consistent friction measurement, a constant planar contact of the two samples to each other must be ensured at all times. Following the primary criterion of low cost with rank 1, the criteria that determine the position of the samples in relation to each other achieve a high weighting with rank 2 due to their importance. According to the following tables, variant 1 with its parallel spring solution achieves the highest score of 3.2 compared to variant 2 with a total score of 2.5 due to the very low implementation costs and the possibility of using this in a preliminary test. If a more rigid, reliable and low-vibration structure will be required for later test series, variant 2 should be preferred, although the total score is below the mean value, caused solely by the cost aspect. The solution variant is therefore not eliminated from further evaluation, as can be seen in Table 2.15. When applying the load, the amount of load, which has to be clearly defined at all times, is the most critical parameter for a reliable and significant measurement result. As can be seen in Table AP 12, this item is the strongest evaluated criterion in this subfunction, directly followed by the parameter of a vibration-independent feature which has to be implemented within the design phase. The following tables show the scores for each individual requirement for variants 1 to 3 of subfunction IV. Due to the fact that the mean value of the three variants is not reached, variant 1, the solution with the mechanical spring, is excluded from further evaluation. The control of how much load really exists in each measurement run was, among other factors, decisive for the poor rating in addition to the typical vibration behaviour of the component. The slightly better fulfilment of the all-time defined load input of variant 3 was decisive for the highest score with an overall



evaluation of 3.8 of the three variants. The lever arm variant was just behind the winning variant with 3.6 points. In the pairwise comparison of the criteria for the fulfilment of subfunction V, as presented in Table AP 16, in addition to the most important parameter of low acquisition costs, all parameters except for the criterion "low inherent friction" were given the identical importance, as this is mandatory for a consistent, reliable force measurement. In the following tables, the evaluation of the requirements was carried out in relation to the two variants. The use of a force transducer, which is actuated by the bearing-mounted ice plate that is displaced as a result of the frictional force, achieved a higher result than a measuring unit that uses a strain transducer, either mounted on a component or via a torque shaft respectively a measuring flange, which would cause considerably higher costs. Table AP 19 lists the determination of the weighting factors for subfunction VI. In addition to the low acquisition costs, the consistent cooling and the uniform temperature of the two samples were rated as the highest.

## **2.10 Assessment for subfunction VI**

The evaluation of the three cooling options were carried out in the tables below. Variant 1 and variant 2 are excluded from further evaluation since the mean value is not met. Variant 3 has achieved the highest overall score due to the possibility of examining the temperature distribution as a result of friction in the area of the ski base - ice during the measurement and to inspect the test stand for proper running properties.

## **2.11 Morphological box – the determination of the overall function**

The method of morphological analysis was developed by F. Zwicky [117] to create a solution system for a complex problem, which represents all conceivable solution possibilities in an ordered, unprejudiced form. In this method, the different variations of solution elements of generated subfunctions are combined to form overall solutions and visually displayed. The morphological box is created by arranging the subfunctions in rows and the solution variants in columns. Its size thus depends on the number of subfunctions and the number of solution variants for each subfunction [109], as seen in Table 2.14. The eliminated solution variants as mentioned in the previous chapters

are listed in the now presented morphological box, but they are not considered when linking to total solution variants, cf. [104].

Table 2.14: Morphological box

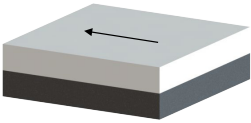

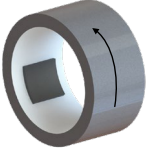


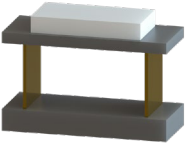
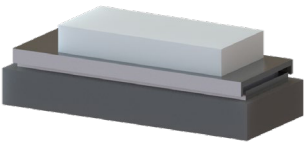

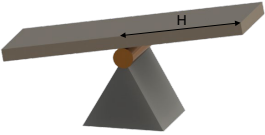
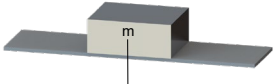
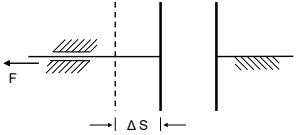
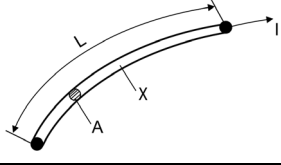
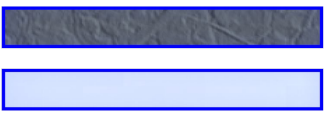


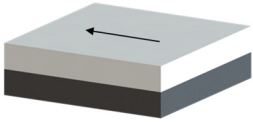

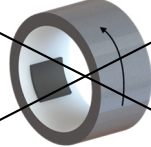

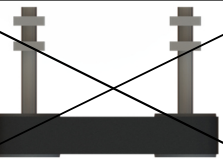
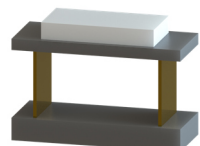
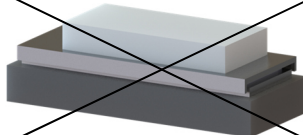

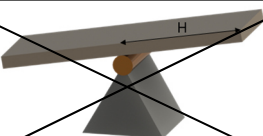
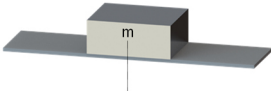
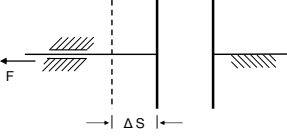
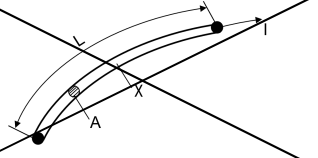
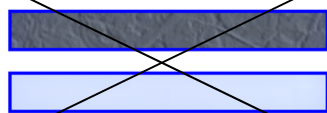
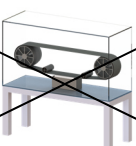

		Solution Variants						
		I		II		III		
		A		B		C		
Subfunctions	I	1						
			A1	Plate-On-Plate	B1	Plate-On-Disc	C1	Plate-On-Ring
	II	2						
			A2	Two-sided bearing	B2	Cantilevered bearing		
	III	3						
			A3	Parallel springs	B3	Rail guide		
	IV	4						
			A4	Mechanical spring	B4	Lever arm	C4	Weight
	V	5						
			A5	Plate distance	B5	Conductor		
	VI	6						
			A6	Individually cooled	B6	Tribometer encapsulated	C6	Cooling cell

Table 1.2: Combination of the solution variants into overall solutions

		Solution Variants					
		I		II		III	
		A		B		C	
Subfunctions	I	1					
			A1	Plate-On-Plate	B1	Plate-On-Disc	C1
	II	2					
			A2	Two-sided bearing	B2	Cantilevered bearing	
	III	3					
			A3	Parallel springs	B3	Rail guide	
	IV	4					
			A4	Mechanical spring	B4	Lever arm	C4
	V	5					
			A5	Plate distance	B5	Conductor	
	VI	6					
			A6	Individually cooled	B6	Tribometer encapsulated	C6

The table below shows the possible combinations of the solution variants into overall solutions. In the following step, the weighting factors of the general requirements have been compared with each other by means of a pairwise comparison and thereby the weighting factors were determined. Afterwards, the overall solutions were evaluated in order to define the design solution to be implemented.

Table 2.16: Possible combinations of sub functions with solution variants

Overall solutions	Combinations
1	A1 – A2 – A3 – B4 – A5 – C6
2	A1 – A2 – A3 – C4 – A5 – C6
3	A1 – A2 – B3 – B4 – A5 – C6
4	A1 – A2 – B3 – C4 – A5 – C6

In order to remain within the recommendation of the VDI [100,101], the subfunctions were included in the pairwise comparison in order to check their value compared to the general requirements. Since the subfunctions have already been evaluated with regard to the fulfilment of the subfunction-specific requirements, the percentage ratio of the total score achieved for the individual subfunctions was converted to the maximum score in the pairwise comparison. Thus, for example, for subfunction I, with a total score of 3.605 and a maximum score of four points to be achieved, the percentage ratio is 90.11 %. In the pairwise comparison, with a maximum of three points to be gained, the above mentioned ratio corresponds accordingly to 2.7 points.

In the assessment of the overall solutions, solution 2, the variant with the parallel springs and a weight to be applied to simulate the jumper's weight, achieved the highest score with 2.93 points. The second highest ranked variant was solution 4, the version with the precision guide rails.

## 2.12 Quality function deployment (QFD)

The "quality function deployment" (QFD) method has been introduced as a method for ensuring customer requirements and for transforming these into describable requirements that can be quantified as far as possible. It is part of the specification and completion of the requirements list and assists in the conduct of methodical product planning. Part of the QFD method is the "House of Quality" (HoQ). The HoQ is composed of several planning boards. The procedure is used to plan and develop quality functions. The overview which will be further developed in the course of the process, provides guidance of requirements and evaluation criteria to be added. [104,107] The procedure for this product planning is shown in Figure 2.13.

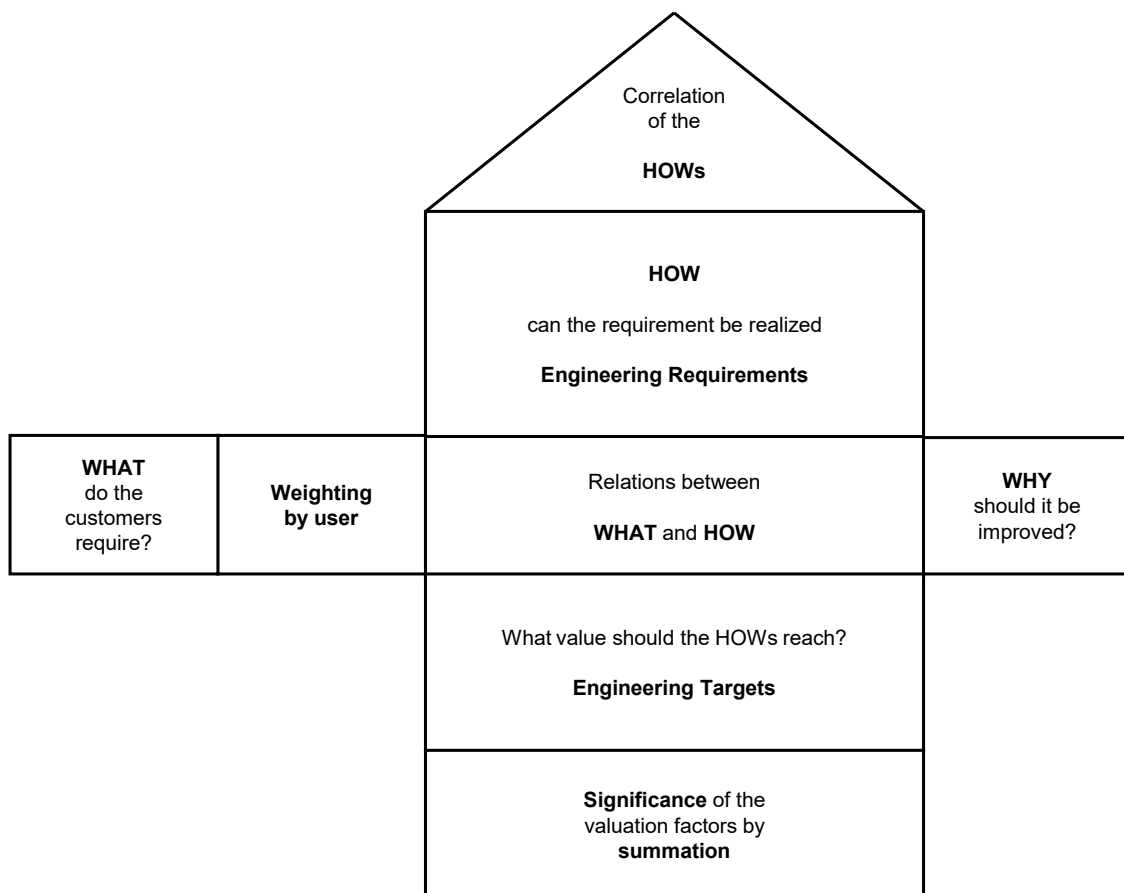


Figure 2.13: Procedure of HoQ (based on [118] and [119])

The HoQ presupposes customer-oriented product development. Since the wear test rig is not intended for sale to the end customer, the HoQ is in this case related to the user, i.e., the operator. In order to be able to capture the requirements of the user, an application profile has first to be created, as can be seen in the following table.

Table 2.17: User profile

---

Engineer or scientific assistant
Age: 20 to 60 years
Safety is essential
Strong mechanical skills
Operating the machine is part of the user's job

---

After the user profile is created, the user-oriented requirements of the test rig need to be described in the user's language, as can be seen in the following table.

Table 2.18: User-oriented requirements

---

Easy mounting of the counter bodies (ski base and ice sample)
Stability of the wear test rig
No risk of injury
Low noise level
Simple operation

---

These requirements are entered in the "What do the customers require?" planning board when the HoQ is created [104,107]. After the user requirements have been described, a weighting was assigned to them. The weighting indicates how important a user requirement is for the user. In order to weight the user requirements according to their importance, a comparison of these requirements was carried out as shown in Table AP 28.

The position in the ranking order, results from the summation of the given points. Based on this ranking, the weighting factors for the HoQ are assigned. Rank 1 receives a weighting factor of 0.3, rank 2 receives a factor of 0.25, while rank 5 reaches 0.1 factor points in this system. Due to the duplication of rank 3 and the subsequent absence of rank 4, the weighting factor of 0.175 is assigned twice. Note that for display reasons, the calculated score in columns "B" has been rounded to two decimal places, but has been calculated with three decimal places. Table 2.20 shows the HoQ comparing the user requirements from Table 2.18 with the design requirements from chapter 2.2.3 in terms of their mutual influence. Based on the strength of the influence, the requirements are weighted in column "A" using numbers from 1 to 3 inclusive, where 1 is little influence and 3 is strong influence. When two requirements have no influence on each other, 0 points are assigned. The weighting points are multiplied per line by the weighting factor of the respective user requirement calculated in Table AP 24.

The addition of all the factors calculated (each in column B) results in the importance of the quality features (machine requirements) of the machine for the user. The higher the sum is, the more important the corresponding requirement is to be classified for the user and is to be included in the subsequent design process [104,107,109].

With the "roof matrix" of the HoQ it is possible to ascertain which user requirements may contradict or be complementary to design requirements and how important the individual design requirements are in the overall concept. In the case of strengthening, a plus sign (+) is entered and in the case of hindering, a minus sign (-). By this method, any weak points in the requirements definition can be identified at an early stage at the beginning of the design process. If the requirements defined in chapter 2.2.3 have no influence on the user requirements, they are not listed in the roof matrix [104,107,109]. In Table 2.19, the legend of the HoQ is provided.

Table 2.19: Legend of the HoQ

A	Relationship Points
B	Importance (A x User Weighting)
<b>Relationship Points</b>	
0	No Influence
1	Little Influence
2	Medium Influence
3	Strong Influence
<b>Correlations</b>	
+	Positive Correlation
-	Negative Correlation





The evaluation of the HoQ results in the following order of importance for the operator:

Table 2.21: Operator's importance ranking

<b>Ranking</b>	<b>Requirement</b>
1	Safety and security
2	Operable by instructed personal
3	Tilt stable
4	Low incidence of vibrations
5	Functions manageable in university environment
6	Measurement with practice-oriented loads and conditions
7	Low maintenance and easy to maintain (low wear)
8	Possibility of disassembly
9	High reproducibility
10	Transportable system
11	Cost-effective (manufacturing / operation)
12	Fast realization
13	Space saving (lab size)

After the evaluation of the individual subfunctions has been completed and the overall function has been derived accordingly, the next chapter focuses on the realisation and design of the tribometer and its subfunctions.



### 3 Ice tribometer architecture

Several methods for implementation of the design were discussed in chapter 2. Variant 2 with the highest score, shown in Table AP 25, supported the realisation of a preliminary cost-restricted form of the design as a proof of concept, to generate initial experience in ice tribology.

#### 3.1 Proof of concept

The tribometer was designed according to subfunction I of chapter 2.3 in a plate-on-plate type of movement where the ski base is conveyed by means of two rollers. A cooling cell with the dimensions of 2.7 x 2.2 x 2.4 m, comprising a 1400 W refrigeration unit with a cooling range of -1 °C to -25 °C (GEKT1201H-02, Glen Dimplex GmbH, Germany), was set up as a temperature-controlled system in which the experiments will be carried out. The ambient temperature and humidity were measured and recorded using a data logger (testo 174-T, Testo GmbH, Germany). In order to describe the manufacturing process required for the individual components, the design of the tribometer was divided into five sub-assemblies in accordance with the developed sub-functions (cf. Table 2.15):

Table 3.1: Design sub-assemblies for proof of concept

1	<b>Frame and base</b>
	<i>Components that determine the stability and provide support for components</i>
2	<b>Main rollers and bearings</b>
	<i>Transfer of the ski base including the bearings required for the main rollers</i>
3	<b>Weight force and force measurement</b>
	<i>Initiation of the weight force and measurement of the frictional force</i>
4	<b>Ski base and ice sample</b>
	<i>Friction partner specification</i>
5	<b>Motor</b>
	<i>Drive of the main rollers</i>

### 3.1.1 Compulsory calculations

#### 3.1.1.1 Operating pattern

Alternative basic operating patterns that are applied during a measurement and are required for motor selection are shown below in Figure 3.1. Either a final speed ( $n_1$ ), corresponding to a certain speed as dictated by the transmission, has to be reached in a predefined time ( $t_1$ ) and then deceleration has to happen as quickly as possible ( $t_2$ ) until total standstill (total cycle =  $t_0$ ). Alternatively, a speed ( $n_1$ ) has to be reached within a defined time ( $t_1$ ), maintained for a defined time ( $t_2$ ) and then again decelerated until total standstill ( $t_3$ ).

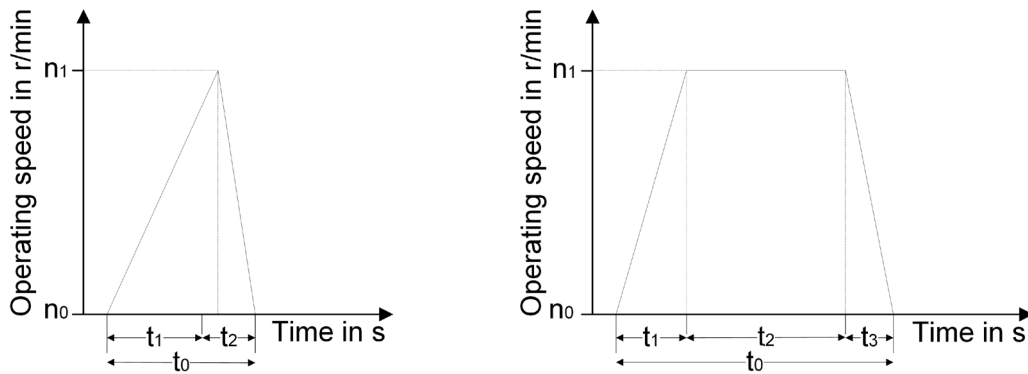


Figure 3.1: Operating pattern with acceleration and immediate deceleration (left) and with acceleration, maintaining speed and subsequent deceleration (right)

#### 3.1.1.2 Dimensioning of the motor

The dimensioning of the motor depends on the starting torque  $M_T$ , which is the sum of the acceleration torque  $M_a$  and the load torque  $M_l$  as can be seen in the equation below:

$$M_T = (M_a + M_l) \quad \text{Eqn. 3.1}$$

The torque required for constant acceleration  $M_a$  is calculated by the following formula (assuming 100% degree of efficiency) [120]:

$$M_a = \left( \Theta + \frac{m_{\text{Belt}} \times d^2}{4} \right) \times \frac{\pi}{30} \times \frac{\Delta n_{\text{in}}}{\Delta t_a} \quad \text{Eqn. 3.2}$$

With:

- $M_a$  - acceleration torque
- $\Theta$  - mass moment of inertia
- $M_{\text{Belt}}$  - mass of the ski belt
- $d$  - diameter of the driven roller
- $\Delta n_{\text{in}}$  - difference in rotational speed
- $\Delta t_a$  - acceleration time

Assuming a diameter of 200 mm and 40 mm for the roller and shafts respectively, a distance between the axes which results in a belt length of 2.4 m and, an acceleration time of 5 seconds to a tangential speed of 27.8 m/s, this generates an acceleration torque  $M_a$  of approximately 53 Nm.

Due to the comparably low normal force of approximately 200 N, only low values are obtained for the calculation of the load torque (cf. Figure 3.2). If a COF of  $\mu = 0.05$  between ice and UHMWPE and a COF of 0.26 between PTFE and UHMWPE is assumed, then the individual frictional forces  $F_{\text{Ice}}$  and  $F_{\text{PTFE}}$  are calculated as 10 N and 52 N respectively, which corresponds to a total load torque  $M_l$  of 6.5 Nm relative to the roller's diameter. According to equation 3.1, the starting torque, which has to be generated by the electric motor at maximum acceleration, can be derived as 59.5 Nm.

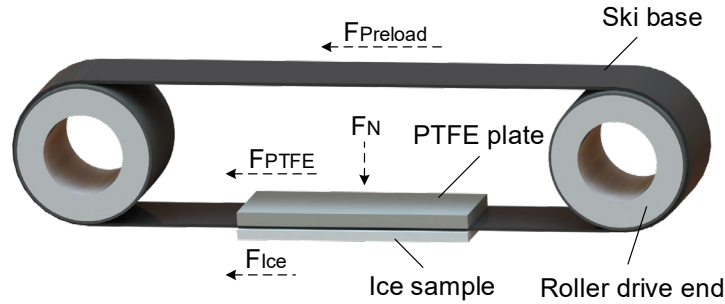


Figure 3.2: Load initiations

### 3.1.1.3 Preload force

The minimum preload force that prevents slipping due to insufficient friction between the ski base and the rubberised roller is calculated according to Eqn. 3.3. Here, the product of the circumferential force and the Euler-Eytelwein rope friction component is added to the centrifugal force of the belt [121].

$$F_P = F_C \times \frac{(e^{\mu \times \varphi} + 1)}{2(e^{\mu \times \varphi} - 1)} + m_L \times v_{\max}^2 \quad \text{Eqn. 3.3}$$

With:

- $F_P$  - preload force
- $F_C$  - circumferential force
- $\mu$  - coefficient of friction
- $\varphi$  - belt's contact angle in radians
- $m_L$  - length weight of the belt
- $v_{\max}$  - maximum speed

As a result, a preload force of approximately 307 N was calculated, denoting the minimum required force which has to be applied via the adjustment mechanism. The preload force also acts as a source of bending stress on the shafts, which was calculated using CAD software. All simulation results can be found in the appendix. In the case

that stainless steel 1.4305 is selected as the shaft material, the bending stress created is calculated to be 4 MPa, far below the 0.2% yield strength  $R_{p0.2}$  of 190 MPa.

#### **3.1.1.4 Torsion analysis of the driving shaft**

The highest occurring torsional stress (shear stress) has been calculated in the case of a blocked bearing within the driving shaft (cf. Figure 3.6) at the maximum torque of the motor and was determined to be  $\tau_t = 57.9$  MPa, a factor of 3 below the  $R_{p0.2}$  of 190 MPa.

#### **3.1.1.5 Bending analysis of the driving shaft**

The preload of the ski base creates an inward bending stress on the roller shafts corresponding to the maximum tensile strength of the ski base. If a maximum tensile force of 2000 N is assumed (cf. Figure 3.23), a bending stress of 25.3 MPa occurs at the bearing seats of the shafts, which is far below the  $R_{p0.2}$ .

#### **3.1.1.6 Bending analysis of the plate's guidance**

Depending on the chosen application of the weight force (see also Figure 3.8 and Figure 3.10), the maximum load on the guiding system occurs when the ski base gets caught. As a result, the maximum torque of the motor generates a tensile force of 572 N which acts on the guiding system. If aluminium 3.3547 is selected, the bending stress of 57 MPa is a factor of 2 below the  $R_{p0.2}$  of 125 MPa.

#### **3.1.1.7 Bending analysis of the parallel springs**

According to [19], a measurement setup was chosen consisting of a parallel arrangement of two brass plates acting as springs and thus enabling an almost frictionless operation. The relationship between the deflection of a beam and the resulting moment distribution is represented by the Euler-Bernoulli beam theory:

$$\frac{d^2y}{dx^2} = \frac{M(x)}{EI} \quad \text{Eqn. 3.4}$$

For the load situation of the clamped-guided beam, the moment distribution is calculated as follows:

$$M(x) = F \times \left( \frac{L}{2} - x \right) \quad \text{Eqn. 3.5}$$

By integrating twice and applying the boundary conditions, the displacement is calculated with the following formula:

$$y(x) = \frac{F}{EI} \times \left( \frac{L}{4}x^2 - \frac{1}{6}x^3 \right) \quad \text{Eqn. 3.6}$$

If the entire length of the springs is used for calculation ( $x = L$ ), the maximum displacement travel is determined by:

$$y(L) = \frac{FL^3}{12EI} = \delta \quad \text{Eqn. 3.7}$$

where  $\delta$  is the displacement as defined in Figure 3.3. If a plate thickness of 0.6 mm is chosen and the maximum deflection of 0.125 mm at 10 N of a force sensor (e.g., Interfaceforce MBP-10) is assumed as  $\delta$ , the required bending force for deflection of the measuring system can be determined and amounts to 1.54 N, which corresponds to approximately 15% of the maximum measured friction force. By reducing the plate thickness, the sensitivity can be increased, but the risk of loading the brass springs outside the elastic load condition also increases.



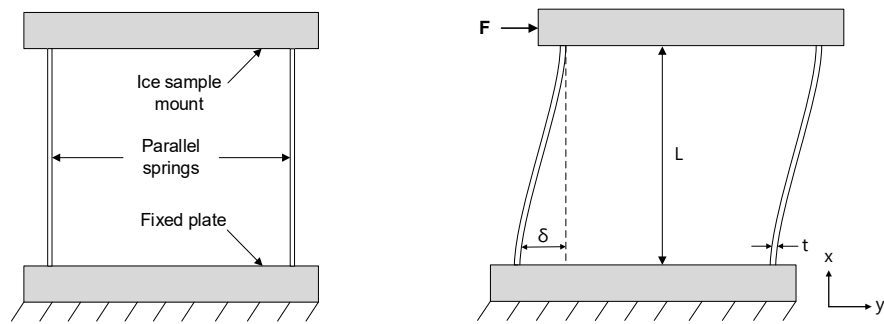


Figure 3.3: Parallel spring setup in unloaded configuration (left) and in loaded configuration (right)

### 3.1.2 Frame and base

The tribometer was mounted on a base frame made of aluminium construction profiles with the overall dimensions of 1330 mm x 1125 mm x 850 mm (X, Y, Z), as can be seen in Figure 3.4. To support the rollers, two 80 mm x 98 mm x 1330 mm 1.4301 stainless steel struts were manufactured and mounted on locating units (Z051, Hasco GmbH + Co. KG, Germany). Thus, the struts could be lifted with a load crane when changing the ski base and then be lowered again in the exact position. Utilisation of the locating units translated to an almost negligible requirement for surface machining, with the exception of the pockets which were necessary for the bearing support.

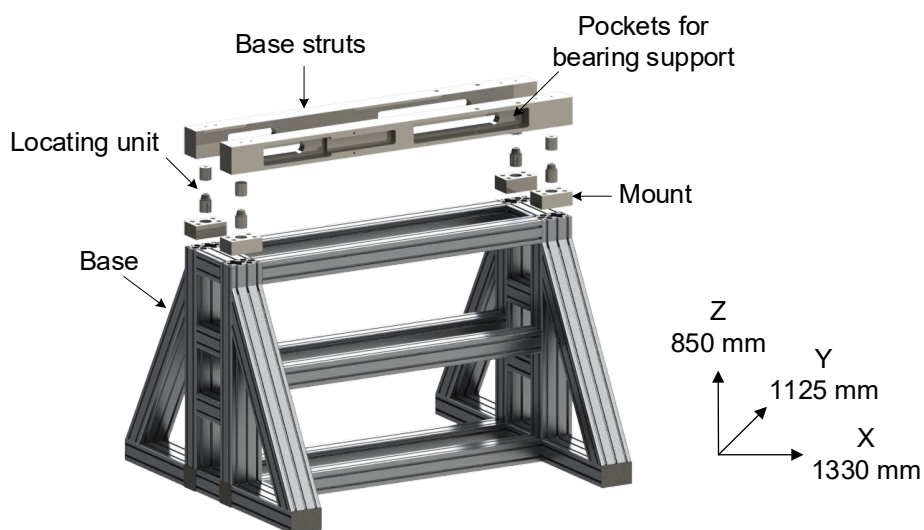


Figure 3.4: Frame and base

To ensure a stable stand, several aluminium cylinders were installed through the floor of the cooling cell onto the concrete floor underneath and the base frame was mounted onto the aluminium cylinders using rubberised machine feet. In addition, the base was secured to the concrete floor with ground anchors. This allowed adjustment of the horizontal position as well as a secure connection to the floor.

### 3.1.3 Main rollers and bearings

When designing the rollers, attention was paid to ensure a sufficient diameter so that the bonding area of the ski base ends (cf. Figure 3.24) only has to withstand a small amount of bending force. The diameter was set to 210 mm and on the basis of the 120 mm width of the ski base, the length of the rollers have been chosen to be 140 mm, as shown in Figure 3.5. The two aluminium EN AW-2007 (3.1645) rollers were provided with a 5 mm EPDM 60 Shore A coating to provide grip between roller and ski base.

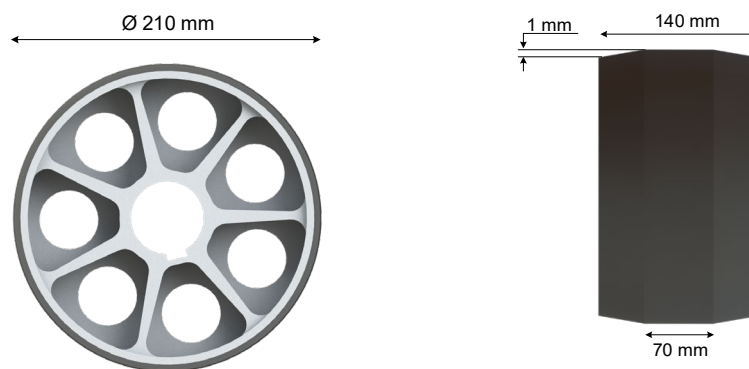


Figure 3.5: Roller from front view (left) and in side view from left (right)

Due to the roller's conical-cylindrical shape with its flanks machined down by 1 mm (as found on crowned pulleys), the increased diameter in the middle area creates higher friction between the roller and the ski base and therefore a guiding of the base is ensured. The main roller assembly is completed by one input and one output shaft each, which are secured with shaft nuts and lock plates (KM8, SKF GmbH, Germany), displayed in Figure 3.6. To ensure smooth running, both rollers were dynamically balanced.

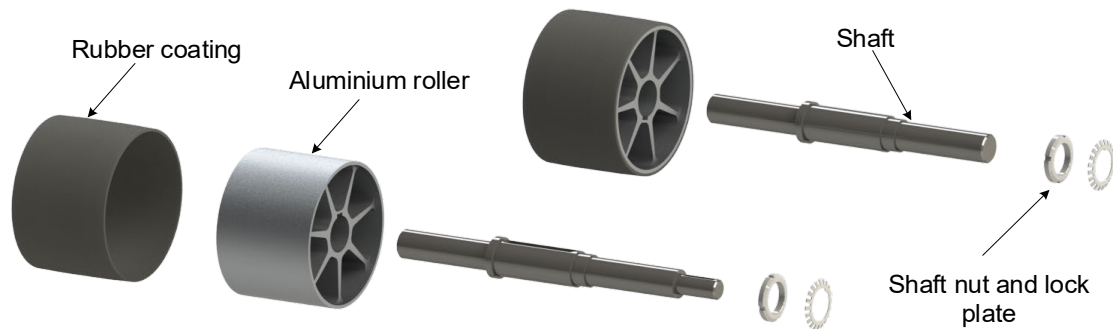


Figure 3.6: Main rollers set-up

In order to tension the ski base via the main rollers, the output end was movably mounted in such a way, that the bearing support with the mounted self-aligning ball bearing (2208 EKTN9, SKF GmbH, Germany) could be traversed in the direction of the longitudinal axis in the milled pockets of the struts. The adjustment of the shaft position was achieved by means of a spindle screw with an optional 7.1 A stepper motor with 6.8 Nm holding torque (M1343031, LAM Technologies, Italy) or manually by means of an Allen key adapter. For the automatic tightening of the ski base during movement by the stepper motor, two infrared light barriers have been installed (GL30-IR/32/40a/98a, Pepperl+Fuchs GmbH, Germany). By using aligning bearings, a compensation of minor misalignments could be obtained. The bearing support with the fixed flange bearings (RCJTZ35-XL, Schaeffler AG & Co. KG, Germany) on the drive side was also designed to be movable to facilitate ski base changing.

However, the supports were secured in position by parallel pins. To measure the speed of both the input and output sides, two incremental encoders (RI 32, Hengstler GmbH, Germany) were installed on the faces of the shafts. The difference between the two signals is used to determine the amount of slippage.

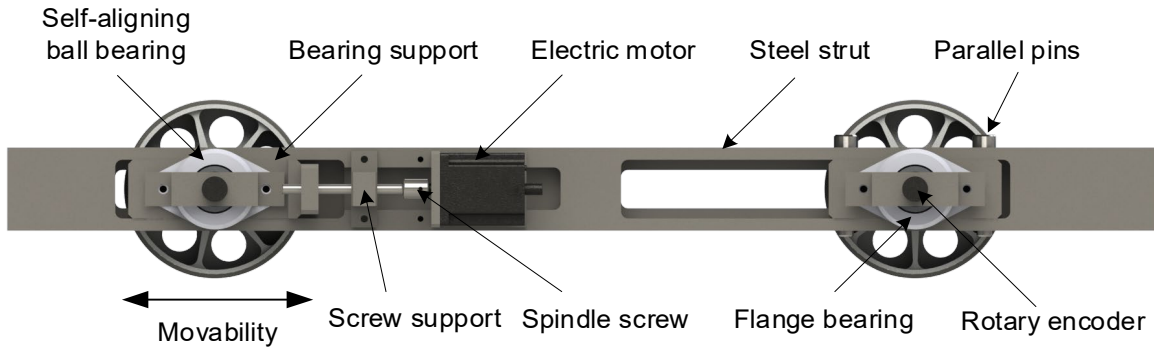


Figure 3.7: Bearing of the main rollers

### 3.1.4 Weight force and force measurement

The required normal force was realised by two approaches: a plate with periodically arranged ball-bearing shafts that creates a line load situation (61804, SKF GmbH, Germany) and a plate with an attached PTFE plate (surface load). Both versions were secured in mountings below the struts by means of parallel pins, as shown in Figure 3.8.

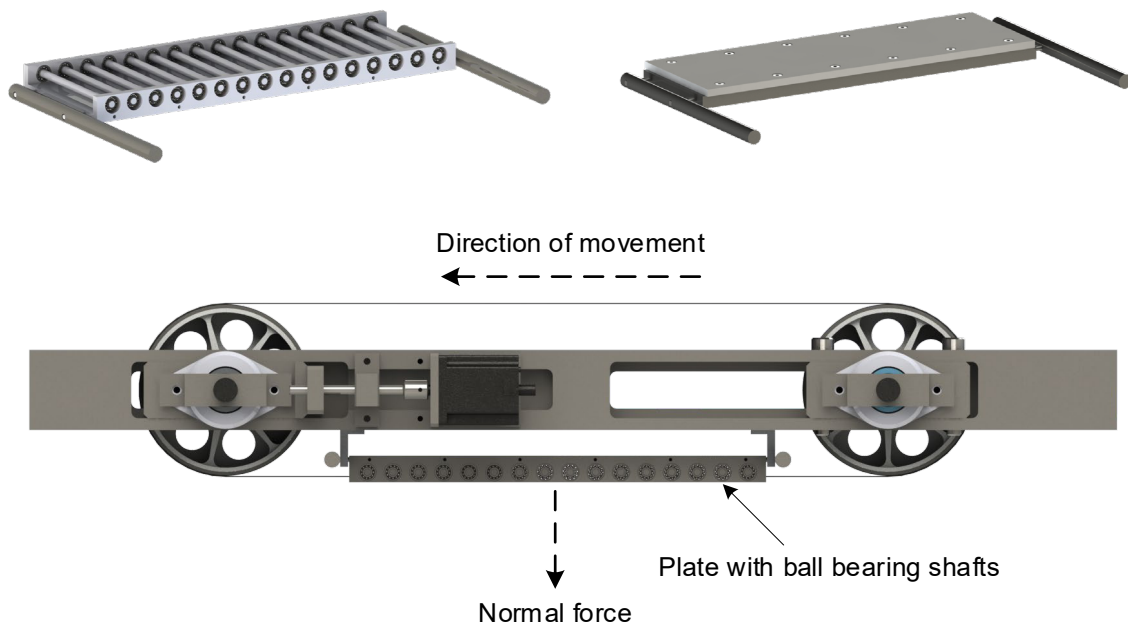


Figure 3.8: Application of normal force: plate with shafts (top left) and plate with screwed-on PTFE plate (top right) and in mounted state (below)

The ski base in combination with a PTFE plate showed an excessive abrasive behaviour despite the relatively low coefficient of friction of PTFE relative to other materials and was discarded as a possible application during the preliminary

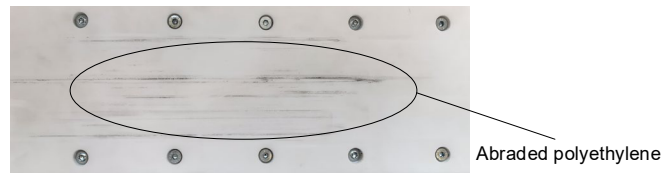


Figure 3.9: Weight force plate after several runs

test, see Figure 3.9. Due to the inherent weight of the roller plate in combination with attached weights, normal forces between 50 N and 120 N were generated.

To determine the COF at a predetermined load, the frictional force was measured directly using a load cell (MBP-10, Interfaceforce e.K., Germany). Figure 3.10 and Figure 3.11 depict the measurement setup with inserted ice sample. The ice sample was placed underneath the ski base on which a defined force was applied by means of the roller plate. The distance between the measuring unit and the ski base could be adjusted by means of an adjusting screw.

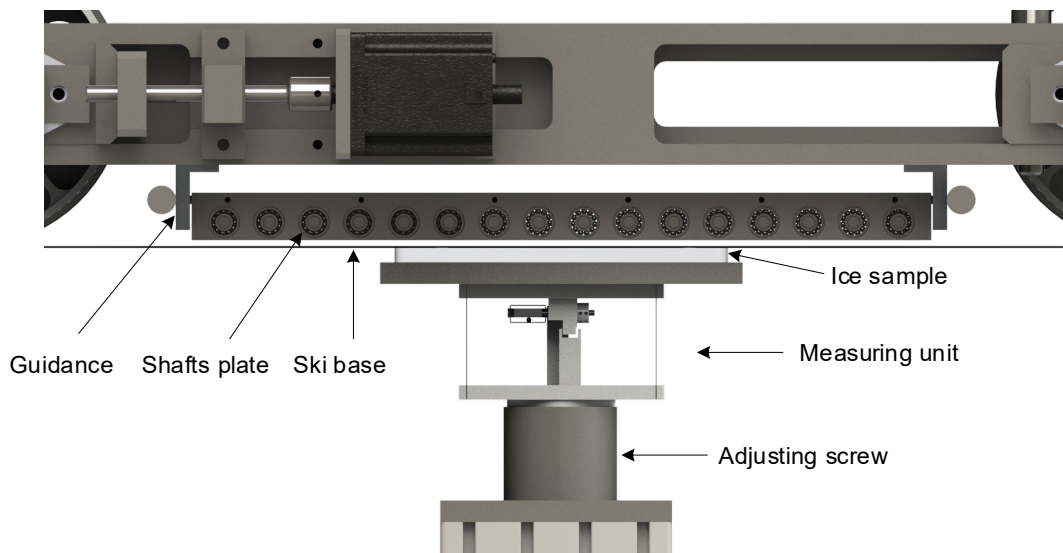


Figure 3.10: Friction force measurement setup

The ice sample was connected to the sample support by means of a form-fit connection and joined to the load cell mount by two brass parallel springs (cf. [19]). Due to the

effect of friction, the ice sample and thus the sample support were deflected in the direction of the force. This actuated the load cell which was mounted on the fixed part of the unit. In order to reduce shocks in the opposite direction, a pressure spring was installed between the force sensor and the sample support.

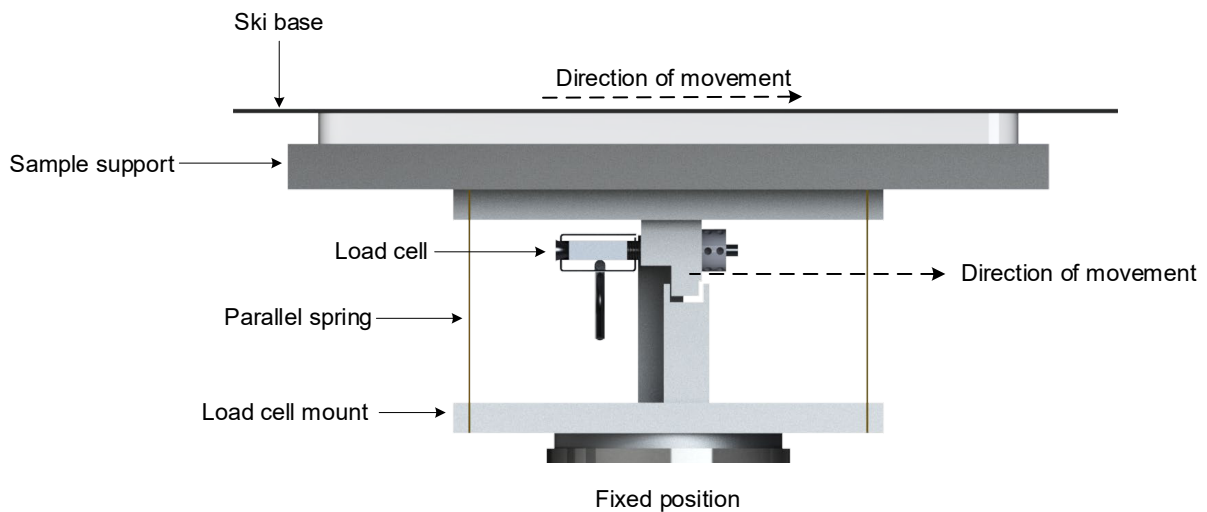


Figure 3.11: Measuring unit

### 3.2 Ice tribometer

Following the initial results of the proof-of-concept version, a more rigid and robust design was designed. While retaining the main components such as the steel struts, rollers, bearings and shafts, the force measurement set-up, mounting of the ice sample as well as load initiation were modified. Furthermore, guiding rollers were installed to ensure the horizontal position of the ski base and the overall stiffness was increased. In the following chapter, the individual design components will be discussed. Table 3.2 displays the design architecture which has been split into 8 sub-assemblies:

Table 3.2: Tribometer sub-assemblies

1	<b>Frame design</b>
	<i>Components that determine the stability and provide support for components</i>
2	<b>Main rollers</b>
	<i>Transfer of the ski base including the shafts required for this purpose</i>
3	<b>Bearings</b>
	<i>Bearing of the main rollers</i>
4	<b>Guidance rollers</b>
	<i>Determine the horizontal movement of the ski base</i>
5	<b>Carriage and force measurement</b>
	<i>Guiding the ice sample and measurement of the frictional force</i>
6	<b>Weight force</b>
	<i>Initiation of the force perpendicular to the ice sample</i>

### 3.2.1 Frame design

To ensure the position of the frame components in relation to each other, the entire construction was mounted on a solid steel plate with the dimensions of 1330 mm x 450 mm x 35 mm as displayed in Figure 3.12. Furthermore, to reduce vibrations, a rubber pad was mounted underneath the plate. The steel plate featured a surface roughness of  $R_z$  6.3 and specified a horizontal parallelism tolerance of 0.02 mm. Hence, the horizontal contact surfaces of the other structural components were manufactured with the corresponding tolerance. The base struts are mounted on detachable fitting struts, which have to be dismantled for a ski base replacement (due to its belt shape) and on the rear side there are additional support struts which increase the stability of the structure. Between the base struts, profiles which limit both deflection and distortion have been mounted for reinforcing reasons and to ensure a defined distance between the contact surfaces of the bearing seats during assembly. For a faster ski base replacement, the reinforcing profiles were designed to hold the front side structure in position as long as the fitting struts are dismantled.

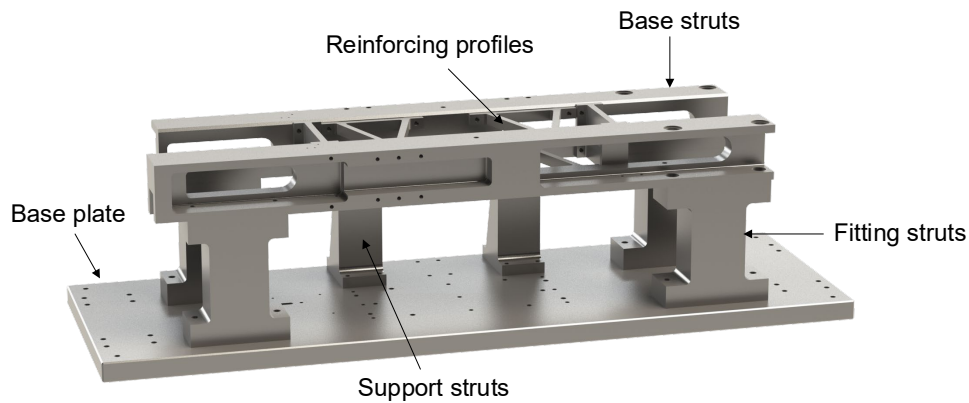


Figure 3.12: Frame design

### 3.2.2 Bearings

The main rollers including the shafts were used unchanged for the bearing selection. A standard bearing arrangement with one fixed and one floating bearing side each was chosen for mounting the rollers, as shown in Figure 3.14. Due to the low internal friction, ball bearings were chosen for installation (W61908, SKF GmbH, Germany). The fixed bearing side was designed with a precision shaft nut (KMTA 7, SKF GmbH, Germany) that clamps the bearing inner ring while the bearing outer ring is braced against the housing shoulder by the housing cover. To achieve an adequate clamping force between the end face of the housing cover and the front face of the bearing outer ring, an axial clearance of 0.02 mm was realised between the cover and the front face of the bearing housing before the screws were tightened [122]. The movable outer bearing ring of the floating side can be axially preloaded with a preload force of up to 520 N by means of compression spring package installed between the housing cover and bearing plate, which minimises the bearing clearance, allows smoother running, and a more precise adjustment of the bearing. In order to allow fast disassembly of the input bearing housings for a ski base change with small lengths, the housings were secured in position with detachable hardened parallel pins. To protect the floating bearing from contamination with foreign particles, a groove was machined into the bearing housing, in which the outer edge of the housing cover protrudes, similar to a labyrinth seal. The bearing arrangement on the output side of the tribometer was designed identically to the input side, however, the bearing housings were configured to be adjustable so that the ski base can be tensioned; either via a stepper motor or manually. The tolerances



of the bearing bores were chosen according to the specifications of the bearing manufacturer and are listed next to the bearing calculation in the appendix.

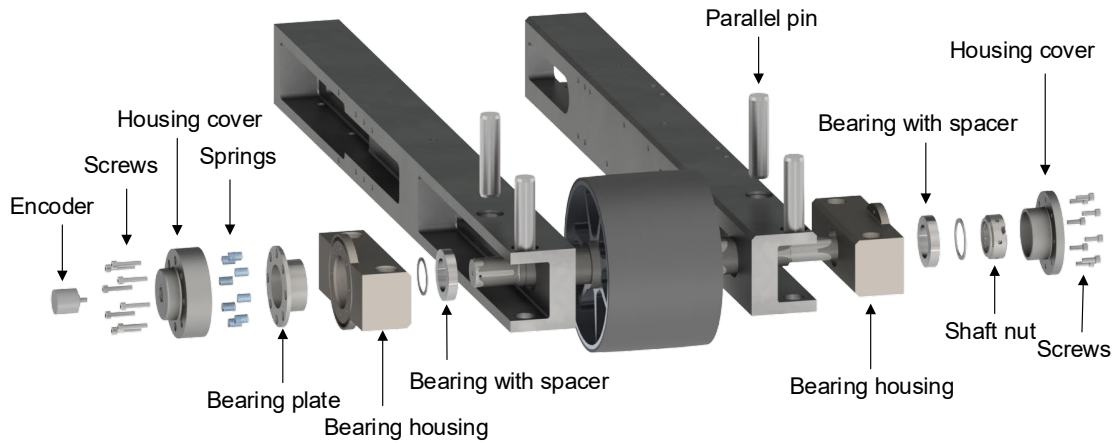


Figure 3.13: Roller bearing arrangement in exploded view

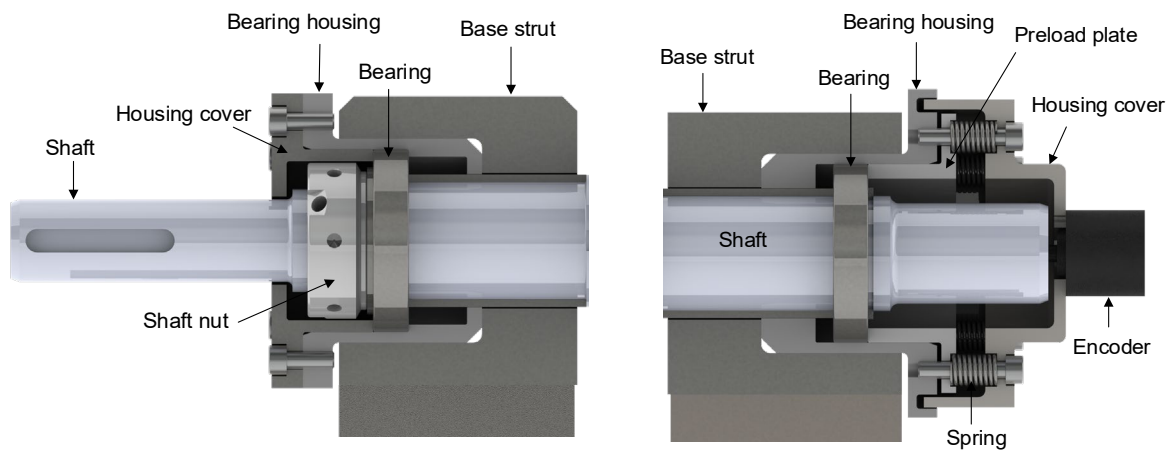


Figure 3.14: Fixed bearing side (left) and floating bearing side (right) in cross section view

### 3.2.3 Guidance rollers

In order to minimise the curvature of the ski base, two guidance rollers were installed which determine the horizontal position in relation to the ice sample as can be seen in the top part of Figure 3.15. Similar to the main rollers, the bearing arrangement was

designed with a fixed and a spring loaded floating bearing side using ball bearings and shaft nut (6003 and KMT 0, SKF GmbH, Germany).

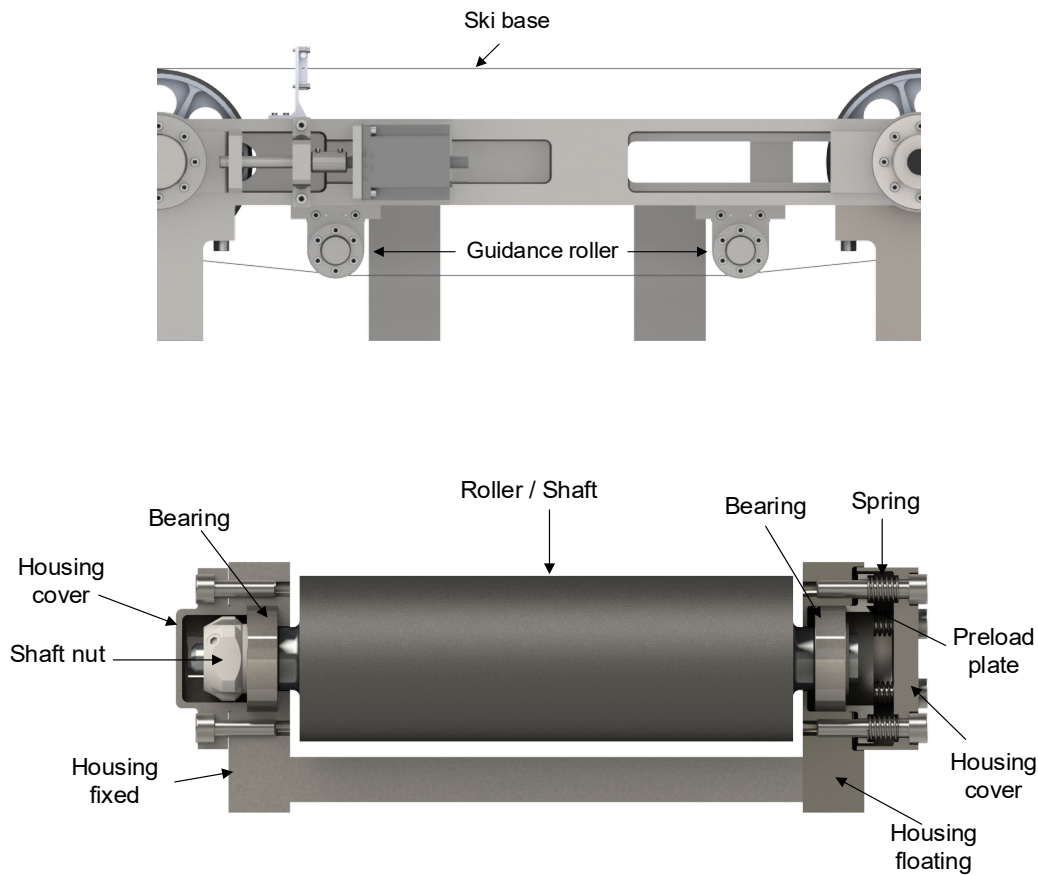


Figure 3.15: Guidance roller in installed condition (top) and roller in cross section view (bottom)

### 3.2.4 Carriage and force measurement

Direct force measurement is carried out by deflecting the ice plate and actuating a force sensor as a result of friction. To allow the ice sample to move in the direction of travel of the ski base, it was mounted on a gliding carriage that is supported on precision rails (LWR 6200, Ewellix GmbH, Germany) as displayed in Figure 3.16. The rails only allow uniaxial movement and can be finely aligned by means of adjusting screws to allow very low bearing friction. Mechanical end stops were fitted to limit the movement of the carriage in both directions (load cell protection) and covers were mounted on each side to protect the precision rails from contamination.

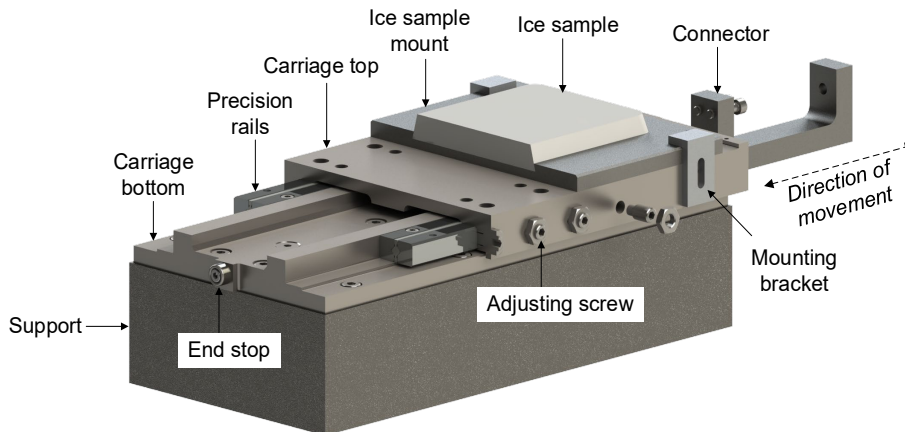


Figure 3.16: Carriage with mounted ice sample

The connector joins both the carriage and spring-loaded measuring system as illustrated in Figure 3.17. The movement of the connector in x-direction is transmitted directly via a cylinder with a screwed-on adapter to the separately mounted force sensor. A damping NBR spacer is placed in between to smooth out the force recording. To ensure that the cylinder is in constant contact with the load cell and that shocks in the opposite direction are absorbed, the connector is preloaded with a spring and secured with a reverse screw. This further stabilises the force recording. Both the threaded mandrel and the bush (here the inner wall of the cylinder) were manufactured to tolerance, which has the advantage of generating the highest possible shear of the grease and thus sufficient viscosity during spring deflection. This increases the sensitivity so that a proper response of the spring is generated even with small forces. In order to further improve the operating characteristics at very low shear rates, a grease with solid lubricant components was used. The infinitely variable adjustment of the spring force via adjusting nut and lock nut has an additional favourable effect on the response behaviour. Furthermore, the spring was supported in a cage with a rounded edge on the cylindrical surface in order to keep the contact surface and thus friction as small as possible and to improve the system behaviour. To prevent tilting and to ensure the spatial position in the y-direction, an automatic alignment of the rod by means of a ball washer and of the rounded cylinder head with a die-cut washer with a rounded opening was provided. For position assurance in z-direction between the measuring system

and the carriage, the load cell mount was aligned on one side of a parallel key in relation to the pin holes of the carriage.

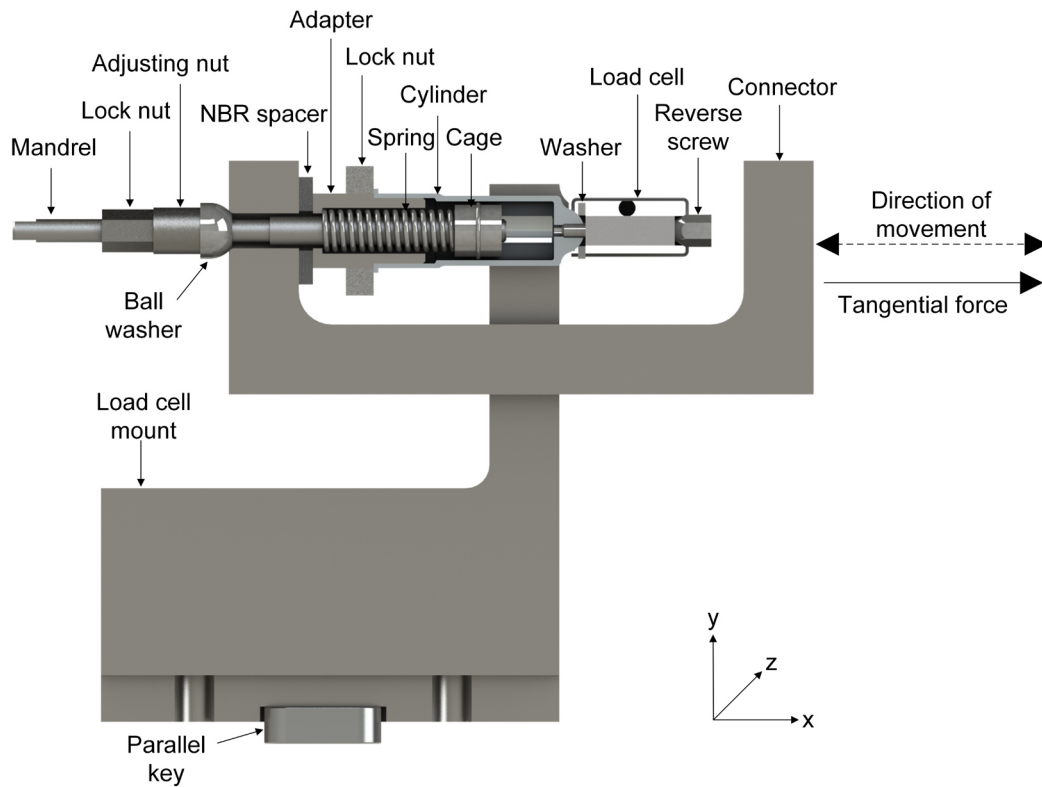


Figure 3.17: Force measurement setup

### 3.2.5 Weight force

The load is transferred to the ski base via a lever-arm mounted plate with installed rollers. To increase the grip, these rollers were coated with EPDM Shore 60. The rollers are beared with grooved ball bearings (W625, SKF GmbH, Germany) and are preloaded via springs to ensure smooth running. In between the bearings, bushings in which the shafts run were mounted on struts to prevent bending. Due to the proportionality of roller diameter and roller speed, in addition to the roller width of 16 mm, the diameter was set to 24 mm, which results in a speed of 22,282 r/min at a tangential speed of 28 m/s. This represents half the limiting speed of the bearings. The total weight of the roller plate corresponds to a maximum load of 140 N that can be applied (additional weights are however possible). In order to keep the distance between the centre axes

of the rollers as small as possible while maintaining a sufficiently large roller diameter, the rollers were arranged in a staggered pattern with 44 mm centre distance, as shown in Figure 3.19. The normal load can be varied in a gradual manner by a lever arm mounted on rod ends (SA 12C, SKF GmbH, Germany) with removable weight discs, which is connected to the roller plate through a steel cable. Assuming a uniform movement of the base, the load distribution situation can be divided into a quasi-static and a dynamic component. The static view for the larger ice sample (cf. chapter 3.2.6) means a load situation of 53 discrete line loads which are generated by the rollers through the base on the entire surface of the ice. In the case of the smaller sample, only 17 rolls are involved, corresponding to the size of the area. The force of 140 N is thus distributed across 53 or 17 gridded rollers (it is assumed that all rollers contact the ice uniformly). For each 16 mm long roller this results in a force of  $140 \text{ N} / 53 = 2.64 \text{ N}$  and  $140 / 17 = 8.24 \text{ N}$ , which is distributed onto a very small surface area. The load areas were roughly estimated by computer simulation (see Figure AP 6) and amount to approximately  $0.17 \text{ mm} \times 16 \text{ mm}$  ( $2.72 \text{ mm}^2$ ) for the large ice sample and  $0.33 \text{ mm} \times 16 \text{ mm}$  ( $5.28 \text{ mm}^2$ ) for the small ice sample (see Table 3.3). The simulation parameters can be found in Table AP 40 in the appendix. If the individual load areas are now added to a total load area, the load area for the large ice sample is  $53 \text{ mm} \times 2.72 \text{ mm} = 144.16 \text{ mm}^2$ , and  $17 \text{ mm} \times 5.28 \text{ mm} = 89.76 \text{ mm}^2$ . Table 3.3 displays the area loads depending on the normal force. The nominal contact pressure was determined by division of load and ice sample area.

Table 3.3: Contact pressure nominal (nom) and simulated (sim), transferred by the roller plate

Ice sample area in $\text{mm}^2$	Load in N	Contact pressure in kPa (nom)	Contact length in mm (sim)	Contact area in $\text{mm}^2$ (sim)	Contact pressure in MPa (sim)
16000	40	2.50	0.10	1.60	1.47
	80	5.00	0.20	3.20	1.47
	110	6.88	0.27	4.32	1.50
	140	8.75	0.33	5.28	1.56
33000	40	1.21	0.04	0.64	1.18
	80	2.42	0.07	1.12	1.35
	110	3.33	0.09	1.44	1.44
	140	4.24	0.17	2.72	0.97

The dynamic component is created by the flexing of the rubber-elastic rollers as they rotate. Another dynamic component is caused by the continuous deformation of the base by the rotating rollers, which also represents flexing. This can lead to temporal-local pressure fluctuations on the ice surface. The pressure of the rollers through the belt on the ice varies locally due to the grid structure of the roller arrangement. The higher the flexibility of the base, the thinner the base and the lower the base tension, the stronger the effect of the grid on the locally dependent pressure distribution at the base/ice interface.

Ski base tension was therefore investigated as a potential factor affecting friction. The base tension is controlled by the horizontal distance between the main rollers. While one of the rollers is fixed, the other can be set to a variable horizontal position, see Figure 3.25. This allows the length of the base to be controlled, which in turn controls the tension of the base. The position of the adjustable roller is measured using a relative scale: at -6 mm the base is just tight against the rollers but not yet under tension. As the roller is moved to larger values, tension is applied to the base, causing it to elongate. The length of the base was measured at various positions, see Table 3.4. At the reference position ("0 mm") i.e. in the standard measuring position, the length of the base was measured to be 2348 mm, which corresponds to an elongation of 0.256 %. Using a tensile testing machine, the base's modulus of elasticity was measured to be 865 MPa at -6 °C. The base's unloaded cross section amounts to 180 mm<sup>2</sup>, if neglecting transverse contraction, corresponds to a nominal tensile force of 398 N and to a nominal tensile stress of 2.21 MPa at the measurement position. In addition, the COF against ice was measured at  $T = -6\text{ °C}$ ,  $v = 9\text{ m/s}$ ,  $p = 2.42\text{ kPa}$  and two-sided hypothesis tests showed no significant effect of base tension on the COF as shown in Figure 3.18. This is consistent with the assumption that the mechanical losses of the roller, which are most likely affected by the base tension, do not contribute to the measured frictional force because they occur before the frictional force is generated and transmitted to the carriage. It is reasonable to assume that, as a result of the base tension, the load distribution situation remains constant during the measurements carried out. Despite that, during all tribological experiments in this work, the base tension was controlled and kept constant by measuring the travel of the tensioning mechanism after a base change and additionally by monitoring the slip.

Table 3.4: Estimation of the ski base's tensile stress while mounted on the tribometer and impact of base tension on COF

Roller position in mm	Base length in mm	Elongation in mm	Elongation in %	Tensile stress in MPa	Tensile force in N	COF in $10^{-2}$
- 6	2343	1	0.043	0.37	66	3.87 +/- 0.18
- 4	2344	2	0.085	0.74	133	3.87 +/- 0.18
- 2	2346	4	0.171	1.48	266	3.87 +/- 0.14
0	2348	6	0.256	2.21	398	3.89 +/- 0.15
+ 2	2349	7	0.299	2.59	465	3.92 +/- 0.17
+ 4	2350	8	0.342	2.95	532	3.94 +/- 0.18

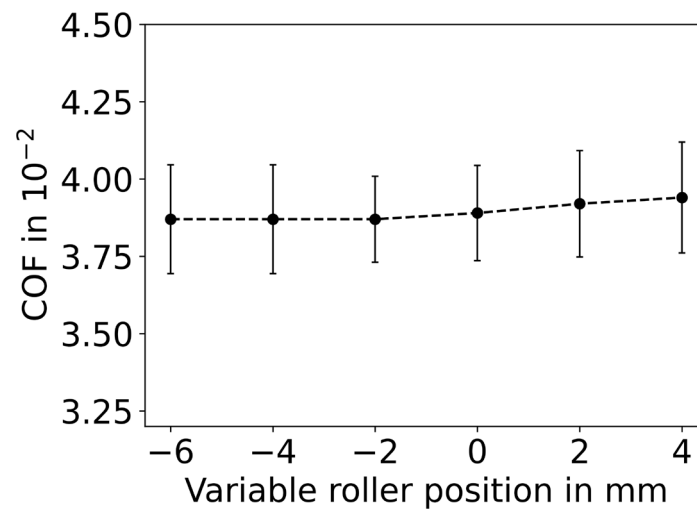


Figure 3.18: Effect of roller distance on COF with 95 % CI ( $v = 9$  m/s,  $p = 2.42$  kPa,  $T = -6$  °C)

Due to the rigidity of the ski base and the resulting two-dimensional distribution of initiating forces, the line loads are "blurred", i.e. the contact pressure is significantly lower than nominally estimated via simulation results. Calculation is, however, complex due to the viscoelastic characteristics of the ski base and exceeds the scope of this thesis. Certainly, the real contact pressure is higher than the assumed nominal pressure. Observations during the series of measurements showed a visible deformation due to the roller imprints not before 400 m sliding distance and thus outside the measuring range used in this work. To allow the plate to adjust itself in height, the roller plate is guided by two parallel pins. The pins have been dimensioned to ensure that in the event of

the ski base catching, the pins do not break off and the torque protection switch of the motor is activated beforehand. Due to the high-frequency shocks that occur, plain bearings could possibly be damaged. Therefore, it was chosen to use a bearing with high pressure grease lubricated O-rings, which are inserted in a 0.2 mm oversized borehole. This provides sufficient movement clearance, similar to a rotary union, with a simultaneous shock-absorbing effect.

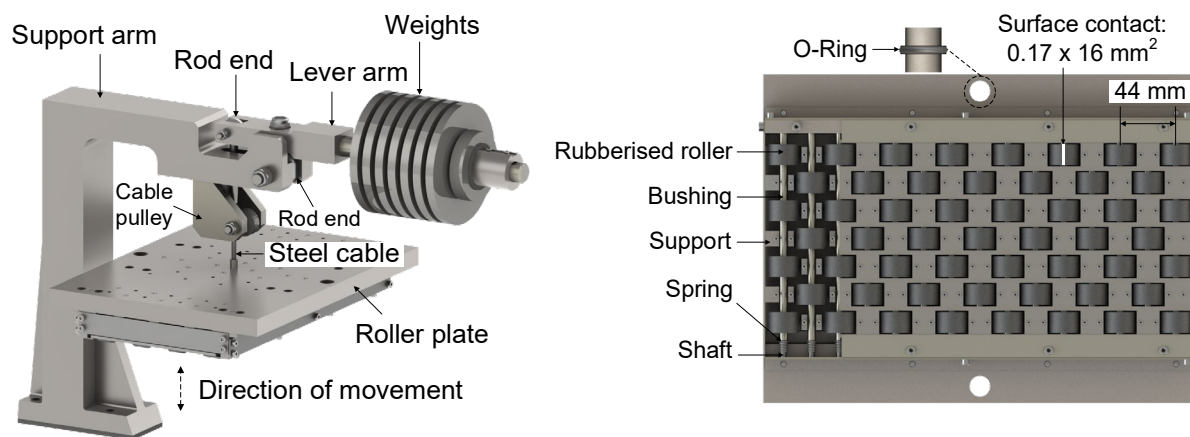


Figure 3.19: Weight force arrangement: lever arm (left) and roller plate (right)

### 3.2.6 Ice sample

As shown in Figure 3.21 and Figure 3.22, the ice samples were prepared in stainless steel moulds. In order to conduct tests with varying surface sizes, two different dimensions, 160 mm x 100 mm and 330 mm x 100 mm, were manufactured. Overall, eight moulds were manufactured, three with dimensions of 330 mm x 100 mm and five with dimensions of 160 mm x 100 mm. The 100 mm width of the ice sample was chosen to be smaller than the width of the ski base (120 mm) to eliminate the influence of the ski base edge. The bottom of the mould features an undercut to secure the ice plate in place while the lid was coated with a polypropylene (PP) film to reduce the surface roughness of the ice sample and also prevented adhesion and therefore simplified the extraction of the ice sample from the mould. The mould was filled in an upright position as shown in Figure 3.22. Furthermore, the produced ice samples should be planar, smooth and their edges should not protrude. A chamfer machined into the ice mould lid allowed for shape deviations due to uneven freezing and capillary forces, so that



only those parts of the ice samples that were not relevant to the frictional contact were affected, see Figure 3.21. The planarity of the ice sample was controlled by using a precision machined lid, whose planarity was less than 0.02 mm. In addition to the screw fastening, the lid was prevented from bending by attached screw clamps. After extracting the samples and before using them in a tribological test, their planarity was controlled with a precision straight edge.

To investigate the influence of the macroscopic contact area and varying surface pressures, ice samples in the sizes 160 mm x 100 mm and 330 mm x 100 mm were manufactured. This allows surface pressures between 1.2 kPa and 8.8 kPa to be set (additional weights are, however, possible). Furthermore, this enables two modes to be set. In linear mode (Figure 3.20 left), the width of the ice plate is less than the width of the ski base and a potential interference of the slightly undulating base edge is therefore eliminated. In perpendicular mode (Figure 3.20 right) the 160 mm wide ice samples can be rotated by 90° and protrude laterally by approx. 20 mm over the ski base. Now the ski base runs with its full width on the ice and as a result, reference surfaces are formed at the side of the running track for comparative wear measurements to determine the abrasion effect.

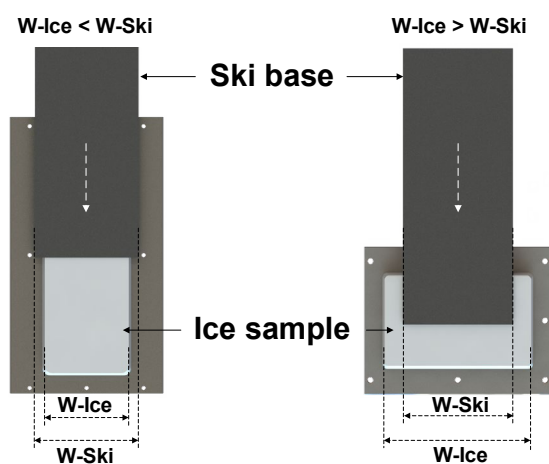


Figure 3.20: Linear mode (left) and perpendicular mode (right)

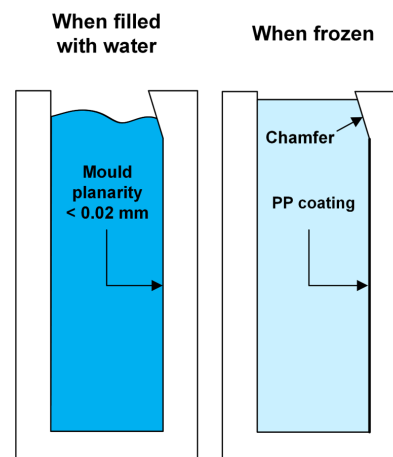


Figure 3.21: Ice sample production principle

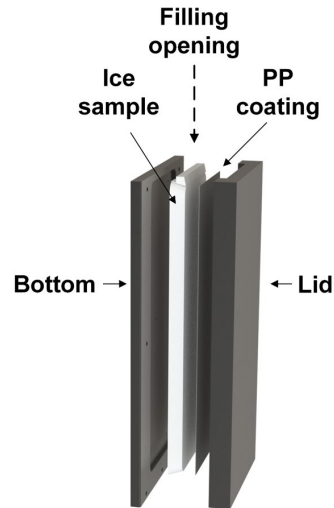


Figure 3.22: Steel mould for ice sample production

### 3.2.7 Ski base sample

In order to achieve a closed belt design, the ski base manufactured by Isosport Verbundbauteile GmbH, Austria, and provided by the German Ski Association (DSV) was scarfed and bonded adhesively at the ends (DP 8005 from 3M, see Figure 3.24 top). During this procedure the newly formed belt was kept free from tensile stresses for about 10 hours. For this purpose, the joint

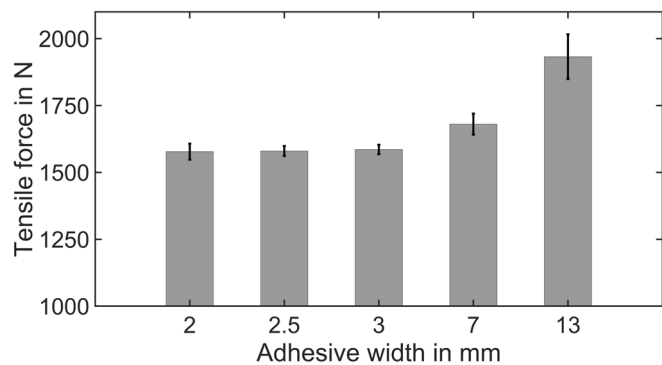


Figure 3.23: Average yield tensile shear force vs. adhesive width at  $-12\text{ }^{\circ}\text{C}$  with standard deviation error bars

overlap was compressed with a pressure force of 50 N. This also ensured a smooth transition between the joined ends of the ski base. The whole procedure was carried out at room temperature, e.g. at about  $20\text{ }^{\circ}\text{C}$ . The tensile shear strength of various adhesive bonds was tested at a sample temperature of  $-12\text{ }^{\circ}\text{C}$  (DIN EN 1465). Figure 3.23 displays the average shear tensile force ( $n = 5$ ), calculated from the yield stress at different adhesive widths. Note that a reduced glue width creates less disturbance when circulating the rollers and passing the ice sample. Since a similar breaking

strength prevailed between 2 mm and 7 mm adhesive width and this corresponds to about 80 percent of the value of the widest test point of 13 mm, an overlap length of 3 mm has been chosen.

### **3.2.8 Motor**

According to chapter 3.1.1.2, a 7.5 kW electric asynchronous motor (MFEMAXX112-22CIC, Lenze GmbH, Germany) with a torque of 20.3 Nm and an 11 kW inverter drive (Inverter Drives 8400, Lenze GmbH, Germany) were installed on a base structure of aluminium construction profiles. The motor was mounted on a linear slide and connected to the 28 mm input shaft by means of a flexible clutch. To reduce vibrations, the drive can be changed to a belt drive if required, whereby the linear slide is laterally shifted on the base.

### **3.2.9 Concept visualisation**

Figure 3.24 and Figure 3.25 show the implemented concept of the novel tribometer. A driven ski base glued at the ends is brought into contact with the ice sample by a weight plate with rubberised rollers by means of dead weights. The ice plate is mounted on a rail guide and actuates a load cell due to friction-induced linear deflection.

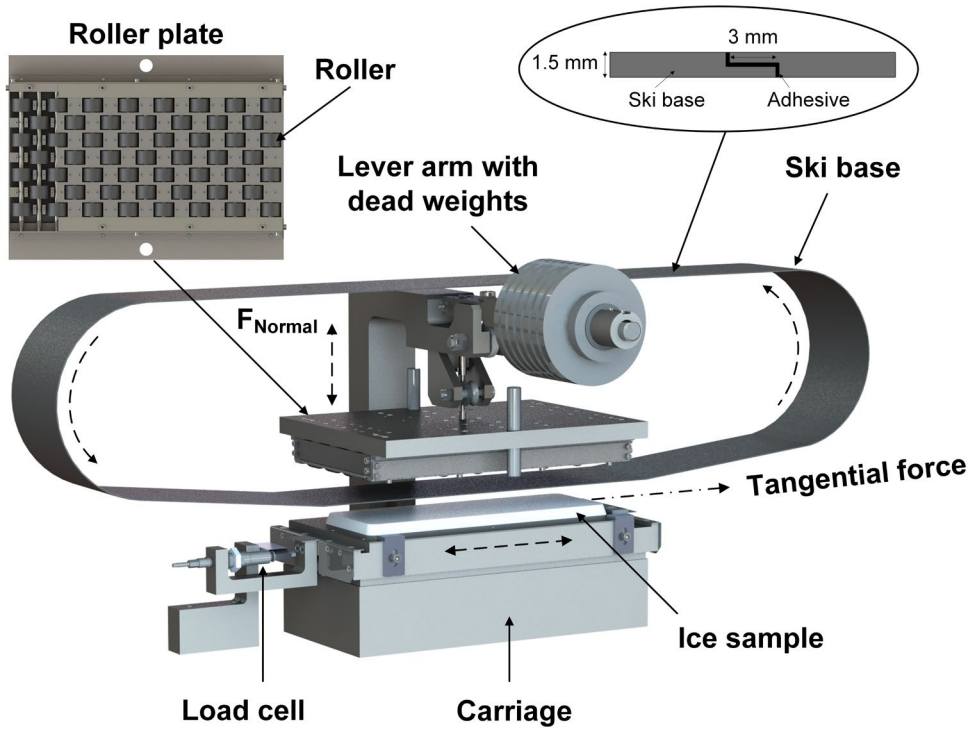


Figure 3.24: Weight force arrangement and sample contact

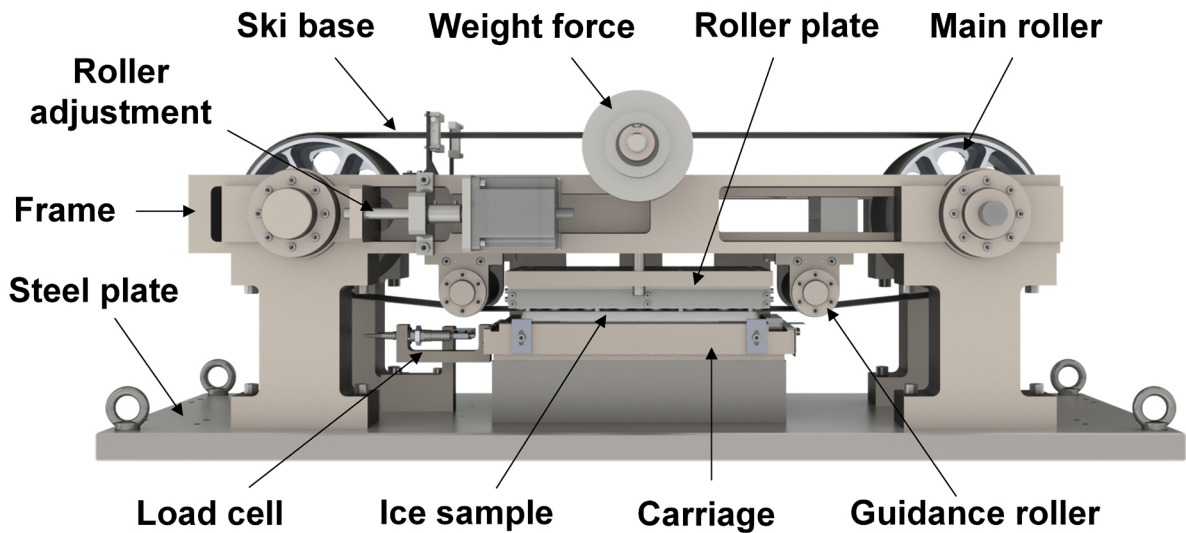


Figure 3.25: Novel linear tribometer

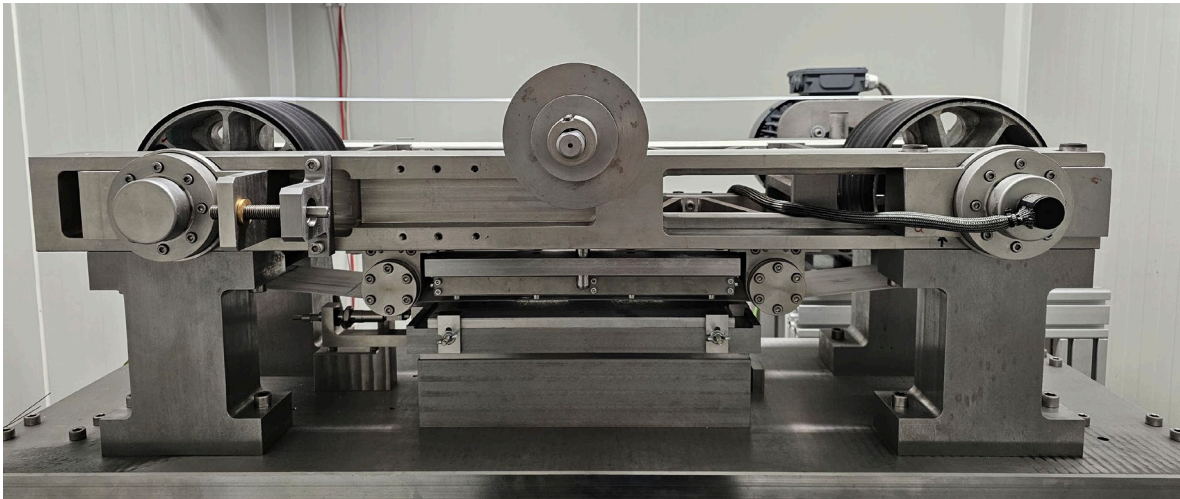


Figure 3.26: Built tribometer located in the cooling cell

### 3.2.10 Parameter settings of the tribometer

The following table shows the range of settings that can be adjusted on the tribometer.

Table 3.5: Parameter range

Normal load (N)	40, 80, 110, 140
Nominal contact pressure (kPa)	1.21, 2.42, 2.50, 3.33, 4.24, 5.00, 6.88, 8.75
Relative sliding speed (m/s)	Up to 28 (user-adjustable)
Acceleration (m/s <sup>2</sup> )	Up to 16 (user-adjustable)
Contact partner	Ice surface and UHMWPE ski base
Surface quality ice	Defined ice surface quality with interchangeable surface roughness due to plastic film
Surface quality ski	All ski base material and widths applicable
Ambient temperature (°C)	-25 to -1
Ice temperature (°C)	Not actively cooled
Air humidity (%)	Not separately adjustable



## **4 Ice tribometer verification**

### **4.1 Sample preparation**

In order to eliminate the influence of the ski base structure, a raw ski base was used for the tests with liquid glide wax. The ski base was manufactured in a peeling process and therefore featured a surface with production-related longitudinal grinding grooves as can be seen in Figure 4.14. These grooves were not removed prior to this study. All investigations in this work were conducted using a single ski base. This approach was chosen based on previous research indicating that extensive laboratory testing does not significantly alter the surface properties of ski bases [65]. By using a single ski base, the variation caused by different ski bases was eliminated, thereby increasing the ability to isolate the impact of fluorine content on friction. In order to investigate the influence of the fluorine content of applied waxes, the ski base was first tested unwaxed and then with waxes of varying fluorine content provided by ZIPPS Skiwachse GmbH, Germany. These were “ZR 41” which does not contain any fluorine and which therefore serves as internal wax reference for this study, “GT 20” which contains 1 wt.-% of a “highly fluorine containing compound” and “H5LF” which contains 4 wt.-% and “ZR NS” which contains 8 wt.-% of this compound. As a result of the waxing process, a visible white wax film was present on the surface, which could also be felt. Between experiments, the ski base was cleaned and reused. The cleaning procedure involved using “C 31 Base Cleaner” from ZIPPS Skiwachse GmbH (Germany), following the manufacturer’s instructions. The effectiveness of the cleaning procedure was periodically validated by measuring the COF between the cleaned ski base and ice using the novel tribometer. To minimize the risk of potential false positive findings caused by the gradual accumulation of wax residues leading to unnoticed shifts in measured friction, the sequence of the investigations in this study was randomized.

### **4.2 Surface characterisation**

Prior to wax application, the surface profile of the ski base was recorded using a stylus profilometer (MahrSurf PS1, Mahr GmbH, Germany). For this, within a lateral range of 100 mm x 100 mm, 10 line scans were conducted at random positions. The scan direction was perpendicular to the sliding direction of the tribometer experiments. Each

line was 5.6 mm long, which corresponded to 7 segments of 0.8 mm each. From these, numeric roughness parameters were obtained according to DIN EN ISO 4287 by using a cut-off length of 0.8 mm. This procedure was repeated after each tribometer experiment, i.e. after a total sliding distance of 20 m, 140 m, 280 m and 470 m respectively. Additionally, the surface profiles of the prepared ice sheets were recorded. This was done indirectly by applying a silicon casting compound (Provil Novo Light Fast Set, Kulzer GmbH, Germany) to the ice surface and letting it cure for approximately two hours. This process resulted in a negative cast of the ice surface profile. The precision of this negative cast was better than 1  $\mu\text{m}$  according to the manufacturer. In contrast to the shiny ice surface, the cast absorbed a considerable amount of light, which prevented overloading of the profilometer's optical sensor even at low surface roughness. Furthermore, the cast could be taken directly in the cooling chamber and transported to the profilometer, avoiding complications such as ice melting during transportation. Additionally, the large closed belt-shaped ski base could not be fixed to the profilometer's sample holder, whereas the casts were small, measuring approximately 120 mm x 70 mm and weighing less than 10 g. Figure 4.1 depicts a silicone cast of the ice surface. The clearly visible longitudinal grooves indicate significant amounts of solid-solid interaction.



Figure 4.1: Silicone cast of an ice sample's surface after 470 m sliding distance

The accuracy of the optical profilometer was validated by measuring several standard roughness samples. Casts were also made of these standard samples and measured with the same optical profilometer. The results of these measurements are shown in Figure 4.2. When directly scanning the standard samples, the profilometer produced



95 % confidence intervals for  $R_a$ ,  $R_z$  and  $R_t$  that included the nominal value of the respective standard sample in most cases (indicated by red bars). However, when measuring the casts, slight deviations from the nominal values were observed. For  $R_a$  values greater than  $0.1 \mu\text{m}$ , these deviations were random. Starting at  $R_a = 0.1 \mu\text{m}$  and below, the deviations became systematic, with the recorded roughness values being higher than the nominal values. Consequently, for such smooth surfaces, the cast was not able to accurately reproduce the surface profile. These deviations were significantly below the manufacturer's published "accuracy" of  $1 \mu\text{m}$  and well below the lowest  $R_a$  value measured for any ice or ski base sample in this work, as shown in Figure 4.15. Therefore, the presented procedure provides a valuable and validated tool for the quantitative investigation of friction in the field of snow and ice tribology.

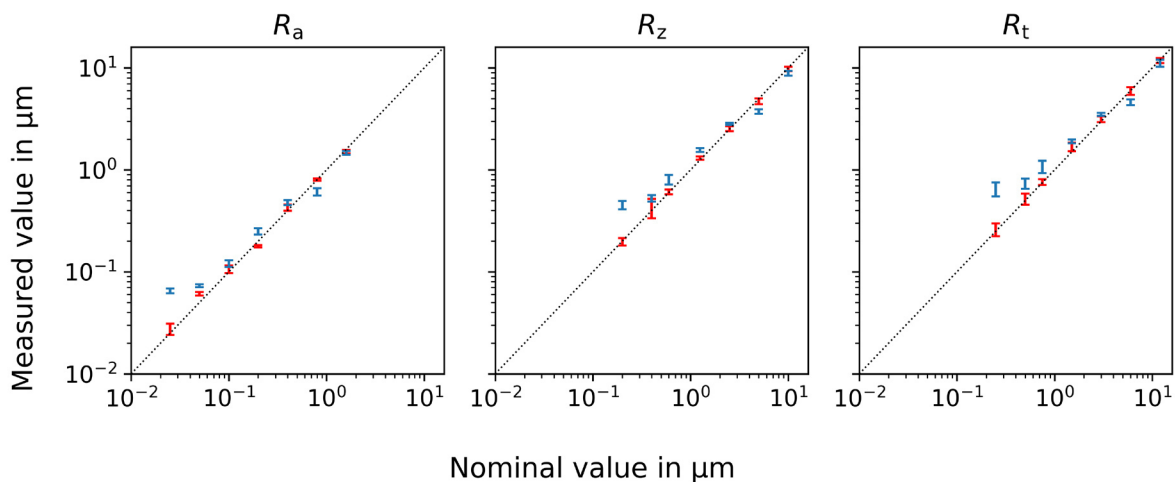


Figure 4.2: Comparison of nominal and measured surface texture parameters. Data was recorded with an optical profilometer according to ISO 21920. Red: standard roughness samples, blue: casts of these standard samples. Bars represent 95 % CIs from 10 individual line measurements.

The surface profile of the cured casts was recorded using a MicroProf 100 white light profilometer (FRT Fries Research & Technology GmbH, Germany). For this purpose, within a lateral range of  $50 \text{ mm} \times 50 \text{ mm}$ , 10 line scans were conducted at random positions. The scan direction was perpendicular to the sliding direction of the tribometer

experiments. Each line was 5.6 mm long, which corresponded to 7 segments of 0.8 mm each. Since the casts represented negatives of the original ice surfaces, the recorded z-data were multiplied by -1 prior to further processing. From these, numeric roughness parameters were obtained according to DIN EN ISO 4287. To account for systematic differences between tactile and optical surface profilometry, the evaluation included a tip needle simulation ( $90^\circ / 5 \mu\text{m}$ ). It was confirmed by measurements with the stylus profilometer on selected ski base locations that this procedure yielded comparative results. Again, this procedure was repeated after each tribometer experiment. Furthermore, a separate ski base was subjected to the same waxing procedure but instead of using it for tribometer experiments, it was cut into pieces in order to be able to record three-dimensional surface profiles. Figure 4.14 exemplarily shows the recorded profiles of the ski base in its as-received state and after waxing with H5LF.

The perpendicular mode shown in Figure 3.20 was used to measure the wear related height loss of the ice plate. In practice, however, there is the difficulty of operating the profilometers to be used for measuring the height loss in the cooling cell. If the ice plate is carried to the profilometer instead, the ambient conditions there quickly lead to frost formation and melting of the surfaces, which considerably reduces the accuracy of the topographical wear measurement. For this reason, the ice plate was removed from the tribometer and a silicon cast imprint was made while still inside the cooling cell, specifically to measure the transition from the wear track to the surrounding reference surface, see Figure 4.3. After the casting compound had hardened, the cast was transported to the profilometer and the wear related height loss was determined. The effect of wear on the surface free energy, the contact angle of water, and diiodomethane were measured with a mobile surface analyser (MSA One-Click SFE, Krüss GmbH, Germany). The droplet volume was  $1 \mu\text{l}$ . Both the unwaxed ski base and the base waxed with four waxes were analysed immediately after the preparation process and as a function of the sliding distance as shown in

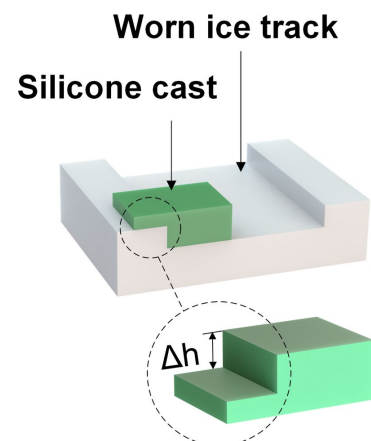


Figure 4.3: Example of an abrasion analysis

Figure 4.19. The contact angle of each droplet was measured five times. This procedure was repeated again five times at predefined locations and out of these repetitions, a mean angle was finally calculated.

### 4.3 Tribometer experiments

The maximum total sliding distance in this study was 470 m, as typically the steady state was reached around 200 m. It is expected that longer tests would not have altered the measurement results, as the focus of this study was to assess the friction-reducing capability of waxes based on steady state coefficients of friction. It was decided not to include the determination of the onset of test specimen and wax failure, as this is beyond the scope of the work. Non-friction related effects, such as vibration during operation or the passage of the ski base's adhesive joint over the tribometer's various rollers, have the potential to affect the measurement of the frictional force. To account for this, a baseline measurement was recorded. The tribometer was operated in the actual test configuration, but without the presence of an ice plate. As a result, the base of the ski did not come into contact with, and exert any force on, the ice plate sample holder. Figure 4.4 shows the baseline measurement obtained, which was then subtracted from all the recorded frictional forces before calculating the coefficient of friction. This procedure was repeated each time a new ski base was mounted on the tribometer, but only within the speed range of the subsequent experiments.

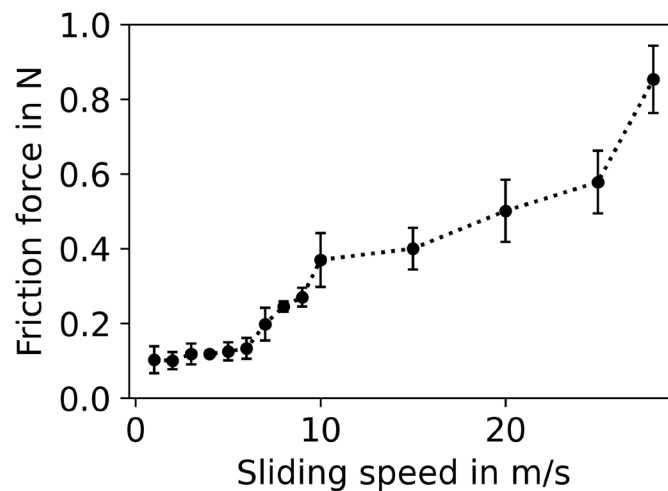


Figure 4.4: Exemplary baseline, measured at  $-6\text{ }^{\circ}\text{C}$

At the outset of each experiment, the ice sample was positioned and secured below the mounted ski base by utilizing the linear configuration, which is illustrated in Figure 3.20. Unless otherwise specified, the ice sample's cross-sectional area was 33,000 mm<sup>2</sup> which corresponded to a nominal contact pressure of 4.2 kPa. All experiments were conducted at a consistent ambient temperature, ranging from -19 °C to -4 °C. To ensure complete temperature equilibrium, all equipment was stored inside the cooling cell for a minimum of 2 hours prior to testing. The experiments were then intermittently conducted. Initially, the ski base was at rest and the required normal force was applied by lowering the roller plate. Each intermittent operation initiated with the acceleration of the ski base to a preset sliding speed. Although the tribometer had the capacity to reach speeds of up to 28 m/s, a maximum sliding speed which ranged from 1.5 m/s to 14 m/s was chosen for this study. The acceleration has been constant during a given experiment and varied from 3 m/s<sup>2</sup> to 15 m/s<sup>2</sup> between test runs. Once the required speed was attained, it was sustained for a certain period of time, known as the "constant speed duration" (CSD). The exact value of this parameter had a significant impact on the test results, as it decisively influenced the amount of friction energy dissipated during each segment. Together with the latency between segments (ISL), which controlled the re-solidification of the molten ice, the parameter determined the amount of water available to build up a lubricating film that could reduce the COF due to the separation of ice and ski base. Since no valid method currently exists to measure the water film that occurs or to control its formation, such a difficult-to-trace lubrication condition was not desired in this study. The main hypothesis of this study was that wax primarily impacted friction in dry sliding and boundary lubrication conditions. Therefore, the amount of water generated during the experiments was minimized. Additionally, the observation and quantification of water films posed significant challenges that have not been fully addressed and were outside the scope of this study. Hence, objective and quantitative evaluation of water films was not feasible. Instead, their presence or absence was determined based on visual inspection immediately after each segment, the formation of surface damages such as grooves, and the observed range of the COF. Therefore, a series of experiments were performed at -6 °C, 4.2 kPa and 3 m/s to determine the maximum value for the constant speed duration before significant amounts of melted water lead to a reduction in COF. The temperature was chosen to take into account the following aspects: in the literature, there are several reference

values for COFs determined by both laboratory and field tests [42,45,49,55,123], and in competition most events take place in this temperature range [108]. In combination with an adequate inter-segment latency (cf. Figure 4.6), the ice temperature is not moved beyond the melting point by the friction-induced energy input since the COF remained constant (no further lubrication) as preliminary tests had shown. Based on the results of these experiments, which are shown in Figure 4.5, the constant speed duration throughout this study was chosen to be between 1.2 s and 1.5 s.

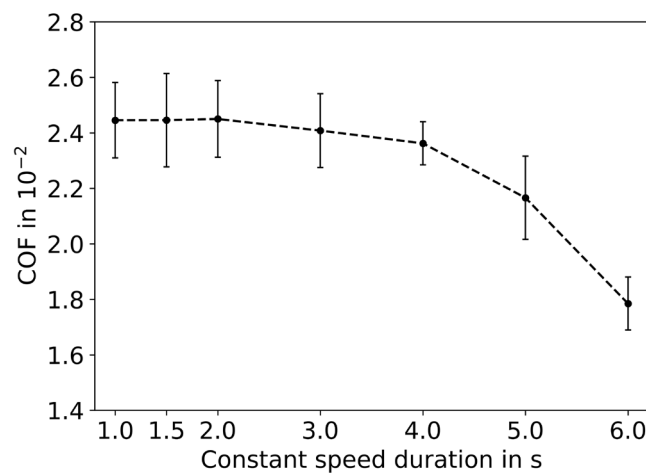


Figure 4.5: Effect of constant speed duration on COF ( $p = 4.2$  kPa,  $T = -6$  °C,  $v = 3$  m/s)

Subsequently, the ski base was decelerated at a rate of  $11 - 15$  m/s<sup>2</sup> until it came to rest. Overall, such a segment took approximately  $1.5 - 3.3$  s, also counting in control latencies (but not the ISL from Figure 4.6). During a segment, friction force, sliding speed, slip, air temperature, and humidity have been measured and written to a segment-specific data file. Figure 4.7 exemplarily displays speed and friction force over time for such an intermittent operation segment. An experiment consists of a series of such segments. To allow dissipation of the generated frictional heat, a pause was included after each segment, which lasted 30 s unless stated otherwise. This value for the inter-segment latency (ISL) has been determined from a series of experiments in which different latencies were utilized, see Figure 4.6.

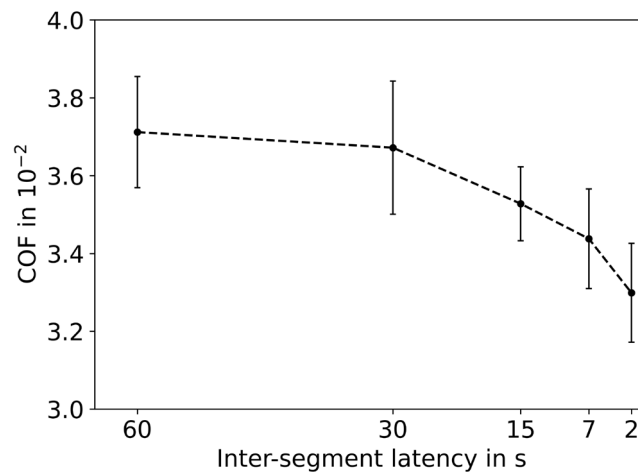


Figure 4.6: COF of the unwaxed ski base as a function of the inter-segment latency ( $p = 2.42$  kPa,  $T = -6$  °C,  $v = 9$  m/s,  $s = 135$  m)

Based on the results of the previously shown experiments, suitable test parameters were defined for the various test series of this study, see Table 4.1. The general guidelines for determining the parameters were the usage of realistic values for  $T$ ,  $v$ ,  $a$ , and  $p$ , the prevention of vibrations and good signal-to-noise ratios. The inclusion of task-specific considerations resulted in slight variations between the series.

Table 4.1: Test parameters of the various test series of this work

Test series – Impact on COF	$p$ in kPa	$v$ in m/s	$T$ in °C	ISL in s	CSD in s	accel., decel. in $m/s^2$
Mould number	2.42	9	-6	30	1.2	11, -11
Base tension ( $N/mm^2$ )	2.42	9	-6	30	1.2	11, -11
Fluorine content (wt-%)	4.2	3	-6	30	1.33	11, -15
Surface roughness ( $\mu m$ )	4.2	3	-6	30	1.33	11, -15
Surface structure	2.42	9	-6	30	1.2	11, -11
Speed and temperature (m/s, °C)	2.42	1.5 to 14	-19 to -4	30	1.2	11, -11
Acceleration ( $m/s^2$ )	4.2	3	-6	30	1.33	3 to 15, -11
Acceleration and deceleration ( $m/s^2$ )	2.42	3 to 9	-6	30	1.2	3 to 9, -3 to -9
Contact pressure (kPa)	1.2 to 8.8	3	-6	30	1.33	11, -11

During a segment, frictional force, sliding speed, slip, air temperature and humidity were measured and written to a segment-specific data file. Slip, i.e. the difference in rotational speed between the driven and the driving roller, was less than 0.5 % in all cases. However, it was irrelevant as it does not affect the relative speed between the ski base and the ice plate and thus on the friction between them. Furthermore, all sliding speeds in this work represent the speed of the driven roller, which takes into account the potential slip. After the experiment, the recorded data files were evaluated, as shown in Figure 4.7. To account for scattering in the friction force data, an average was calculated. The observed scattering is likely attributed to vibrations in the sliding direction, which are most likely caused by the drive and the spring/damper setup located between the ice sample holder and the load cell. It is assumed that these vibrations do not significantly impact the overall level of the friction force, and thus no other signal post-processing than arithmetic averaging was applied. The boundaries of the averaging interval were smoothed (dotted line) [124] and from the smoothed data the boundaries were afterwards determined algorithmically (dash dot and dashed lines) [125]. The average COF was determined by dividing the averaged friction force by the applied normal load. Furthermore, the data was plotted for visual inspection.

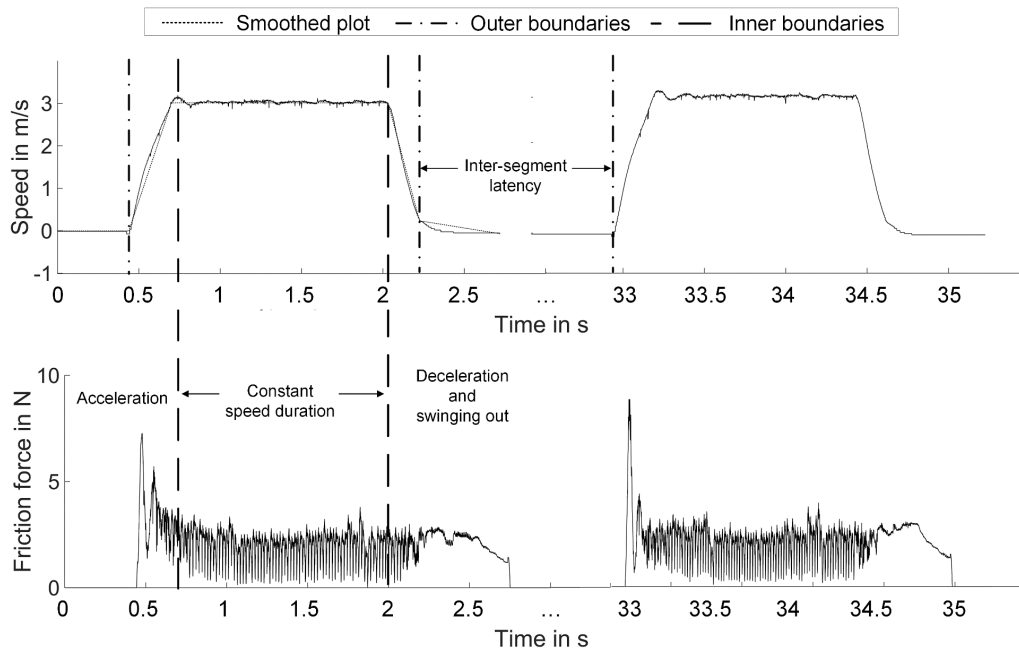


Figure 4.7: Determination of the friction force calculation range with speed over time (top) and friction force over time (bottom)

All tests were performed repetitively to improve the statistical significance of the experiment results. The exact number of individual experiments, not to be confused with the number of segments per experiment, varied between the different parts of this study and are described in each part. Repetitive tests that were conducted with the same surface condition of the ski base, e.g., unwaxed or waxed with a specific wax, constituted a series of tests, whose individual numerical results for a given quantity were treated as statistical samples. The size of these statistical samples was equal to the number of observations they contained. Arithmetic means and standard deviations were calculated from these samples. For an automatic analysis, a programme was designed that determines the constant speed curve in the created data files and then transfers the corresponding measurement values into a new file for evaluation and graphical display. The mean value is calculated afterwards and the procedure is repeated for the remaining experiment files. When a set was finished, a graph was created for the single tests as well as for the entire series of measurements. Figure 4.8 shows the flow chart of this analysis process.

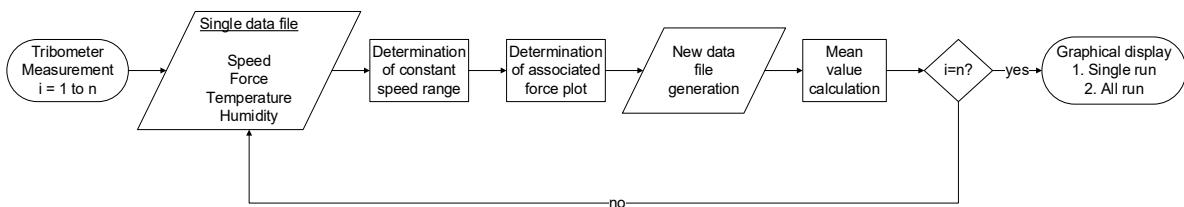


Figure 4.8: Flow chart of the automatic data analysis

#### 4.4 Precision analysis

Despite the observed scattering, the overall precision of the procedure described in chapter 4.3 has been found to be excellent. The precision of a test procedure regarding a given quantity is represented by the standard deviation of a series of measurements of the quantity in question. The precision of the novel tribometer was evaluated based on the average of the standard deviations that were obtained from the test series on waxes with different fluorine content, see chapter 4.5.1, which was  $0.08 \times 10^{-2}$ . This is only 7.5 % of the COF of  $1.07 \times 10^{-2}$  that was found for the wax with the lowest COF.



In contrast to precision, which is a measure for the repeatability of the COF measurement for a given combination of test sample type and test parameters, resolution is a measure for the smallest difference between the arithmetic means of two combinations that a procedure can determine to be "significantly different" from each other. In general, resolution depends on the standard deviation, sample size, and confidence interval (CI). In order to calculate the resolution of the novel tribometer and procedure, series of two-sided  $t$ -tests were conducted. During this, the previously computed (average) standard deviation was used, and the confidence interval (95 % and 99 %) and sample size (2 – 20) were varied. Figure 4.9 depicts the results of this procedure. The curves represent the boundary lines where the result of the  $t$ -tests transitions from "non-significant difference" to "significant difference". Therefore, the areas above the curves represent differences in COF between two samples that can be classified as "significantly different", while the areas below the curves represent situations where the numerical differences are considered insufficient to represent an actual effect. According to Breitschädel et al. [81], the resolution of a testing procedure should be better than 0.001. For the experiments conducted and the test procedures, this is achieved for  $n > 6$  for a confidence interval of 95 % and for  $n > 10$  for a confidence interval of 99 %. While this is slightly higher than for the experiment setup of Auganæs et al. [65], which requires only 2 to 5 individual tests to achieve this limit, the test setup in this study requires much less effort per individual test and is therefore at least as efficient. Further experiments were carried out with a number of individual tests between 6 and 15.

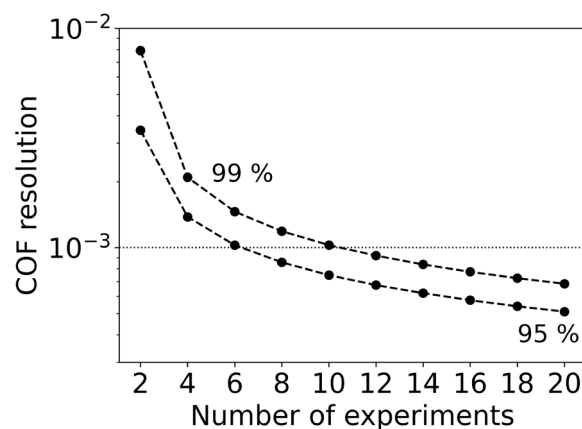


Figure 4.9: Resolution vs. number of experiments with resolution criterion according to [81]

The linearity of the recorded friction force at an applied normal force of 140 N was verified using a calibrated load cell. Instead of allowing the ski base to slide over the ice, the frictional force was simulated by pressing a calibrated load cell against the carriage, in the direction of sliding. By this method, the applied tangential force mimicked the frictional force that would otherwise be generated by the ski base as it slid over the ice sample. The tangential force was gradually increased and at each step it was recorded from the calibrated load cell and the corresponding "frictional force" on the load cell of the tribometer. As shown in Figure 4.10, the recorded force deviates insignificantly from the nominal force, resulting in a linearity error of only 6.6 %, which is far below the typical scatter observed in repeated tribological experiments. In addition, the fact that the slope is so close to 1 shows that the total friction losses of the mechanical setup are negligible compared to the linearity error. It is important to note that only mechanical losses that occur between the frictional contact and the tribometer's friction force load cell affect the recorded friction. Therefore, for example, frictional losses of the rollers do not affect the measured friction. The reason for this is that the rollers are located "before" the frictional contact. Here "before" refers to the position of the potential losses within the force transmission line that starts at the drive, passes through the rollers into the ski base, from there into the ice sample and the sample holder, and finally through the carriage into the load cell.

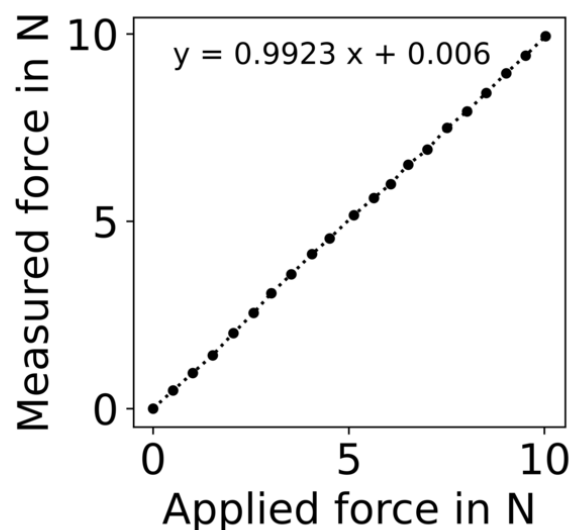


Figure 4.10: Linearity of the load cell used for measuring the friction force

As described in chapter 3.2.6, several moulds were made for each of the two sample sizes. During tribometer operation, these were used alternately to produce a continuous supply of ice samples. The impact of each mould on the measured COF was therefore investigated by performing tests where the used mould number was explicitly noted and the results were grouped by this mould number.

A normal force of 80 N corresponding to a nominal contact stress of 2.42 kPa was used in all tests on a 330 mm x 100 mm ice sample at an ambient temperature of -6 °C, a sliding speed of 9 m/s, an CSD of 1.2 s, an ISL of 30 s, and an acceleration and deceleration rate of 11 m/s<sup>2</sup>. The ski base travelled 18 m per intermittent operation, with each experiment comprising three such intermittent operations, giving a total sliding distance of 54 m per experiment. For each mould, five experiments were conducted, resulting in a total of 15 experiments. The ski base was cleaned of all wax residues for these experiments and, to prevent drift, the mould number was changed after every three experiments. The COFs measured for each mould are shown as 95 % confidence intervals in Figure 4.11. Two-sided hypothesis tests showed that there was no statistically significant difference in the averages and standard deviations between all three moulds.

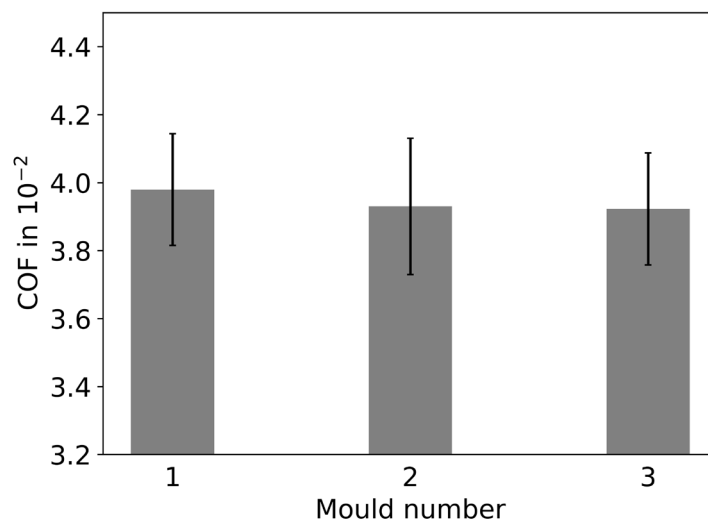


Figure 4.11: Result of the mould comparison study

## 4.5 Results and discussion

### 4.5.1 Fluorine content experiments

In all experiments, a normal force of 140 N was applied, corresponding to a nominal contact stress of 4.2 kPa, an ambient temperature of  $-6\text{ }^{\circ}\text{C}$ , a sliding speed of 3 m/s, an ISL of 30 s, and a CSD of 1.33 s. The pressure of 4.2 kPa was chosen in order to improve the signal-to-noise ratio during this part of the study. This was motivated by the presumably very small differences between the waxes due to their different fluorine contents. Acceleration and deceleration rates of  $11\text{ m/s}^2$  and  $15\text{ m/s}^2$  were used, respectively. Deceleration was higher than acceleration as to reduce the amount of frictional energy that was dissipated. Acceleration was not chosen higher due to vibrations that occurred above  $11\text{ m/s}^2$ . In total, the ski base travelled 4.7 m per intermittent operation, see also Table 4.1. 100 intermittent operations were carried out per experiment, resulting in a total sliding distance of 470 m. Six experiments were conducted for each wax and for the unwaxed ski base. A new ice plate was installed before each experiment. Overall, the tests were carried out in two series. The first series aimed to measure the COF of differently prepared ski bases with maximum accuracy. For this series, Figure 4.12 shows the calculated average COF as a function of sliding distance for the unwaxed ski base and for the ski base waxed with four waxes.

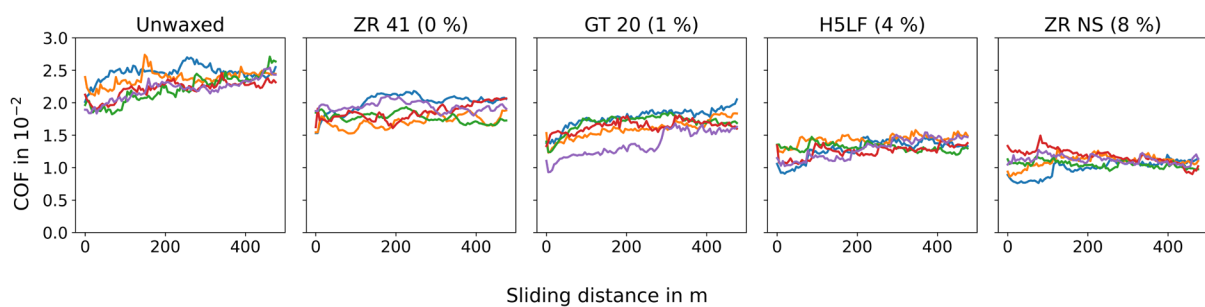


Figure 4.12: COF vs. sliding distance of six individual experiments per wax grade and for the unwaxed ski base ( $T = -6\text{ }^{\circ}\text{C}$ ,  $v = 3\text{ m/s}$ ,  $p = 4.2\text{ kPa}$ )

In each case, a pronounced running-in was observed, with the COF slowly increasing with the sliding distance. In addition, a notable scatter was observed between the individual trials. This has been observed previously and explained by the increase in real contact area between the ski base and the ice, the abrasion of the ice surface in multi-pass experiments (as in this study), the melting and re-freezing of water caused by friction and the resulting change in surface roughness [34,45,49]. Additionally, variable brushing quality and variable amounts of applied wax potentially impacted scattering. All of these effects are uncontrolled parameters during this study. However, starting from a sliding distance of 300 m, scattering between experiments significantly abated. Using a two-sided hypothesis test at a 95 % confidence level, the difference between a fluorine content of 1 % and 8% became statistically significant after 26 intermittent operations, i.e. at a sliding distance of 122 m, the difference between 4 and 8 % fluorine content after 174 m, and the difference between 1 % and 4 % after 280 m. Therefore, the test segments between 280 m and 470 m were considered to represent the steady states of the experiments. Figure 4.13 and Table 4.2 show the 95 % CIs of the COF of the four investigated waxes and for the unwaxed ski base. The data shows that all waxes reduce friction compared to the unwaxed ski base, and that the fluorine content significantly impacts this reduction. These observations are consistent with long-term experience from field testing and competition, as confirmed by the German Ski Association.

Table 4.2: Average steady-state COFs of the fluorine content test series

Experiment number	Unwaxed	ZR 41 (0 %)	GT 20 (1 %)	H5LF (4 %)	ZR NS (8 %)
1	0.0247	0.0204	0.0188	0.0137	0.0109
2	0.0242	0.0178	0.0171	0.0148	0.0111
3	0.0240	0.0171	0.0173	0.0127	0.0103
4	0.0229	0.0196	0.0168	0.0131	0.0108
5	0.0231	0.0189	0.0158	0.0145	0.0109
6	0.0231	0.0188	0.0152	0.0127	0.0105
<b>Standard deviation</b>	0.0007	0.0012	0.0012	0.0009	0.0003
<b>95 % CI</b>	0.0237 ± 0.0008	0.0188 ± 0.0013	0.0168 ± 0.0013	0.0136± 0.0009	0.0108 ± 0.0003

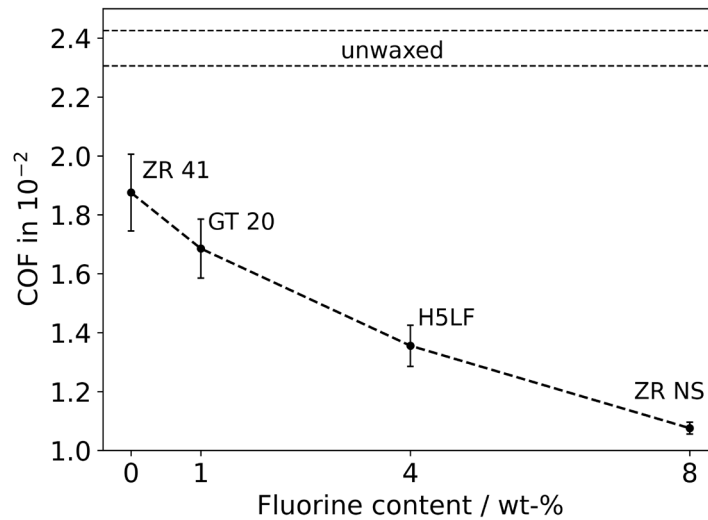


Figure 4.13: Impact of fluorine content of the applied waxes on the steady-state COF (95 % CI). The horizontal dashed lines represent the 95 % CI of the COF of the unwaxed ski base.

To verify the significance of the results, a two-tailed hypothesis test was performed for all wax combinations. The null hypothesis  $H_0$  to be tested assumed, that the friction forces are comparable in their mean value and therefore no significant difference exists. This leads to the mathematical expression of the null and alternative hypothesis  $H_0 : \bar{x}_1 = \bar{x}_2$  and therefore  $H_1 : \bar{x}_1 \neq \bar{x}_2$ . Assuming a 95 % significance level, the rejection region  $Z$  is defined as  $Z \leq Z_{-0.5}$  and  $Z \geq Z_{0.5}$ . With a degree of freedom of 10 ( $2 \times n - 2$ ) the rejection zone yielded a value of 2.228 based on the t-distribution [126]. According to Eqn. 4.1, the Z-score is calculated for each wax combination and compared with the rejection zone [127].

$$Z = \frac{\bar{x}_1 - \bar{x}_2}{\sqrt{\frac{\sigma_1^2 + \sigma_2^2}{n}}} \quad \text{Eqn. 4.1}$$

With:

- Z - Z-score
- $\bar{x}_i$  - Mean sample force
- $\sigma_i^2$  - Variance
- n - Sample rate

Table 4.3 presents the Z-scores of the different combinations. The rejection of the null hypothesis  $H_0$  could be demonstrated for all combinations. The observed difference is therefore significant, and the order of suitability derived from this hypothesis can thus be considered objectively proven.

Table 4.3: Hypothesis test

Combination	Z-Score	Response to $H_0$	
Unwaxed – ZR 41	8.487	False	✓
Unwaxed – GT 20	11.532	False	✓
Unwaxed – H5LF	21.097	False	✓
Unwaxed – ZR NS	39.335	False	✓
ZR 41 – GT 20	2.772	False	✓
ZR 41 – H5LF	8.517	False	✓
ZR 41 – ZR NS	15.965	False	✓
GT 20 – H5LF	5.182	False	✓
GT 20 – ZR NS	11.620	False	✓
H5LF – ZR NS	7.268	False	✓

The data indicates that every wax reduces friction compared the unwaxed ski base and that the wax' fluorine-content, which wasn't disclosed numerically by its manufacturer, significantly reduces friction between ski base and ice at the chosen test conditions. It has been confirmed by the German Ski Association that this observation is in accordance with long-term experience from field testing and competition [108].

#### 4.5.2 Surface roughness

Breitschädel investigated the influence of waxing on the surface roughness of ski bases and did not find any significant impact [81]. However, there are very few reports in

the literature on this question. Therefore, it was also investigated in this work in a separate test series, which aimed at elucidating the evolution of the surface roughness parameters of the ski-base and of the ice as well as the evolution of the wear-related height loss within the wear track on the ice as a function of sliding distance, Table 4.4 shows the results of the surface profilometry investigations. The change in surface parameters  $R_a$ ,  $R_z$  and  $R_t$  of the ice cast, the unwaxed ski base, and the waxed ski base as a function of sliding distance were thus determined and the 95 % CI were plotted for all parameters.

Table 4.4: Numeric results of the roughness measurements of the ice sample and additionally the unwaxed and waxed ski bases before (0 m) and after the tribometer experiments (20 m - 470 m)

		Sliding distance in m				
		0	20	140	280	470
Ice	$R_a / \mu\text{m}$	0.26 ± 0.20	0.33 ± 0.06	0.33 ± 0.03	0.46 ± 0.06	0.59 ± 0.15
	$R_z / \mu\text{m}$	1.22 ± 0.11	1.78 ± 0.32	2.57 ± 0.37	3.67 ± 0.50	4.41 ± 0.57
	$R_t / \mu\text{m}$	2.03 ± 0.36	3.17 ± 0.55	5.20 ± 1.29	7.83 ± 1.26	15.90 ± 2.50
Unwaxed	$R_a / \mu\text{m}$	0.82 ± 0.06	0.92 ± 0.07	0.93 ± 0.09	0.90 ± 0.07	0.91 ± 0.10
	$R_z / \mu\text{m}$	5.15 ± 0.41	5.05 ± 0.27	4.84 ± 0.38	5.08 ± 0.27	5.27 ± 0.40
	$R_t / \mu\text{m}$	7.46 ± 0.92	7.49 ± 1.42	7.31 ± 0.78	7.02 ± 1.00	7.20 ± 0.92
ZR 41	$R_a / \mu\text{m}$	0.67 ± 0.10	0.69 ± 0.10	0.71 ± 0.12	0.77 ± 0.11	0.71 ± 0.07
	$R_z / \mu\text{m}$	3.23 ± 0.39	2.82 ± 0.32	3.35 ± 0.20	3.44 ± 0.54	3.58 ± 0.42
	$R_t / \mu\text{m}$	3.12 ± 0.42	3.91 ± 0.55	5.28 ± 1.07	4.86 ± 0.87	4.93 ± 0.85
GT 20	$R_a / \mu\text{m}$	0.60 ± 0.09	0.70 ± 0.10	0.69 ± 0.11	0.70 ± 0.10	0.65 ± 0.06
	$R_z / \mu\text{m}$	3.17 ± 0.28	3.20 ± 0.31	3.54 ± 0.30	3.49 ± 0.35	3.54 ± 0.33
	$R_t / \mu\text{m}$	4.40 ± 0.76	4.45 ± 0.66	5.16 ± 0.97	4.80 ± 0.44	4.92 ± 0.89
H5LF	$R_a / \mu\text{m}$	0.60 ± 0.11	0.52 ± 0.03	0.46 ± 0.03	0.60 ± 0.08	0.76 ± 0.08
	$R_z / \mu\text{m}$	2.47 ± 0.25	2.85 ± 0.32	3.04 ± 0.20	3.09 ± 0.39	3.80 ± 0.23
	$R_t / \mu\text{m}$	3.33 ± 0.40	4.68 ± 1.51	5.75 ± 1.03	4.48 ± 0.79	4.41 ± 0.90
ZR NS	$R_a / \mu\text{m}$	0.68 ± 0.13	0.63 ± 0.06	0.77 ± 0.09	0.65 ± 0.14	0.61 ± 0.06
	$R_z / \mu\text{m}$	3.57 ± 0.22	3.18 ± 0.33	3.24 ± 0.26	3.72 ± 0.34	3.60 ± 0.40
	$R_t / \mu\text{m}$	4.58 ± 0.80	4.89 ± 0.68	5.47 ± 0.68	4.85 ± 1.07	4.94 ± 1.16

Figure 4.14 shows two 3D profile scans of an unwaxed ski base (left) and of a base that was freshly waxed with H5LF (right). Above these two, y-averaged projections of the 3D profiles are also shown.



The grooves in the y-direction originate from the original peeling process and can be seen for the unwaxed and the waxed sample. Because the differences in surface roughness are rather subtle and not perfectly obvious to the naked eye, additional line measurements were made for the unwaxed ski base and for the ice sample as well as for all investigated waxes as shown in Figure 4.15. For each, 10 lines at random positions were recorded. From these scans, surface texture parameters according to DIN EN ISO 4287 were determined.

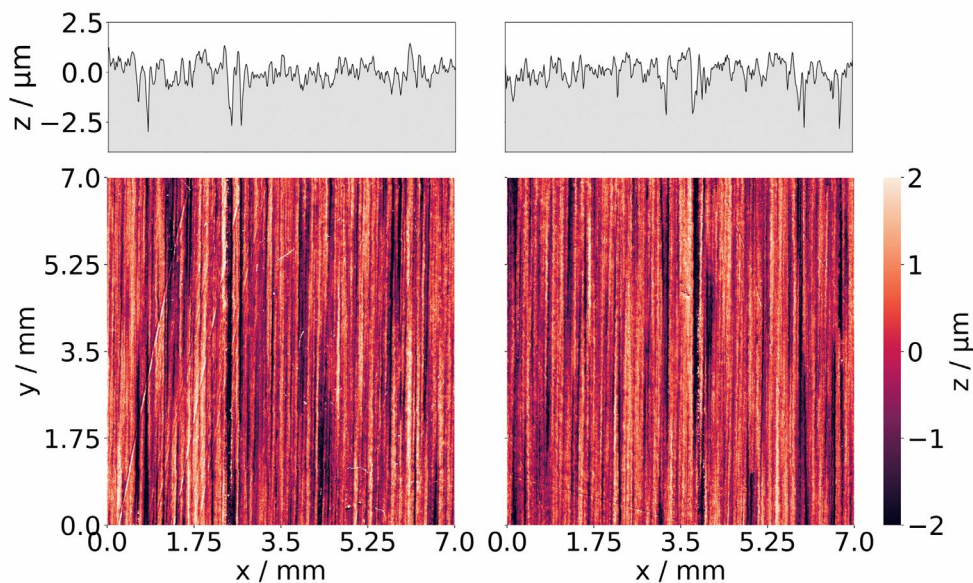


Figure 4.14: 3D-Scan of the unwaxed ski base (left) and as an exemplary representation waxed with H5LF (right)

The surface parameters  $R_a$ ,  $R_z$  and  $R_t$  clearly show that waxing significantly reduce surface roughness. While this was true for all four investigated waxes and for all computed parameters, no significant differences between the individual waxes were found. Furthermore, they indicate that, on the ski side, changes in surface roughness mainly happen in the very early phase of the experiment, i.e., between 0 m and 20 m. But even then, the changes are not statistically significant. After 20 m, surface roughness does not change significantly as sliding distance increases. This agrees with the COF vs. sliding distance data shown in Figure 4.12, which also shows a weak breaking-in effect and then a more or less stable steady state. In contrast to this, for the ice sample,

all three surface texture parameters increased as the sliding distance increased. This clearly indicates that there must have been significant solid-solid interaction between the ski base and the ice. Notably, the surface of the ski base was much less roughened than the surface of the ice sample. This is consistent with the observations from Figure 4.1 which shows that grooves were formed on the ice surface as a result of the ski base continuously sliding over it.

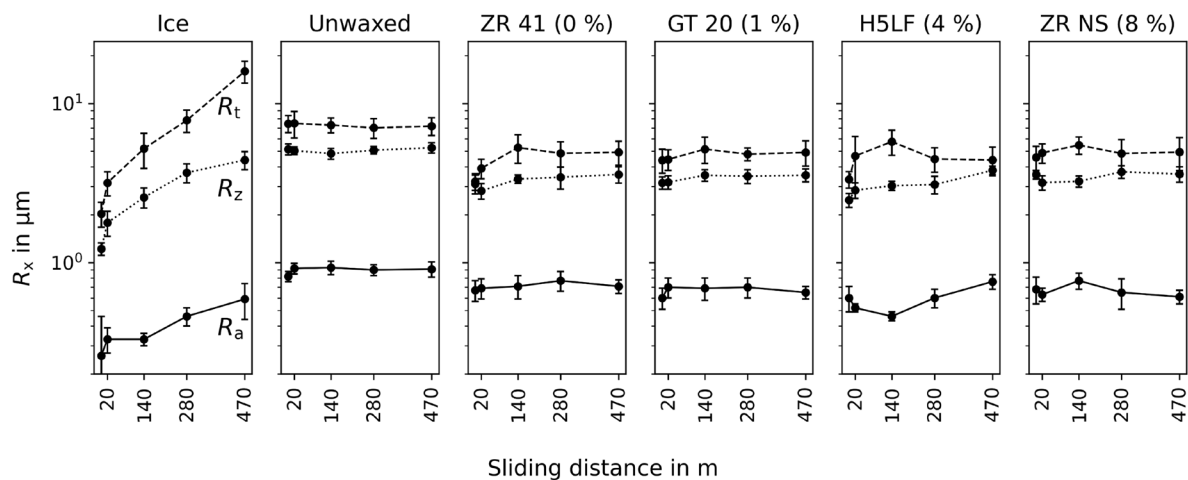


Figure 4.15: Roughness comparison of different waxes with the unwaxed ski base and ice surface (CI = 95 %)

In order to quantify the change in surface roughness and the wear-related height loss, silicone casts were produced at every sliding distance interval, i.e. at 20 m, 140 m, 280 m and 470 m. This caused a delay that would have allowed any formed water to resolidify by the time the casts were made, potentially affecting the results. Figure 4.16 shows exemplary line scans that show the evolution of such grooves with increasing sliding distance.

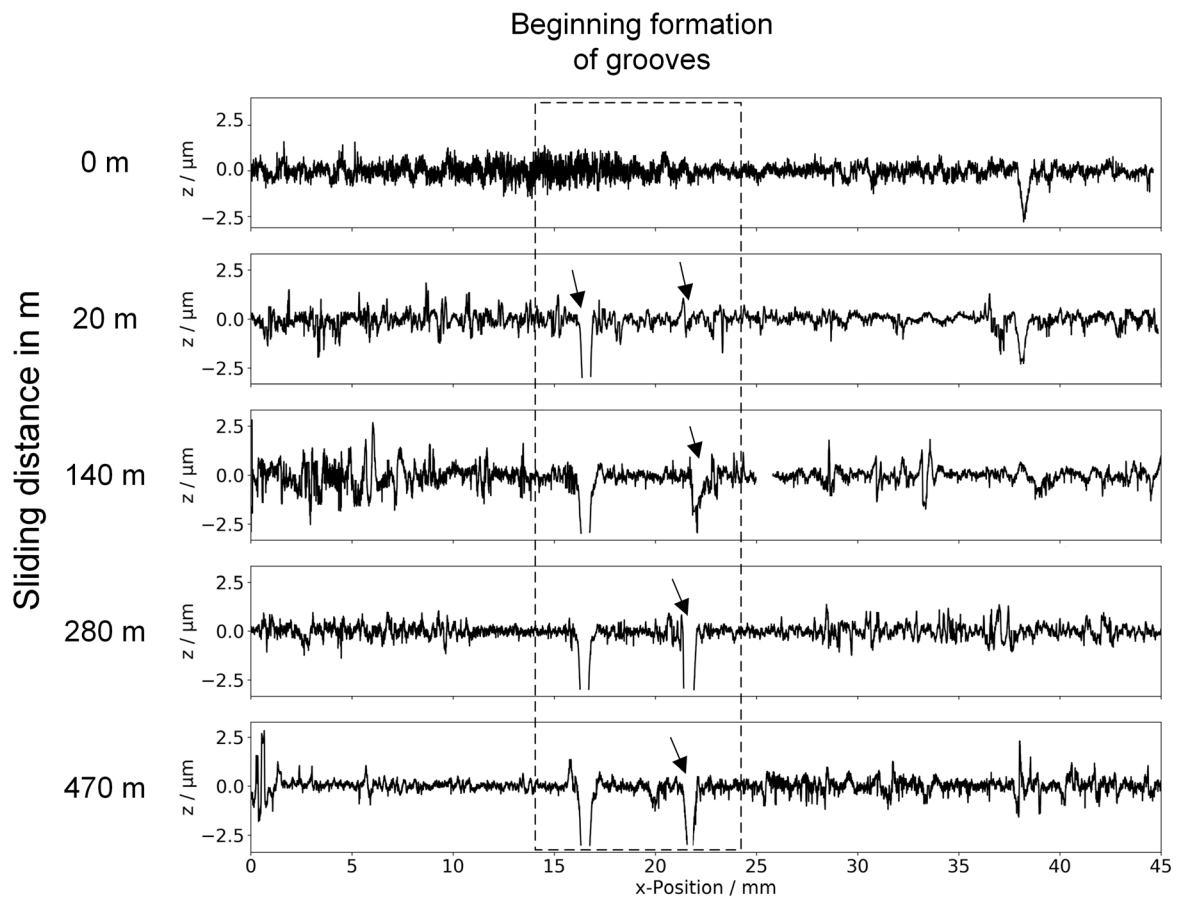


Figure 4.16: Formation of grooves on the ice sample with increasing sliding distance

### 4.5.3 Surface structure

A systematic variation regarding the surface structure of the ice samples was not possible within the scope of this work. In the literature, only few data on the effect of a surface structuring can be found, and if so, only a description of the surface conditions in qualitative terms (smooth, fine, course, etc. [19]). However, the effect of an ice surface modification was still investigated. The surfaces of the ice samples were treated with 180 grit fleeces to determine a possible effect. At  $-6\text{ }^{\circ}\text{C}$ ,  $2.42\text{ kPa}$  and  $9\text{ m/s}$ , a total of 15 trials were conducted for each surface modification and ice mould, see also Table 4.1. To prevent a shift, the ice mould was interchanged between the individual segments. Two-sided hypothesis tests showed that there was no statistically significant

difference in the averages and standard deviations between the untreated and structured ice samples.

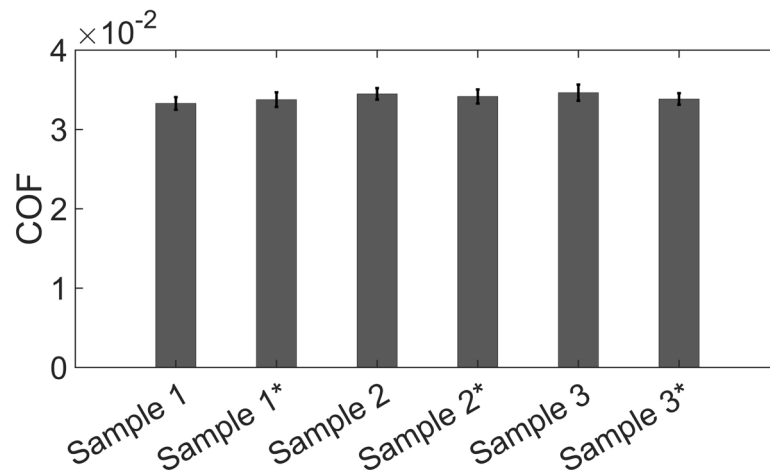


Figure 4.17: Surface structure modification (sample 1\* - 3\*) at  $p = 2.42$  kPa,  $v = 9$  m/s and  $T = -6$  °C

#### 4.5.4 Wear-related surface alteration

Figure 4.18 shows that the increase of sliding distance also causes a steady and significant increase of the wear related height loss as sliding distance increases. At 20 m, the height loss was below the detection limit of the utilized evaluation procedure, and therefore no data could be obtained for this sliding speed.

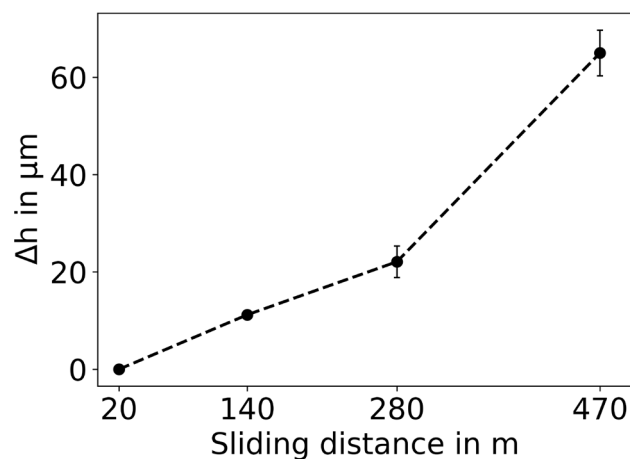


Figure 4.18: Wear-related height loss as a function of sliding distance with a CI of 95 % (perpendicular mode, refer to Figure 4.3)

However, afterwards there was a steady and significant increase in the wear-related height loss as the sliding distance increased. At 470 m, the total height loss of 65  $\mu\text{m}$  corresponds to a total volume loss of  $0.065 \text{ mm} \times 120 \text{ mm} \times 100 \text{ mm} = 780 \text{ mm}^3$  (see Figure 3.20, right). Consistent with this large volume loss, fine ice powder abrasion was observed. However, this powder was not stable and, presumably due to the low humidity in the cooling cell and its very large surface-to-volume ratio, dissipated rather quickly. Therefore, it could not be collected for weighing and validation of the profilometric results. These findings support the conclusion that can be drawn from the profilometric investigations, i.e., the lubrication regime in our experiments was mixed lubrication with significant contributions from solid-solid contacts. While the observed height loss could also occur due to melting and subsequent hydrodynamic sliding, the formation of grooves and the increase in surface roughness are incompatible with the assumption of hydrodynamic lubrication and instead indicate the prevalence of solid-solid interaction. This conclusion is also in agreement with the observed COFs (see Figure 4.12 and Figure 4.13), which are all above the 0.01 threshold typically used to discern mixed from hydrodynamic lubrication.

#### 4.5.5 Contact angle measurements

It is known from field trials and from experience from competition that the friction reducing effect of waxes wears off after a certain sliding distance, which typically starts at about two to four kilometres. The reason for this is the gradual removal of the wax from the ski base and the adhesion of impurities that have been gathered from the snow track [81,128,129]. Therefore, in order to quantify any potential wax degradation during the experiments, the contact angle between the ski base and water and diiodomethane were determined after each sliding interval as described in chapter 4.2. This was done intermittently after 20, 140, 280, and 470 m, i.e., together with the profilometric measurements when the ski base was removed from the tribometer. The ice samples used degrade with excessive use. To exclude effect overlap, the maximum sliding distance was set at 470 m to ensure comparability. Figure 4.19 shows the surface free energy as a function of the sliding distance of the unwaxed and waxed bases.

The unwaxed ski base shows the highest free energy, whereas the wax with the highest fluorine content (ZR NS) exhibited the lowest free energy over the entire sliding distance, with the ZR 41, GT 20 and H5LF waxes in between.

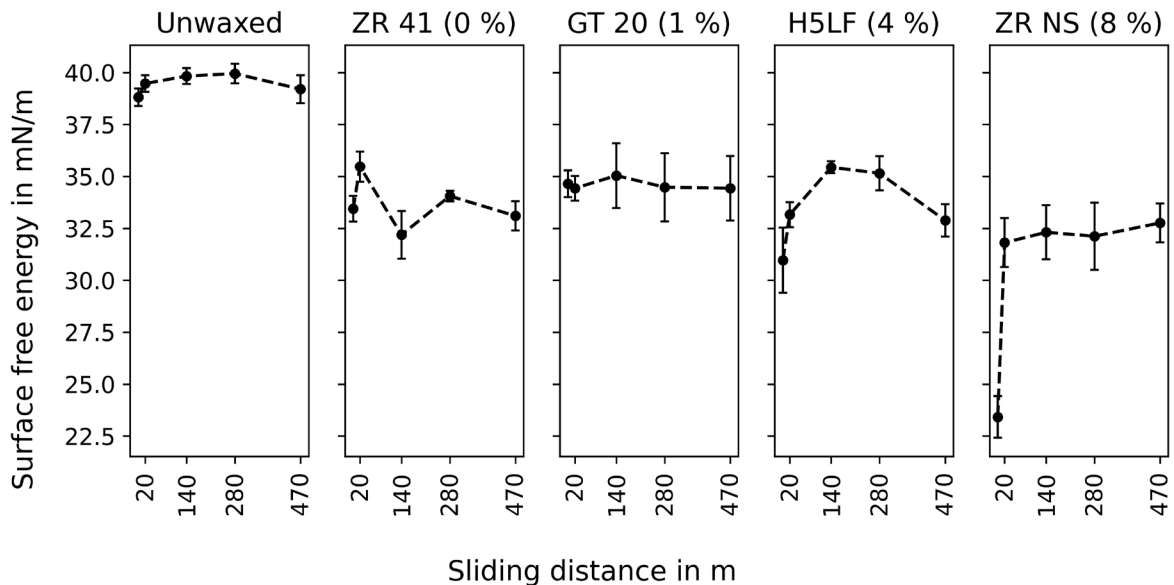


Figure 4.19: Surface free energy as a function of sliding distance (95 % CIs)

Comparing the surface free energy data to the COF data from Figure 4.13 shows a correlation between the COF and surface free energy after the base has been prepared (see Figure 4.20). However, if the surface free energy is not averaged over the entire sliding distance (as in Figure 4.20) and only the values at 280 m and 470 m are considered, the correlation remains, but the differences between the individual waxes become smaller. The differences in the COF, which are still pronounced after 470 m, are now offset by very small differences in surface free energy, making it a less reliable predictor of the COF than Figure 4.20 suggests. Therefore, tribometer tests such as those presented in this work remain the only reliable tool, apart from field tests, for quantifying the friction-reducing potential of a wax.

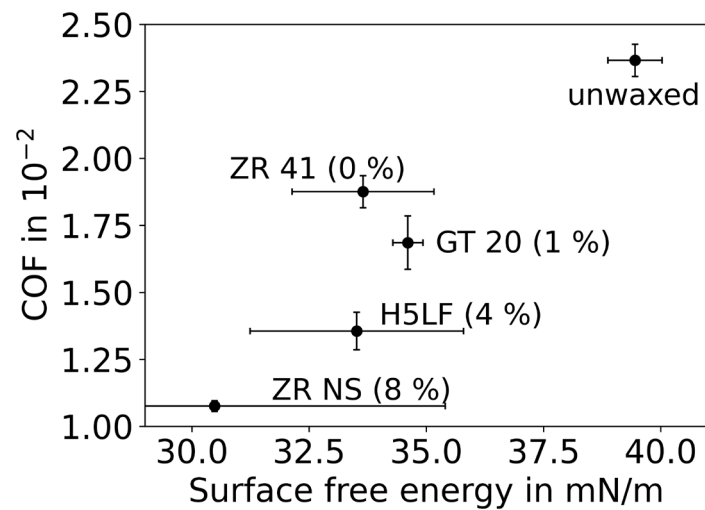


Figure 4.20: Correlation between the COF in steady-state (see Figure 4.13) and the average surface free energy (see Figure 4.19)

#### 4.5.6 Sliding speed and temperature

In order to investigate the influence of sliding speed on the COF, experiments were conducted with sliding speeds of 1.5, 3.0, 9.0, and 14.0 m/s with a contact pressure of 2.42 kPa, see also Table 4.1. The acceleration was 11 m/s<sup>2</sup> for all tests, and the constant speed duration was 1.2 s in all cases, resulting in total sliding distances of 24.2, 50.6, 228.8, and 295.9 m, respectively. The steady-state COFs were determined using the last 10 % of the total sliding distance. These tests were performed at air temperatures of -2 °C, -4 °C, and -19 °C to investigate the influence of temperature. The results of these experiments are shown in Table 4.5 and Figure 4.21. As the ice temperature decreased, the COF increased for all sliding speeds. This might be because, at lower temperatures, the dissipated frictional energy produces less molten water that can form a water film. Therefore, solid state friction may contribute to a higher extent at lower temperatures. Additionally, the COF increased with increasing sliding speed due to the viscoplasticity of ice, which increases shear stress as shear rate increases [130]. This observation and explanation have been made by other tribologists as well [42,44,131]. The increase in surface roughness during sliding, as seen in Figure 4.15, suggests that

an increase in adhesion is unlikely to contribute to the observed increase of COF with increasing sliding speed.

Table 4.5: Numeric COF results of sliding speed vs. temperature (CI 95 %)

		Sliding speed in m/s			
		1.5	3	9	14
Temperature in °C	-4	0.0124 ±0.0008	0.0145 ±0.0011	0.0431 ±0.0034	0.0473 ±0.0043
	-12	0.0209 ±0.0013	0.0330 ±0.0019	0.0511 ±0.0048	0.0546 ±0.0042
	-19	0.0245 ±0.0015	0.0385 ±0.0022	0.0878 ±0.0072	0.0942 ±0.0056

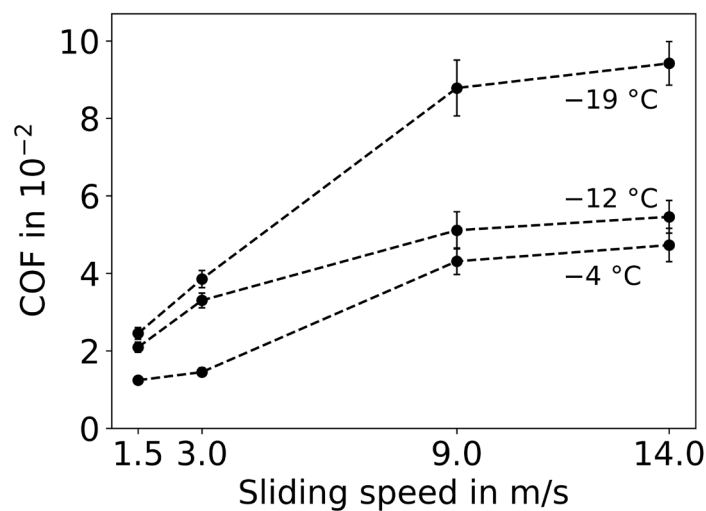


Figure 4.21: COF as a function of sliding speed and temperature (CI = 95 %)

#### 4.5.7 Acceleration and deceleration

In order to investigate the influence of the acceleration on the COF, experiments were conducted at an ambient temperature of -6 °C with a contact pressure of 4.2 kPa. The acceleration to a sliding speed of 3 m/s was varied to 3, 5, 10 and 15 m/s<sup>2</sup>, as can be seen in Table 4.1. This caused the acceleration distance to vary between 1.5, 0.9, 0.45 and 0.3 m. Each experiment consisted of 3 intermittent operations and with a steady constant speed duration of 1 s, the total sliding distance changed between 15.3, 13.5,



12.15, and 11.7 m. A total of 3 experiments were conducted per mould, resulting in 9 experiments per acceleration set. It should be noted that changing the acceleration results in an increase in the total sliding distance. As previously shown in Figure 4.12, the sliding distance influences the COF and possible effects of the acceleration variation could be superimposed. Table 4.6 presents the friction results of these experiments as 95 % CIs, and Figure 4.22 plots them as a function of acceleration variation.

Table 4.6: Numeric COF results of ski base acceleration

Experiment number	Acceleration in m/s <sup>2</sup>			
	3	5	10	15
1	0.02716	0.02605	0.02574	0.02521
2	0.02691	0.02596	0.02516	0.02441
3	0.02599	0.02570	0.02452	0.02450
<b>Standard deviation</b>	0.00050	0.00015	0.00050	0.00036
<b>95 % CI</b>	0.02669 ± 0.00125	0.02590 ± 0.00037	0.02514 ± 0.00124	0.02471 ± 0.00089

During the test series, a slight decrease of the COF with increasing acceleration was observed. This can be explained by the higher energy input and thus a variation within the friction regime due to partial melting of the surface. However, compared to the change in ambient temperature and contact pressure as shown in Figure 4.21, the influence of acceleration is not very pronounced. By means of two-sided hypothesis tests, a statistically significant difference in the averages could only be detected between the variations 3 m/s<sup>2</sup> - 5 m/s<sup>2</sup>, 5 m/s<sup>2</sup> - 10 m/s<sup>2</sup>, and 5 m/s<sup>2</sup> - 15 m/s<sup>2</sup>.

No significant difference was found in the standard deviations. In order to keep the acceleration influence at a constant level, the acceleration was kept uniform for the remaining investigations of the friction influencing parameters.

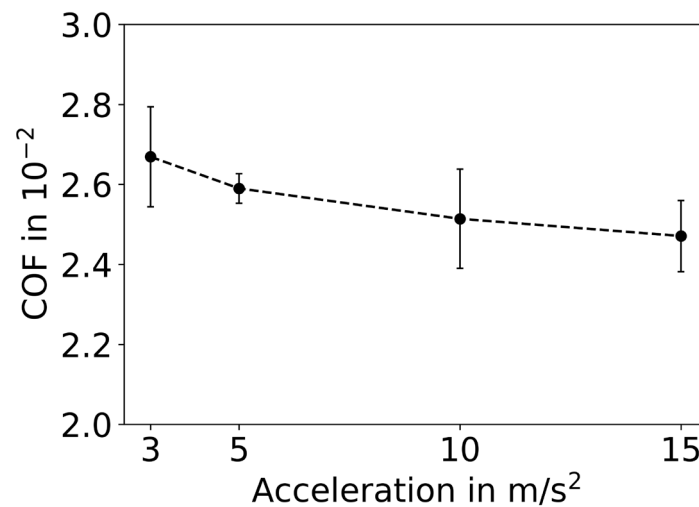


Figure 4.22: Effect of acceleration on COF at  $v = 3$  m/s,  $p = 4.2$  kPa,  $T = -6$  °C

Recently, Kalliorinne et al. conducted friction measurements of skis sliding on snow and found that the COF was higher during the acceleration phase compared to the deceleration phase [132]. In order to investigate this phenomenon, a series of analogous tests were conducted in this study. The sliding speeds in the tests were set to 3, 6, or 9 m/s, while the corresponding accelerations were 3, 6, and 9  $m/s^2$ , respectively. This resulted in an acceleration phase of 1 s in each test. The deceleration phase matched the acceleration phase in terms of magnitude, resulting in a trapezoidal shape of the speed vs. time curve (ramp-up/ramp-down experiment). The CSD was set to 1.5 s and ISL to 30 s (compare Table 4.1). For each acceleration value, 20 segments were performed. To prevent running-in effects from leading to false positives, the overall 60 segments were conducted in a randomized order. Additionally, the ice sample was changed after 30 segments to minimize any potential sample-specific effects. Figure 4.22 shows an exemplary result of such a test.

In contrast to the findings of Kalliorinne et al., the experiments conducted in this study revealed a lower friction during the acceleration phase compared to the deceleration phase as shown in Figure 4.24. This observation was consistent across all three applied accelerations.

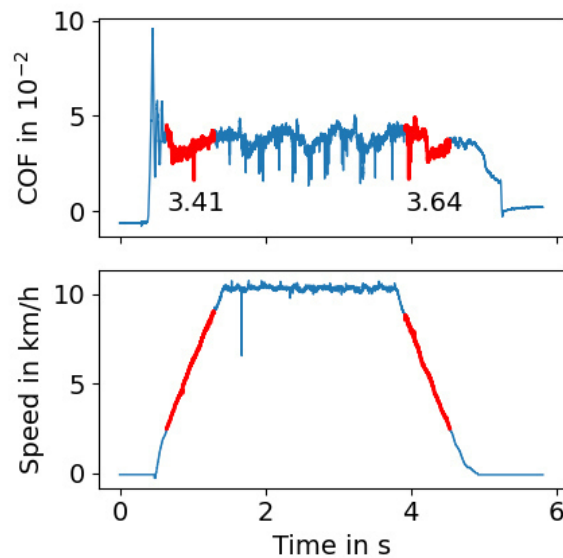


Figure 4.23: Exemplary result of a ramp-up/ramp-down-experiment to verify the difference in COF between acceleration and deceleration. The red sections indicate the areas where the COFs were determined for the two phases. The two numbers indicate the COFs that were calculated for this specific curve.

One possible explanation for this discrepancy could be attributed to the differences in the experimental setup. Specifically, in the tribometer used in this study, the friction force transducer remained stationary, whereas in the case of Kalliorinne et al., it was accelerated together with the ski. In addition, the acceleration and deceleration phases of the experiments had significantly different height, speed, and acceleration profiles. Therefore, not only the absolute values of the acceleration and deceleration were different during the two distinct stages of their experiments, but also the average sliding speeds. Given the significant dependency of the COF on sliding speed found in this work (cf. Figure 4.21), it seems reasonable to assume that sliding speed could have had an impact on the COF in their experiments as well. Thus, the observed differences must not have been solely due to the question of acceleration or deceleration but rather a question of different sliding speeds. Additionally, although neither the present study nor Kalliorinne's study explicitly investigated the formation of meltwater films, it can be assumed that the very different experimental setups and environmental conditions

could have led to differences in this respect as well. It is worth noting that further investigation and analysis are required to fully understand the underlying factors contributing to the observed differences in the COF during acceleration and deceleration phases.

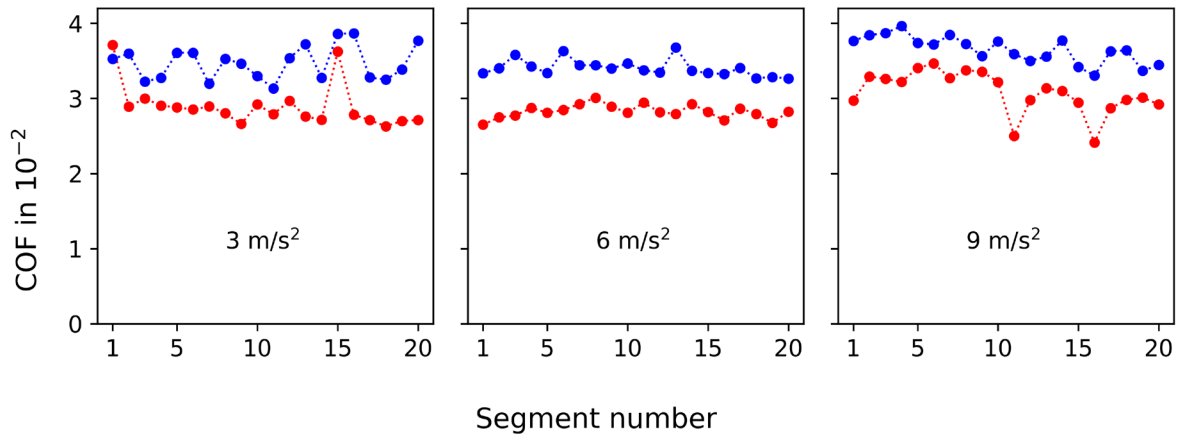


Figure 4.24: COF during acceleration (red dots) and deceleration (blue dots) for 20 test segments

#### 4.5.8 Contact pressure

In order to investigate the influence of contact pressure on the COF, experiments were conducted at an ambient temperature of  $-6 \text{ }^\circ\text{C}$  with contact pressures of 1.21, 2.42, 3.33, 4.24, 6.88, and 8.75 kPa. The acceleration to a sliding speed of 3 m/s was  $11 \text{ m/s}^2$  for all tests, and the constant speed duration was 1.33 s in all cases as shown in Table 4.1. Each experiment consisted of 3 intermittent operations, resulting in a total sliding distance of 14.1 m per experiment. A total of 3 experiments were conducted per mould, resulting in 9 experiments per pressure. Table 4.7 presents the results of these tests as 95 % CIs, and Figure 4.25 plots them as a function of the contact pressure. The observed decrease in the COF with increasing pressure is consistent with the findings of other researchers [32,42,44,45]. This decrease is also consistent with the elastic deformation of asperities within the real contact area, which is a well-known characteristic of many polymers [133], and in particular of UHMWPE, the material from which the ski base of this study is made [55]. Elastic asperity deformation has also been described for ice [67]. An alternative hypothesis involving a reduction of the COF due to an increasing amount of melt water and thus increasing frictional energy with

increasing pressure can be rejected, as this should also have been observed in the velocity-variable experiments, which was not the case. Additionally, Albracht et al. observed a decrease in the COF for PTFE sliding on ice at  $-10\text{ }^{\circ}\text{C}$  with increasing pressure at a sliding speed of only  $0.262\text{ m/s}$  and at normal forces of only  $3 - 7\text{ N}$  [44], supporting the idea that the observed decrease in the COF in this study is most likely due to elastic contact deformation and not increased melting. This is in agreement with the results of Bäurle et al. from 2006 [19,45].

Table 4.7: 95 % CIs of the COF from contact pressure study ( $T = -6\text{ }^{\circ}\text{C}$ ,  $v = 3\text{ m/s}$ )

Experiment number	Contact pressure in kPa					
	1.2	2.4	3.3	4.2	6.9	8.8
1	0.02441	0.02412	0.02419	0.02374	0.02047	0.02258
2	0.02577	0.02370	0.02455	0.02418	0.02152	0.02158
3	0.02611	0.02501	0.02370	0.02540	0.02299	0.02182
<b>Standard deviation</b>	0.00073	0.00054	0.00035	0.00070	0.00103	0.00043
<b>95 % CI</b>	0.02543 $\pm 0.00182$	0.02428 $\pm 0.00135$	0.02415 $\pm 0.00087$	0.02444 $\pm 0.00175$	0.02166 $\pm 0.00257$	0.02199 $\pm 0.00106$

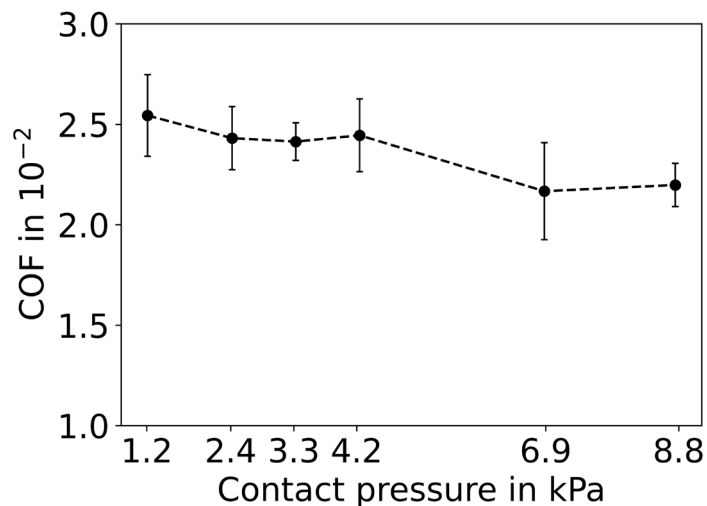


Figure 4.25: COF of the unwaxed ski base sliding against ice at different contact pressures



## 5 Limitations

Currently, the tribometer's sample holder is designed only to accept ice plates. While this makes the results highly relevant for ski jumping, the question arises as to how applicable they are to the broader field of alpine skiing, which primarily takes place on compacted snow. This design decision was deliberate, as ice is easier to produce and handle in a laboratory, and it is less susceptible to changes in morphology caused by compaction from multiple passes. Using the tribometer with samples of compacted snow would require the development of a suitable sample holder and the introduction of snow handling and processing equipment and procedures within a laboratory, which are currently unavailable. However, this represents an interesting topic for future investigations, particularly since compacted snow becomes more similar to ice in terms of microstructure and COF as it undergoes multiple pass-overs [19,49]. A common issue in ski jumping is collisions between the side walls of the ski and the side walls of the track. Although this study did not investigate this problem, it could be addressed by using the materials of the track's side walls instead of the ice sample. However, it remains to be determined whether the material used for the ski's side wall could be manufactured into a closed belt that can withstand the necessary tensile stress.

Although the tribometer is designed to operate at speeds up to 28 m/s, vibrations currently limit its practical speed range to 14 m/s. Future work is required to either reduce the generation of vibrations, such as by decoupling the drive and the rollers through a belt drive, or to improve vibration damping more effectively. One possible approach would be to optimize the adhesive joint. Despite the current speed limitation, which only covers the early portion of a ski jump, the presented results are still relevant, especially for assessing ski waxes and developing novel fluorine-free low friction waxes.

Due to the uneven load distribution below the roller plate, the true local contact pressure acting on the ice sample is unknown. One approach could be the installation of a locally resolving pressure measuring plate between the ski base and the ice sample with measurement technology prepared for low temperatures.

Finally, as the COF has been found to increase under a wide range of testing conditions (see Figure 4.21), the upper end of the load cell's measurement range is reached

at speeds above 14 m/s. In the future, this limitation needs to be addressed by using a load cell with a wider measurement range.



## 6 Summary

The overview of literature on ice friction has shown that not all factors influencing friction on ice or snow and their sliding effects are yet fully understood. Further academic research is required to identify and thoroughly comprehend all physical mechanisms. The analytical review of the existing tribometer variants revealed that no currently available tribometer using ice or snow samples can be reliably used to distinguish waxes with regard to their sliding behaviour. At present, selection of waxes, grinds etc. still has to be done solely based on field and indoor tests. Full-size ski systems require large investments and must be able to operate with high accelerations in order to bring the ski up to speed in just a few metres. Test rigs that use smaller ski base samples perform measurements with forces, surface pressures and speeds that are far from the reality seen in competition. Therefore, valid predictions of wax performance are difficult to achieve.

In order to bridge the gap between field tests and reliable friction results from laboratory tests, a concept for a linear tribometer was methodically developed, designed and submitted for manufacture. Its main novelty, compared to existing snow or ice tribometers, is the utilization of a full-size ski base as a test specimen within a laboratory-scale tribometer. The methodical design included the definition of the necessary sub-function requirements for the assemblies based on a specification list. Using a methodical approach, partial solutions were developed and evaluated with the help of weighting factors. A previously conducted feasibility study helped to identify weak points for the final solution variant, and based on these results, the concept with the highest evaluation score was passed on to manufacturing. The plate-on-plate test rig is located in a cooling cell and uses a full-size ski base which is shafted at the ends, glued and thereby connected to form an endless band. Similar to a conveyor belt, two rollers rotate the base under tension. A mechanism with mounted rubberised rollers transmits the normal force to the ski base and to the ice sample underneath. The normal force can be adjusted by dead weights on a lever arm and thus leads to different surface pressures under the ski base. The deflection of the ice sample due to the generated friction leads to actuation of a load cell, which is spring-preloaded with the ice sample on a sliding carriage. Testing parameters such as speed, acceleration, ambient temperature and

surface pressure can be set in the range relevant to skiing. The tribometer is capable of measuring not only typical ski jumping base lengths and widths but also cross-country and alpine bases and can therefore be used across all ski disciplines.

Extensive trial experiments have been conducted to determine its precision, resolution, and linearity for measuring the COF and the impact of the individual ice sample-manufacturing moulds on the measurement of the COF. Overall, these tests confirmed the operational capability and suitability of the tribometer. Furthermore, a series of experiments were performed to elucidate the impact of the fluorine content of selected waxes on the COF. To find the average friction force of a particular wax, consecutive measurements were carried out and the friction forces were recorded in the constant speed range. For each wax modification, the procedure was repeated a total of six times. Finally, the corresponding overall mean value for each wax was determined over the range of the steady-state region and the COF was calculated. With a confidence of at least 95 %, the differences in the mean friction force between the measured waxes as a function of their fluorine content could be validated and proven. Throughout the experiments conducted, white light profilometry has shown that the surface roughness of the ice significantly increases during sliding and that grooves form over time. In combination with a clearly measurable height loss of the wear track on the ice sample, abrasion has been found as the predominant wear mechanism, especially since the utilized test parameters do not produce melt water at an elevated rate. At the same time, a correlation was found between the wax-induced change of surface free energy and the COF in the steady state. Thus, the hypothesis is supported that the hydrophobic effect of the wax, which is clearly related to the fluorine content of the wax, has a noticeable influence on the COF. Moreover, this remains consistent with the presence of mixed friction with high contributions to friction from asperity interaction. The suitability ranking of the waxes observed in steady state, with respect to their friction-mitigating effect agrees perfectly with observations and empirical data obtained from competition and field testing.

For the first time, it was demonstrated that waxes can be differentiated with regard to their fluorine content on a tribometer. Furthermore, the suitability order of the German Ski Association and the wax manufacturer could be reproduced. While a partial corre-

lation between contact angle and COF has been observed, contact angle measurements cannot be used as the sole predictor for the ability of a specific wax to reduce friction effectively.

Given the selected experimental conditions, the profilometric investigations clearly showed mixed lubrication with pronounced solid contact as the superior lubrication regime. The presence of partial solid contact clearly led to measurable abrasion and roughening of the ice surface. Nevertheless, stationary friction conditions could be reproducibly established. At the same time, a correlation was found between the wax-induced change of surface free energy and the coefficient of sliding friction in the steady-state. This is a clear indication that the hydrophobic effect of the wax at the specified conditions, being related to the fluorine content of the wax, has a noticeable influence on the coefficient of sliding friction. Furthermore, this is consistent with the presence of mixed friction. Additional tests have elucidated the impact of sliding speed, temperature, contact pressure, acceleration, and deceleration on the COF. The results also support the hypothesis that the novel tribometer, when operated according to the results of the parameter trials, produces a mixed friction lubrication regime with significant contribution from asperity interaction. This is most likely why it has been so successful in highlighting the difference between the individual waxes in such a significant way.

The new laboratory tribometer accommodates entire ski bases, maintains realistic surface pressures and thus ensures that the measured friction forces have a reasonable signal-to-noise ratio. The rapid ice sample replacement eliminates the need for time-consuming ice surface preparation and permits testing of various waxes consecutively and comparing their performance with each other. This and the fast conversion to different ski dimensions is a novelty compared to the existing tribometers. The developed tribometer represents a reliable tool for the selection of wax candidates for a new era of novel fluorine-free waxes and for assessing them in terms of their sliding performance.



## References

- [1] Carmigniani, R.; Cao, X.; Savourey, S.; Martinier, C.; Nuytten, S.; Margarit, A.; Jaulmes, L.; Clanet, C. *Ski Jump Flight*, 2012, 100–107.
- [2] FIS - International Ski Federation. *The International Ski Competition Rules (ICR): Book III Ski Jumping*, 2018.
- [3] Gasser Hans-Heini. *Jumping Hills Construction-Norm 2018 Implementing Provisions for Art. 411 of the ICR Ski Jumping*.
- [4] Virmavirta, M.; Isolehto, J.; Komi, P.; Schwameder, H.; Pigozzi, F.; Massazza, G. Take-off analysis of the Olympic ski jumping competition (HS-106m). *Journal of Biomechanics* 2009, 42, 1095–1101.
- [5] Hay, J. G. Citius, altius, longius (faster, higher, longer): The biomechanics of jumping for distance. *Journal of Biomechanics* 1993, 26, 7–21.
- [6] Verschleißschutz und Korrosionsschutz. <https://www.ceramtec-industrial.com/de/industrien/verschleisschutz/alotec> (accessed January 27, 2022).
- [7] FIS - International Ski Federation. *Specifications for Competition Equipment, Edition 2019*.
- [8] Quetelet, A. *Recherches sur le poids de l'homme aux différents âges. Nouveaux mémoires de l'Académie Royale des Sciences et Belles-Lettres de Bruxelles* 1832.
- [9] Virmavirta, M.; Kivekäs, J. Is it still important to be light in ski jumping? *Sports Biomechanics* 2019, 1–12.
- [10] Luca Oggiano; Lars Sætran; Margaret Estivalet; Pierre Brisson. Effects of Body Weight on Ski Jumping Performances under the New FIS Rules (P3). *The Engineering of Sport* 7, 2008, pp 1–9.
- [11] Scherge M.; Höfflin J. *Wie entstehen moderne Skischliffe*, Gliding 2020.
- [12] Döppenschmidt, A.; Butt, H.-J. Measuring the Thickness of the Liquid-like Layer on Ice Surfaces with Atomic Force Microscopy. *Langmuir* 2000, 16, 6709–6714.

- [13] Kietzig, A.-M.; Hatzikiriakos, S. G.; Englezos, P. Ice friction: The effects of surface roughness, structure, and hydrophobicity. *Journal of Applied Physics* 2009, 106, 24303.
- [14] Marmo, B. A.; Blackford, J. R.; Jeffree, C. E. Ice friction, wear features and their dependence on sliding velocity and temperature. *J. Glaciol.* 2005, 51, 391–398.
- [15] Ducret, S.; Zahouani, H.; Midol, A.; Lanteri, P.; Mathia, T. G. Friction and abrasive wear of UHMWPE sliding on ice. *Wear* 2005, 258, 26–31.
- [16] Strausky, H.; Krenn, J. R.; Leitner, A.; Aussenegg, F. R. Sliding plastics on ice: fluorescence spectroscopic studies on interfacial water layers in the  $\mu\text{m}$  thickness regime. *Appl Phys B* 1998, 66, 599–602.
- [17] Heinrich, D.; Mössner, M.; Kaps, P.; Nachbauer, W. Calculation of the contact pressure between ski and snow during a carved turn in Alpine skiing. *Scandinavian journal of medicine & science in sports* 2010, 20, 485–492.
- [18] Mössner, M.; Schindelwig, K.; Heinrich, D.; Hasler, M.; Nachbauer, W. Effect of load, ski and snow properties on apparent contact area and pressure distribution in straight gliding. *Cold Regions Science & Technology* 2023, 208, 103799.
- [19] Bäurle, L. Sliding friction of polyethylene on snow and ice, ETH Zurich, 2006.
- [20] Makkonen, L.; Tikanmäki, M. Modeling the friction of ice. *Cold Regions Science & Technology* 2014, 102, 84–93.
- [21] Schindelwig, K.; Hasler, M.; van Putten, J.; Rohm, S.; Nachbauer, W. Temperature Below a Gliding Cross Country Ski. *Procedia Engineering* 2014, 72, 380–385.
- [22] Erik Simon. Personal communication; Pirmasens, 2022.
- [23] Georg Reichert. Personal communication; Pirmasens, 2015.
- [24] Faraday M. XXIV. On regelation, and on the conservation of force. *The London, Edinburgh, and Dublin Philosophical Magazine and Journal of Science* 1859, 17, 162–169.

- [25] Bowden F. P.; Hughes T. P. The mechanism of sliding on ice and snow. *Proc. R. Soc. Lond. A* 1939, 172, 280–298.
- [26] Reynolds O. *Papers on Mechanical and Physical Subjects*. *Nature* 1901, 64, p. 737.
- [27] Bowden F. P. Friction on snow and ice. *Proceedings of the Royal Society of London. Proc. R. Soc. Lond. A* 1953, 217, 462–478.
- [28] Cohen S. C.; Tabor D. The friction and lubrication of polymers. *Proc. R. Soc. Lond. A* 1966, 291, 186–207.
- [29] Evans D. C. B. The Kinetic Friction of Ice. *Proc. R. Soc. Lond. A* 1976, 347, 493–512.
- [30] Kuroiwa, D. The Kinetic Friction on Snow and Ice. *J. Glaciol.* 1977, 19, 141–152.
- [31] Ambach, W.; Mayr, B. Ski gliding and water film. *Cold Regions Science and Technology* 1981, 5, 59–65.
- [32] Oksanen, P.; Keinonen, J. The mechanism of friction of ice. *Wear* 1982, 78, 315–324.
- [33] Glenne, B. Sliding Friction and Boundary Lubrication of Snow. *Journal of Tribology* 1987, 109, 614–617.
- [34] Colbeck, S. C. The Kinetic Friction of Snow. *J. Glaciol.* 1988, 34, 78–86.
- [35] Colbeck, S. C. A Review of the Processes that Control Snow Friction. *COLD REGIONS RESEARCH AND ENGINEERING LAB HANOVER NH* 1992.
- [36] Colbeck, S. C. A review of the friction of snow skis. *Journal of sports sciences* 1994, 12, 285–295.
- [37] Dosch, H.; Lied, A.; Bilgram, J. H. Glancing-angle X-ray scattering studies of the premelting of ice surfaces. *Surface Science* 1995, 327, 145–164.
- [38] Lied, A.; Dosch, H.; Bilgram, J. H. Surface melting of ice Ih single crystals revealed by glancing angle x-ray scattering. *Physical review letters* 1994, 72, 3554–3557.

- [39] Elbaum M.; Schick M. Application of the theory of dispersion forces to the surface melting of ice. *Physical review letters* 1991, 66, 1713–1716.
- [40] Persson, B. N. J. *Sliding Friction: Physical Principles and Applications*, Second Edition; Springer International Publishing, 2000.
- [41] Wettlaufer, J. S. Impurity Effects in the Premelting of Ice. *Phys. Rev. Lett.* 1999, 82, 2516–2519.
- [42] Buhl, D.; Fauve, M.; Rhyner, H. The kinetic friction of polyethylene on snow: the influence of the snow temperature and the load. *Cold Regions Science and Technology* 2001, 33, 133–140.
- [43] Bluhm, H.; Ogletree, D. F.; Fadley, C. S.; Hussain, Z.; Salmeron, M. The pre-melting of ice studied with photoelectron spectroscopy. *J. Phys.: Condens. Matter* 2002, 14, L227-L233.
- [44] Albracht, F.; Reichel, S.; Winkler, V.; Kern, H. Untersuchung von Einflussfaktoren auf das tribologische Verhalten von Werkstoffen gegen Eis: On the influences of friction on ice. *Mat.-wiss. u. Werkstofftech.* 2004, 35, 620–625.
- [45] Bäurle, L.; Szabó, D.; Fauve, M.; Rhyner, H.; Spencer, N. D. Sliding friction of polyethylene on ice: tribometer measurements. *Tribol Lett* 2006, 24, 77–84.
- [46] Winkler, V.; Albracht, F.; Reichel, S. Tribologische Untersuchungen zur Minimierung der Reibung von Sprungski in einer vereisten Anlaufspur. *BISp-Jahrbuch : Forschungsförderung ...* 2007, 339–343.
- [47] Kietzig, A.-M.; Hatzikiriakos, S. G.; Englezos, P. Ice friction: the effect of thermal conductivity. *Journal of Glaciology* 2010.
- [48] Kietzig, A.-M.; Hatzikiriakos, S. G.; Englezos, P. Physics of ice friction. *Journal of Applied Physics* 2010, 107, 81101.
- [49] Hasler, M.; Schindelwig, K.; Mayr, B.; Knoflach, C.; Rohm, S.; van Putten, J.; Nachbauer, W. A Novel Ski–Snow Tribometer and its Precision, *Tribology letters*, 2016, 63.
- [50] Was unter den Brettern passiert. *DER STANDARD*, Oct 5, 2012. <https://www.derstandard.at/story/1348285149636/was-unter-dem-ski-passiert> (accessed April 12, 2021).



- [51] Fessler Eva. Blitzschneller Alles-Messer: zukunft forschung 0212. <https://sport1.uibk.ac.at/fzssa/pdf/blitzschnell.pdf> (accessed April 15, 2021).
- [52] Makkonen, L. A thermodynamic model of sliding friction. *AIP Advances* 2012, 2, 12179.
- [53] Oksanen, P. Friction and Adhesion of ice; Technical Research Centre of Finland: Espoo, 1983.
- [54] Scherge, M.; Böttcher, R.; Spagni, A.; Marchetto, D. High-Speed Measurements of Steel–Ice Friction: Experiment vs. Calculation. *Lubricants* 2018, 6, 26.
- [55] Böttcher, R. Zur Tribologie von strukturierten Skibelägen auf Eis und Schnee: Hochschulschrift, 2015.
- [56] Böttcher, R.; Seidelmann, M.; Scherge, M. Sliding of UHMWPE on ice: Experiment vs. modeling. *Cold Regions Science & Technology* 2017, 141, 171–180.
- [57] Hertz, H. Über die Berührung fester elastischer Körper. In *Journal für die reine und angewandte Mathematik Band 92*; Crelle, A. L., Borchardt, C. W., Schellbach, Eds.; De Gruyter, 1882; pp 156–171.
- [58] Scherge Matthias. Gliding: Skischliffe falsch interpretiert, Team Snowstorm. Open Access Series ISSN 2509-9442. Article 1(2017) 1-6 2017.
- [59] Canale, L.; Comtet, J.; Niguès, A.; Cohen, C.; Clanet, C.; Siria, A.; Bocquet, L. Nanorheology of Interfacial Water during Ice Gliding. *Phys. Rev. X* 2019, 9.
- [60] Lever, J. H.; Taylor, S.; Song, A. J.; Courville, Z. R.; Lieblappen, R.; Weale, J. C. The mechanics of snow friction as revealed by micro-scale interface observations. *J. Glaciol.* 2018, 64, 27–36.
- [61] Velkavrh; Lungevičs; Jansons; Klien; Voyer; Ausserer. The Influence of Isotropic Surface Roughness of Steel Sliders on Ice Friction Under Different Testing Conditions. *Lubricants* 2019, 7, 106.
- [62] Velkavrh, I.; Voyer, J.; Wright, T.; Lungevičs, J.; Jansons, E.; Boiko, I. Variations of ice friction regimes in relation to surface topography and applied operating parameters. *IOP Conf. Ser.: Mater. Sci. Eng.* 2021, 1140, 12033.

- [63] Liefferink, R. W.; Hsia, F.-C.; Weber, B.; Bonn, D. Friction on Ice: How Temperature, Pressure, and Speed Control the Slipperiness of Ice. *Phys. Rev. X* 2021, 11.
- [64] Lemmettylä, T.; Heikkinen, T.; Ohtonen, O.; Lindinger, S.; Linnamo, V. The Development and Precision of a Custom-Made Skitester. *Front. Mech. Eng.* 2021, 7.
- [65] Auganæs, S. B.; Buene, A. F.; Klein-Paste, A. Laboratory testing of cross-country skis – Investigating tribometer precision on laboratory-grown dendritic snow. *Tribology International* 2022, 168, 107451.
- [66] Theile, T.; Szabo, D.; Luthi, A.; Rhyner, H.; Schneebeli, M. Mechanics of the Ski–Snow Contact. *Tribol Lett* 2009, 36, 223–231.
- [67] Weber, B.; Nagata, Y.; Ketzetzi, S.; Tang, F.; Smit, W. J.; Bakker, H. J.; Backus, E. H. G.; Bonn, M.; Bonn, D. Molecular Insight into the Slipperiness of Ice. *The journal of physical chemistry letters* 2018, 9, 2838–2842.
- [68] Baran, L.; Llombart, P.; Rzyško, W.; MacDowell, L. G. Ice friction at the nanoscale, 2022.
- [69] Fenre M. D. Development of a Linear Tribometer, Norwegian University of Science and Technology, Trondheim, 2016.
- [70] Moldestad, D. A. Some aspects of ski base sliding friction and ski base structure, Fakultet for ingeniørvitenskap og teknologi, Trondheim, 1999.
- [71] Stachowiak, G. W.; Batchelor, A. W. *Engineering tribology*; Butterworth-Heinemann: Place of publication not identified, 1993.
- [72] Halling, J. *Principles of tribology*; Macmillan: London, 1978.
- [73] Williams, J. A. *Engineering tribology*; Oxford University Press: Oxford, 1994.
- [74] Cann, P.; Ioannides, E.; Jacobson, B.; Lubrecht, A. A. The lambda ratio, a critical re-examination. *Wear* 1994, 175, 177–188.
- [75] Taylor, R. I. Rough Surface Contact Modelling—A Review. *Lubricants* 2022, 10, 98.

- [76] Olver, A. V.; Spikes, H. A. Prediction of traction in elastohydrodynamic lubrication. *Proceedings of the Institution of Mechanical Engineers, Part J: Journal of Engineering Tribology* 1998, 212, 321–332.
- [77] Budde, R.; Himes, A. High-resolution friction measurements of cross-country ski bases on snow. *Sports Eng* 2017, 20, 299–311.
- [78] Rogowski, I.; Leonard, D.; Gauvrit, J.-Y.; Lanteri, P. Influence of fluorine-based additive content on the physical and physicochemical properties of ski gliding wax. *Cold Regions Science & Technology* 2007, 49, 145–150.
- [79] Styring, P.; Routh, A. F.; Parkinson, S. Friction reduction using self-waxing alpine skis. *Sports Eng* 2012, 15, 117–127.
- [80] Scherge M. Zur Wirkung von Fluorwachsen: Open Access Series ISSN 2509-9442. *Gliding* 2019.
- [81] Breitschädel, F.; Haaland, N.; Espallargas, N. A Tribological Study of UHMWPE Ski Base Treated with Nano Ski Wax and its Effects and Benefits on Performance. *Procedia Engineering* 2014, 72, 267–272.
- [82] Scherge Matthias, T. L. Are fluorinated ski waxes really the non plus ultra? Open Access Series ISSN 2509-9442. Article 3(2020) 14-19 2020.
- [83] Haaland, N. H. Nano ski wax, effects and benefits, Institutt for produktutvikling og materialer. 2013
- [84] FIS - International Ski Federation. The International Ski Competition Rules (ICR). Book III Ski jumping. 2021.
- [85] Scherge M. Wie sinnvoll sind Skitests?, Open Access Series ISSN 2509-9442. *Gliding* 2017.
- [86] Müller, E.; Schwameder, H.; Kornexl, E.; Raschner, C. *Science and skiing*, First edition; [Taylor & Francis]: London, date of publication not identified.
- [87] Nachbauer, W.; Kaps, P.; Hasler, M.; Mössner, M. Friction Between Ski and Snow. In *The Engineering Approach to Winter Sports*; Braghin, F., Cheli, F., Maldifassi, S., Melzi, S., Sabbioni, E., Eds.; Springer New York: New York, NY, 2016; pp 17–32.

- [88] Takeda, M.; Nikki, K.; Nishizuka, T.; Abe, O. Friction of the short model ski at low velocity. *J. Phys.: Conf. Ser.* 2010, 258, 12007.
- [89] Scherge, M.; Böttcher, R.; Richter, M.; Gurgel, U. High-Speed Ice Friction Experiments under Lab Conditions: On the Influence of Speed and Normal Force. *ISRN Tribology 2013*, 2013, 1–6.
- [90] Seymour-Pierce, A.; Lishman, B.; Sammonds, P. Recrystallization and damage of ice in winter sports. *Philosophical transactions. Series A, Mathematical, physical, and engineering sciences* 2017, 375.
- [91] Hong, J.; Talalay, P.; Zhang, N.; Fan, X. Controlling Mechanism of Temperature Dependence of Kinetic Friction of Ice. *Journal of Tribology* 2020, 142.
- [92] McGhee J.R.; Thurman H.O. Determining the kinetic coefficient of ice using a tribometer. *H-SC Journal of sciences vol. IV* 2015.
- [93] Roberts, A. D.; Richardson, J. C. Interface study of rubber-ice friction. *Wear* 1981, 67, 55–69.
- [94] Kennedy, F. E.; Schulson, E. M.; Jones, D. E. The friction of ice on ice at low sliding velocities. *Philosophical Magazine A* 2000, 80, 1093–1110.
- [95] Montagnat, M.; Schulson, E. M. On friction and surface cracking during sliding of ice on ice. *J. Glaciol.* 2003, 49, 391–396.
- [96] Kim, D.; Jung, S.; Lee, J. Friction coefficient measurements on jumping ski patterned running surfaces. *Tribology International* 2022, 175, 107858.
- [97] Verein Deutscher Ingenieure e.V. VDI-Richtlinie 2221:1993-05: Systematic approach to the development and design of technical systems and products; Beuth Verlag GmbH, Berlin, 1993.
- [98] Schuh, G., Ed. *Handbuch Produktion und Management*, 2. vollst. neu bearb. u. erw. Aufl.; Springer Vieweg: Berlin, 2011.
- [99] Verein Deutscher Ingenieure e.V. VDI-Richtlinie 2220:1980-05: Product planning; flow, terms and organization; Beuth Verlag GmbH, Berlin, 1980.

- [100] Verein Deutscher Ingenieure e.V. VDI-Richtlinie 2221 Blatt 1:2019-11: Design of technical products and systems - Model of product design; Beuth Verlag GmbH, Berlin, 2019.
- [101] Verein Deutscher Ingenieure e.V. VDI-Richtlinie 2221 Blatt 2:2019-11: Entwicklung technischer Produkte und Systeme - Gestaltung individueller Produktentwicklungsprozesse; Beuth Verlag GmbH, Berlin, 2019.
- [102] Herstatt, C.; Lüthje, C. Quellen für Neuproduktideen. In Handbuch Technologie- und Innovationsmanagement: Strategie - Umsetzung - Controlling, 1st ed.; Albers, S., Ed.; Gabler Verlag: Wiesbaden, 2015; pp 265–284.
- [103] Ehrlenspiel, K.; Meerkamm, H. Integrierte Produktentwicklung: Denkabläufe, Methodeneinsatz, Zusammenarbeit, 6., überarbeitete und erweiterte Aufl.; Hanser: München, op. 2017.
- [104] Pahl, G.; Beitz, W.; Feldhusen, J.; Grote, K.-H. Konstruktionslehre: Grundlagen erfolgreicher Produktentwicklung Methoden und Anwendung, 7. Aufl.; Springer-Verlag Berlin Heidelberg: Berlin, Heidelberg, 2007.
- [105] Naefe, P. Basiswissen Methodisches Konstruieren: Für Studium und Praxis, 1. Aufl.; Vieweg, F: Wiesbaden, 2008.
- [106] Naefe, P. Einführung in das Methodische Konstruieren: Für Studium und Praxis; mit ... 30 Tabellen, 2., überarb. und erw. Aufl.; Vieweg + Teubner: Wiesbaden, 2012.
- [107] Ponn, J.; Lindemann, U. Konzeptentwicklung und Gestaltung technischer Produkte; Springer Berlin Heidelberg: Berlin, Heidelberg, 2011.
- [108] Zipp F. Entwicklungsleiter Deutscher Skiverband. Personal communication, 2022.
- [109] Conrad, K.-J. Grundlagen der Konstruktionslehre: Methoden und Beispiele für den Maschinenbau und die Gerontik ; mit 107 Tabellen, zahlreichen Kenntnisfragen und Aufgabenstellungen mit Lösungen, 6., aktualisierte und erw. Aufl.; Hanser: München, 2013.

- [110] Roth, K. Konstruieren mit Konstruktionskatalogen: Band 1: Konstruktionslehre, 3. Auflage, erweitert und neu gestaltet; Springer Berlin Heidelberg: Berlin, Heidelberg, 2000.
- [111] Verein Deutscher Ingenieure e.V. VDI-Richtlinie 2222 Blatt 1: Konstruktionsmethodik - Methodisches Entwickeln von Lösungsprinzipien; Beuth Verlag GmbH, Berlin, 1997.
- [112] Forbo Siegling GmbH. Elastische Bänder: Empf. Anlagenkonstruktion 2017.
- [113] Ewellix AB. Präzisionsschienenführungen Katalog, 1–116.
- [114] Koller, R.; Kastrup, N. Prinziplösungen zur Konstruktion technischer Produkte, 2., neubearb. Aufl.; Springer: Berlin, 1998.
- [115] Fischer, U. Tabellenbuch Metall, 45., neu bearb. und erw. Aufl.; Europa-Lehrmittel: Haan-Gruiten, 2011.
- [116] Dankert, J.; Dankert, H. Technische Mechanik: Statik, Festigkeitslehre, Kinetik/Kinetik, 7. Aufl. 2013; Springer Vieweg: Wiesbaden, 2013.
- [117] Zwicky, F. The Morphological Approach to Discovery, Invention, Research and Construction. In *New Methods of Thought and Procedure*; Zwicky, F., Wilson, A. G., Eds.; Springer Berlin Heidelberg: Berlin, Heidelberg, 1967; pp 273–297.
- [118] Srinivasan, N. House of Quality (HOQ) & QFD. Lean Six Sigma, Six Sigma Certification, Feb 7, 2018. <http://www.sixsigmacertificationcourse.com/house-of-quality-hoq-qfd/> (accessed March 12, 2021).
- [119] Technische Universität Braunschweig. House of Quality - Methods. <https://methodos.ik.ing.tu-bs.de/methode/HouseofQuality.html> (accessed March 12, 2021).
- [120] Kafader, U. Auslegung von hochpräzisen Kleinstantrieben: [Grundlagen, Beispiele, Maxon selection program], 1. Aufl.; Verl. Maxon Acad: Sachseln, 2006.
- [121] Grote, K.-H.; Feldhusen, J. *Dubbel*; Springer Berlin Heidelberg: Berlin, Heidelberg, 2014.
- [122] SKF Gruppe. SKF Hochgenauigkeitslager SKF Hochgenauigkeitslager der Reihe „Super-precision bearings“, 2014.

- [123] Tjørstad, R. N.; Rabault, J.; Gundersen, O.; Jensen, A. A field investigation of the friction between cross-country skis and snow, 2021.
- [124] The MathWorks, Inc. Smooth response data. <https://de.mathworks.com/help/curvefit/smooth.html> (accessed November 22, 2022).
- [125] The MathWorks, Inc. Find abrupt changes in signal. <https://de.mathworks.com/help/signal/ref/findchangepts.html> (accessed November 22, 2022).
- [126] Bortz, J. Statistik für Human- und Sozialwissenschaftler: Mit 242 Tabellen, 6., vollst. überarb. und aktualisierte Aufl.; Springer: Berlin, Heidelberg, New York, 2005.
- [127] Herzog, M. H. a.; Francis, G.; Clarke, A. Understanding statistics and experimental design: How to not lie with statistics / Michael H. Herzog, Gregory Francis, Aaron Clarke; Springer: Cham, Switzerland, 2019.
- [128] Kuzmin, L.; Tinnsten, M. Dirt absorption on the ski running surface — quantification and influence on the gliding ability. *Sports Eng* 2006, 9, 137–146.
- [129] Rohm, S.; Unterberger, S. H.; Hasler, M.; Gufler, M.; van Putten, J.; Lackner, R.; Nachbauer, W. Wear of ski waxes: Effect of temperature, molecule chain length and position on the ski base. *Wear* 2017, 384-385, 43–49.
- [130] Montagnat, M.; Duval, P. The viscoplastic behaviour of ice in polar ice sheets: experimental results and modelling. *Comptes Rendus Physique* 2004, 5, 699–708.
- [131] Fiorio B., Meyssonier J., Boulon M. Experimental study of the friction of ice over concrete under simplified ice–structure interaction conditions. *Canadian Journal of Civil Engineering* 2002, pp. 347-359(13).
- [132] Kalliorinne, K.; Sandberg, J.; Hindér, G.; Holmberg, H.-C.; Supej, M.; Larsson, R.; Almqvist, A. A Novel Method for Quantifying Ski-Snow Friction Using an Rtk-Gnss Equipped Sled, 2023.
- [133] Tanaka, K. Kinetic friction and dynamic elastic contact behaviour of polymers. *Wear* 1984, 100, 243–262.

## Figures

Figure 1.1: Geometrical elements for the jumping hill, based on .....	3
Figure 1.2: The four technical parts of a ski jump .....	4
Figure 1.3: In-run track in Klingenthal, Germany (left), track milled into ice surface (middle) and milled grooves in ice track (shown as black areas).....	5
Figure 1.4: Ice track after competition with accumulations of ice (left) and damage to the ice profile due to occurring load (right) in Klingenthal, Germany ..	6
Figure 1.5: Profile width according to the FIS specifications .....	8
Figure 1.6: Running surface with longitudinal structure and grooves .....	8
Figure 1.7: Surface images.....	10
Figure 1.8: Tribological system ski base on ice for ski jumping .....	27
Figure 1.9: Stribeck curve illustration for ice friction .....	29
Figure 2.1: Types of design .....	35
Figure 2.2: General procedure for developing and designing (specific model of a product design process) .....	36
Figure 2.3: Tribometer design process as business process diagram.....	38
Figure 2.4: Process of creating the list of requirements.....	42
Figure 2.5: Hierarchical structure of general requirements on the test rig .....	44
Figure 2.6: Black-Box .....	45
Figure 2.7: Black box of a tribometer.....	46
Figure 2.8: Top level functional structure of a tribometer.....	47
Figure 2.9: Tribometer's subfunctions and their lists of requirements.....	53
Figure 2.10: Plate-on-plate variant .....	57
Figure 2.11: Ski base tensioning .....	57
Figure 2.12: Guidance rollers installation .....	58
Figure 2.13: Procedure of HoQ.....	67
Figure 3.1: Operating pattern with acceleration and immediate deceleration .....	74
Figure 3.2: Load initiations.....	76
Figure 3.3: Parallel spring setup in unloaded configuration (left) and in loaded configuration (right).....	79
Figure 3.4: Frame and base .....	79
Figure 3.5: Roller from front view (left) and in side view from left (right).....	80
Figure 3.6: Main rollers set-up .....	81



Figure 3.7: Bearing of the main rollers.....	82
Figure 3.8: Application of normal force .....	82
Figure 3.9: Weight force plate after several runs .....	83
Figure 3.10: Friction force measurement setup .....	83
Figure 3.11: Measuring unit.....	84
Figure 3.12: Frame design.....	86
Figure 3.13: Roller bearing arrangement in exploded view .....	87
Figure 3.14: Fixed bearing side (left) and floating bearing side (right) in cross section view .....	87
Figure 3.15: Guidance roller in installed condition (top) and roller in cross section view (bottom).....	88
Figure 3.16: Carriage with mounted ice sample .....	89
Figure 3.17: Force measurement setup.....	90
Figure 3.18: Effect of roller distance on COF with 95 % CI.....	93
Figure 3.19: Weight force arrangement: lever arm (left) and roller plate (right) .....	94
Figure 3.20: Linear mode (left) and perpendicular mode (right).....	95
Figure 3.21: Ice sample production principle .....	95
Figure 3.22: Steel mould for ice sample production.....	96
Figure 3.23: Average yield tensile shear force vs. adhesive width at -12 °C with standard deviation error bars .....	96
Figure 3.24: Weight force arrangement and sample contact .....	98
Figure 3.25: Novel linear tribometer .....	98
Figure 3.26: Built tribometer located in the cooling cell .....	99
Figure 4.1: Silicone cast of an ice sample's surface after 470 m sliding distance. ....	102
Figure 4.2: Comparison of nominal and measured surface texture parameters. ...	103
Figure 4.3: Example of an abrasion analysis .....	104
Figure 4.4: Exemplary baseline .....	105
Figure 4.5: Effect of constant speed duration on COF.....	107
Figure 4.6: COF of the unwaxed ski base as a function of the inter-segment latency .....	108
Figure 4.7: Determination of the friction force calculation range with speed over time (top) and friction force over time (bottom) .....	109

Figure 4.8: Flow chart of the automatic data analysis.....	110
Figure 4.9: Resolution vs. number of experiments with resolution criterion .....	111
Figure 4.10: Linearity of the load cell used for measuring the friction force.....	112
Figure 4.11: Result of the mould comparison study.....	113
Figure 4.12: COF vs. sliding distance of six individual experiments per wax grade and for the unwaxed ski base.....	114
Figure 4.13: Impact of fluorine content of the applied waxes on the steady-state COF .....	116
Figure 4.14: 3D-Scan of the unwaxed ski base (left) and as an exemplary representation waxed with H5LF (right).....	119
Figure 4.15: Roughness comparison of different waxes with the unwaxed ski base and ice surface .....	120
Figure 4.16: Formation of grooves on the ice sample with increasing sliding distance .....	121
Figure 4.17: Surface structure modification .....	122
Figure 4.18: Wear-related height loss as a function of sliding distance .....	122
Figure 4.19: Surface free energy as a function of sliding distance .....	124
Figure 4.20: Correlation between the COF in steady-state and the average surface free energy.....	125
Figure 4.21: COF as a function of sliding speed and temperature.....	126
Figure 4.22: Effect of acceleration on COF .....	128
Figure 4.23: Exemplary result of a ramp-up/ramp-down-experiment to verify the difference in COF between acceleration and deceleration .....	129
Figure 4.24: COF during acceleration (red dots) and deceleration (blue dots).....	130
Figure 4.25: COF of the unwaxed ski base sliding against ice at different contact pressures.....	131
Figure AP 1: Mises stress of the input shaft .....	186
Figure AP 2: Mises stress of the output shaft .....	187
Figure AP 3: Torsional stress of the input shaft .....	188
Figure AP 4: Torsional stress of the output shaft.....	189
Figure AP 5: Mises stress of the parallel pins.....	190
Figure AP 6: Simulation visualisation .....	193

## Tables

Table 1.1: Classification of jumping hills.....	1
Table 1.2: Nomenclature for Figure 1.1 .....	2
Table 1.3: Nomenclature for Figure 1.6.....	7
Table 1.4: Conclusions of the literature review.....	26
Table 1.5: Overview of existing tribometers for measuring friction between ski base and snow/ice .....	32
Table 2.1: Project partners' list of requirements .....	39
Table 2.2: Internal and external sources related to university environment.....	40
Table 2.3: Creativity techniques .....	41
Table 2.4: General list of requirements.....	43
Table 2.5: List of subfunctions.....	48
Table 2.6: Analysis of the tribological system for ski jumping.....	51
Table 2.7: List of requirements .....	51
Table 2.8: Solution concept for subfunction I.....	55
Table 2.9: Solution concept for subfunction II.....	58
Table 2.10: Solution concept for subfunction III.....	59
Table 2.11: Solution concept for subfunction IV .....	60
Table 2.12: Solution concept for subfunction V .....	60
Table 2.13: Solution concept for subfunction VI .....	61
Table 2.14: Morphological box.....	64
Table 2.15: Combination of the solution variants into overall solutions .....	65
Table 2.16: Possible combinations of sub functions with solution variants.....	66
Table 2.17: User profile .....	68
Table 2.18: User-oriented requirements .....	68
Table 2.19: Legend of the HoQ .....	69
Table 2.20: HoQ (user requirements versus design requirements .....	70
Table 2.21: Operator's importance ranking .....	71
Table 3.1: Design sub-assemblies for proof of concept.....	73
Table 3.2: Tribometer sub-assemblies .....	85
Table 3.3: Contact pressure nominal (nom) and simulated (sim), transferred by the roller plate .....	91

Table 3.4: Estimation of the ski base's tensile stress while mounted on the tribometer and impact of base tension on COF .....	93
Table 3.5: Parameter range.....	99
Table 4.1: Test parameters of the various test series of this work.....	108
Table 4.2: Average steady-state COFs of the fluorine content test series.....	115
Table 4.3: Hypothesis test .....	117
Table 4.4: Numeric results of the roughness measurements of the ice sample and additionally the unwaxed and waxed ski bases .....	118
Table 4.5: Numeric COF results of sliding speed vs. temperature.....	126
Table 4.6: Numeric COF results of ski base acceleration.....	127
Table 4.7: 95 % CIs of the COF from contact pressure study.....	131
Table AP 1: Summary of key statements .....	156
Table AP 2: Weighting factors for subfunction I .....	163
Table AP 3: Assessment of solution variant 1 .....	164
Table AP 4: Assessment of solution variant 2 .....	164
Table AP 5: Assessment of solution variant 3 .....	165
Table AP 6: Pairwise comparison - bearings installation .....	165
Table AP 7: Assessment for solution variant 1 .....	166
Table AP 8: Assessment for solution variant 2 .....	166
Table AP 9: Pairwise comparison – mounting of the ice specimen .....	167
Table AP 10: Assessment of solution variant 1 .....	168
Table AP 11: Assessment of solution variant 2 .....	168
Table AP 12: Pairwise comparison – load application .....	169
Table AP 13: Assessment of solution variant 1 .....	170
Table AP 14: Assessment of solution variant 2 .....	170
Table AP 15: Assessment of solution variant 3 .....	171
Table AP 16: Pairwise comparison – friction measurement.....	172
Table AP 17: Assessment of solution variant 1 .....	173
Table AP 18: Assessment of solution variant 2 .....	173
Table AP 19: Pairwise comparison – cooling.....	174
Table AP 20: Assessment of solution variant 1 .....	175
Table AP 21: Assessment of solution variant 2 .....	175
Table AP 22: Assessment of solution variant 3 .....	176

Table AP 23: Pairwise comparison of general requirements including subfunctions .....	177
Table AP 24: Assessment of overall solution 1.....	178
Table AP 25: Assessment of overall solution 2.....	179
Table AP 26: Assessment of overall solution 3.....	180
Table AP 27: Assessment of overall solution 4.....	181
Table AP 28: Weighting factors for the user's requirements.....	182
Table AP 29: Tolerances main roller bearings.....	182
Table AP 30: Tolerances ski base preload .....	183
Table AP 31: Tolerances guidance Roller .....	183
Table AP 32: Tolerances roller plate .....	184
Table AP 33: Tolerances shoulder screw .....	185
Table AP 34: Tolerances parallel pin.....	185
Table AP 35: Simulation results of the input shaft at bending stress .....	186
Table AP 36: Simulation results of the output shaft at bending stress.....	187
Table AP 37: Simulation results of the input shaft at torque stress.....	188
Table AP 38: Simulation results of the output shaft at torque stress .....	189
Table AP 39: Simulation results of the parallel pins at bending stress .....	190
Table AP 40: Simulation results of the roller's contact deformation length under load.....	191

## Formulas

Eqn. 1.1 .....	6
Eqn. 1.2 .....	28
Eqn. 3.1 .....	74
Eqn. 3.2 .....	75
Eqn. 3.3 .....	76
Eqn. 3.4 .....	78
Eqn. 3.5 .....	78
Eqn. 3.6 .....	78
Eqn. 3.7 .....	78
Eqn. 4.1 .....	116

## Appendix

Table AP 1: Summary of key statements

### **Faraday M., “On regelation, and on the conservation of force”, 1859 [24]**

- Assumption of the existence of a pre-melted layer of water on ice
- Designated as “quasi-liquid” or “liquid-like” due to different properties in comparison to an usual liquid

### **Bowden F. P. et al., “The mechanism of sliding on ice and snow”, 1939 [25]**

- Low kinetic friction of ice is due to a partial lubricating water layer formed by frictional heat
- The kinetic friction coefficient is independent of velocity, normal force and apparent contact area, but decreases with decreasing temperature
- Pressure melting not alone responsible for creating a water film

### **Bowden F. P., “Friction on snow and ice”, 1953 [27]**

- Friction is independent of the apparent surface area
- Amontons’ law is applicable in the field of ice friction
- Contact area is temperature dependent since the hardness of ice is also temperature dependent
- Ratio of real to apparent contact area is estimated to be 1/30000
- Increase of friction with decreasing sliding speed
- Thermally conductive slider produces higher friction due to an insufficient water film
- Indication that heat conduction plays an important role in ice friction

### **Cohen S. C. et al., “The friction and lubrication of polymers”, 1966 [28]**

- Water is an effective lubricant for hydrophilic (polyamide) plastics as opposed to hydrophobic (polyethylene) ones
- If surface tension of polyethylene is lowered and surface wettability is increased, the COF can be decreased due to sufficient lubrication performance of the water film

### **Evans D. C. B., “The Kinetic Friction of Ice”, 1976 [29]**

- Development of Bowden and Hughes frictional heating theory
- Calculation of heat loss in contact area during friction
- Frictional heat is conducted into the samples as well as into the ice surface
- Ice surface temperature is raised until melting point is reached
- Thermal energy used for melting the ice is low, most of the energy is conducted into the sample and ice surface

### **Kuroiwa, D., “The Kinetic Friction on Snow and Ice”, 1977 [30]**

- Sliding on snow deforms snow grains due to stick-slip friction with accompanied fractures and abrasions
- Measuring and calculation of the real contact area
- Real contact area is only 3.8 % of the nominal contact area
- Average real contact area is around 0.04 mm<sup>2</sup>
- If circular shape is assumed, average contact diameter is around 200 μm
- Estimated that only 1 % of the frictional energy is used to melt the snow (the rest is conducted into the snow and sample)

#### **Ambach, W. et al., “Ski gliding and water film”, 1981 [31]**

- Measuring the thickness of a water film during frictional measurements on snow with a capacitor installed into the ski
- Real skis have been used
- Measurement during natural sliding conditions
- Assumed several micrometres thick water film during sliding (5 μm at -4 °C snow temperature)

#### **Oksanen, P. et al., “The mechanism of friction of ice”, 1982 [32]**

- Further development of the frictional heating theory of Evans
- Assumed that the frictional force is caused by viscous shearing of the water film layers between the sample and ice
- Real contact area was calculated from the quotient of the normal force and indentation hardness of the ice
- Calculated the friction partner's COF and its dependence on temperature, velocity and normal force
- Performed pin-on-disc tribometer tests to validate results

#### **Glennie, B., “Sliding Friction and Boundary Lubrication of Snow”, 1987 [33]**

- Consideration of wet and dry snow
- Total sliding resistance is the sum of dry friction, wet friction, compaction and impact resistances

#### **Colbeck, S. C., “The Kinetic Friction of Snow “, “A review of the friction of snow skis”, “A Review of the Processes that Control Snow Friction”, 1988 – 1994 [34–36]**

- Developed the mathematical description of friction on snow
- Friction experiments lead to the assumption of three friction mechanisms which dominate the water film thickness: dry friction, boundary lubrication as a result of melt water, and capillary drag effects due to water bridge formation
- Heat generated by friction is stored in snow grains: generates water and therefore lubrication
- Repeated passing of the sample on snow creates ice-like surface

- Water film thicknesses ranging from 0.2 to 1.2  $\mu\text{m}$  have been determined

**Dosch, H. et al., “Glancing-angle X-ray scattering studies of the premelting of ice surfaces”, “Surface melting of ice”, 1994 – 1995 [37,38]**

- Studied mirror-like ice surfaces by glancing-angle X-ray scattering
- Investigated surface melting of ice surfaces and its quasi-liquid layers
- Strong evidence that “pre-melting” of the surface builds up water layers below 0 °C
- Ice builds up a quasi-liquid layer at about -13 °C and the water layer develops to several nanometres in thickness at -5 °C

**Strausky, H. et al., “Sliding plastics on ice”, 1998 [16]**

- Performed fluorescence spectroscopy in combination with pin-on-disc experiments
- Sample structure both polished (PMMA) and grooved (ski running base)
- Identification of interfacial water layers
- Limited velocity of 0.005 to 0.1 m/s at a temperature of -2 °C
- Experimental detection limit was 50 nm for PMMA and 250 nm for ski running base
- No water film has been detected
- COF of 0.03 at -2 °C was measured

**Persson, B. N. J., “Sliding Friction: Physical Principles and Applications”, 2000 [40]**

- Developed general principles of heat flow during sliding
- Detailed discussion of interfacial lubrication
- Addressing the question of hydrodynamic boundary conditions in the region of a solid-fluid interface
- Focus on interfacial lubrication and dry friction dynamics
- Theoretical basis for the explanation of snow and ice friction and the development of a numerical simulation by Bäurle in 2006 [19]

**Döppenschmidt, A. et al., “Measuring the Thickness of the Liquid-like Layer on Ice Surfaces with Atomic Force Microscopy”, 2000 [12]**

- Used atomic force microscopy to study the surface melting of ice
- Measured a liquid-like film thickness of approximately 11 nm at -10 °C and 32 nm at a temperature of -1 °C
- Similar layer thicknesses to those described by Dosch et al. [37,38]
- Investigated increasing effect on surface melting due to influence of impurities

**Buhl, D. et al., “The kinetic friction of polyethylene on snow”, 2001 [42]**

- Investigation of sliding process of polyethylene on snow
- Both laboratory pin-on-disc tribometer and field experiments



- Limited test speed of 5 m/s with tribometer
- Large dependence of the COF on the snow temperature was found
- Minimum COF of 0.02 between -3 °C and 0 °C snow temperature
- Increase of COF was observed at higher and lower temperatures
- Increase of surface temperature due to repeated travel of sample over ice surface
- Difference of jumper weight on COF was only measured below -6 °C

**Bluhm, H. et al., “The premelting of ice studied with photoelectron spectroscopy”, 2002 [43]**

- Addressed the existence of a liquid-like layer at the ice surface near its melting point through utilization of electron spectroscopy
- A liquid-like water film exists even at temperatures down to approximately -20 °C
- In the range of 0 °C, the water film is about 2 nm in thickness
- Hydrocarbon particles as contamination material highly increase the pre-melting of ice

**Albracht, F. et al., “Untersuchung von Einflussfaktoren auf das tribologische Verhalten von Werkstoffen gegen Eis“, 2004 [44]**

- Development of a pin-on-disc tribometer
- Spiral inward movement of the measuring arm during a measurement to prevent smoothing and polishing of the ice surface
- 1.2 m stationary disc speed of max. 9.4 m/s with normal forces of up to 10 N at -30 °C to +30 °C

**Bäurle, L. et al., “Sliding friction of polyethylene on snow and ice”, 2006 [19], “Sliding friction of polyethylene on ice”, 2006 [19,45]**

- Development of a 1.8 m pin-on-disc tribometer
- Investigated the formation of the water film caused by friction
- Characterization of contact surface by using scanning electron microscopy, X-ray computed tomography and optical profilometry
- Using numerical modelling to explain energy dissipation mechanisms (dry friction and melt-water film generation)
- Water film thickness and relative contact area are the main factors influencing the friction
- Calculated a film thickness between 30 and 250 nm at -5 °C
- Averaged static contact area between ski and snow surface was found to be 5% of the total surface area (diameter of contact points approximating 100 µm at -10 °C)
- Friction process can be explained solely by meltwater film, surface topology and real contact area (even without capillary action, as assumed by Glenne [20] and Colbeck [21-23])
- COFs of approximately 0.06 were measured at -10 °C

- At higher temperatures, a strong dependence of normal force to COF was observed

**Winkler, V. et al., “Tribologische Untersuchungen zur Minimierung der Reibung von Sprungski in einer vereisten Anlaufspur“, 2007 [46]**

- Used pin-on-disc tribometer to study ice friction of UHMW-PE against a planed off ice surface (developed version of Albracht 2004 [44])
- Reproducible measurements up to 2 m/s
- Specimen generates “line load”
- Decrease of COF due to an increase in normal force (independent of sliding speed and temperature)
- COF decreased with increasing friction speed
- It was concluded that by structuring the ski base, the surface pressure can be increased (increased water film formation is stimulated) and thus a decreased friction force is generated
- Measured COF of 0.013 at -5 °C and 3N normal force

**Kietzig, A.-M. et al., “Ice friction: The effects of surface roughness, structure, and hydrophobicity”, 2009 [13], “Ice friction: the effect of thermal conductivity”, 2010 [47], “Physics of ice friction”, 2010 [48]**

- Friction experiments using a modified parallel-plate rheometer
- Sliding velocities of 0.0036 m/s to 1.45 m/s at temperatures of -1.5 °C to -10°C with thermally insulated samples
- The higher the insulation performance, the lower the measured values of COF
- Classification of ice friction in dry, boundary, mixed and hydrodynamic friction
- Region of interfacial friction was described as a very thin quasi-liquid film layer
- Influence of thermal conductivity on ice friction decreases with increasing sliding speed, while surface wettability becomes more important
- Only at very low velocities is there an influence of the sample structuring on the measured COF
- Existence of a temperature-dependent minimum of the COF was stated
- Under atmospheric conditions no real dry friction can develop
- Even at low temperatures a very thin liquid-like film is formed
- The temperature in the contact zone is below the melting temperature of ice
- Mixed friction occurs when the surface temperature within the contact zone exceeds the melting temperature of ice

**Hasler, M. et al., “Novel Ski–Snow Tribometer and its Precision”, 2016 [49], Fessler E., „Blitzschneller Alles-Messer“, accessed April 15, 2021 [51]**

- Design of a linear-type tribometer
- Complete ski structure with UHMW-PE ski base
- The ski is accelerated to 27.8 m/s (100 km/h) in approx. 0.4 seconds with a maximum speed-dependent measurement section of 18 m
- Loads can be varied between 50 to 700 N at temperatures up to -20 °C
- Indication that a plateau is formed when passing over a snow surface several times

- COFs in the range of 0.04 with a friction speed of 6 m/s at -5 °C have been measured

### **Makkonen, L. et al., “Modelling the friction of ice”, 2014 [20]**

- Developed a thermodynamic model of kinetic ice friction
- Squeeze-out of water and the effect of contact pressure were included
- Model is limited by the absence of mechanical deformation mechanisms
- Size and shape of contact area has to be estimated
- A constantly behaving contact surface was assumed
- Central statement: the energy of the surface is reduced due to heat dissipation into the environment
- The thermodynamic system is not able to perform mechanical work parallel to the sliding movement
- Makkonen disagrees with Kietzig et al.
- No relevance of the region of boundary friction for ice friction
- Temperature in the mixed friction region cannot be above the melting temperature of ice
- Calculation of a COF of 0.05 and a water film thickness of 0.05  $\mu\text{m}$  at -10 °C

### **Böttcher, R. et al., “Zur Tribologie von strukturierten Skibelägen auf Eis und Schnee“, 2015 [55], “Sliding of UHMWPE on ice”, 2017 [56]**

- Developed a 1.6 m plate-on-plate linear tribometer
- Measured a COF of 0.05 at -10 °C with structured UHMW-PE ski bases
- Forces of up to 100 N with temperatures up to -20 °C and max. 1 m/s sliding speed
- Combination of friction model of Makkonen et al. [20] and elastic contact model of Hertz [57]
- Linked the measured friction values with characteristics of the ski structuring
- Temperature of the sliding partners was identified as a decisive factor
- Hardness of the sliding bodies changes with temperature
- Both factors are significantly responsible for temperature-dependent behaviour of the coefficient of friction

### **Scherge M., “Gliding: Skischliffe falsch interpretiert“, 2017 [58]**

- Presented a more energetic view of ski grinds on snow
- Mechanistic view of friction process leads to contradictions
- Question: how much frictional power is generated during sliding contact?
- Capillary forces account for a large proportion of the resistance when a ski glides over snow
- Most of the friction power is converted into heat; water film thickness increases with increasing sliding speed or heavier ski (increased surface pressure)
- Skier does not come within the range of hydrodynamics because skis offer too little surface area

- Increase in speed and/or decrease in pressure on the ski, results in a decrease in friction
- Contrary effects: Water quantity increases with increasing friction power density, but the water film is squeezed out of the friction contact faster with increasing pressure

**Canale, L. et al., “Nanorheology of Interfacial Water during Ice Gliding”, 2019 [59]**

- Studied microscopic mechanisms of ice lubrication using a stroke-probe AFM
- Observation of viscoelastic properties of meltwater
- Measured viscosity was up to 2 orders of magnitude higher than that of pure water
- Due to “oily” behaviour, meltwater is an excellent lubricant
- No temperature increase as a result of friction was measured
- Formation of water film due to abrasion and not melting

**Velkavrh et al., “The Influence of Isotropic Surface Roughness of Steel Sliders on Ice Friction Under Different Testing Conditions” 2019 [61], “Variations of ice friction regimes in relation to surface topography and applied operating parameters”, 2021 [61,62]**

- Ice friction experiments on inclined ice track tribometer and oscillating plate-on-plate tribometer
- Observation of inverse roughness-friction correlation dependent-on measuring set-up and temperature
- Comparison of results generated by different measuring devices must be undertaken with caution

**Liefferink et al., “How Temperature, Pressure, and Speed Control the Slipperiness of Ice”, 2021 [63]**

- Addressed the hardness of an ice surface as one of the dominant variables (pressure and temperature dependent)
- At contact pressures well below the hardness of ice and at temperatures in the range of the melting temperature, friction is dependent on the mobility of water molecules
- When contact pressure is increased to within the range of ice hardness, ploughing of the friction partner through the ice surface becomes dominant
- Only low material dependence if all samples are hydrophilic in character
- No friction-related dependence on thermal conductivity at low speeds

**Lemmettylä et al., “The Development and Precision of a Custom-Made Skitester”, 2021 [64]**

- Introduction of a linear snow tribometer with real ski sizes
- 14 m length and with realistic normal forces and surface pressures

- Simulation of a ski-kicking situation
- Huge variation and influence on measurement results due to ski preparation
- No comparable results

**Auganæs et al., “Laboratory testing of cross-country skis”, 2022 [65]**

- Similar ski-snow linear tribometer as Hasler et al.
- Accommodation of full-size cross-country skis with realistic force situation
- Four different snow tracks
- Similar high precision as Hasler, though with precision variation between snow tracks
- No attempt to distinguish between waxes in terms of their sliding behaviour

Table AP 2: Weighting factors for subfunction I (dominance matrix based on [109])

Evaluation Criteria Subfunction I	Evaluation Criteria Subfunction I										
	Low induced vibration	Acceleration of 5.6 m/s <sup>2</sup> can be achieved	Speed of 100 km/h can be achieved	At least several speed and acceleration gradations possible	Friction direction of the ski base in the direction of structuring	Sufficient sample size to achieve real surface pressure	Planar contact of the samples to each other	No transversal movement of samples to each other	Ice surface preparation	Temperature measurement of ski and ice sample during friction measurement	Fast change of ski and ice sample
3 = less important	1	3	3	1	3	3	1	2	2	1	1
2 = equally important	1	1	3	1	3	2	2	2	2	3	1
1 = more important	3	3	3	3	3	3	3	3	3	3	1
Friction direction of the ski base in the direction of structuring	1	1	1	1	2	1	1	2	1	1	1
Sufficient sample size to achieve real surface pressure	1	1	1	1	2	1	1	1	1	1	1
Planar contact of the samples to each other	3	2	3	1	3	3	3	2	2	2	1
No transversal movement of samples to each other	2	2	3	1	2	3	1	1	1	2	1
Ice surface preparation	2	2	3	1	3	2	3	3	3	1	1
Temperature measurement of ski and ice sample during friction measurement	3	1	3	1	3	2	2	2	3	3	1
Fast change of ski and ice sample	3	3	3	3	3	3	3	3	3	3	3
<b>Total (Σ=220)</b>	20	19	26	12	28	29	17	22	19	18	10
<b>Ranking</b>	5	6	3	10	2	1	9	4	6	8	11
<b>Weighting Factor (Σ=1)</b>	0.091	0.086	0.118	0.055	0.127	0.132	0.077	0.100	0.086	0.082	0.045

Table AP 3: Assessment of solution variant 1

<b>Solution Variant 1 – Plate-on-Plate</b>			
<b>Points</b> <b>1 = Does not fulfil</b> <b>4 = Completely fulfilled</b>			
<b>Requirement</b>	<b>Weighting Factor</b>	<b>Points</b>	<b>Product</b>
Low induced vibration	0.091	3	0.273
Acceleration of 5.6 m/s <sup>2</sup> can be achieved	0.086	4	0.345
Speed of 28 m/s can be achieved	0.118	4	0.473
At least several speed and acceleration gradations possible	0.055	4	0.218
Friction direction of the ski base in the direction of structuring	0.127	4	0.509
Sufficient sample size to achieve real surface pressure	0.132	3	0.395
Planar contact of the samples to each other	0.077	4	0.309
No transversal movement of samples to each other	0.100	4	0.400
Ice surface preparation	0.086	3	0.259
Temperature measurement of ski and ice sample during friction measurement	0.082	4	0.327
Fast change of ski and ice sample	0.045	4	0.182
<b>Total Score</b>			<b>3.691</b>

Table AP 4: Assessment of solution variant 2

<b>Solution Variant 2 – Plate-on-Disc</b>			
<b>Points</b> <b>1 = Does not fulfil</b> <b>4 = Completely fulfilled</b>			
<b>Requirement</b>	<b>Weighting Factor</b>	<b>Points</b>	<b>Product</b>
Low induced vibration	0.091	2	0.182
Acceleration of 5.6 m/s <sup>2</sup> can be achieved	0.086	3	0.259
Speed of 28 m/s can be achieved	0.118	3	0.355
At least several speed and acceleration gradations possible	0.055	4	0.218
Friction direction of the ski base in the direction of structuring	0.127	1	0.127
Sufficient sample size to achieve real surface pressure	0.132	4	0.527
Planar contact of the samples to each other	0.077	3	0.232
No transversal movement of samples to each other	0.100	2	0.200
Ice surface preparation	0.086	1	0.086
Temperature measurement of ski and ice sample during friction measurement	0.082	3	0.245
Fast change of ski and ice sample	0.045	1	0.045
<b>Total Score</b>			<b>2.477</b>

Table AP 5: Assessment of solution variant 3

<b>Solution Variant 3 – Plate-on-Ring</b>			
<b>Points</b> 1 = Does not fulfil 4 = Completely fulfilled			
Requirement	Weighting Factor	Points	Product
Low induced vibration	0.091	4	0.364
Acceleration of 5.6 m/s <sup>2</sup> can be achieved	0.086	4	0.345
Speed of 28 m/s can be achieved	0.118	4	0.473
At least several speed and acceleration gradations possible	0.055	4	0.218
Friction direction of the ski base in the direction of structuring	0.127	4	0.509
Sufficient sample size to achieve real surface pressure	0.132	4	0.527
Planar contact of the samples to each other	0.077	2	0.155
No transversal movement of samples to each other	0.100	4	0.400
Ice surface preparation	0.086	2	0.173
Temperature measurement of ski and ice sample during friction measurement	0.082	4	0.327
Fast change of ski and ice sample	0.045	1	0.045
<b>Total Score</b>			<b>3.536</b>
<b>Average of total score</b>			<b>3.235</b>

Table AP 6: Pairwise comparison - bearings installation

<u>Evaluation Criteria</u>					
3 = less important  2 = equally important  1 = more important	Cost-effective	Possibility for a pre-version with a lower cost input	Easy bearings installation	Easy replacement of the ski base	Low induced vibrations
Cost-effective		2	1	1	1
Possibility for a pre-version with a lower cost input	2		1	1	2
Easy bearings installation	3	3		3	3
Easy replacement of the ski base	3	3	1		3
Low induced vibrations	3	2	1	1	
<b>Total (<math>\Sigma=40</math>)</b>	11	10	4	6	9
<b>Ranking</b>	<b>1</b>	<b>2</b>	<b>5</b>	<b>4</b>	<b>3</b>
<b>Weighting Factor (<math>\Sigma=1</math>)</b>	<b>0.275</b>	<b>0.250</b>	<b>0.100</b>	<b>0.150</b>	<b>0.225</b>

Table AP 7: Assessment for solution variant 1

<b>Solution Variant 1 – Two-sided bearing</b>			
<b>Points</b> 1 = Does not fulfil 4 = Completely fulfilled			
<b>Requirement</b>	<b>Weighting Factor</b>	<b>Points</b>	<b>Product</b>
Cost-effective	0.275	4	1.100
Possibility for a pre-version with a lower cost input	0.250	4	1.000
Manageable bearings installation	0.100	3	0.300
Easy replacement of the ski base	0.150	1	0.150
Low induced vibrations	0.225	3	0.675
<b>Total Score</b>			<b>3.225</b>

Table AP 8: Assessment for solution variant 2

<b>Solution Variant 2 – Cantilevered bearing</b>			
<b>Points</b> 1 = Does not fulfil 4 = Completely fulfilled			
<b>Requirement</b>	<b>Weighting Factor</b>	<b>Points</b>	<b>Product</b>
Cost-effective	0.275	2	0.550
Possibility for a pre-version with a lower cost input	0.250	2	0.500
Manageable bearings installation	0.100	2	0.200
Easy replacement of the ski base	0.150	4	0.600
Low induced vibrations	0.225	3	0.675
<b>Total Score</b>			<b>2.525</b>
<b>Average of total score</b>			<b>2.875</b>



Table AP 9: Pairwise comparison – mounting of the ice specimen

<b><u>Evaluation Criteria</u></b>  3 = less important 2 = equally important 1 = more important	Low-cost implementation	Planar contact with ski base sample	Sufficient size to achieve real surface pressure	Low inherent friction	Fast change of ice sample	Low-vibration mounting	Exclusion of tilting of the ice sample
Low-cost implementation		2	1	1	1	1	1
Planar contact with ski base sample	2		1	1	1	2	2
Sufficient size to achieve real surface pressure	3	3		2	1	3	3
Low inherent friction	3	3	2		1	3	3
Fast change of ice sample	3	3	3	3		3	3
Low-vibration mounting	3	2	1	1	1		3
Exclusion of tilting of the ice sample	3	2	1	1	1	1	
<b>Total (<math>\Sigma=84</math>)</b>	17	15	9	9	6	13	15
<b>Ranking</b>	1	2	5	5	7	4	2
<b>Weighting Factor (<math>\Sigma=1</math>)</b>	<b>0.202</b>	<b>0.179</b>	<b>0.107</b>	<b>0.107</b>	<b>0.071</b>	<b>0.155</b>	<b>0.179</b>

Table AP 10: Assessment of solution variant 1

<b>Solution Variant 1 – Parallel spring</b>			
<b>Points</b> <b>1 = Does not fulfil</b> <b>4 = Completely fulfilled</b>			
Requirement	Weighting Factor	Points	Product
Low-cost implementation	0.202	4	0.810
Planar contact with ski base sample	0.179	2	0.357
Sufficient size to achieve real surface pressure	0.107	4	0.429
Low inherent friction	0.107	4	0.429
Fast change of ice sample	0.071	4	0.286
Low-vibration mounting	0.155	1	0.155
Exclusion of tilting of the ice sample	0.179	1	0.179
<b>Total Score</b>			<b>2.643</b>

Table AP 11: Assessment of solution variant 2

<b>Solution Variant 2 – Rail Guide</b>			
<b>Points</b> <b>1 = Does not fulfil</b> <b>4 = Completely fulfilled</b>			
Requirement	Weighting Factor	Points	Product
Low-cost implementation	0.202	1	0.202
Planar contact with ski base sample	0.179	4	0.714
Sufficient size to achieve real surface pressure	0.107	4	0.429
Low inherent friction	0.107	3	0.321
Fast change of ice sample	0.071	4	0.286
Low-vibration mounting	0.155	4	0.619
Exclusion of tilting of the ice sample	0.179	4	0.714
<b>Total Score</b>			<b>2.571</b>
<b>Average of total score</b>			<b>2.607</b>

Table AP 12: Pairwise comparison – load application

<b><u>Evaluation Criteria</u></b>	Load (surface pressure) equivalent to real jumper weight	Homogeneous load distribution	Vibration-independent	Adjustable	Load must be defined at all times
Load (surface pressure) equivalent to real jumper weight		3	3	2	3
Homogeneous load distribution	1		2	3	3
Vibration-independent	1	2		1	2
Adjustable	2	1	3		3
Load must be defined at all times	1	1	2	1	
<b>Total (<math>\Sigma=40</math>)</b>	5	7	10	7	11
<b>Ranking</b>	<b>5</b>	<b>3</b>	<b>2</b>	<b>3</b>	<b>1</b>
<b>Weighting Factor (<math>\Sigma=1</math>)</b>	<b>0.125</b>	<b>0.175</b>	<b>0.250</b>	<b>0.175</b>	<b>0.275</b>

Table AP 13: Assessment of solution variant 1

<b>Solution Variant 1 – Mechanical Spring</b>			
<b>Points</b> <b>1 = Does not fulfil</b> <b>4 = Completely fulfilled</b>			
Requirement	Weighting Factor	Points	Product
Load (surface pressure) equivalent to real jumper weight	0.125	4	0.500
Homogeneous load distribution	0.175	4	0.700
Vibration-independent	0.25	1	0.250
Adjustable	0.175	4	0.700
Load must be defined at all times	0.275	2	0.550
<b>Total Score</b>			<b>2.700</b>

Table AP 14: Assessment of solution variant 2

<b>Solution Variant 2 – Lever Arm</b>			
<b>Points</b> <b>1 = Does not fulfil</b> <b>4 = Completely fulfilled</b>			
Requirement	Weighting Factor	Points	Product
Load (surface pressure) equivalent to real jumper weight	0.125	4	0.500
Homogeneous load distribution	0.175	4	0.700
Vibration-independent	0.25	4	1.000
Adjustable	0.175	3	0.525
Load must be defined at all times	0.275	3	0.825
<b>Total Score</b>			<b>3.550</b>

Table AP 15: Assessment of solution variant 3

<b>Solution Variant 3 – Weight</b>			
<b>Points</b> <b>1 = Does not fulfil</b> <b>4 = Completely fulfilled</b>			
<b>Requirement</b>	<b>Weighting Factor</b>	<b>Points</b>	<b>Product</b>
Load (surface pressure) equivalent to real jumper weight	0.125	4	0.500
Homogeneous load distribution	0.175	4	0.700
Vibration-independent	0.25	4	1.000
Adjustable	0.175	3	0.525
Load must be defined at all times	0.275	4	1.100
<b>Total Score</b>			<b>3.825</b>
<b>Average of total score</b>			<b>3.358</b>

Table AP 16: Pairwise comparison – friction measurement

<p><b>Evaluation Criteria</b></p> <p><b>3 = less important</b></p> <p><b>2 = equally important</b></p> <p><b>1 = more important</b></p>	Low-cost implementation	Force measurement with low inherent friction	Direct force measurement (no influence by bending of attachments)	Vibration resistant	Minus temperature range
	Low-cost implementation		1	1	1
Force measurement with low inherent friction	3		3	3	3
Direct force measurement (no influence by bending of attachments)	3	1		2	2
Vibration resistant	3	1	2		2
Minus temperature range	3	1	2	2	
<b>Total (<math>\Sigma=40</math>)</b>	<b>12</b>	<b>4</b>	<b>8</b>	<b>8</b>	<b>8</b>
<b>Ranking</b>	<b>1</b>	<b>5</b>	<b>2</b>	<b>2</b>	<b>2</b>
<b>Weighting Factor (<math>\Sigma=1</math>)</b>	<b>0.3</b>	<b>0.1</b>	<b>0.2</b>	<b>0.2</b>	<b>0.2</b>

Table AP 17: Assessment of solution variant 1

Solution Variant 1 – Plate Distance			
<b>Points</b> 1 = Does not fulfil 4 = Completely fulfilled			
Requirement	Weighting Factor	Points	Product
Low-cost implementation	0.3	4	1.2
Force measurement with low inherent friction	0.1	3	0.3
Direct force measurement (no influence by bending of attachments)	0.2	4	0.8
Vibration resistant	0.2	3	0.6
Minus temperature range	0.2	4	0.8
<b>Total Score</b>			<b>3.7</b>

Table AP 18: Assessment of solution variant 2

Solution Variant 2 – Conductor			
<b>Points</b> 1 = Does not fulfil 4 = Completely fulfilled			
Requirement	Weighting Factor	Points	Product
Low-cost implementation	0.3	3	0.9
Force measurement with low inherent friction	0.1	3	0.3
Direct force measurement (no influence by bending of attachments)	0.2	3	0.6
Vibration resistant	0.2	3	0.6
Minus temperature range	0.2	3	0.6
<b>Total Score</b>			<b>3.0</b>
<b>Average of total score</b>			<b>3.35</b>

Table AP 19: Pairwise comparison – cooling

<b>Evaluation Criteria</b>  <b>3 = less important</b>  <b>2 = equally important</b>  <b>1 = more important</b>	Low-cost implementation	Adjustable	Ski base and ice sample are cooled during measurement	Ski base and ice are at the same temperature during measurement	Consistent during measurement	Possibility to examine ice and ski sample during measurement
	Low-cost implementation		1	1	1	1
Adjustable	3		1	3	3	3
Ski base and ice sample are cooled during measurement	3	3		3	3	3
Ski base and ice are at the same temperature during measurement	3	1	1		2	3
Consistent during measurement	3	1	1	2		2
Possibility to examine ice and ski sample during measurement	1	1	1	1	2	
<b>Total (<math>\Sigma=60</math>)</b>	13	7	5	10	11	14
<b>Ranking</b>	<b>2</b>	<b>5</b>	<b>6</b>	<b>4</b>	<b>3</b>	<b>1</b>
<b>Weighting Factor (<math>\Sigma=1</math>)</b>	<b>0.217</b>	<b>0.117</b>	<b>0.083</b>	<b>0.167</b>	<b>0.183</b>	<b>0.233</b>



Table AP 20: Assessment of solution variant 1

<b>Solution Variant 1 – Both samples cooled individually</b>			
<b>Points</b> <b>1 = Does not fulfil</b> <b>4 = Completely fulfilled</b>			
<b>Requirement</b>	<b>Weighting Factor</b>	<b>Points</b>	<b>Product</b>
Low-cost implementation	0.217	3	0.650
Adjustable	0.117	2	0.233
Ski base and ice sample are cooled during measurement	0.083	2	0.167
Ski base and ice are at the same temperature during measurement	0.167	2	0.333
Consistent during measurement	0.183	2	0.367
Possibility to examine ice and ski sample during measurement	0.233	3	0.700
<b>Total Score</b>			<b>2.450</b>

Table AP 21: Assessment of solution variant 2

<b>Solution Variant 2 – Tribometer encapsulated</b>			
<b>Points</b> <b>1 = Does not fulfil</b> <b>4 = Completely fulfilled</b>			
<b>Requirement</b>	<b>Weighting Factor</b>	<b>Points</b>	<b>Product</b>
Low-cost implementation	0.217	3	0.650
Adjustable	0.117	3	0.350
Ski base and ice sample are cooled during measurement	0.083	4	0.333
Ski base and ice are at the same temperature during measurement	0.167	4	0.667
Consistent during measurement	0.183	4	0.733
Possibility to examine ice and ski sample during measurement	0.233	1	0.233
<b>Total Score</b>			<b>2.967</b>

Table AP 22: Assessment of solution variant 3

<b>Solution Variant 3 – Cooling cell</b>			
<b>Points</b> 1 = Does not fulfil 4 = Completely fulfilled			
Requirement	Weighting Factor	Points	Product
Low-cost implementation	0.217	2	0.433
Adjustable	0.117	4	0.467
Ski base and ice sample are cooled during measurement	0.083	4	0.333
Ski base and ice are at the same temperature during measurement	0.167	4	0.667
Consistent during measurement	0.183	3	0.550
Possibility to examine ice and ski sample during measurement	0.233	4	0.933
<b>Total Score</b>			<b>3.383</b>
<b>Average of total score</b>			<b>2.933</b>

Table AP 23: Pairwise comparison of general requirements including subfunctions

<b>Evaluation Criteria</b>																			
	Cost-effective (manufacturing / operation)	Fast realization	Possibility of disassembly	Space saving (lab size)	Safety and security	Functions manageable in university environment	Low maintenance and easy to maintain (low wear)	Low incidence of vibrations	Tilt stable	Measurement with practice-oriented loads and conditions	High reproducibility	Operable by instructed personal	Transportable System	Subfunction I	Subfunction II	Subfunction III	Subfunction IV	Subfunction V	Subfunction VI
Cost-effective (manufacturing / operation)	3	1	1	1	3	2	1	1	1	1	1	3	1	1	1	1	1	1	1
Fast realization	3	3	1	3	3	3	3	3	3	3	3	2	3	3	3	3	3	3	3
Possibility of disassembly	3	3	3	3	3	3	3	3	3	3	3	2	3	3	3	3	3	3	3
Space saving (lab size)	3	1	1	3	2	1	3	3	3	3	3	2	2	3	3	3	3	3	3
Safety and security	1	1	1	1	1	1	1	1	1	1	2	1	1	1	1	1	1	1	1
Functions manageable in university environment	3	1	1	2	3	2	3	3	2	2	2	2	1	1	1	1	1	1	1
Low maintenance and easy to maintain (low wear)	3	1	1	3	3	2	3	3	3	3	3	2	3	3	3	3	3	3	3
Low incidence of vibrations	3	1	1	1	3	1	1	3	2	2	2	3	2	2	2	2	2	2	2
Tilt stable	3	1	1	1	3	1	1	1	3	3	2	2	3	3	3	3	3	3	3
Measurement with practice-oriented loads and conditions	3	1	1	1	3	2	1	2	1	3	3	1	3	3	3	3	3	3	3
High reproducibility	3	1	1	1	3	2	1	2	1	1	2	1	3	3	3	3	3	3	3
Operable by instructed personal	1	1	1	1	2	2	1	2	2	1	2	1	2	2	2	2	2	2	2
Transportable System	3	2	2	2	3	2	2	1	2	3	3	3	3	3	3	3	3	3	3
Subfunction I	3	1	1	2	3	3	1	2	1	1	1	2	1	2	2	2	2	2	2
Subfunction II	3	1	1	1	3	3	1	2	1	1	1	2	1	2	2	2	2	2	2
Subfunction III	3	1	1	1	3	3	1	2	1	1	1	2	1	2	2	2	2	2	2
Subfunction IV	3	1	1	1	3	3	1	2	1	1	1	2	1	2	2	2	2	2	2
Subfunction V	3	1	1	1	3	3	1	2	1	1	1	2	1	2	2	2	2	2	2
Subfunction VI	3	1	1	1	3	3	1	2	1	1	1	2	1	2	2	2	2	2	2
<b>Total (<math>\Sigma=685</math>)</b>	50	21	19	27	53	41	24	37	32	32	35	43	26	40	41	41	41	41	41
<b>Ranking</b>	2	18	19	15	1	4	17	11	13	13	12	3	16	10	4	4	4	4	4
<b>Weighting Factor (<math>\Sigma=1</math>)</b>	0.073	0.031	0.028	0.039	0.077	0.060	0.035	0.054	0.047	0.047	0.051	0.063	0.038	0.058	0.060	0.060	0.060	0.060	0.060

Table AP 24: Assessment of overall solution 1

<b>Overall Solution 1 - A1 – A2 – A3 – B4 – A5 – C6</b>			
<b>Points</b> <b>1 = Does not fulfil</b> <b>4 = Completely fulfilled</b>			
<b>Requirement</b>	<b>Weighting Factor</b>	<b>Points</b>	<b>Product</b>
Cost-effective (manufacturing / operation)	0.073	3.000	0.219
Fast realization	0.031	3.000	0.092
Possibility of disassembly	0.028	4.000	0.111
Space saving (lab size)	0.039	4.000	0.157
Safety and security	0.077	2.000	0.154
Functions manageable in university environment	0.060	4.000	0.239
Low maintenance and easy to maintain (low wear)	0.035	3.000	0.105
Low incidence of vibrations	0.054	2.000	0.108
Tilt stable	0.047	2.000	0.093
Measurement with practice-oriented loads and conditions	0.047	3.000	0.140
High reproducibility	0.051	2.000	0.102
Operable by instructed personal	0.063	4.000	0.250
Transportable system	0.038	2.000	0.076
Subfunction I	0.058	2.703	0.157
Subfunction II	0.060	2.419	0.144
Subfunction III	0.060	1.982	0.118
Subfunction IV	0.060	2.663	0.159
Subfunction V	0.060	2.775	0.166
Subfunction VI	0.060	2.538	0.151
<b>Total Score</b>		<b>2.741</b>	

Table AP 25: Assessment of overall solution 2

<b>Overall Solution 2 - A1 – A2 – A3 – C4 – A5 – C6</b>
---

<p><b>Points</b>  <b>1 = Does not fulfil</b>  <b>4 = Completely fulfilled</b></p>
---

Requirement	Weighting Factor	Points	Product
Cost-effective (manufacturing / operation)	0.073	4.000	0.292
Fast realization	0.031	4.000	0.122
Possibility of disassembly	0.028	4.000	0.111
Space saving (lab size)	0.039	4.000	0.157
Safety and security	0.077	2.000	0.154
Functions manageable in university environment	0.060	4.000	0.239
Low maintenance and easy to maintain (low wear)	0.035	4.000	0.140
Low incidence of vibrations	0.054	2.000	0.108
Tilt stable	0.047	2.000	0.093
Measurement with practice-oriented loads and conditions	0.047	3.000	0.140
High reproducibility	0.051	2.000	0.102
Operable by instructed personal	0.063	4.000	0.250
Transportable system	0.038	3.000	0.114
Subfunction I	0.058	2.703	0.157
Subfunction II	0.060	2.419	0.144
Subfunction III	0.060	1.982	0.118
Subfunction IV	0.060	2.869	0.171
Subfunction V	0.060	2.775	0.166
Subfunction VI	0.060	2.538	0.151

<b>Total Score</b>
--------------------

<b>2.930</b>
--------------

Table AP 26: Assessment of overall solution 3

<b>Overall Solution 3 - A1 – A2 – B3 – B4 – A5 – C6</b>
---

<p><b>Points</b>  <b>1 = Does not fulfil</b>  <b>4 = Completely fulfilled</b></p>
---

Requirement	Weighting Factor	Points	Product
Cost-effective (manufacturing / operation)	0.073	1.000	0.073
Fast realization	0.031	1.000	0.031
Possibility of disassembly	0.028	4.000	0.111
Space saving (lab size)	0.039	4.000	0.157
Safety and security	0.077	2.000	0.154
Functions manageable in university environment	0.060	4.000	0.239
Low maintenance and easy to maintain (low wear)	0.035	3.000	0.105
Low incidence of vibrations	0.054	4.000	0.215
Tilt stable	0.047	4.000	0.186
Measurement with practice-oriented loads and conditions	0.047	4.000	0.186
High reproducibility	0.051	4.000	0.204
Operable by instructed personal	0.063	4.000	0.250
Transportable system	0.038	2.000	0.076
Subfunction I	0.058	2.703	0.157
Subfunction II	0.060	2.419	0.144
Subfunction III	0.060	1.929	0.115
Subfunction IV	0.060	2.663	0.159
Subfunction V	0.060	2.775	0.166
Subfunction VI	0.060	2.538	0.151

<b>Total Score</b>
--------------------

<b>2.880</b>
--------------

Table AP 27: Assessment of overall solution 4

<b>Overall Solution 4 - A1 – A2 – B3 – C4 – A5 – C6</b>
---

<p><b>Points</b>  <b>1 = Does not fulfil</b>  <b>4 = Completely fulfilled</b></p>
---

Requirement	Weighting Factor	Points	Product
Cost-effective (manufacturing / operation)	0.073	1.000	0.073
Fast realization	0.031	1.000	0.031
Possibility of disassembly	0.028	4.000	0.111
Space saving (lab size)	0.039	4.000	0.157
Safety and security	0.077	2.000	0.154
Functions manageable in university environment	0.060	4.000	0.239
Low maintenance and easy to maintain (low wear)	0.035	3.000	0.105
Low incidence of vibrations	0.054	4.000	0.215
Tilt stable	0.047	4.000	0.186
Measurement with practice-oriented loads and conditions	0.047	4.000	0.186
High reproducibility	0.051	4.000	0.204
Operable by instructed personal	0.063	4.000	0.250
Transportable system	0.038	2.000	0.076
Subfunction I	0.058	2.703	0.157
Subfunction II	0.060	2.419	0.144
Subfunction III	0.060	1.929	0.115
Subfunction IV	0.060	2.869	0.171
Subfunction V	0.060	2.775	0.166
Subfunction VI	0.060	2.538	0.151

<b>Total Score</b>
--------------------

<b>2.892</b>
--------------

Table AP 28: Weighting factors for the user's requirements

<b>Evaluation Criteria</b>					
<b>3 = less important</b>					
<b>2 = equally important</b>					
<b>1 = more important</b>					
	Easy mounting of the counter bodies	Stability of the wear test rig	No risk of injury	Low noise level	Simple operation
Easy mounting of the counter bodies		3	3	1	2
Stability of the wear test rig	1		3	1	1
No risk of injury	1	1		1	1
Low noise level	3	3	3		3
Simple operation	2	3	3	1	
<b>Total (<math>\Sigma=40</math>)</b>	7	10	12	4	7
<b>Ranking</b>	<b>3</b>	<b>2</b>	<b>1</b>	<b>5</b>	<b>3</b>
<b>Weighting Factor (<math>\Sigma=1</math>)</b>	<b>0.175</b>	<b>0.25</b>	<b>0.3</b>	<b>0.1</b>	<b>0.175</b>

Table AP 29: Tolerances main roller bearings

<b>Part</b>	<b>Part Number</b>	<b>Basic Size of Fit [mm]</b>	<b>Tolerance Limits [mm]</b>	<b>Min./Max. Size [mm]</b>
Bearing	N62	Ø 62	0 -0.013	62 61.987
		Ø 40	0 -0.012	40 39.988
Bearing Seats	04-01 04-02	69.15 g6	-0.01 -0.029	69.14 69.121
		Ø 62 H7	+0.03 0	62.03 62
		Ø 19.5	+0.02 0	19.52 19.5
		69.15 g6	-0.01 -0.029	69.14 69.121
Bearing Seats	04-03 04-04	Ø 62 H7	+0.03 0	62.03 62
		Ø 40 k5	+0.013 +0.002	40.013 40.002
Shaft	03-04	Ø 40 k5	+0.013 +0.002	40.013 40.002
		Ø 19.5 m6	+0.021 +0.008	19.521 19.508
Base Strut	02-07 02-08	69.15 H7	+0.03 0	69.18 69.15



Parts Joined	Basic Size of Fit	Lowest Interference	Highest Interference
Bearing / Bearing Seat	Ø 62	-0.043	0
Bearing / Shaft	Ø 40	+0.002	+0.025
Bushing / Bearing Seat	Ø 19.5	+0.006	+0.021
Bearing Seat / Base Strut	69.15	-0.059	-0.01

Table AP 30: Tolerances ski base preload

Part	Part Number	Basic Size of Fit [mm]	Tolerance Limits [mm]	Min./Max. Size [mm]
Bearing	N70	Ø 28	0	28
			-0.009	27.991
		Ø 12	0	12
			-0.008	11.992
Bearing Seat	04-11	Ø 28 H7	+0.021	28.021
			0	28
Shaft	04-10	Ø 12 h7	0	12
			-0.018	11.982
Parts Joined		Basic Size of Fit	Lowest Interference	Highest Interference
Bearing / Bearing Seat		Ø 28	-0.03	0
Bearing / Shaft		Ø 12	-0.018	+0.008

Table AP 31: Tolerances guidance Roller

Part	Part number	Basic Size of Fit [mm]	Tolerance Limits [mm]	Min./Max. Size [mm]
Bearing	N69	Ø 35	0	35
			-0.011	34.989
		Ø 17	0	17
			-0.008	16.992
Bearing Block	05-03 05-04	Ø 35 H7	+0.025	35.025
			0	35
Shaft	05-07	Ø 17 k5	+0.009	17.009
			+0.001	17.001
Housing Cover	05-05	Ø 35 f7	-0.03	34.970
			-0.05	34.950

Parts Joined	Basic Size of Fit	Lowest Interference	Highest Interference
Bearing / Bearing Block	Ø 35	-0.036	0
Bearing / Shaft	Ø 17	+0.001	+0.017
Bearing Block / Housing Cover	Ø 35	-0.03	-0.075

Table AP 32: Tolerances roller plate

Part	Part Number	Basic Size of Fit [mm]	Tolerance Limits [mm]	Min./Max. Size [mm]
Bearing	N64	Ø 16	0	16
			-0.008	15.992
		Ø 5	0	5
			-0.008	4.992
Roller	07-22	Ø 16 N7	-0.005	15.995
			-0.023	15.977
Shaft	07-12	Ø 5 h6	0	5
			-0.008	4.992
Strut 1+4	07-13 07-14	Ø 5 H7	+0.012	5.012
			0	5
Strut 2+3	07-20 07-21	Ø 7 H7	+0.012	7.012
			0	7
Bushing	07-15 07-16 07-17 07-18 07-19	Ø 7 n6	+0.019	7.019
			+0.01	7.01
		Ø 5 J7	+0.006	5.006
			-0.006	4.994

Parts Joined	Basic Size of Fit	Lowest Interference	Highest Interference
Bearing / Roller	Ø 16	-0.003	-0.023
Bearing / Shaft	Ø 5	-0.008	+0.008
Shaft / Strut 1+4	Ø 5	-0.02	0
Shaft / Strut 2+3	Ø 7	-0.02	0
Bushing / Strut 2+3	Ø 7	-0.002	+0.019
Shaft / Bushing	Ø 5	-0.014	+0.006

Table AP 33: Tolerances shoulder screw

Part	Part Number	Basic Size of Fit [mm]	Tolerance Limits [mm]	Min./Max. Size [mm]
Shoulder Screw	04-12	Ø 20 f9	-0.02	19.98
			-0.07	19.93
Fitting Strut	02-01	Ø 20 H7	+0.02	20.02
	02-02		0	20
Base Strut	02-07	Ø 21 H13	+0.39	21.39
	02-08		0	21
Bearing Seat	04-03	Ø 20 H7	+0.02	20.02
	04-04		0	20

Parts Joined	Basic Size of Fit	Lowest Interference	Highest Interference
Shoulder Screw / Fitting Strut	Ø 20	-0.02	-0.09
Shoulder Screw / Base Strut	Ø 20	-1.02	1.46
Shoulder Screw / Bearing Seat	Ø 20	-0.02	-0.09

Table AP 34: Tolerances parallel pin

Part	Part Number	Basic Size of Fit [mm]	Tolerance Limits [mm]	Min./Max. Size [mm]
Parallel Pin	04-12	Ø 25 m6	+0.021	25.021
			+0.008	25.008
Base Strut	02-07	Ø 25 H7	+0.021	25.021
	02-08		0	25
Bearing Seat	04-03	Ø 25 H7	+0.021	25.021
	04-04		0	25

Parts Joined	Basic Size of Fit	Lowest Interference	Highest Interference
Parallel Pin / Base Strut	Ø 25 H7/m6	25.013	25.021
Parallel Pin / Bearing Seat	Ø 25 H7/m6	25.013	25.021

Table AP 35: Simulation results of the input shaft at bending stress

<b>Mesh information</b>	
<b>Meshing type</b>	Volumetric meshing
<b>Meshing type used</b>	Standard mesh
<b>Jacobi-Points</b>	4 points
<b>Element size</b>	4.16397 mm
<b>Tolerance</b>	0.208199 mm
<b>Total number of knots</b>	84,235
<b>Total number of elements</b>	57,108
<b>Maximum aspect ratio</b>	13.693
<b>% of elements with aspect ratio &lt; 3</b>	98.7
<b>% of elements with aspect ratio &gt; 10</b>	0.0158
<b>% of distorted elements (Jacobi)</b>	0
<b>Results</b>	
<b>Force input</b>	307 N
<b>Type</b>	Mises criterion
<b>Min.</b>	1.29e-07 MPa / Knots: 81,681
<b>Max.</b>	2.22 MPa / Knots: 68,437

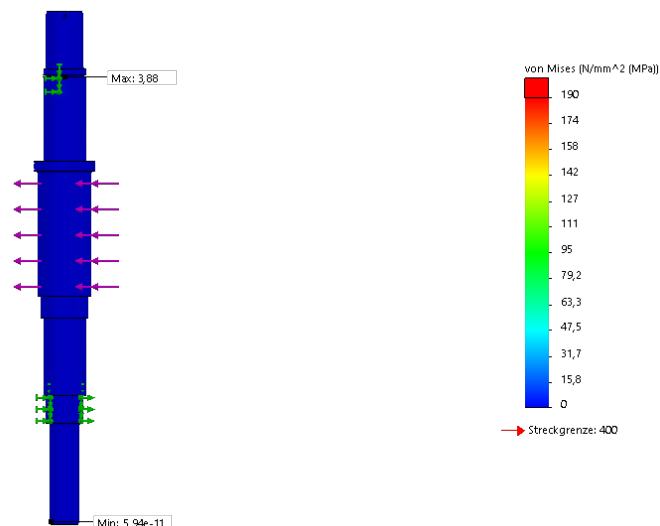


Figure AP 1: Mises stress of the input shaft

Table AP 36: Simulation results of the output shaft at bending stress

<b>Mesh information</b>	
<b>Meshing type</b>	Volumetric meshing
<b>Meshing type used</b>	Standard mesh
<b>Jacobi-Points</b>	4 points
<b>Element size</b>	4.24012 mm
<b>Tolerance</b>	0.212006 mm
<b>Total number of knots</b>	82,405
<b>Total number of elements</b>	55,538
<b>Maximum aspect ratio</b>	13.415
<b>% of elements with aspect ratio &lt; 3</b>	98.6
<b>% of elements with aspect ratio &gt; 10</b>	0.0108
<b>% of distorted elements (Jacobi)</b>	0
<b>Results</b>	
<b>Force input</b>	2000 N
<b>Type</b>	Mises criterion
<b>Min.</b>	3.87e-10 MPa / Knots: 73,436
<b>Max.</b>	3.87e-10 MPa / Knots: 73,436

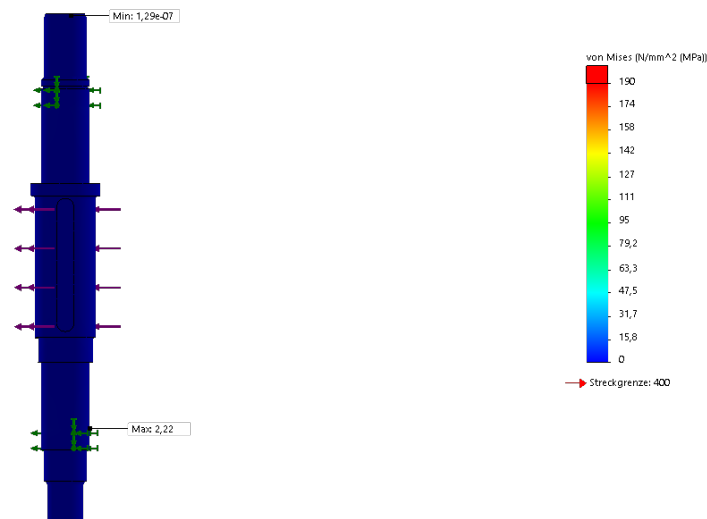


Figure AP 2: Mises stress of the output shaft

Table AP 37: Simulation results of the input shaft at torque stress

<b>Mesh information</b>	
<b>Meshing type</b>	Volumetric meshing
<b>Meshing type used</b>	Standard mesh
<b>Jacobi-Points</b>	4 points
<b>Element size</b>	4.14035 mm
<b>Tolerance</b>	0.207365 mm
<b>Total number of knots</b>	82,419
<b>Total number of elements</b>	53,379
<b>Maximum aspect ratio</b>	13.429
<b>% of elements with aspect ratio &lt; 3</b>	98.2
<b>% of elements with aspect ratio &gt; 10</b>	0.0111
<b>% of distorted elements (Jacobi)</b>	0
<b>Results</b>	
<b>Torque input</b>	60 Nm
<b>Type</b>	Mises criterion
<b>Min.</b>	5e-10 MPa / Knots: 34,879
<b>Max.</b>	33.6 MPa / Knots: 1,021

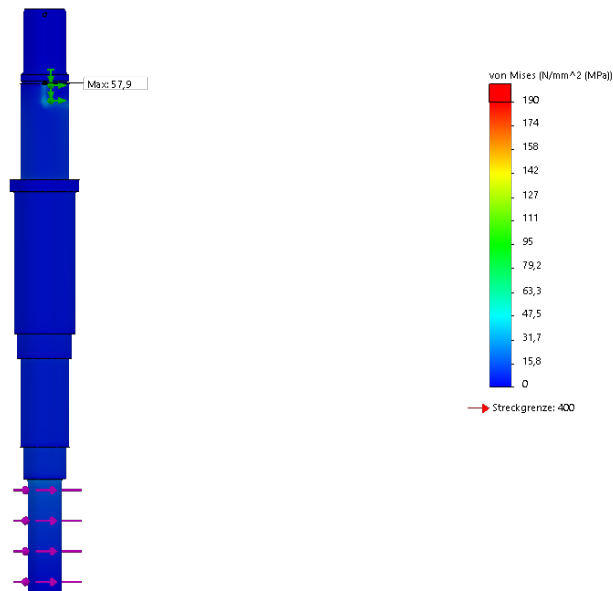


Figure AP 3: Torsional stress of the input shaft

Table AP 38: Simulation results of the output shaft at torque stress

<b>Mesh information</b>	
<b>Meshing type</b>	Volumetric meshing
<b>Meshing type used</b>	Standard mesh
<b>Jacobi-Points</b>	4 points
<b>Element size</b>	4.24012 mm
<b>Tolerance</b>	0.212006 mm
<b>Total number of knots</b>	82,405
<b>Total number of elements</b>	55,538
<b>Maximum aspect ratio</b>	13.415
<b>% of elements with aspect ratio &lt; 3</b>	98.6
<b>% of elements with aspect ratio &gt; 10</b>	0.0108
<b>% of distorted elements (Jacobi)</b>	0
<b>Results</b>	
<b>Torque input</b>	60 Nm
<b>Type</b>	Mises criterion
<b>Min.</b>	5e-11 MPa / Knots: 34,444
<b>Max.</b>	33.9 MPa / Knots: 1,024

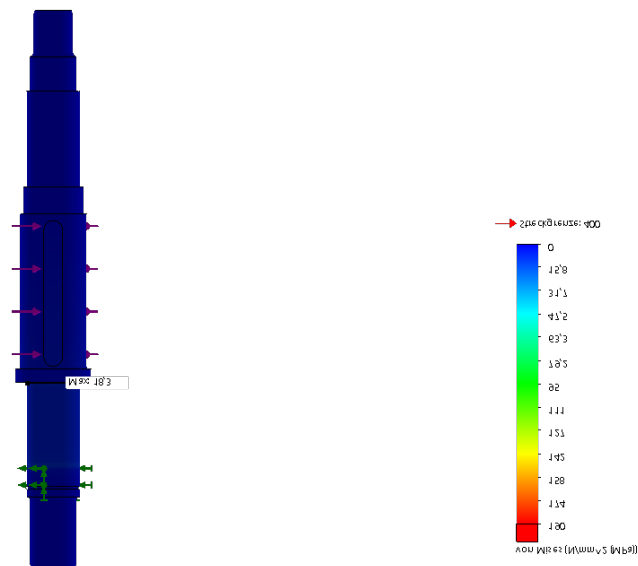


Figure AP 4: Torsional stress of the output shaft

Table AP 39: Simulation results of the parallel pins at bending stress

<b>Mesh information</b>	
<b>Meshing type</b>	Volumetric meshing
<b>Meshing type used</b>	Standard mesh
<b>Jacobi-Points</b>	4 points
<b>Element size</b>	1.35901 mm
<b>Tolerance</b>	0.0679505 mm
<b>Total number of knots</b>	62,977
<b>Total number of elements</b>	42,901
<b>Maximum aspect ratio</b>	4.602
<b>% of elements with aspect ratio &lt; 3</b>	99.9
<b>% of elements with aspect ratio &gt; 10</b>	0.0108
<b>% of distorted elements (Jacobi)</b>	0
<b>Results</b>	
<b>Torque input</b>	286 Nm
<b>Type</b>	Mises criterion
<b>Min.</b>	1.53e-06 MPa / Knots: 2,786
<b>Max.</b>	1.53e-06 MPa / Knots: 61,624

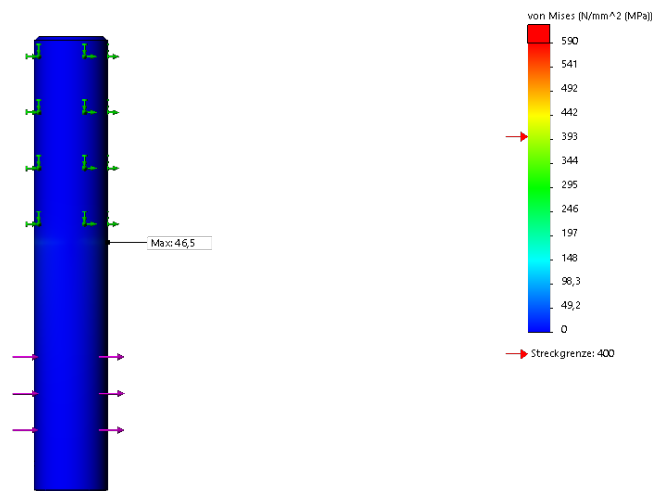


Figure AP 5: Mises stress of the parallel pins



Table AP 40: Simulation results of the roller's contact deformation length under load

<b>Material information</b>	
<b>Name</b>	EPDM (ethylene propylene diene monomer)
<b>Model type</b>	Linear, elastic, isotropic
<b>Tensile strength</b>	24 MPa
<b>Young's modulus</b>	3 MPa
<b>Poisson's ratio</b>	0.495
<b>Mass density</b>	900 kg/m <sup>3</sup>
<b>Study properties</b>	
<b>Type of analysis</b>	Non-linear, static
<b>Solver type</b>	FFEPPlus
<b>Incompatible connection options</b>	Simplified
<b>Control method</b>	Force
<b>Iterative method</b>	Newton-Raphson
<b>Integration method</b>	Newmark
<b>Mesh information</b>	
<b>Meshing type</b>	Volumetric meshing
<b>Meshing type used</b>	Curve-based mesh
<b>Jacobi-Points</b>	4 points
<b>Element size</b>	4.90554 mm
<b>Total number of knots</b>	5,423
<b>Total number of elements</b>	3,074
<b>Maximum aspect ratio</b>	3.5201
<b>% of elements with aspect ratio &lt; 3</b>	99.9
<b>% of elements with aspect ratio &gt; 10</b>	0
<b>% of distorted elements (Jacobi)</b>	0
<b>Results</b>	
<b>Normal force</b>	0.75 N
<b>Type</b>	Mises criterion
<b>Min.</b>	5.125e-16 MPa / Knots: 1,039
<b>Max.</b>	3.434e-03 MPa / Knots: 16
<b>Deformation length at contact</b>	0.04 mm
<b>Results</b>	
<b>Normal force</b>	1.51 N
<b>Type</b>	Mises criterion
<b>Min.</b>	1.031e-15 MPa / Knots: 1,039
<b>Max.</b>	6.914e-03 MPa / Knots: 16
<b>Deformation length at contact</b>	0.07 mm

<b>Results</b>	
<b>Normal force</b>	2.08 N
<b>Type</b>	Mises criterion
<b>Min.</b>	1.419e-16 MPa / Knots: 1,039
<b>Max.</b>	9.524e-03 MPa / Knots: 16
<b>Deformation length at contact</b>	0.09 mm

---

<b>Results</b>	
<b>Normal force</b>	2.35 N
<b>Type</b>	Mises criterion
<b>Min.</b>	1.603e-16 MPa / Knots: 1,039
<b>Max.</b>	1.076e-02 MPa / Knots: 16
<b>Deformation length at contact</b>	0.1 mm

---

<b>Results</b>	
<b>Normal force</b>	2.64 N
<b>Type</b>	Mises criterion
<b>Min.</b>	1.710e-15 MPa / Knots: 1,039
<b>Max.</b>	1.148e-02 MPa / Knots: 16
<b>Deformation length at contact</b>	0.17 mm

---

<b>Results</b>	
<b>Normal force</b>	4.71 N
<b>Type</b>	Mises criterion
<b>Min.</b>	3.205e-15 MPa / Knots: 1,039
<b>Max.</b>	2.158e-02 MPa / Knots: 16
<b>Deformation length at contact</b>	0.2 mm

---

<b>Results</b>	
<b>Normal force</b>	6.47 N
<b>Type</b>	Mises criterion
<b>Min.</b>	4.394e-15 MPa / Knots: 1,039
<b>Max.</b>	2.964e-02 MPa / Knots: 16
<b>Deformation length at contact</b>	0.27 mm

---

<b>Results</b>	
<b>Normal force</b>	8.24 N
<b>Type</b>	Mises criterion
<b>Min.</b>	5.586e-15 MPa / Knots: 1,039
<b>Max.</b>	3.776e-02 MPa / Knots: 16
<b>Deformation length at contact</b>	0.33 mm

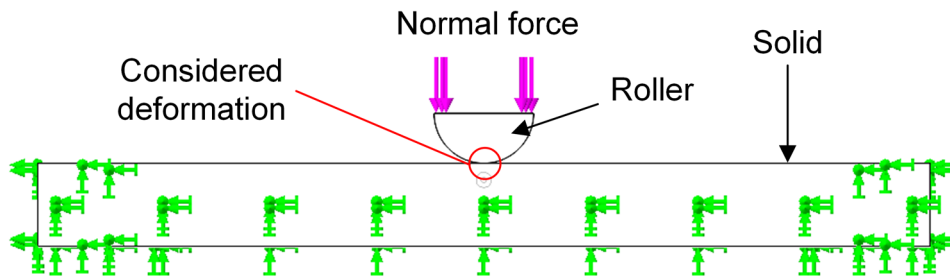


Figure AP 6: Simulation visualisation

## Publications contributions

### Peer-reviewed publications

1. Lutz J., Gebhard A., Zipp F., Schuster J. Investigation of the impact of the fluorine-content of ski wax on the friction between ice and ski base using a novel tribometer. DOI: 10.1016/j.triboint.2023.108705
2. Müller, D., Gottmann, J., Lutz, J., Schuster, J., Fischer, U. Modification of EPDM-seals to prevent aroma carry-over during the bottling of wine. DOI: 10.1016/j.aiepr.2022.08.004
3. Schuster, J.; Lutz, J.; Shaik, Y.; Yaddavalli, V. Recycling of fluoro-carbon-elastomers – a review. DOI: 10.1016/j.aiepr.2022.08.002
4. Kazmi, S. M. R.; Schuster, J.; Lutz, J. Exploring the Potential to Uniquely Manufacture Curved VARTM Epoxy Composites Using Cost-Effective FDM Molds. DOI: 10.4236/ojcm.2020.103004
5. Schuster, J.; Schütz, M.; Lutz, J.; Lempert, L. Prediction of the Enhanced Out-of-Plane Thermal Conductivity of Carbon Fiber Composites Produced by VARTM. DOI: 10.4236/ojcm.2016.64010

### Conference contributions

6. Lutz J., Reichart, G. Tribologische Studie von UHMW-Polyethylen auf Eis
7. Lutz J., Schuster J. Evaluierung eines Eistribometers-Tribologische Untersuchungen an ultrahochmolekularem Polyethylen auf Eis
8. Lutz J., Schuster J. Wissenschaft und Wintersport am Campus Pirmasens
9. Schuster, J., Lutz, J., Brandl, R., Reichart, G. Characterization and improvement of friction between ice and coated bases of jumping skis to increase take-off velocity

### Patents

10. Schuster J., Lutz J., Mesostrukturelle Aufrauvorrichtung für den Reibpartner Schnee oder Eis bei Tribometern mit umlaufenden Bändern, DE102021117038

## Curriculum Vitae

### Personal data

Name	Johannes Alexander Lutz
Place of birth	Rodalben
Nationality	German

### Work experience

07/2023 – present	Operations Manager, profine GmbH, Pirmasens
01/2023 – 05/2023	Test engineer, Deutscher Skiverband Leistungssport GmbH, Planegg
08/2021 – 12/2022	Project engineer, Hochschule Kaiserslautern
09/2019 – 07/2021	Freelance engineer
03/2018 – 10/2018	Lecturer employment, IHK Pfalz, Ludwigshafen
10/2013 – 08/2019	Project engineer, Hochschule Kaiserslautern
11/2011 – 04/2012	Laboratory engineer, Hochschule Darmstadt
05/2011 – 10/2011	Research Associate, Hochschule Darmstadt

### Education

03/2011 – 08/2013	Master's program in plastic technology, Hochschule Darmstadt (M. Eng.)  Master's thesis: „Development and evaluation of low-cost manufacturing methods for low-volume structural composite products”, Centre for Advanced Composite Materials, University of Auckland, New Zealand
09/2007 – 03/2011	Bachelor's program in plastic technology, Hochschule Kaiserslautern (B. Eng.)  Bachelor's thesis: „Novel bagging concepts for out-of-autoclave processing”, Center for Composite Materials, University of Delaware, USA
01/2004 – 07/2006	Professional training as a process mechanic for plastics and rubber technology, profine GmbH, Pirmasens